# Electroweak Interactions and Fundamental Symmetries in Light Nuclei with Short-range Effective Field Theories

A Dissertation Presented for the

Doctor of Philosophy

Degree

The University of Tennessee, Knoxville

Zichao Yang

December 2021

© by Zichao Yang, 2021

All Rights Reserved.

雄关漫道真如铁，而今迈步从头越

# Acknowledgments

Firstly, I would like to express my thanks of gratitude to my advisor, Dr. Lucas Platter, roughly around a thousand times, for his endless guidance, assistance, intelligence, as well as kindness, great sense of humor and friendship through the years. I won't be able to finish this dissertation without all his help. I will give my special thanks to Dr. Wael Elkamhawy for his friendship and intelligence, knowledge, and participation in the first project. Dr. Emanuele Mereghetti was very instrumental in the completion of the rest projects in this dissertation. It was indeed a pleasure to have his collaboration. I want to express my deepest appreciation to him. I was also fortunate to collaborate with Dr. Hans-Werner Hammer, Dr. Matthias Schindler, and Dr. Jared Vanasse.

I would like to thank Dr. Thomas Papenbrock for lecturing the graduate Nuclear Physics courses and being very creative and patient in teaching. He also serves as my committee member, together with two other respectable gentlemen, Dr. Miguel Madurga and Dr. Lawrence Heilbronn. I appreciate their helps, effort, time, and kindness more than I could say. At UT, I also enjoy learning from Dr. Christian Batista, Dr. George Siopsis, and Dr. Maxim Lavrentovich in QM, QFT, and biophysics, respectively.

I also appreciate the conversations, joys, and friendship with my colleagues, Dr. Samuel Emmons, Dr. Daniel Odell, Dr. Jose Bonilla, Dr. Jonas Braun, and Dr. Marcel Schmidt. At Knoxville, my roommates and best friends, Dr. Hao Zhang and Dr. Xin Wen, both also in the Department of Physics and Astronomy, helped me a lot both in studying and living a good life. Additionally, I would express my thanks to my friends at the nuclear theory group, including Dr. Spencer Beloin, Dr. Sophia Han, Dr. Xingfu Du, Dr. Aaina Bansal, Dr. Mohammad Al-Mamum, Dr. Chenyi Gu, and Dr. Chinmay Mishra. Also, special thanks to Ms. Chrisanne Romeo, Dr. Marianne Breinig and Ms. Maria Fawver as well as other

staff members in the Department of Physics and Astronomy for their perpetual kindness and helps during all theses years. All names above are in time order.

At last, I want to thank my wife, Yukun Ma, for her endless support during the past years. She holds half the sky and deserves half the honor. My father, Xingyun Yang, and my mother, Weihua Yu, value education above anything. I will simply thank my parents for everything since I don't think words are enough to express my gratitude.

# Abstract

Effective field theories(EFTs) are powerful tools to study nuclear systems that display separation of scales. In this dissertation, we present halo EFT results for the $\beta$-delayed proton emission from $^{11}$Be, and pionless EFT results for three-nucleon systems.

Halo nuclei are simply described by a tightly bound core and loosely bound valence nucleons. Using the halo EFT, we calculate the rate of the rare decay $^{11}$Be, which is a well-known halo nucleus, into $^{10}\mathrm{Be} + p + e^- + \bar{\nu}_e$. We assume a shallow $1/2^+$ resonance in the $^{10}\mathrm{Be}-p$ system with an energy consistent with a recent experiment by Ayyad *et al.* and obtain a branching ratio and a resonance width of this decay. Our calculation shows that the experimental branching ratio and resonance parameters of Ayyad *et al.* are consistent with each other. Thus, no exotic mechanism (such as beyond the standard model physics) is needed to explain the experimental decay rate.

Electric dipole moments (EDMs) of nucleons receive negligible contributions from the CKM mechanism and are thus, extremely sensitive probes of CP-violation beyond the Standard Model. Using the pionless EFT, we calculate the EDMs of three-nucleon systems at leading order. Neglecting the Coulomb interaction, we consider the triton and $^3$He, and also investigate them in the Wigner-SU(4) symmetric limit. We also calculate the electric dipole form factor and find numerically that the momentum dependence of the electric dipole form factor in the Wigner limit is, up to an overall constant (and numerical accuracy), the same as the momentum dependence of the charge form factor. At last, under the same framework, charge form factors with Coulomb interactions are considered both perturbatively and non-perturbatively to NLO. The third Zemach moment of $^3$He is evaluated and compared to experimental results.

Keywords: Effective field theory, halo nuclei, beta decay, electric dipole moment, form factor

# Table of Contents


**1 Introduction** **1**

**2 Effective Field Theory** **3**

2.1 Effective Field Theories in a Nutshell . . . . . 3

2.1.1 What is an Effective Field Theory? . . . . . 3

2.1.2 Why EFT in Nuclear Physics? . . . . . 4

2.1.3 How to Construct an EFT? . . . . . 5

2.2 A Brief Review of Nucleon-Nucleon Scattering . . . . . 7

2.3 Pionless Effective Field Theory . . . . . 10

2.3.1 Renormalizing Pionless EFT . . . . . 11

2.3.2 Dimer Field Formalism . . . . . 14

2.4 Halo Nuclei and Halo Effective Field Theory . . . . . 16

2.4.1 Halo Nuclei . . . . . 16

2.4.2 Lagrangian of Halo EFT . . . . . 18

2.4.3 Renormalization of the Core-Neutron System . . . . . 19

**3 $\beta$-delayed proton emission from $^{11}$Be** **25**

3.1 Introduction . . . . . 25

3.2 Theoretical Foundations . . . . . 28

3.3 Weak Matrix Element and Decay Rate . . . . . 30

3.4 Beta-strength Sum Rule . . . . . 31

3.5 Hadronic Current without Resonant Final State Interactions . . . . . 32

3.6 Hadronic Current with Resonant Final State Interactions . . . . . 33

3.7 Results without Resonant Final State Interactions . . . . . 34
3.8 Results with Resonant Final State Interactions . . . . . 36
3.9 Numerical Implementation . . . . . 39
3.10 Conclusion . . . . . 39

**4 Electric Dipole Moments of Three-nucleon Systems in the Pionless Effective Field Theory 42**

4.1 Introduction . . . . . 42
4.2 Theoretical Building Blocks . . . . . 46
4.2.1 The three-nucleon bound state vertex function . . . . . 49
4.3 The T-odd vertex function . . . . . 52
4.3.1 Integral equations in the SU(4) limit . . . . . 53
4.4 Three-nucleon form factors . . . . . 54
4.5 Results . . . . . 57
4.6 Summary . . . . . 64

**5 $^3$He with Coulomb Interactions in the Pionless Effective Field Theory 67**

5.1 Introduction . . . . . 67
5.2 Effective Lagrangian . . . . . 68
5.3 $^3$He Vertex Function . . . . . 71
5.3.1 Wavefunction Renormalization . . . . . 77
5.3.2 The "Ks" diagram . . . . . 79
5.3.3 The "Kc" diagram . . . . . 81
5.3.4 The triangle diagrams, "Kt1" and "Kt2" . . . . . 83
5.3.5 The box diagram "Kb" . . . . . 85
5.3.6 Off-shell Vertex Functions Kernels . . . . . 88
5.4 Calculations of Charge Form Factor Diagrams . . . . . 91
5.4.1 Diagram A . . . . . 91
5.4.2 Diagram B . . . . . 93
5.4.3 Diagram C . . . . . 94
5.4.4 Diagram B-tri 1 . . . . . 95

5.4.5 Diagram B-tri 2 . . . . . 97
5.4.6 Diagram B-tri 3 . . . . . 99
5.4.7 Diagram B-box . . . . . 101
5.4.8 Diagram C-spectators . . . . . 103
5.4.9 Diagram C-pp . . . . . 105
5.5 The Third Zemach Moment and Numerical Implementation . . . . . 109
5.6 Results . . . . . 110

**Bibliography** **113**

**Appendices** **129**

A Special Functions . . . . . 130
A.1 Coulomb wave function . . . . . 130
A.2 The Coulomb function of the first kind . . . . . 131
A.3 The Coulomb function of the second kind . . . . . 132
A.4 Partial-wave projected Coulomb Green's function . . . . . 132
A.5 Whittaker function . . . . . 133
A.6 Kummer functions . . . . . 134
A.7 Tricomi function . . . . . 134
A.8 Gamow-Sommerfeld factor . . . . . 134
B Hadronic Amplitudes for Gamow-Teller and Fermi Transitions . . . . . 136
B.1 Energy conservation (with recoil) . . . . . 136
B.2 Energy Conservation (without recoil) . . . . . 137
B.3 Hadronic current without resonant final state interactions in S-wave . 137
B.4 Hadronic current without resonant final state interactions in P-wave . 139
B.5 $S$-wave halo nuclei with final state interaction . . . . . 140
C Projectors and Indices Projections . . . . . 143
C.1 Two and Three Body Projectors . . . . . 144
C.2 Indices of the $^3$He Vertex Functions . . . . . 146
D The deuteron electric dipole form factor and EDM . . . . . 149
E Expressions for electric form factors $F_C$ and $F_{\mathrm{I}}$ . . . . . 151

F Expressions for form factor $F_{\mathrm{II}}$ . . . . . 155
F.1 Boosted vertex functions (of Diagram A) . . . . . 155
F.2 Diagram A . . . . . 157
F.3 Diagrams B and D . . . . . 157
F.4 Diagrams C and E . . . . . 158
G Expressions for form factor $F_{SU(4)}$ . . . . . 160

**Vita** **162**

# List of Tables

3.1 Summary of parameters used in numerical implementation of $\beta$-delayed proton emission from $^{11}$Be. . . . . 40

4.1 Coefficients of the $^{3}$H EDM low-energy constants for different values of the cutoff $\Lambda$. . . . . 60

4.2 Square radii of the two-body EDFF induced by the CPV operators in Eq. (4.2.8), computed at $\Lambda = 60$ GeV. The $C^{(1)}_{^1S_0-^3P_0}$ squared radii have a numerical error of approximately 10 % since the corresponding dipole moments are relatively small. The other radii have few-percent numerical uncertainties, which we do not show. . . . . 66

# List of Figures


2.1 Diagrammatic representation of a two-body scattering amplitude, which can be expressed as a sum of diagrams including the $C_0$ vertex contribution. . . . 17

2.2 Dyson equation with auxiliary dimer fields representing two-body bound states. The thick double line is the dressed dimer propagator while the thin double line represents the bare dimer propagator. Single solid lines are single nucleon propagators. . . . . 17

2.3 Confirmed and suggested halo nuclei. Neutron halo nuclei are shown by green square and candidates of neutron halo are shown by light green. Orange squares show the proton halos. This figure is taken from Ref. [148]. . . . . 17

2.4 A schematic diagram of $^{11}$Be, which is known as a one-neutron halo nucleus. Red and blue balls represent proton and neutron, respectively. . . . . 20

2.5 Diagrammatatic form of the Dyson equation. The thick black line denotes the dressed $S$-wave halo propagator, the grey line denotes the bare halo propagator and the thin solid and dashed line denote the neutron and core propagator, resepctively. . . . . 20

2.6 Diagrammatic representation of the Dyson equation for the dressed $P$-wave halo propagator. The thick (thin) double line denotes the dressed (bare) $P$-wave halo propagator. . . . . 24

3.1 $(a)$: Feynman diagram for the weak decay of a one-neutron halo nucleus into the corresponding core and a proton with Coulomb final state interactions only. $(b)+(c)$: Contributions of resonant final state interactions. The thin double line in the middle denotes the dressed $^{10}\mathrm{Be}-p$ propagator. The shaded ellipse denotes the Coulomb Green's function. . . . . 35

3.2 Differential decay rate $d\Gamma/dE$ for $\beta$-delayed proton emission from $^{11}$Be as a function of the final-state particle energy $E$. The dash-dotted line shows our EFT result without resonant final state interactions while the solid line gives the result obtained by Baye and Tursunov [11]. The dashed line shows the EFT result including a resonance at $E_R = 0.196$ MeV in the outgoing channel at NLO. The colored bands give the EFT uncertainty. . . . . 35

3.3 Possible resonance parameter combinations fulfilling the sum rule. The dash-dotted line shows the combinations for $r_0 = 0$ fm at LO corresponding to $r_0^C = 0$ fm while the dashed line shows the combinations for $r_0 = 2.7$ fm at NLO corresponding to $r_0^C = 1.5$ fm. The green bands show the resonance parameters given in Ref. [9]. . . . . 37

3.4 Partial decay rate as a function of the resonance energy at NLO using the corresponding resonance width in accordance with the sum rule (see Fig 3.3). Explanation of curves and bands is given in inset. . . . . 40

4.1 Diagrammatic representation of the LO three-body CP-even vertex function. The (dashed) double line denotes a dressed spin-singlet (spin-triplet) dibaryon propagator. . . . . 51

4.2 $\not{P}\not{T}$ vertex function. A blue square denotes the $\not{P}\not{T}$ vertex function, while a black square an insertion of the operators in Eq. (4.2.8). Remaining notation as in Fig. 4.1. . . . . 51

4.3 Diagrams contributing to the one-body component of the EDFF, defined in Eq. (4.4.3). Here, the double line can denote a spin-triplet or singlet dimer. The black square denotes an insertion of the nucleon EDM, defined in Eq. (4.2.6). 56

4.4 Diagrams for the three-nucleon EDM form factor at LO that involve a CP-odd two-nucleon interaction. . . . . 56
4.5 Cutoff dependence of the $^3$H EDM two-nucleon contributions. . . . . 60
4.6 The EDFF contributions arising from five different two-nucleon CP-odd operators as a function of $q^2$. . . . . 61

5.1 Diagrammatic representation of the LO three-body ($^3$He) coulomb vertex function. The double line denotes a dressed spin-triplet dibaryon propagator. The dashed double line (with dot) denotes a dressed spin-singlet np (pp) channel dibaryon propagator. The wavy lines represent Coulomb photon propagators. . . . . 72
5.2 Partial diagrams contribute to the homogeneous terms of the $^3$He vertex function. The double solid line here represents either deuteron dimer propagator or a spin-singlet np dimer propagator to avoid verbosity. The dashed double line with dot denotes a spin-singlet pp dimer propagator. The wavy lines represent Coulomb photon propagators. The (c) and (d) are mostly called "triangular" diagrams in the literatures, while (e) is called the "box" diagram. The kernels of diagram (a) to (e) are denoted as $K_s$, $K_c$, $K_{t1}$, $K_{t2}$ and $K_b$, respectively. . . . . 76
5.3 The self-energy is represented by the sum of three diagrams. The solid, dashed and dashed-dot double lines represents the spin-triplet, spin-singlet-np, and spin-singlet-pp dimer propagators, respectively. . . . . 78
5.4 Diagrams contributing to the $^3$He charge form factor. Blue circles represent the $^3$He vertex function with full Coulomb interactions. Wavy lines are Coulomb photons. The double line denotes either spin-triplet or spin-singlet dimers. Solid ellipse in (j) represent Coulomb bubbles. The complex conjugate diagrams of (d), (e), (f) and (g), which are not displayed here for simplicity, also contributing to the charge form factors. (a), (b) and (c) are also the full diagrams contribute to charge form factors without Coulomb, but with no Coulomb vertex functions. . . . . 90

5.5 Leading order results, in the absence of Coulomb interactions, of the charge form factors of $^3$H and $^3$He as functions of $q$. . . . . 111
5.6 Leading order results of the charge form factors of $^3$He with and without Coulomb interactions as functions of $q$. The charge form factor without Coulomb is evaluated at triton binding energy. . . . . 111
7 The first re-scattering process considered in the final state interaction. The thin double line in the middle is the bare boron-11 dimer propagator. Solid eclipses are coulomb bubbles. Single solid and dashed line are nucleon field and core field, respectively. . . . . 150
8 Diagrams contribute to the deuteron EDM. The black squares denote insertions of CP-odd operators. We omitted the diagrams that have the CP-odd operators to the right of the photon-nucleon vertex. . . . . 150

# Chapter 1

# Introduction

Our world displays interesting physics emerges at all different scales. On the other hand, the richness of physical phenomena enhances the complexity of discovering principles of nature. To be more specific, it is a tedious and almost impossible task if one wants to calculate observables of low-energy nuclear systems starting with Quantum Chromodynamics (QCD). Effective field theory (EFT) frameworks are widely used in modern theoretical nuclear physics studies. EFTs are quantum field theories apply to specific momenta scales with carefully selected degrees of freedoms, and can make calculations concise and with controllable error. In general, this dissertation is an application of short-range EFTs to low-energy nuclear systems.

In this work, we investigate two different but related systems, one neutron halo nuclei and three-nucleon bound states.

Halo nuclei are a set of exotic nuclei with a tightly bound core and loosely bound valence nucleons. Thus, halo nuclei can be considered as effective few-body systems. $^{11}$Be is a one neutron halo consists of a $^{10}$Be core and a valence neutron. A neutron can decay into a proton and emits an electron and neutrino through $\beta$-decay. The weak decay of the valence neutron of $^{11}$Be is studied within the halo EFT framework for in this thesis. The neutron lifetime puzzle has bothered people for decades [159]. $^{11}$Be is a perfect natural laboratory to verify possible theories. The success of halo EFT eliminates the necessity of an unknown dark decay mode proposed by Fornal and Grinstein [48] to explain this puzzle.

In the Standard Model (SM), the breaking of fundamental discrete symmetries of charge conjugation $C$, charge conjugation and parity $CP$ is a necessary condition for the dynamical generation of a matter-antimatter asymmetry in the Universe [129]. All observed $CP$ violation (CPV) in the kaon and $B$ meson systems can be explained by the Cabibbo-Kobayashi-Maskawa (CKM) mechanism. CPV in the SM fails to generate the observed matter-antimatter asymmetry of the Universe by several orders of magnitude [52, 54, 53, 75]. Electric dipole moments (EDMs) of leptons, nucleons, atomic and molecular systems receive negligible contributions from the CKM mechanism. The existence of non-zero EDM from light nuclei are thus, extremely sensitive probes of CPV beyond the SM. $^3$H and $^3$He are typical three-nucleon systems. Here, using the pionless EFT framework on three-nucleon systems, theoretical scattering amplitudes can be directly related to corresponding non-zero EDM measurements. In addition, we can also describe $^3$He's properties including Coulomb interactions within the pionless EFT framework.

This thesis is organized as follows: Firstly, in Chapter 2, we explain the ideas of effective field theories. The pionless EFT and halo EFT, which are essential for this dissertation, are introduced specifically. Renormalization and the dimer formalism of both EFTs are discussed as well as the phenomenology of halo nuclei. In Chapter 3, halo EFT is applied to $^{11}$Be to study the beta-delayed proton emission from $^{11}$Be. We report the branching ratio of the decay into the continuum with a resonance in the final state $^{11}$B. Recent experiment [9] confirmed the work. In Chapter 4, the three-nucleon systems, $^3$H and $^3$He, are investigated at leading order in pionless effective field theory. We calculate the electric dipole moments together with electric dipole form factors without Coulomb interactions. In Chapter 5, we study the three-body system of $^3$He with the pionless EFT including the Coulomb interactions between protons. The non-perturbative vertex function and charge form factors with Coulomb interactions are studied both analytically and numerically. In addition, the third Zemach moment of $^3$He is calculated. In the Appendices, we include more details about the special functions, hadronic currents of halo beta decay, and one and two body electric dipole form factor diagrams.

# Chapter 2

# Effective Field Theory

Low energy effective field theories (EFT) are applied to few-body nuclear systems in this dissertation. It is essential to introduce EFT first before we present the progress we made. The majority of this section providing background knowledge about EFT. First, we explain the concept of effective theory and effective field theory. Then we illustrate the benefits and necessity of why we need EFTs in theoretical nuclear physics. We then discuss the basic ideas about constructing an EFT with the example of the gravitational potential of a particle moving close to Earth's surface. We then review the low-energy nucleon-nucleon scattering covered in basic quantum mechanics as well as the effective range expansion. Finally, we describe the pionless effective field theory, which is considered as the cornerstone of this dissertation, in detail.

## 2.1 Effective Field Theories in a Nutshell

### 2.1.1 What is an Effective Field Theory?

In science, almost all of the currently known theories are effective theories. An effective theory should always be "effective" within its range of application. We will consider theory to be effective if it satisfies two requirements. First, it should have the ability to explain existing experiments and predict results within specific errors. Second, it should be relatively easy to use and straightforward. The first requirement is obvious. The second requirement

guarantees that even in a future, where we have an "ultimate" theory, people will still prefer to use effective theories in the range of application. A straightforward example is that people's photos on ID cards do not have extremely high resolutions, but already enough to prove identity, even though we can provide photos with much higher resolution nowadays.

In physics, in order to probe short-distance phenomena, we need large momenta, which is due to the Compton wavelength. One can also try to measure something very precisely by increasing energy levels. For example, the resolution of an optical microscope is limited by the natural light wavelength, which has an energy level of a few electron volts, which is usually good enough for medical and biology studies. To get molecule-to-atom-level details, we need to use electron microscopes, which have an energy level up to 40 keV, which is the energy scale usually needed typically in material physics. In particle physics, we accelerate protons from GeV to TeV to study the structure and properties of elementary particles.

On the other hand, at a low energy scale, we could have predictive and concise theories without considering all the details about short-distance physics. One example is Newtonian mechanics, which works well in daily life without considering any relativistic or quantum effects. Now we say that an effective field theory (EFT) is a quantum field theory that includes the appropriate degrees of freedom to describe physical phenomena occurring at a chosen length scale or energy scale while ignoring substructure and degrees of freedom at shorter distances. All currently know quantum field theories are EFTs [80].

Before we dive into more details, we give additional references materials for references. General introductions of effective field theories by Polchinski [112], Howard Georgi [55], and David Kaplan [80] are classic and heuristic. Matthew Schwartz's textbook on quantum field theories is in the perspective of EFTs [135]. Weinberg also provides rich information about EFTs in his textbook [158]. For low-energy EFTs and few-body applications, Hammer, König, and Platter provide valuable reviews [63, 109].

### 2.1.2 Why EFT in Nuclear Physics?

Studying nuclei with a phenomenological nucleon-nucleon potential has been very successful, which I will refer to as the traditional approach in nuclear physics. By firstly constructing an NN-potential and use it to fit the NN-scattering phase shift data, one can tune the necessary

parameters and use the potential to predict and explain nuclear observables. Weinberg first suggested that effective field theories can describe nuclei and nuclear matter equally or even better [156, 157]. He stated that the chiral effective Lagrangian contains two parts. First, the nucleon-pion couplings represent long-distance nuclear interactions. While short-range physics is included through contact interactions. In this work, we will not discuss details of chiral EFTs. What we learned from the example above is that just like using a nuclear potential, EFT coupling constants can be fit to reproduce experimental data and then to predict and explain future experiments.

Since both ways are solid, why do we have to use EFTs? There are several benefits of using EFT in nuclear physics. First of all, using an EFT gives us a more natural framework. The effective Lagrangian and relative Feynman diagrams depict the long and short-range physics clearer than a potential can do. Second, in an EFT, it is easy to identify the error and estimate the level of accuracy. Last, it is more straightforward and convenient to consider relativistic effects, dynamical processes in an EFT framework than a potential model. So far, numerous progress has been made on effective field theories, which are considered modern approaches in nuclear physics.

### 2.1.3 How to Construct an EFT?

To describe the physics at some momentum scale $m$, we do not need to know the detailed dynamics of what is going on at momentum scales $\Lambda \gg m$, which is considered a key principle of EFT.

The most crucial requirement to construct an EFT is the identification of at least two separated scales. The ratio of these two scales is used to construct a small expansion parameter. In the most simple case, we need one low scale, Q, and a high scale, $M_{hi}$. Q associated with the typical momentum of the physical system that we want to describe. $M_{hi}$, which is also called the breakdown scales, associated with the physics that our EFT does not need to resolve.

The basic steps to describe a physical system using EFT are as follows.

- Step 1: Determine relevant degrees of freedom, i.e., what fields will be used.

- Step 2: Consider the symmetries of the system, i.e., determine the structures of interactions.

- Step 3: Consider the expansion parameters and find a leading-order description, i.e., a power counting.

There are, in general, two directions, top-down and bottom-up, of constructing effective field theories. We prefer the top-down approach when high energy theory is understood, but we find it is easier to construct a more straightforward theory at low energy. For example, we do not need to include quarks to calculate hydrogen energy levels. We want to make the bottom-up approach when the underlying theory is unknown or non-perturbative. The Standard Model is such an example of a bottom-up approach.

To illustrate the ideas above to everyone, now we look at an elementary problem. Suppose we have a particle of mass $m$ moving close to Earth's surface. Now let us construct an effective theory for it:

- Step 1: Determine the degrees of freedom. Degrees of freedom are coordinates of tangent space $(x, y, z)$, whose origin is on the ground.

- Step 2: Symmetries of the system. The interaction, the gravitational potential $V$, is invariant under translations along $x$ and $y$ and rotations around $z$. As for space inversion, $V$ is even for $x, y$, odd for $z$. Thus we determine $V = V(z)$ contains all powers of $z$. Be aware that the breakdown scale is the Earth's radius, $R$, which is much larger than $|z|$.

- Step 3: Power counting. Since $V(z) = \sum_{n=0}^{\infty} c_n z^n$ all terms should be equal in size at the breakdown scale. We conclude $c_1 R^1 \sim c_n R^n$. Since $c_n \sim c_1 R^{n-1}$, we say $c_n z^n \sim c_1 z (z/R)^{n-1}$. Thus we have a power counting and $V(z) = \sum_{n=0}^{\infty} c_1 z (z/R)^{n-1}$. If it is really close to the surface so that $z$ is much smaller than $R$, we could ignore most of the terms in $V(z)$.

Matching: The potential we've got have roughly no difference from what we learn in middle school, $\Delta V = -mgz$. Consider a relatively more precise theory, $V(z) = -\frac{GMm}{R+z}$,

whose Taylor expansion is just the EFT we have above. We just need to match our EFT to this theory to get constants to all orders. And we got $c_n = n!GMm(-1/R)^{n+1}$, $c_0 = -GMm/R$.

## 2.2 A Brief Review of Nucleon-Nucleon Scattering

Low energy nucleon-nucleon (NN) scattering typically refers to neutron-neutron(n-n), neutron-proton(n-p) and proton-proton(p-p) scattering. Here we will neglect electromagnetic interactions, spin structures, and the mass difference between proton and neutron. Consider a short-range nucleon-nucleon potential, $V_{NN}$, the Hamiltonian of such a system is

$$H = \frac{\boldsymbol{p}_1^2}{2M_N} + \frac{\boldsymbol{p}_2^2}{2M_N} + V_{NN} \ , \tag{2.2.1}$$

where particle 1 and 2 are labeled. It is more intuitive to work in the center-of-mass frame. The Hamiltonian becomes

$$H = \frac{\mathbf{P}^2}{2M_{tot}} + \frac{\boldsymbol{k}^2}{2M_R} + V_{NN} \ , \tag{2.2.2}$$

where total mass $M_{tot} = 2M_N$, reduced mass $M_R = M_N/2$, $\mathbf{P} = \boldsymbol{p}_1 + \boldsymbol{p}_2$, and $\boldsymbol{k} = (\boldsymbol{p}_1 - \boldsymbol{p}_2)/2$. Now the two-body problem is reduced to an effective one-body problem. Through out this dissertation, we will use a very similar principle to solve nuclear systems with a so-called dimer formalism. We notice that the NN potential depends only on the center-of-mass variables. From now on, our discussion is limited only in the center-of-mass frame. In quantum mechanics, we describe the scattering process with an incoming plane wave and an outgoing scattered wave. In an elastic scattering process, we describe the incoming and outgoing relative momenta as $\boldsymbol{k}$, with energy $E = \frac{k^2}{2M_R}$. Then the asymptotic form of the wave function is

$$\psi_E^{(+)}(\mathbf{r}) \underset{r\to\infty}{\longrightarrow} (2\pi)^{-3/2} \left( e^{i\mathbf{k}\cdot\mathbf{r}} + f(k,\theta,\phi)\frac{e^{ikr}}{r} \right) \ , \tag{2.2.3}$$

where $\theta = \arccos(k_{in}k_{out})$ is the scattering angle. The scattering amplitude $f(k,\theta,\phi)$ carries out all the physical information, and directly related to scattering differential cross section,

which is a physical observable, by

$$\frac{d\sigma}{d\Omega}(k,\theta,\phi) = |f(k,\theta,\phi)|^2 \ . \tag{2.2.4}$$

Notice that we have ignored the spin-structures, the scattering amplitude $f(k,\theta,\phi) \to f(k,\theta)$ is independent of $\phi$. We can expand the wave function in spherical coordinates,

$$\psi(r,\theta) = \sum_{l=0}^{\infty} c_l \frac{u_l(r)}{r} P_l(\cos\theta) \ , \tag{2.2.5}$$

where the radial function $u_l(r)$ satisfies the radial Schrödinger equation,

$$\frac{d^2 u_l}{dr^2} - \left( \frac{l(l+1)}{r^2} + 2M_R V_{NN} - k^2 \right) u_l(r) = 0 \ . \tag{2.2.6}$$

The scattering amplitude $f$ can be decoupled into partial waves with a central potential,

$$f(k,\theta) = \sum_{l=0}^{\infty} (2l+1) f_l(k) P_l(\cos\theta). \tag{2.2.7}$$

With the help of asymptotic form of plane wave expansion of the incoming wave,

$$e^{i\mathbf{k}\cdot\mathbf{r}} \underset{r\to\infty}{\longrightarrow} \sum_{l=0}^{\infty} (2l+1) P_l(\cos\theta) \frac{(-1)^{l+1} e^{-ikr} + e^{ikr}}{2ikr} \ , \tag{2.2.8}$$

we can give asymptotic wave function with distinct incoming and outgoing spherical waves,

$$\psi_E^{(+)}(\mathbf{r}) \underset{r\to\infty}{\longrightarrow} (2\pi)^{-3/2} \sum_{l=0}^{\infty} (2l+1) P_l(\cos\theta) \frac{(-1)^{l+1} e^{-ikr} + S_l(k) e^{ikr}}{2ikr} \ , \tag{2.2.9}$$

where the partial wave S-matrix is related to the phase shifts $\delta_\ell(k)$ and scattering amplitude $f_\ell(k)$ by,

$$S_l(k) = 1 + 2ik f_l(k) = e^{2i\delta_l(k)} \ . \tag{2.2.10}$$

It is very common to write the partial wave scattering amplitude $f_\ell$ as,

$$f_l(k) = \frac{1}{k^{2\ell+1} \cot\delta_l(k) - ik} \ . \tag{2.2.11}$$

The term, $k^{2\ell+1}\cot\delta_l(k)$, has a power series expansion in $k^2$. For $\ell = 0$, the expansion is given,

$$k\cot\delta_0(k) = -\frac{1}{a_0} + \frac{1}{2}r_0k^2 + \cdots \ , \tag{2.2.12}$$

where $a_0$ is the S-wave scattering length, and $r_0$ is the S-wave effective range. Eq. (2.2.12) is the so-called effective range expansion(ERE). One can find a more general expression of higher partial waves [80]. In this thesis, we will only focus on S-wave scattering. The scattering length is one of the most fundamental parameters in low-energy scattering. For example, in the 2-body sector, the universal properties depend only on the scattering length [24]. It represents the radial intercept of the slope of the radial wave function at the outer asymptotic region. In a more classic point of view, the scattering length can be viewed as the actual size of one particle in a scattering process. In fact, it is related to the mean square separation by $\langle r^2\rangle = \frac{1}{2a_0^2}$. Scattering length always plays a crucial role in our effective theories.

The effective range expansion for hard-sphere scattering with radius $R$ is $a_0 = R$, $r_0 = 2R/3$ [130]. More generally, while $r_0 \sim R$, if $a_0 \sim R$, it is called "natural" scattering length. If $|a_0| \gg R$, it is called "unnatural" scattering length. The latter one contains more interesting physics. Furthermore, it is relevant for a realistic NN scattering process. These two terms are mentioned here in advance since we will meet them again later. There are many discussions in graduate quantum mechanics textbooks about the natural and unnatural scattering length [130]. In short, with a positive scattering length, $a > 0$, we will have a shallow bound state. In S-wave, the binding energy is related to scattering length by $B = \frac{\hbar^2}{2M_Ra_0^2}$. If $a < 0$, we will have a virtual bound state.

Here we should note that the effective range expansion initially shows us that, at low energies, the structure of a short-range potential can not be revealed. From the perspective of effective field theory, the low-energy theory is determined by a few low-energy constants(LECs) containing limited high-energy features that affect low-energy physics. Such an effective field theory which reproduces the ERE and consistently extend it to include the coupling to external probes is called pionless effective field theory, which we will dive deeper into in the next section.

## 2.3 Pionless Effective Field Theory

At low momentum below the pion mass, $M_\pi$, one can use the so-called pionless effective field theory ($\not\pi$EFT) [84, 83]. It is a systematic generalization of the effective range expansion(ERE) with nonperturbative nature in a quantum field theoretical framework.

Pionless EFT consists only of non-relativistic nucleons and contact interactions. Let us first look at a system consist of identical bosonic, spin-less, non-relativistic particles with short-range contact interactions. The breakdown scale is $M_{hi}$ and the nucleon mass is denoted as $M_N$. The Lagrangian density of such a system with contact interactions is [65]

$$\mathcal{L} = \phi^\dagger \left( \mathrm{i}\partial_t + \frac{\nabla^2}{2m} \right) \phi - \frac{C_0}{4} \left(\phi^\dagger \phi\right)^2 - \frac{C_2}{4} \left(\nabla \left(\phi^\dagger \phi\right)\right)^2 + \frac{D_0}{36} \left(\phi^\dagger \phi\right)^3 + \cdots \ . \tag{2.3.1}$$

By doing naive dimension analysis, we find the dimensions of the coupling constants

$$C_0 \sim \frac{1}{M_N M_{\mathrm{hi}}}, \quad C_2 \sim \frac{1}{M_N M_{\mathrm{hi}}^3}, \quad D_0 \sim \frac{1}{M_N M_{\mathrm{hi}}^4} \ . \tag{2.3.2}$$

Here, we will keep the first term as a leading order theory, including exclusively two-body force. Now we are left with a leading order contact interaction in our Lagrangian density,

$$\mathcal{L} = \phi^\dagger \left( \mathrm{i}\partial_t + \frac{\nabla^2}{2m} \right) \phi - \frac{C_0}{4} \left(\phi^\dagger \phi\right)^2 \ , \tag{2.3.3}$$

which can be used to describe the two-body scattering problem. Notice that the operators are Galilean invariant, which implies that the Lagrangian density form remains invariant under boosting. Eq. (2.3.3) is already very close to the form of Lagrangian density of pionless EFT. We will take this equation and discuss it further.

The EFT expansion needs a class of diagrams to sum over, which gives the scattering amplitude $i\mathcal{A}$ to the desired order in a $p/\Lambda$ expansion, where $p$ is the relative momentum of each nucleon in the center of the mass frame. This process is described schematically in Fig. 2.1. The scattering amplitude is related to the S-matrix by

$$S = 1 + i\frac{M_N p}{2\pi}\mathcal{A} \ . \tag{2.3.4}$$

Recall what we just reviewed previously, in quantum mechanics, the S-wave amplitude $\mathcal{A}$ is expressed in terms of phase shift $\delta_0$ by,

$$\mathcal{A} = \frac{4\pi}{M_N}\frac{1}{k\cot\delta_0 - ik} \ . \tag{2.3.5}$$

As we have discussed, at low energies, we can perform the so-called effective range expansion. At least, ERE results should be reproduced with our effective field theory. Then in our EFT framework, it will be more intuitive also to include electromagnetic and weak interactions.

Let us firstly try to do a Taylor expansion of $\mathcal{A}$ in Eq. (2.3.5) in powers of $p$,

$$\mathcal{A} \stackrel{?}{=} \frac{-4\pi a}{M_N}\left[1 - iap + (\frac{ar_0}{2} - a^2)p^2 + O(p^3/\Lambda^3)\right] \ , \tag{2.3.6}$$

where $a$ and $r_0$ are known as the scattering length and effective range. $\Lambda$ is the hard cutoff, which is of the order or larger than the breakdown scale. This expansion is valid conditionally. Since effective ranges are generally at the order of inverse cutoff, our only problem is the scattering length, which can take on any value. In the next section, we will see the analysis with so-called "natural" and "unnatural" scattering lengths , and a new necessary strategy of renormalization for pionless EFT.

### 2.3.1 Renormalizing Pionless EFT

Let us look at Fig. 2.1 and consider the summation of all diagrams on the right-hand side. To computer loops, one then encounters renormalization. That is what we are going to cover in this section. One needs to realize that this equation of diagrams is the graphical Dyson equation. In our case, due to the fact that each particle can consider the contact interaction as an external short-range potential, the Dyson equation and the Lippmann-Schwinger equation are the same.

The sum of diagrams can be expressed as a geometric series and we obtain,

$$\mathcal{A} = \frac{1}{-\frac{1}{C_0} + \mathcal{I}(E,\Lambda)} \ , \tag{2.3.7}$$

where $\mathcal{I}(E,\Lambda)$ is the one loop integral,

$$\mathcal{I}(E,\Lambda) = \int^{\Lambda} \frac{d^3q}{(2\pi)^3} \frac{1}{E - \frac{\mathrm{q}^2}{m} + i\epsilon} = -\frac{m\Lambda}{2\pi^2} + \frac{m}{4\pi}\sqrt{-mE - i\epsilon} \ . \tag{2.3.8}$$

Here we've regulated the loop with a hard cutoff $\Lambda$. It is convenient to rearrange the equation in the following form

$$\mathcal{A}(k) = \frac{1}{-\frac{1}{C_0} - \frac{M_N\Lambda}{2\pi^2} - i\frac{M_N k}{4\pi}} = \frac{4\pi}{M_N}\frac{1}{\left(-\frac{4\pi}{M_N\overline{C}_0} - ik\right)} \ ,$$

where

$$\frac{1}{\overline{C}_0} = \frac{1}{C_0} - \frac{M_N\Lambda}{2\pi^2}. \tag{2.3.9}$$

The $\overline{C}_0$ is related to real physical observable, scattering length, by

$$\overline{C}_0 = \frac{4\pi a}{M_N}. \tag{2.3.10}$$

Put above $\overline{C}_0$ back to the amplitude, we just get the quantum mechanics result,

$$\mathcal{A}(k) = \frac{4\pi}{M_N}\frac{1}{-1/a - ik} \ . \tag{2.3.11}$$

Thus, we adjust the bare coupling constant to eliminate the cutoff dependence [158]. This is because we have high momentum loop contribution that incorrectly goes into our theory. This shows how we can renormalize the theory.

However, this is not the full story. For example, all the analysis above is based on the fact that the expansion in Eq. (2.3.6) is valid and able to converges up to momenta $p \sim \Lambda$, which requires $1/|a| \simeq \Lambda$ is the so-called "natural" scattering length. Let us firstly consider natural scattering length only, and we need to determine a useful subtraction scheme. The minimal subtraction (MS) is suitable for this case. The loop integral is now evaluated by

$$
\begin{aligned}
\mathcal{I} =& (\mu/2)^{4-D} \int \frac{\mathrm{d}^{(D-1)}q}{(2\pi)^{(D-1)}} \left( \frac{1}{E - q^2/M_N + i\epsilon} \right) \\
=& - M_N(-M_N E - i\epsilon)^{(D-3)/2} \Gamma\left(\frac{3-D}{2}\right) \frac{(\mu/2)^{4-D}}{(4\pi)^{(D-1)/2}} \ ,
\end{aligned} \tag{2.3.12}
$$

where $\mu$ is the renormalization scale. It clear that there is no pole as we take the $D \to 4$ limit. We can evaluate the equation above with no problem. The result under MS gives

$$
\mathcal{I}^{MS} = \left(\frac{M}{4\pi}\right) \sqrt{-ME - i\epsilon} = -i \left(\frac{M}{4\pi}\right) p \ . \tag{2.3.13}
$$

In this way, we can reproduce the relation in Eq. (2.3.10). So we have successfully written down an effective field theory that can reproduce ERE results.

The analysis above is useful but not realistic. In the real world, low-energy nucleon-nucleon scattering processes have unnaturally large scattering lengths. The spin-singlet ($^1S_0$) channel of NN-scattering has a scattering length of $a_0 = -23.7\text{fm} \simeq 1/(8\text{MeV})$, which is way much larger than the inverse pion mass. In such case, the expansion in Eq. (2.3.6) fails. The related scattering lengths are considered as "unnatural". This problem was first addressed and solved by Kaplan, Savage and Wise [83, 84] with the so-called power divergence subtraction(PDS) scheme. For a unnatural scattering length, instead of the previously shown expansion, one needs to expand in powers of $p/\Lambda$ while retaining $ap$ to all orders,

$$
\mathcal{A} = -\frac{4\pi}{M} \frac{1}{(1/a + ip)} \left[ 1 + \frac{r_0/2}{(1/a+ip)} p^2 + \frac{(r_0/2)^2}{(1/a+ip)^2} p^4 + \frac{(r_1/2\Lambda^2)}{(1/a+ip)} p^4 + \ldots \right] \ . \tag{2.3.14}
$$

In order to reproduce the scattering results emerge from the expansion above, PDS scheme subtracts also poles in lower dimensions, in addition to the $1/(D-4)$ poles in MS. The loop integral in Eq. (2.3.12) has a pole in $D = 3$, which can be removed by including an additional counterterm,

$$
\delta\mathcal{I} = -\frac{M_N \mu}{4\pi(D-3)} \ . \tag{2.3.15}
$$

Adding MS results together, we get the

$$\mathcal{I}^{PDS} = \mathcal{I}^{MS} + \delta\mathcal{I} = -\left(\frac{M_N}{4\pi}\right)(\mu + ip) \ . \tag{2.3.16}$$

More analysis and details can be found in [83, 84, 80]. Now with PDS scheme, our scattering amplitude is now,

$$\mathcal{A} = \frac{-C_0}{\left[1 + \frac{C_0 M_N}{4\pi}(\mu + ip)\right]} \ , \tag{2.3.17}$$

and coupling constant is $\mu$ dependent,

$$C_0(\mu) = \frac{4\pi}{M}\left(\frac{1}{-\mu + 1/a}\right) \ . \tag{2.3.18}$$

One can check that this meets the needs for the renormalization group equation. Now we are able to use such an effective field theory without worrying about legitimacy. The benefit of our previous efforts is that we can include electromagnetic and weak interaction systematically, as we will see later in this dissertation.

### 2.3.2 Dimer Field Formalism

In classical mechanics, a three-body problem could have only some special solutions. There is no general closed-form solution for such problems. A quantum three-body problem is always hard to resolve, too. However, for a bound state, we can simplify this system with the help of auxiliary fields representing few-body bound states.

Kaplan, Savage, and Wise [84] introduced the so-called dimer field to represent the two-body bound state. Bedaque, Hammer and van Kolck [17] were the first to consider the three-body system using this formalism. We will use auxiliary fields like the dimer field in all projects. It is important to take a look at it.

Under the view of dimer fields, the Dyson equation of a bounded two-body state is graphically express as in Fig. 2.2. The so called dressed propagator is equal to the sum of all possible loop diagrams.

Consider the bosonic system with three-body contact force,

$$\mathcal{L} = \psi^\dagger \left( i\frac{\partial}{\partial t} + \frac{1}{2m}\nabla^2 \right) \psi - \frac{g_2}{4} \left(\psi^\dagger \psi\right)^2 - \frac{g_3}{36} \left(\psi^\dagger \psi\right)^3 \ , \tag{2.3.19}$$

where $\psi$ is the non-relativistic bosonic field. By using the dimeron formalism, we can rewrite the Lagrangian density as,

$$\mathcal{L} = \psi^\dagger \left( i\frac{\partial}{\partial t} + \frac{1}{2m}\nabla^2 \right) \psi + \frac{g_2}{4} d^\dagger d - \frac{g_2}{4} \left( d^\dagger \psi^2 + \psi^{\dagger 2} d \right) - \frac{g_3}{36} d^\dagger d \psi^\dagger \psi \ , \tag{2.3.20}$$

where $d$ represents the dimeron field. If we consider the equation of motion relative to $d^\dagger$, we will have

$$\begin{aligned} d - \psi^2 - \frac{g_3}{9g_2} d\psi^\dagger \psi = 0 \ , \\ \Rightarrow d = \frac{\psi^2}{1 - \frac{g_3}{9g_2}\psi^\dagger \psi} \ . \end{aligned} \tag{2.3.21}$$

Now we get the relations between dimer fields and mono fields in the case of boson. Put this back to the Lagrangian to eliminate $d$ we have

$$\mathcal{L} = \psi^\dagger \left( i\frac{\partial}{\partial t} + \frac{1}{2m}\nabla^2 \right) \psi - \frac{g_2}{4} \frac{\left(\psi^\dagger \psi\right)^2}{1 - \frac{g_3}{9g_2}\psi^\dagger \psi} \ . \tag{2.3.22}$$

If we expand the interacting term, we will restore our original Lagrangian. This shows the equivalence of dimer field formalism and traditional quantum field theory.

With such a dimer field, a two-body problem was translated into a quasi-single-body problem. Furthermore, we could still use our known two-body observable, $g_2$, to predict three-body behavior. We need to know one more three-body observable, binding energy, for example, to get all the coefficients needs to know at this level. Then we could reduce the three-body problem to a two-body problem.

## 2.4 Halo Nuclei and Halo Effective Field Theory

The physics of halo nuclei is very exciting and suitable for short-range EFT. One can apply so-called halo EFT, which is correlated to pionless EFT, to such systems. In this section, we will first introduce the phenomenology of halo nuclei. Then we will introduce halo-eft briefly.

### 2.4.1 Halo Nuclei

Halo nuclei are simply described by a tightly bound core and loosely bound valence nucleons [69, 79, 119, 146]. The valence nucleons are considered as "halos". The term "halo" was first applied to such nuclei by Hansen and Jonson in 1987 [68]. Halo nuclei are usually found at the neutron-proton drip line since they represent the strong force's range limit. The first halo nucleus, $^{11}$Li, was discovered at Lawrence Berkeley Laboratory's Bevalac in 1985 [147]. The halo is consists of no more than two valence nucleons, mostly neutron. Thus we will refer a specific halo nucleus to one (or two)-neutron(or proton) halo nucleus. This "halo" gives halo nuclei several unique properties compared to other isotopes.

Halo nuclei have much larger radii than that predicted by the liquid drop model. This gives most of the halo nuclei a very good separation of scales, which makes us will not be surprised that the shell model and mean-field approaches break down and indicate us to apply effective field theory.

Halo nuclei have very short lifetimes. Due to the small separation energy, the valence nucleon can easily get out of the potential barrier because of quantum effects. Most of the halo nucleus will only expect a half time of a few milliseconds. For example, $^{11}$Li has a half-life of 8.75 ms [100]. Because of the short lifetimes, halo nuclei are difficult to study in the laboratory.

In Fig. 2.3, we show some currently known halo nuclei. As we discussed above, halo nuclei are mostly close to the drip line. There are more neutron halos than proton halos, which is due to the Coulomb barrier. This dissertation will focus on only one-neutron halo nucleus and the halo EFT relative to it. $^{11}$Be is the leading character among all halo nuclei in this work. In Fig. 2.4 we illustrate the structure of $^{11}$Be, which has a valence neutron and a core

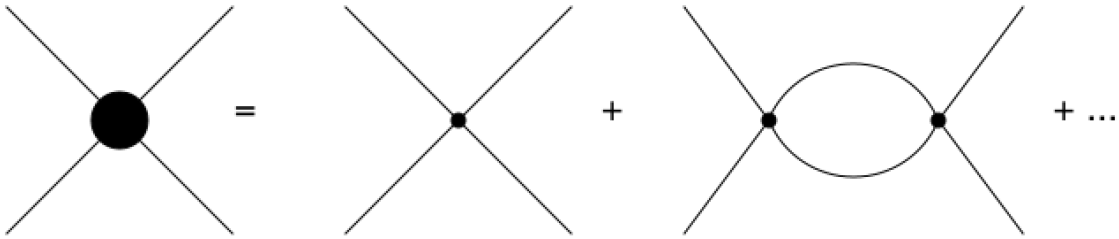


**Figure 2.1:** Diagrammatic representation of a two-body scattering amplitude, which can be expressed as a sum of diagrams including the $C_0$ vertex contribution.

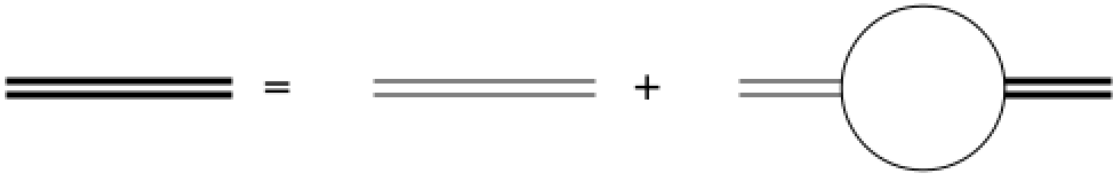


**Figure 2.2:** Dyson equation with auxiliary dimer fields representing two-body bound states. The thick double line is the dressed dimer propagator while the thin double line represents the bare dimer propagator. Single solid lines are single nucleon propagators.

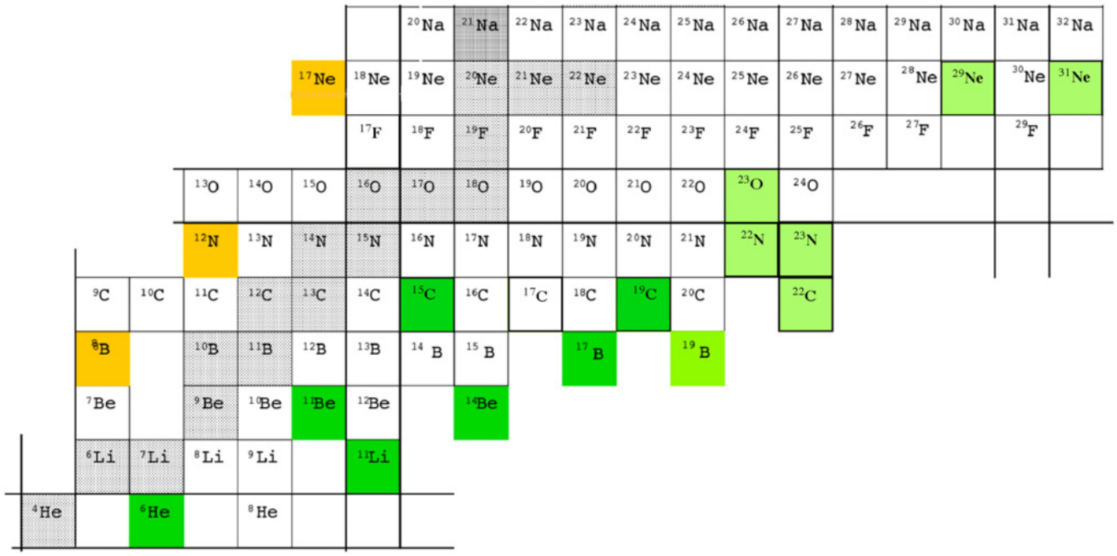


**Figure 2.3:** Confirmed and suggested halo nuclei. Neutron halo nuclei are shown by green square and candidates of neutron halo are shown by light green. Orange squares show the proton halos. This figure is taken from Ref. [148].

consists of four protons and six neutrons. It has two shallow bound states. $J^P = 1/2^+$ is the s-wave ground state, which has one-neutron separation energy of 500 keV. The first excited state, $J^P = 1/2^-$ is p-wave with a one-neutron separation energy of 180 keV [5]. Notice that the first excitation of the core of $^{10}$B is 3.4 MeV [4], which displays a large separation of scales implies a short-range EFT. Apply the short-range EFT to halo systems was firstly carried out on the one-neutron halo, $^5$He [19, 13]. Now we are able to take a look at the halo EFT approach in the next section.

### 2.4.2 Lagrangian of Halo EFT

We apply the Halo EFT to the $^{11}$Be system. We will first introduce the Lagrangian density in the one-neutron halo in S-wave and P-wave bound states. Then we carry out the renormalization in the case of both states. This work will focus only on one-neutron halo nucleus, a two-body system consisting of a core field and valence neutron field. We will take advantage of the auxiliary dimer fields mentioned previously. Thus, the Lagrangian density $\mathcal{L}$ of Halo EFT at leading order can be written as

$$\mathcal{L} = \mathcal{L}_0 + \mathcal{L}_{\sigma_s} + \mathcal{L}_{\pi_s} \ . \tag{2.4.1}$$

The free Lagrangian of the core and neutron, $\mathcal{L}_0$, is given by

$$\mathcal{L}_0 = c^\dagger \left( i\partial_t + \frac{\nabla^2}{2m_c} \right) c + n^\dagger \left( i\partial_t + \frac{\nabla^2}{2m_n} \right) n \ . \tag{2.4.2}$$

where $c$ and $n$ are core and neutron field, respectively. $m_c$ and $m_n$ are the masses of core and neutron. The part of the Lagrangian that describes the $S$-wave core and neutron interaction, $\mathcal{L}_{\sigma_s}$, reads

$$\mathcal{L}_{\sigma_s} = \sigma_s^\dagger \left[ \eta_0 \left( i\partial_t + \frac{\nabla^2}{2M_{nc}} \right) + \Delta_0 \right] \sigma_s - g_0 \left[ c^\dagger n^\dagger \sigma_s + \text{H.c.} \right] \ . \tag{2.4.3}$$

where $\sigma_s$ is the spinor field and $M_{nc}$ is the total mass of neutron and core. We describe $P$-wave interactions with $\mathcal{L}_{\pi_s}$ given by

$$\mathcal{L}_{\pi_s} = \pi_s^\dagger \left[ \eta_1 \left( i\partial_t + \frac{\nabla^2}{2M_{nc}} \right) + \Delta_1 \right] \pi_s - g_1 \left[ \left( c \overleftrightarrow{\nabla}_i \, n_\alpha \right) \pi_\beta^\dagger \, C^{J\beta}_{(1i)(\frac{1}{2}\alpha)} + \text{H.c.} \right] , \tag{2.4.4}$$

where $\pi_s$ is the p-wave field dimer field. $\overleftrightarrow{\boldsymbol{\nabla}} \equiv m_R \left[ {m_c}^{-1} \overleftarrow{\boldsymbol{\nabla}} - {m_n}^{-1} \overrightarrow{\boldsymbol{\nabla}} \right]$ is the Galilean-invariant derivative. The coefficient $C^{J\beta}_{(1i)(\frac{1}{2}\alpha)}$ is a Clebsch-Gordan coefficient coupling the neutron spin and the core-neutron relative angular momentum to the total angular momentum of the dimer field. $\eta_0$, $\eta_1$ are either plus or minus signs.

### 2.4.3 Renormalization of the Core-Neutron System

The renormalization of the low-energy constants in the $S$- and $P$-wave the sector has been discussed in detail in Ref. [67]. Here we will briefly summarize the relevant results to define the notation we will use throughout this work. Let us firstly look at the s-wave renormalization.

The spinor field $\sigma$ is used to express the $1/2^+$ state. The corresponding bare dimer propagator is given by

$$B_\sigma(p) = \frac{1}{\Delta_0 + \eta_0[p_0 - \boldsymbol{p}^2/(2M_{nc})] + i\epsilon} \, . \tag{2.4.5}$$

Due to the non-perturbative nature of the interaction, we need to re-sum the self-energy diagrams to all orders. We therefore obtain the *dressed* propagator

$$\begin{aligned} D_\sigma(p) &= B_\sigma(p) + B_\sigma(p)\Sigma_\sigma(p)D_\sigma(p) \\ &= \frac{1}{\Delta_0 + \eta_0[p_0 - \boldsymbol{p}^2/(2M_{nc})] + i\epsilon - \Sigma_\sigma(p)} \, , \end{aligned} \tag{2.4.6}$$

where $p = (p_0, \boldsymbol{p})$ and $\Sigma(p)$ is the LO irreducible core-neutron self-energy given by

$$\Sigma_\sigma(p) = -\frac{m_R g_0^2}{2\pi} \left[ i\sqrt{2m_R \left( p_0 - \frac{\boldsymbol{p}^2}{2M_{nc}} \right)} + \mu \right] \, . \tag{2.4.7}$$

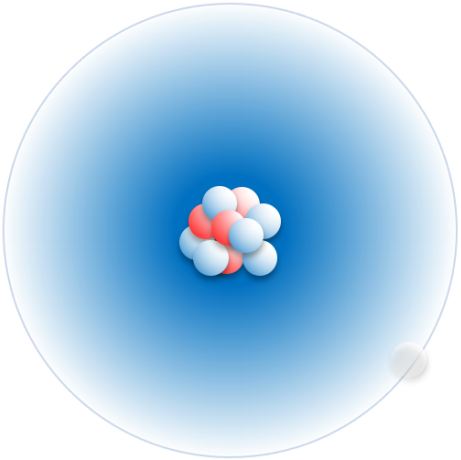

**Figure 2.4:** A schematic diagram of $^{11}$Be, which is known as a one-neutron halo nucleus. Red and blue balls represent proton and neutron, respectively.

**Figure 2.5:** Diagrammatatic form of the Dyson equation. The thick black line denotes the dressed $S$-wave halo propagator, the grey line denotes the bare halo propagator and the thin solid and dashed line denote the neutron and core propagator, resepctively.

It is evaluated in the power divergence subtraction (PDS) scheme [82] where $\mu$ is the corresponding renormalization scale.

The full two-body scattering amplitude in the $S$-wave channel reads

$$-it_0 = (-ig_0)(iD_\sigma(E,\mathbf{0}))(-ig_0) = -ig_0^2 D_\sigma(E,\mathbf{0}) \ . \tag{2.4.8}$$

This yields the two-body t-matrix

$$t_0 = \frac{2\pi}{m_R}\left[\left(\frac{2\pi}{m_R g_0^2}\Delta_0 + \mu\right) + \frac{1}{2}\left(\frac{2\pi\eta_0}{m_R^2 g_0^2}\right)p^2 + ip\right]^{-1} \tag{2.4.9}$$

Matching the expression above to the effective range expansion allows us to relate the low-energy constants to the effective range parameters by

$$a_0^{-1} = \frac{2\pi}{m_R g_0^2}\Delta + \mu \ , \tag{2.4.10}$$

$$r_0 = -\frac{2\pi\eta_0}{m_R^2 g_0^2} \ . \tag{2.4.11}$$

In the vicinity of the pole, the dressed propagator can be written as

$$D_\sigma(p) = \frac{2\pi\gamma_0}{m_R^2 g_0^2}\frac{1}{1-r_0\gamma_0}\frac{1}{p_0 - \boldsymbol{p}^2/(2M_{nc}) + B_0} + R_\sigma(p) \ , \tag{2.4.12}$$

where $B_0$ is the binding energy of the $S$-wave state and $R_\sigma(p)$ denotes the regular part. The $Z$-factor required to calculate physical observables is given by the residue of the full dimer propagator and can be read off Eq. (2.4.12)

$$\begin{aligned} Z_\sigma &= \frac{2\pi\gamma_0}{m_R^2 g_0^2}(1-r_0\gamma_0)^{-1} \\ &= \frac{2\pi\gamma_0}{m_R^2 g_0^2}(1 + r_0\gamma_0 + \cdots) \ , \end{aligned} \tag{2.4.13}$$

with $\gamma_0$ being the binding momentum of the $S$-wave state.

Now we look at the p-wave renormalization. The dressed $P$-wave dimer propagator is given by

$$D_{\pi_s}(p) = \frac{1}{\Delta_1 + \eta_1[p_0 - \boldsymbol{p}^2/(2M_{nc})] + i\epsilon - \Sigma_\pi(p)} \ , \tag{2.4.14}$$

where the p-wave self-energy $\Sigma_\pi(p)$ in the PDS scheme reads

$$\Sigma_\pi(p) = -\frac{m_R g_1^2}{6\pi} 2m_R \left(p_0 - \frac{\boldsymbol{p}^2}{2M_{nc}}\right) \left[i\sqrt{2m_R\left(p_0 - \frac{\boldsymbol{p}^2}{2M_{nc}}\right)} + \frac{3}{2}\mu\right] \ . \tag{2.4.15}$$

Inserting this self-energy in Eq. (2.4.14) yields

$$D_\pi = \frac{6\pi}{m_R g_1^2}\left[\left(\frac{6\pi}{m_R g_1^2}\Delta_1\right) + \left(\frac{3\pi\eta_1}{m_R^2 g_1^2} + \frac{3}{2}\mu\right)p^2 + ip^3\right]^{-1} \ . \tag{2.4.16}$$

We match the resulting $P$-wave t-matrix to the scattering amplitude expressed in terms of the effective range parameters

$$t_1 = g_1^2 \boldsymbol{k}\cdot\boldsymbol{k}' D_\pi = \frac{6\pi}{m_R}\frac{\boldsymbol{k}\cdot\boldsymbol{k}'}{1/a_1 - \frac{1}{2}r_1 p^2 + ip^3} \tag{2.4.17}$$

and hence achieve the following matching conditions for the coupling constants

$$a_1 = \frac{1}{\left(\frac{6\pi}{m_R g_1^2}\Delta_1\right)} \ , \tag{2.4.18}$$

$$r_1 = -\left(\frac{6\pi\eta_1}{m_R^2 g_1^2} + 3\mu\right) \ . \tag{2.4.19}$$

Since the amplitude has a pole at $p = i\gamma_1$ with $\gamma_1$ being the binding momentum of the $P$-wave state, we can relate the scattering volume $a_1$ to the $P$-wave effective momentum $r_1$ via

$$\frac{1}{a_1} + \frac{1}{2}r_1\gamma_1^2 + \gamma_1^3 = 0 \ . \tag{2.4.20}$$

In the vicinity of the pole, the dressed propagator can be expressed as

$$D_\pi = -\frac{6\pi}{m_R g_1^2}\frac{1}{r_1 + 3\gamma_1}\frac{1}{p_0 - \frac{\boldsymbol{p}^2}{2M_{nc}} + B_1} + R_\pi(p) \ , \tag{2.4.21}$$

where $R_\pi(p)$ denotes the regular part.

The wave function renormalization constant of the $P$-wave state $Z_\pi$ can be read off from Eq. (2.4.21)

$$Z_\pi = -\frac{6\pi}{m_R^2 g_1^2}\frac{1}{r_1 + 3\gamma_1} \ . \tag{2.4.22}$$

The conclusions above will be directly applied to the following chapter, in which we will discuss the beta delayed proton emission from $^{11}$Be.

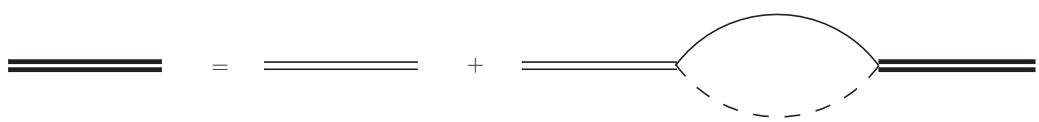


**Figure 2.6:** Diagrammatic representation of the Dyson equation for the dressed $P$-wave halo propagator. The thick (thin) double line denotes the dressed (bare) $P$-wave halo propagator.

# Chapter 3

# $\beta$-delayed proton emission from $^{11}$Be

This chapter is mainly based on the manuscript [46] with more details included. In this chapter, we calculate the rate of the rare decay $^{11}$Be into $^{10}$Be$+p+e^-+\bar{\nu}_e$ using Halo effective field theory, thereby describing the process of beta-delayed proton emission. We assume a shallow $1/2^+$ resonance in the $^{10}$Be$-p$ system with an energy consistent with a recent experiment by Ayyad *et al.* and obtain $b_p = 4.9^{+5.6}_{-2.9}(\text{exp.})^{+4.0}_{-0.8}(\text{theo.}) \times 10^{-6}$ for the branching ratio of this decay, predicting a resonance width of $\Gamma_R = (9.0^{+4.8}_{-3.3}(\text{exp.})^{+5.3}_{-2.2}(\text{theo.}))$ keV. Our calculation shows that the experimental branching ratio and resonance parameters of Ayyad *et al.* are consistent with each other. Moreover, we analyze the general impact of a resonance on the branching ratio and demonstrate that a wide range of combinations of resonance energies and widths can reproduce branching ratios of the correct order. Thus, no exotic mechanism (such as beyond the standard model physics) is needed to explain the experimental decay rate.

## 3.1 Introduction

The emergence of the halo degrees of freedom is a fascinating aspect of nuclei away from the valley of stability. It can be considered a consequence of the quantum tunneling of halo neutrons out of the core potential to the classically forbidden region. The halo nucleons in the core potential spend most of their time in the classically forbidden region outside of the range of the core potential. This is analog to the tunnel effect. But since the halo nucleons

are bound to the core, they always have to come back into the core potential. This separation of scales can be used to treat these systems using an effective field theory (EFT) approach called Halo EFT [20, 18, 64]. Common to all EFTs is that observables are described in a systematic low-energy expansion and that the accuracy of a calculation can be systematically improved. Halo EFT has been applied to a number of observables, including electromagnetic capture reactions and photodissociation processes [67, 123, 126, 166, 72, 116, 167].

Here we will consider, for the first time, the weak decay of the valence neutron of the halo nucleus $^{11}$Be into the continuum, $^{11}\mathrm{Be} \to {}^{10}\mathrm{Be} + p + e^- + \bar{\nu}_e$, within Halo EFT.

First experimental results for this rare decay mode were presented in Refs. [23, 120]. Riisager et al. [121] measured a surprisingly large branching ratio for this decay process, $b_p = 8.3(9) \times 10^{-6}$, which could only be understood in their Woods-Saxon model analysis if the decay proceeds through a new single-particle resonance in $^{11}$B. Their measured branching ratio is also more than two orders of magnitude larger than the cluster model prediction by Baye and Tursunov [11]. This led Pfützner and Riisager [108] to suggest that $\beta$-delayed proton emission in $^{11}$Be is also a possible pathway to detect a dark matter decay mode as proposed by Fornal and Grinstein [48]. More recently, this branching ratio was remeasured by Ayyad *et al.* [9] as $b_p = 1.3(3) \times 10^{-5}$, similar in size to the previous measurement. They also presented new evidence for a low-lying resonance in $^{11}$B with resonance energy $E_R = 0.196(20)$ MeV and width $\Gamma_R = 12(5)$ keV. Using these parameters, the authors calculated the decay rate in a Woods-Saxon model assuming a pure Gamow-Teller transition. They obtained $b_p = 8 \times 10^{-6}$, which has the correct order of magnitude but is only consistent within a factor of two with their experimental result. The work by Ayyad et al. was criticized in a recent comment by Fynbo et al. [50]. A new experiment by Riisager et al. [122] gives an upper limit of $b_p \leq 2.2 \times 10^{-6}$ for the branching ratio but some questions remain due to inconsistencies between different measurements. In conclusion, the branching ratio for $\beta$-delayed proton emission in $^{11}$Be remains an important unsolved problem.

The ground state of $^{11}$Be is a well-understood $S$-wave halo nucleus. From the ratio of the one-neutron separation energy of $^{11}$Be and the excitation energy of the $^{10}$Be core, one can extract the expansion parameter for a description with the core and valence neutron as effective degrees of freedom, $R_{\mathrm{core}}/R_{\mathrm{halo}} \approx 0.4$ [67]. Here $R_{\mathrm{core}}$ and $R_{\mathrm{halo}}$ are the length scales

of the core and halo, respectively. In principle, both the $^{10}$Be core and the halo neutron can $\beta$-decay. Since the half-life of the neutron ($T_{1/2} = 10$ min) is much shorter than the half-life of the core ($T_{1/2} = 10^6$ a), it is safe to assume that for $\beta$-delayed proton emission it is always the halo neutron that decays in the halo picture. Therefore, one would naively expect the nucleus to emit this proton due to the repulsive Coulomb interaction:

$$^{11}\text{Be} \to {}^{10}\text{Be} + p + e^- + \bar{\nu}_e \ . \tag{3.1.1}$$

This process, called $\beta$-delayed proton emission, has well-defined experimental signatures. However, it is also known that short-distance mechanisms such as the decay into excited states of $^{11}$B (that are beyond the halo interpretation) dominate the total $\beta$-decay rate of $^{11}$Be [118, 85].

Halo EFT offers a new perspective on $\beta$-delayed proton emission from $^{11}$Be by providing a value for the decay rate with a robust uncertainty estimate. It uses the appropriate degrees of freedom and parametrizes the decay observables in terms of a few measurable parameters. Thus, it is perfectly suited for the theoretical description of low-energy processes such as $\beta$-delayed proton emission from halo nuclei. Kong and Ravndal [88] used these ideas to successfully describe the inverse process of $pp$-fusion into a deuteron and leptons. In contrast to the previous calculation in Ref. [11], we will use new experimental input parameters and put additional emphasis on the uncertainties associated with using effective degrees of freedom. The halo neutron can $\beta$-decay through both the Gamow-Teller and Fermi operators. The Fermi operator can only connect states in the same isospin multiplet. If all neutrons in $^{11}$Be contribute to the $\beta$-decay, this implies that the final state must have $T = 3/2$ for a Fermi transition. No such states are currently known in $^{11}$B within the $\beta$-decay window. However, due to the halo character of $^{11}$Be we expect that only the halo neutron decays, such that the final state has no definite isospin. Thus, we will keep our analysis general and consider both the scenarios of Gamow-Teller and Fermi decay as well a pure Gamow-Teller decay in the following. Specifically, we will show that based on the measured branching ratio, a low-lying resonance is the likely reason for the large partial decay rate, confirming the suggestion of Ref. [121]. Furthermore, in $^{11}$B, we explore the impact of the resonance

energy and width on the decay rate and show that the recent results for the resonance energy and width of a low-lying resonance are consistent with the experimentally measured branching ratio.

In order to keep our presentation self-contained, we start by summarizing the concepts of Halo EFT for $S$-wave halo nuclei. We discuss the calculation of decay rates with and without resonant final state interactions and then display our results. Note that these are EFTs for two different scenarios. Formally, we perform calculations up to corrections of order $R_{\text{core}}/R_{\text{halo}}$ in both scenarios but because of the different physics assumptions these cannot be directly compared. We conclude with a summary.

## 3.2 Theoretical Foundations

The Halo EFT Lagrangian $\mathcal{L}$ for $^{11}$Be as well as the low-lying resonance in $^{11}$B up to next-to-leading order can be written as $\mathcal{L} = \mathcal{L}_0 + \mathcal{L}_d$, where $\mathcal{L}_0$ is the free Lagrangian of the $^{10}$Be core, neutron and proton

$$\begin{aligned}\mathcal{L}_0 = c^\dagger \left(i\partial_t + \frac{\nabla^2}{2m_c}\right) c + n^\dagger \left(i\partial_t + \frac{\nabla^2}{2m_n}\right) n \\ + p^\dagger \left(i\partial_t + \frac{\nabla^2}{2m_p}\right) p \ ,\end{aligned} \tag{3.2.1}$$

with $c$, $n$ and $p$ the core, neutron and proton fields, respectively. The masses of core, neutron and proton are denoted by $m_c = 9327.548$ MeV, $m_n = 939.565$ MeV and $m_p = 938.272$ MeV. The $S$-wave core-neutron as well as core-proton interaction are described by $\mathcal{L}_d$, which reads

$$\begin{aligned}\mathcal{L}_d = d_{\text{Be}}^\dagger \left[\eta \left(i\partial_t + \frac{\nabla^2}{2M_{nc}}\right) + \Delta\right] d_{\text{Be}} \\ + d_{\text{B}}^\dagger \left[\tilde{\eta} \left(i\partial_t + \frac{\nabla^2}{2M_{pc}}\right) + \tilde{\Delta}\right] d_{\text{B}} \\ - g \left[c^\dagger n^\dagger d_{\text{Be}} + \text{H.c.}\right] - \tilde{g} \left[c^\dagger p^\dagger d_{\text{B}} + \text{H.c.}\right] ,\end{aligned} \tag{3.2.2}$$

where $d_{\text{Be}}$ and $d_{\text{B}}$ are spinor fields, with spin indices suppressed, that represent the $J^P = 1/2^+$ ground state of $^{11}$Be and the $J^P = 1/2^+$ low-lying resonance in $^{11}$B, respectively, while $M_{nc} = m_n + m_c$ and $M_{pc} = m_p + m_c$.

The renormalization of the low-energy constants for $^{11}$Be has been discussed in Ref. [67]. Here, we will briefly summarize the relevant results to define our notation. Due to the non-perturbative nature of the interaction, we need to resum the self-energy diagrams to all orders. After matching the low-energy constants for $^{11}$Be appearing in Eq. (3.2.2) to the effective range expansion, we obtain the full two-body $T$-matrix

$$T_0(E) = \frac{2\pi}{m_R}\left[\frac{1}{a_0} - r_0 m_R E - \sqrt{-2m_R E - i\epsilon}\right]^{-1} . \tag{3.2.3}$$

where $m_R$ is the reduced mass, and $a_0$, $r_0$ are the $S$-wave $^{10}$Be$-n$ scattering length and effective range, respectively. The residue at the bound state pole of Eq. (3.2.3) is required to calculate physical observables, $Z = \frac{2\pi\gamma_0}{m_R^2}/(1 - r_0\gamma_0)$ , with $\gamma_0 = (1 - \sqrt{1 - 2r_0/a_0})/r_0 \equiv \sqrt{2m_R S_n}$ the binding momentum of the $S$-wave halo state, and $S_n$ the one-neutron separation energy of the halo nucleus.

In order to investigate $\beta$-delayed proton emission from $^{11}$Be, we include the weak interaction current allowing transitions of a neutron into a proton, electron and antineutrino which corresponds to the hadronic one-body current. Moreover, we have to consider hadronic two-body currents that appear in the dimer formalism once the effective range is included. The corresponding Lagrangian is given by

$$\mathcal{L}_{\text{weak}} = -\frac{G_F}{\sqrt{2}} l_-^\mu \left( \left(J_\mu^+\right)^{\text{1b}} + \left(J_\mu^+\right)^{\text{2b}} \right) , \tag{3.2.4}$$

where $l_-^\mu = \bar{u}_e \gamma^\mu (1 - \gamma^5) v_{\bar{\nu}}$ and $\left(J_\mu^+\right)^{\text{1b}} = (V_\mu^1 - A_\mu^1) + i(V_\mu^2 - A_\mu^2)$ denote the leptonic and hadronic one-body currents, respectively. Here the hadronic one-body current is decomposed into vector and axial-vector contributions. At leading order, the contributions to this current are $V_0^a = N^\dagger \frac{\tau^a}{2} N$, $A_k^a = g_A N^\dagger \frac{\tau^a}{2} \sigma_k N$, where $|g_A| \simeq 1.27$ is the ratio of the axial-vector to vector coupling constants [145]. Terms with more derivatives and/or more fields (many-body currents) will appear at higher orders. The first and second term give the conventional Fermi and Gamow-Teller operators, respectively. Including resonant core-proton final state interactions, we have to take into account the two-body current arising here from the auxiliary field formalism with no unknown constants. It is also decomposed into vector and axial-vector

contributions and reads

$$\left(J_\mu^+\right)^{2\mathrm{b}} = \begin{cases} -d_\mathrm{B}^\dagger\, d_\mathrm{Be} & \mu = 0\ , \\ g_A\, d_\mathrm{B}^\dagger\, \sigma_k\, d_\mathrm{Be} & \mu = k = 1,2,3\ . \end{cases} \tag{3.2.5}$$

There is also an unknown contribution usually denoted as $L_{1A}$ that normally appears at the same order. However, in the case with Coulomb interaction, this piece is suppressed by $(R_\mathrm{core}/R_\mathrm{halo})^{1/2}$ compared to the two-body current in Eq. (3.2.5).[1] Therefore, it contributes only at NNLO allowing us to make predictions up to NLO. Note that our power counting including resonant final state interactions implies a suppression of $(R_\mathrm{core}/R_\mathrm{halo})^{1/2}$ going from order to order instead of $R_\mathrm{core}/R_\mathrm{halo}$ as in the case without resonant final state interactions.

## 3.3 Weak Matrix Element and Decay Rate

We ignore recoil effects in the $\beta$-decay and take both the Gamow-Teller and Fermi transitions into account. After lepton sums, spin averaging, and partial phase space integration, we obtain the decay rate

$$\begin{aligned}\Gamma =& \int \frac{d^3p_c}{(2\pi)^3} \int \frac{d^3p_p}{(2\pi)^3} \int \frac{d^3p_e}{(2\pi)^3\,(2E_e)} \int \frac{d^3p_{\nu_e}}{(2\pi)^3\,(2E_{\nu_e})} C^2(\eta_e)\ \overline{|\mathcal{A}(\mathbf{p})|^2} (2\pi)^4 \delta^{(4)}\left(p_A - \sum_i p_i\right) \\ =& \frac{G_F^2(1+3g_A^2)}{4\pi^5} \int dp \int dp_e p^2 p_e^2 (E_0 - E - E_e)^2\ C^2(\eta_e)\ \overline{|\mathcal{A}(\mathbf{p})|^2}\ \Theta(E_0 - E - E_e)\ , \end{aligned} \tag{3.3.1}$$

where $\mathcal{A}$ is the *reduced* hadronic amplitude for Gamow-Teller and Fermi transitions whose operator coefficients have been factored out and $\Theta$ is the Heaviside step function. Moreover, $\mathbf{p}$ is the relative momentum of the outgoing proton and core, while $E = p^2/(2m_R)$ is their kinetic energy. Furthermore, $E_0 = \Delta m - S_n$, where $\Delta m = 1.29$ MeV is the mass difference between neutron and proton, and $E_e = \sqrt{m_e^2 + p_e^2}$ is the energy of the electron with $m_e = 0.511$ MeV denoting the electron mass.

[1] The scaling of $r_0^C \sim 1/k_C$ leads to the suppression of the counterterm contribution $L_{1A}$.

The Sommerfeld factor of the electron is given by

$$C^2(\eta_e) = \frac{2\pi\eta_e}{(e^{2\pi\eta_e} - 1)} \,, \tag{3.3.2}$$

where $\eta_e = \alpha Z Z_e E_e/|\mathbf{p_e}|$ with $\alpha \simeq 1/137$ is the fine structure constant. We use $Z = Z_p$ in order to ensure that we reproduce the free neutron decay width in the limit of a vanishing one-neutron separation energy of $^{11}$Be. This means that the electron is only interacting with the outgoing proton. We assume this to be a good approximation since the $^{10}$Be core is far away from the decaying valence neutron due to the small one-neutron separation energy. If a pure Gamow-Teller transition is considered, the factor $1 + 3g_A^2$ is replaced by $3g_A^2$. This results in a reduction of the decay rate by 17 %.

## 3.4 Beta-strength Sum Rule

The so-called Fermi and Gamow-Teller sum rules (also collectively known as beta-strength sum rule) count the number of weak charges that can decay in the initial state. We will require that this beta-strength sum rule is fulfilled exactly at each order within our EFT power counting. The beta-strenghts are related to the comparative half-life of a decay, the so-called $ft$ value given by

$$ft = \frac{B}{B_{\rm F} + g_A^2 B_{\rm GT}} \,, \tag{3.4.1}$$

where $B = 2\pi^3 \ln 2/(m_e^5 G_F^2)$ is the $\beta$-decay constant. In this chapter, we will use the value $B = 6144.2$ s [107, 70]. With $B_{\rm GT} = 3B_{\rm F}$, we find

$$B_{\rm F} = \frac{B}{(1 + 3g_A^2)} \frac{1}{ft} \,. \tag{3.4.2}$$

The inverse $ft$ value is directly related to the transition matrix element $\mathcal{M}$ of $^{11}$Be into $^{10}\text{Be} + p$,

$$\begin{aligned}\frac{1}{ft} &= \frac{1}{B}\,\overline{|\mathcal{M}|^2} \\ &= \frac{1}{B}\frac{(1+3g_A^2)}{2\pi^2}\int dE\, m_R\sqrt{2m_R E}\;\overline{|\mathcal{A}(\mathbf{p})|^2}\,.\end{aligned} \tag{3.4.3}$$

For a transition into the continuum, the sum rule is exactly fulfilled when integrating the differential beta-strengths

$$\frac{dB_{\text{F}}}{dE} = \frac{1}{2\pi^2}\; m_R\sqrt{2m_R E}\;\;\overline{|\mathcal{A}(\mathbf{p})|^2}\,, \tag{3.4.4}$$

$$\frac{dB_{\text{GT}}}{dE} = 3\frac{dB_{\text{F}}}{dE}\;, \tag{3.4.5}$$

over the whole continuum leading to the sum rules $B_{\text{F}} = 1$ and $B_{\text{GT}} = 3$. In the halo picture, we therefore expect beta-strengths $B_{\text{F}}$ and $B_{\text{GT}}$ to be at most 1 and 3, respectively, when integrating over the available $Q$-window. At LO where the full non-perturbative solution for a zero-range interaction is used in the incoming as well as outgoing channel, the sum rule is always satisfied. At NLO where range corrections are included, the sum rule puts strong constraints on the ranges in the incoming and outgoing channels such that only certain combinations are allowed.

## 3.5 Hadronic Current without Resonant Final State Interactions

The amplitude for the charge changing weak transition of a two-body system is illustrated as diagram $(a)$ of Fig. 3.1. It was first calculated in pionless EFT by Kong and Ravndal [88]. The details are provided in B.3. The corresponding hadronic current can be written as [127]

$$\mathcal{A}_C^{(a)}(\mathbf{p}) = -ig\sqrt{Z}C(\eta_p)e^{i\sigma_0}\frac{2m_R}{\mathbf{p}^2+\gamma_0^2}e^{2\eta_p\arctan(|\mathbf{p}|/\gamma_0)}\,, \tag{3.5.1}$$

where $\sigma_0$ is the Coulomb phase and $C^2(\eta_p)$ is the Sommerfeld factor from Eq. (3.3.2). In the $^{10}\text{Be} - p$ system, the Sommerfeld parameter is $\eta_p = \alpha Z_p Z_c m_R/|\mathbf{p}| = k_C/|\mathbf{p}|$, with $Z_p = 1$

and $Z_c = 4$. The amplitude above is in S-wave, which is the case of $^{11}$Be ground state. For a detailed P-wave calculation, see Appendix B.4.

## 3.6 Hadronic Current with Resonant Final State Interactions

The current (3.5.1) includes only the final state interaction from the exchange of Coulomb photons. We now consider resonant final state interactions whose signature is a low-lying resonance in the $^{10}\text{Be}-p$ channel up to NLO. These contributions are shown as diagrams ($b$) and ($c$) of Fig. 3.1. Diagram (c) contributes only at NLO to the amplitude. It arises from a two-body current (with known coupling strength) that appears as a result of the energy-dependent interactions used in the initial state (see Eq. (3.2.2)) and the final state (see Ref. [71]). The thin double line together with the shaded ellipses that represent Coulomb Green's functions as depicted in diagram ($b$) essentially combine to the strong scattering amplitude $T_{CS}$ given either in Eq. (3.6.1) or (3.6.7) [71, 88].

The degrees of freedom in Halo EFT are the emitted outgoing proton and $^{10}$Be. Our treatment of the resonance follows Ref. [71]. The corresponding strong scattering amplitude modified by Coulomb corrections is [71]

$$T_{CS} = \frac{-4\pi/m_R}{\left(r_0^C - \frac{1}{3k_C}\right)(p^2 - k_R^2) + \frac{p^2}{3k_C} - 4k_C H(\eta_p)} \ , \tag{3.6.1}$$

where $H(\eta_p) = \text{Re}[\psi(1+i\eta_p)] - \ln\eta_p + \frac{i}{2\eta_p}C^2(\eta_p)$ , with the digamma function $\psi(z)$. The parameters in Eq. (3.6.1) are directly related to the complex pole momentum $k^* = k_R - ik_I$:

$$-\frac{1}{a_0^C} = -\left(r_0^C - \frac{1}{3k_C}\right)\frac{k_R^2}{2}, \tag{3.6.2}$$

$$r_0^C = -\frac{2\pi k_C}{k_R k_I}\frac{1}{e^{2\pi k_c/k_R} - 1} + \frac{1}{3k_C}, \tag{3.6.3}$$

where $a_0^C$ and $r_0^C$ are the Coulomb-modified scattering length and effective range, respectively. Within our power counting, the parameters $k_C$, $k_R$, $k_I$ as well as $\gamma_0$ scale as $1/R_{\text{halo}}$ implying that both Coulomb-modified scattering parameters $a_0^C$ and $r_0^C$ scale as $R_{\text{halo}}$.

The diagrams $(b)$ and $(c)$ of Fig. 3.1 lead to

$$\mathcal{A}_{CS}^{(b)} = -ig\sqrt{Z}4m_R^2 C(\eta_p)e^{i\sigma_0}\mathcal{I}T_{CS} \ , \tag{3.6.4}$$

$$\mathcal{A}_{CS}^{(c)} = -ig\sqrt{Z}4m_R^2 C(\eta_p)e^{i\sigma_0}\left(\frac{\sqrt{r_0 r_0^C}}{8\pi}\right)T_{CS} \ , \tag{3.6.5}$$

with the complex-valued integral

$$\mathcal{I} = \int \frac{d^3\mathbf{q}}{(2\pi)^3}\frac{C^2(\eta_q)e^{2\eta_q \arctan(|\mathbf{q}|/\gamma_0)}}{\mathbf{q}^2+\gamma_0^2}\frac{1}{\mathbf{p}^2-\mathbf{q}^2+i\epsilon} \ . \tag{3.6.6}$$

The total amplitude $\mathcal{A}$ is the sum of the amplitudes with and without resonance $\mathcal{A} = \mathcal{A}_C^{(a)} + \mathcal{A}_{CS}^{(b)} + \mathcal{A}_{CS}^{(c)}$.

At LO, the Coulomb-modified effective range in the $^{10}\text{Be} - p$ system is zero and the amplitude reduces to

$$T_{CS} = -\frac{2\pi}{m_R}\left[\frac{1}{-1/a_0^C - 2k_C H(\eta_p)}\right] \ . \tag{3.6.7}$$

To keep the main body be concise and clean, more details about the calculations in this section are given in Appendix B.5.

## 3.7 Results without Resonant Final State Interactions

We consider two scenarios: beta-delayed proton emission with and without resonant final state interactions from a low-lying resonance in $^{11}$B. We start with the first scenario and use the one-neutron separation energy of $^{11}$Be $S_n = 0.5016$ MeV [85]. In Fig. 3.2, we plot the differential decay rate $d\Gamma/dE$ as a function of the kinetic energy $E$ of the outgoing hadrons. The solid line gives the result obtained by Baye and Tursunov [11]. The dash-dotted line shows the EFT result with an uncertainty band obtained by adding an uncertainty of order $R_{\text{core}}/R_{\text{halo}} \approx 40$ % from higher order corrections where we use the smallest value of $R_{\text{halo}}$

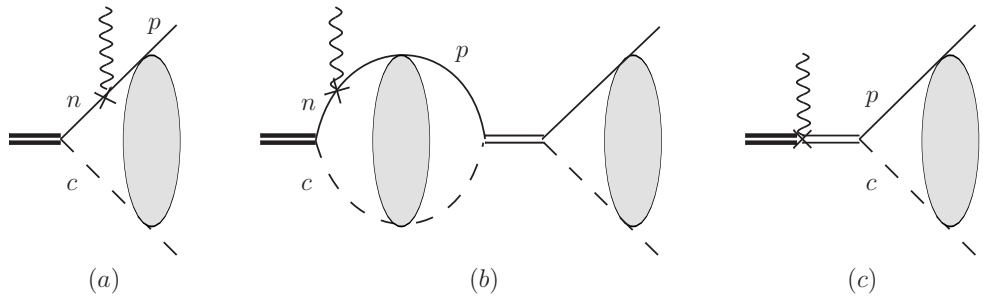


**Figure 3.1:** $(a)$: Feynman diagram for the weak decay of a one-neutron halo nucleus into the corresponding core and a proton with Coulomb final state interactions only. $(b)+(c)$: Contributions of resonant final state interactions. The thin double line in the middle denotes the dressed $^{10}$Be$-p$ propagator. The shaded ellipse denotes the Coulomb Green's function.

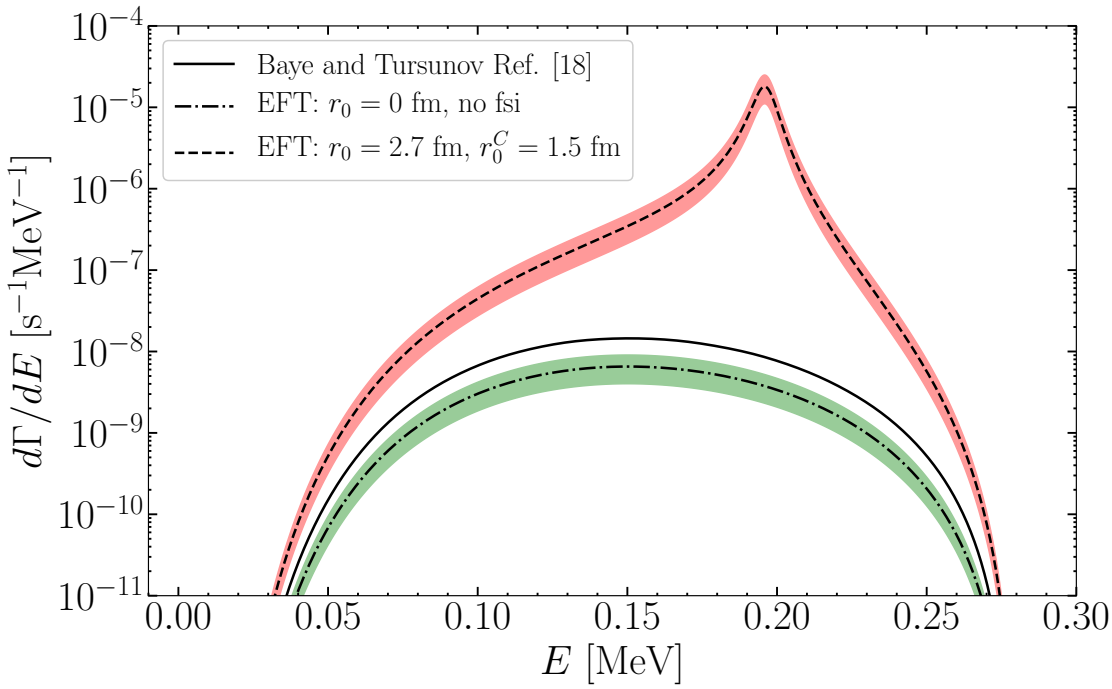


**Figure 3.2:** Differential decay rate $d\Gamma/dE$ for $\beta$-delayed proton emission from $^{11}$Be as a function of the final-state particle energy $E$. The dash-dotted line shows our EFT result without resonant final state interactions while the solid line gives the result obtained by Baye and Tursunov [11]. The dashed line shows the EFT result including a resonance at $E_R = 0.196$ MeV in the outgoing channel at NLO. The colored bands give the EFT uncertainty.

given by $1/\gamma_0$ while we estimate $R_{\rm core}$ by the effective range $r_0$ as a conservative estimate. The remaining curve includes resonant final state interactions and will be discussed below.

For the branching ratio, we obtain $b_p = \Gamma/\Gamma_{\rm total} = (1.31 \pm 0.51) \times 10^{-8}$ where the EFT uncertainty is again estimated to be of the order of 40 %. Correspondingly, we obtain for the decay rate $\Gamma = (6.6 \pm 2.6) \times 10^{-10}$ s$^{-1}$. Baye and Tursunov [11] obtain $\Gamma = 1.5 \times 10^{-9}$ s$^{-1}$ which differs by a factor of 2.3 from our result. We note, however, that they used a Woods-Saxon potential with Coulomb interactions tuned to reproduce $^{11}$B properties in the final state. Both theoretical results are significantly smaller than the experimental results reported in Refs. [23, 120, 121, 9].

## 3.8 Results with Resonant Final State Interactions

We now discuss the second scenario including final state interactions. In Fig. 3.3, we show the possible resonance parameter combinations that fulfill the beta-strength sum rule. The dash-dotted line is the result at LO where the effective range in the incoming channel as well as the Coulomb-modified effective range in the outgoing channel are zero. At NLO, we use $r_0 = 2.7$ fm determined in Ref. [67] from the measured $B$(E1) strength for Coulomb dissociation of $^{11}$Be. The one-neutron separation energy as well as the effective range of $^{11}$Be determine the Coulomb-modified effective range in the outgoing channel to be $r_0^C = 1.5$ fm. The sum rule is then satisfied to very good approximation for a wide range of Coulomb-modified scattering lengths in the outgoing channel. The square shows the experimentally measured resonance parameter combinations given in Ref. [9]. We note that the value of $r_0^C$ is determined independently from the experimental resonance parameters. Our NLO curve depicted as the dashed line corresponding to $r_0^C = 1.5$ fm exhibits combinations of $E_R$ and $\Gamma_R$ that are in agreement with this measurement as indicated by the overlap of the square and the curve.

In Fig. 3.4, we show the results for the decay rate as a function of the resonance energy at NLO while using the corresponding resonance width that satisfies the sum rule as shown in Fig. 3.3. The black line represents the decay rate obtained moving along the NLO curve in Fig. 3.3 while the red shaded envelope gives the theoretical uncertainty estimated from the

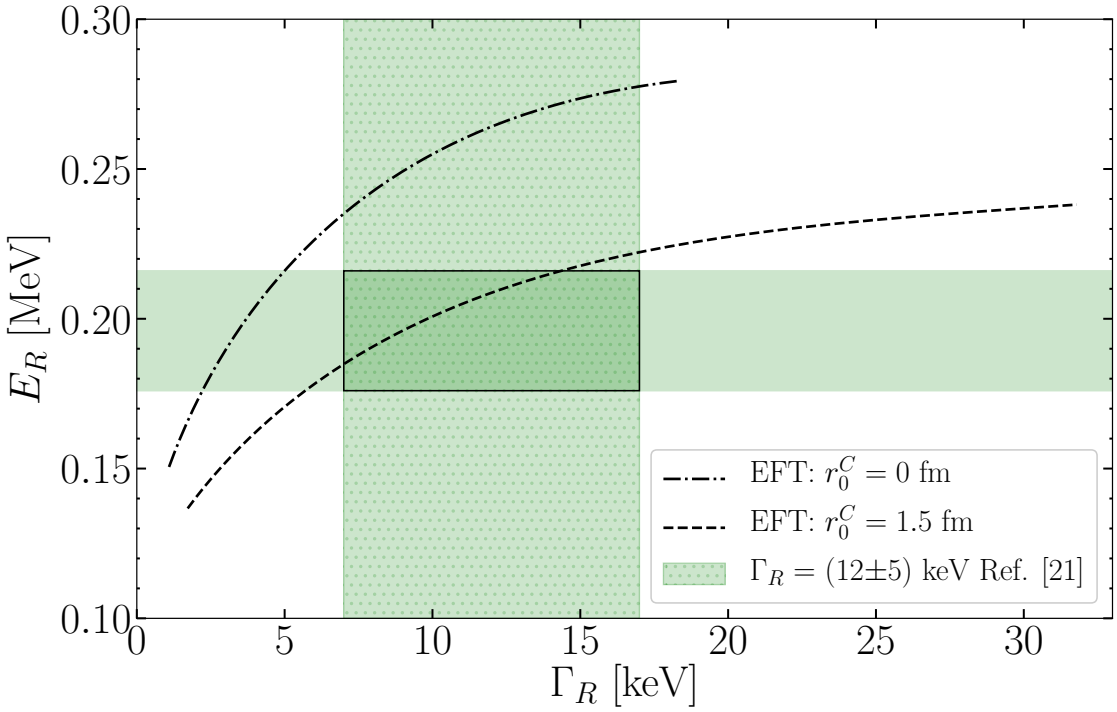


**Figure 3.3:** Possible resonance parameter combinations fulfilling the sum rule. The dash-dotted line shows the combinations for $r_0 = 0$ fm at LO corresponding to $r_0^C = 0$ fm while the dashed line shows the combinations for $r_0 = 2.7$ fm at NLO corresponding to $r_0^C = 1.5$ fm. The green bands show the resonance parameters given in Ref. [9].

counterterm contribution in the axial current scaling with $R_{\rm core}/R_{\rm halo} \approx 40$ %. The green bands show the experimentally measured branching ratio and resonance energy of Ref. [9]. The horizontal blue dashed line denotes the result of the model calculation carried out in Ref. [9] whereas the horizontal blue dash-dotted line gives the upper bound of Ref. [122]. Comparing our results with Ref. [122], we find that resonance energies $E_R \geq 0.214$ MeV give results compatible with this upper bound. The corresponding resonance widths can be read off in Fig. 3.3. When comparing our results with Ref. [9], we find that the low-lying resonance measured in Ref. [9] with $E_R = 0.196(20)$ MeV and width $\Gamma_R = 12(5)$ keV is consistent with their experimentally measured branching ratio as indicated by the overlap of the square and the red shaded band. According to Fig. 3.3, we determine the width corresponding to the resonance energy $E_R = 0.196(20)$ MeV as $\Gamma_R = (9.0^{+4.8}_{-3.3}(\text{exp.})^{+5.3}_{-2.2}(\text{theo.}))$ keV, which agrees well with the experimental value. At LO, the resonance width scales as $k_C^2/m_R$ whereas at NLO this value is enhanced by a factor of $1/(1-3k_C r_0^C)$. This enhancement for Coulomb halos is well known [125, 94, 133]. Using $E_R = 0.196(20)$ MeV, we calculate the logarithm of the comparative half-life $\log(ft) = 3.0$ with $B_{\rm GT} = 2.88$ and $B_{\rm F} = 0.96$ for a decay including both Gamow-Teller and Fermi transitions and $\log(ft) = 3.1$ with $B_{\rm GT} = 2.88$ for a pure Gamow-Teller transition. The latter result can be compared to $\log(ft) = 4.8(4)$ calculated by Ayyad *et al.* [9] which was obtained using a pure Gamow-Teller transition as well, but is significantly larger than our result. This large $\log(ft)$ value was also criticized in the comment by Fynbo *et al.* [50]. Ayyad *et al.* corrected the value to $\log(ft) = 2.8(4)$ in their recent erratum [9]. This new value is now in good agreement with our result. Using the half-life for $^{11}$Be given in Ref. [85] we convert the Halo EFT result for $E_R = 0.196(20)$ MeV and $\Gamma_R = (9.0^{+4.8}_{-3.3}(\text{exp.})^{+5.3}_{-2.2}(\text{theo.}))$ keV into the final result for the branching ratio $b_p = 4.9^{+5.6}_{-2.9}(\text{exp.})^{+4.0}_{-0.8}(\text{theo.}) \times 10^{-6}$. The corresponding differential decay rate is shown by the dashed line in Fig. 3.2.

## 3.9 Numerical Implementation

The calculation is relatively straightforward. In the case without final state interactions, one take the only Eq. (3.5.1). Including final state interactions, one should notice that beta-strength sum rule is taken as an input. We integrate Eq. (3.4.4) from zero to infinity and adjust $r_0^C$ to get $B_F = 1$. As a result, the choices of resonance parameters are not arbitrary, as illustrated in Fig. 3.3. The complex-valued integral of Eq. (3.6.6) is evaluated separately for the principal value part and the imaginary part. Then the norm is used in calculating the squared amplitude. Constant parameters used in the calculation are given in Table. 3.1.

## 3.10 Conclusion

In this chapter, we considered $\beta$-delayed proton emission from $^{11}$Be. We compared the scenario with no strong final state interactions with the scenario of a resonant enhancement in the final $^{10}$Be$-p$ channel up to NLO. In the case of no strong final state interactions, we obtained results that are in qualitative agreement with Baye and Tursunov with remaining small differences that can be explained by the different treatment of the final state channel. Including a low-lying resonance with the energy measured in Ref. [9] results in a resonance width and partial decay rate in agreement with this experiment. Thus, our model-independent calculation supports the experimental finding of a low-lying resonance.[2] Furthermore, we have explored the sensitivity of the partial decay rate to the resonance energy and decay width and found that this problem is fine tuned, *i.e.* only certain combinations of width and resonance energy can reproduce the partial decay rate. In contrast to the model calculation in Ref. [9], we included both, Fermi and Gamow-Teller transitions. However, if a pure Gamow-Teller decay is considered, their partial decay rate can also be reproduced with slightly smaller resonance parameters. Thus, our result implies that $^{11}$Be is not a good laboratory to detect dark neutron decays since no exotic mechanism is needed to explain the partial decay rate.

The uncertainties are largely determined by higher order contributions of the EFT expansion. The next contribution within our power counting that we did not include is

[2] See Ref. [103] for another recent theoretical calculation in support of this resonance.

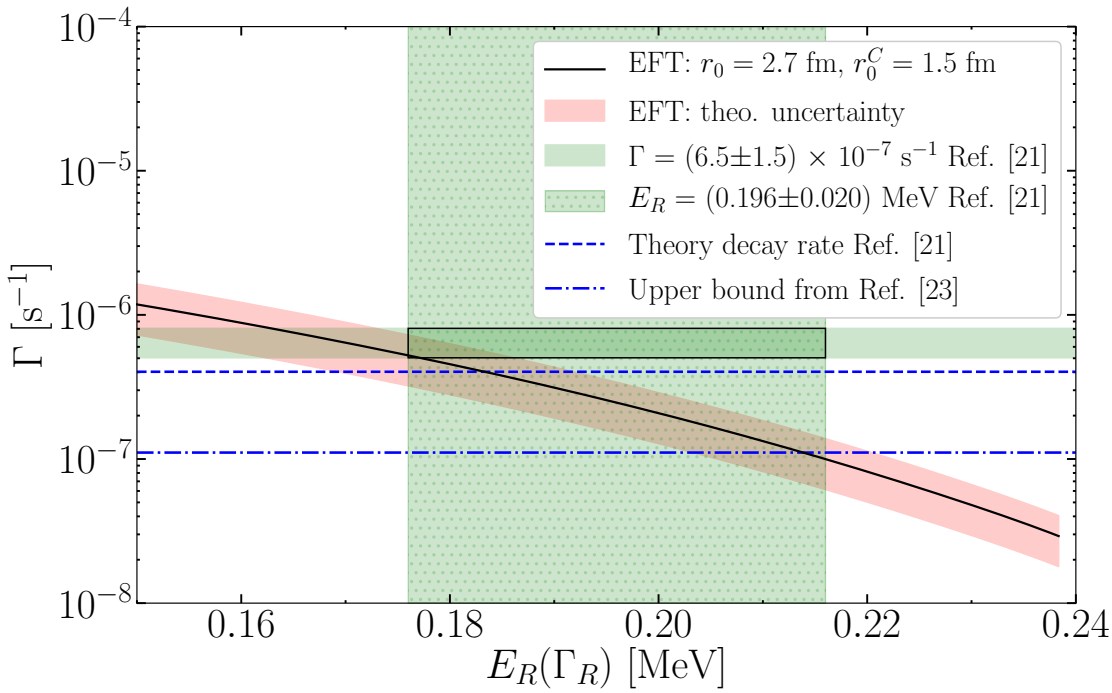


**Figure 3.4:** Partial decay rate as a function of the resonance energy at NLO using the corresponding resonance width in accordance with the sum rule (see Fig 3.3). Explanation of curves and bands is given in inset.

**Table 3.1:** Summary of parameters used in numerical implementation of $\beta$-delayed proton emission from $^{11}$Be.

| Constants used in this chapter | | |
|---|---|---|
| Name | Symbol | Value |
| $^{11}$Be core mass | $m_c$ | 9327.548 MeV |
| Neutron mass | $m_n$ | 939.565 MeV |
| Proton mass | $m_p$ | 938.272 MeV |
| Electron mass | $m_e$ | 0.511 MeV |
| Axial-vector coupling constant | $\|g_A\|$ | 1.27 |
| $\beta$-decay constant | B | 6144.2 s |
| fine structure constant | $\alpha$ | 1/137 |
| $^{11}$Be one-neutron separation energy | $S_n$ | 0.5016 MeV |

a counterterm contribution in the axial current scaling with $R_{\rm core}/R_{\rm halo}$. Uncertainties of the $S$-wave input parameter (the one-neutron separation energy) do not impact the total uncertainty significantly. Therefore, we estimate the uncertainty in the final decay rate to be approximately $R_{\rm core}/R_{\rm halo} \approx 40$ %. Experimental data with higher precision could be used to constrain the $^{10}$Be$-n$ and $^{10}$Be$-p$ interactions. It will be interesting to test whether the inclusion of this resonance changes the Halo EFT predictions for deuteron induced neutron transfer reactions off $^{11}$Be which were investigated in Ref. [134].

# Chapter 4

# Electric Dipole Moments of Three-nucleon Systems in the Pionless Effective Field Theory

This chapter is another application of short-range EFTs. It is mainly based on the manuscript [165] with more details included. In pionless effective field theory, we calculate the electric dipole moments (EDMs) of three-nucleon systems at leading order. The one-body contributions that arise from permanent proton and neutron EDMs and the two-body contributions that arise from CP-odd nucleon-nucleon interactions are taken into account. Neglecting the Coulomb interaction, we consider the triton and $^3$He, and also investigate them in the Wigner-SU(4) symmetric limit. We also calculate the electric dipole form factor and find numerically that the momentum dependence of the electric dipole form factor in the Wigner limit is, up to an overall constant (and numerical accuracy), the same as the momentum dependence of the charge form factor. Finally, we study the cutoff dependence of these observables and find that they are properly renormalized.

## 4.1 Introduction

The breaking of the discrete symmetries of charge conjugation $C$ and charge conjugation and parity $CP$ is a necessary condition for the dynamical generation of a matter-antimatter

asymmetry in the Universe [129]. In the Standard Model (SM) of particle physics, $C$ is maximally broken by the different gauge interactions of left- and right-handed quarks and leptons. The breaking of $CP$ is much more subtle. In the SM with three generations of quarks, $CP$ is broken by the phase of the Cabibbo-Kobayashi-Maskawa (CKM) mixing matrix [87] and by the QCD $\bar{\theta}$ term [143, 142]. While all observed $CP$ violation (CPV) in the kaon and $B$ meson systems can be explained by the CKM mechanism, CPV in the SM fails to generate the observed matter-antimatter asymmetry of the Universe by several orders of magnitude [52, 54, 53, 75]. Baryogenesis thus requires the existence of new sources of CPV.

Electric dipole moments (EDMs) of leptons, nucleons, atomic and molecular systems receive negligible contributions from the CKM mechanism [115, 136, 164, 163] and are thus extremely sensitive probes of CPV beyond the SM (BSM). Currently, the best limits are on the electron EDM, $|d_e| < 1.1 \cdot 10^{-16}$ $e$ fm (90% C.L.), deduced from experiments with ThO and HfF molecules [7, 29], on the neutron EDM, $|d_n| < 1.8 \cdot 10^{-13}$ $e$ fm (90% C.L.) [1], and on the EDM of $^{199}$Hg, $|d_{^{199}\mathrm{Hg}}| < 6.2 \cdot 10^{-17}$ $e$ fm [57]. Constraints on the diamagnetic atoms $^{129}$Xe and $^{225}$Ra are presently weaker [22, 128], but, particularly in the case of $^{225}$Ra, they are expected to improve by several orders of magnitude in the coming years [22]. These bounds can be naively converted into new physics scales in the range of $10 - 100$ TeV, making EDM experiments extremely competitive with direct searches at the Large Hadron Collider (LHC). For this reason, there exists an extensive experimental program with the goal of improving existing bounds by one or two orders of magnitude and to search for EDMs in new systems. In particular, there are proposals to measure the EDMs of charged particles, including muons, protons and light nuclei, in dedicated storage ring experiments [104, 117, 3, 144]. These experiments might reach a sensitivity of $10^{-16}$ $e$ fm, comparable with the next generation of neutron EDM experiments, and they provide a much more direct connection with the microscopic sources of CPV compared to EDMs of diamagnetic atoms, whose interpretation is affected by the large nuclear theory uncertainties in the calculations of nuclear Schiff moments [10, 47]. Thus, the measurement of the EDMs of the proton and light nuclei might play a crucial role not only for the discovery of BSM physics, but also in disentangling different high-energy mechanisms of CPV [37, 42, 25].

A description of EDM observables that employs nuclear degrees of freedom is therefore clearly needed for the interpretation of experimental data. Chiral effective field theory is particularly useful in this endeavor since it can relate measured EDMs to their underlying sources, such as the QCD $\bar{\theta}$-term or CPV operators from BSM physics. In Weinberg's power counting, the EDMs are for several BSM mechanisms dominated by pion-range CPV interactions [37, 25], whose strength is related by chiral symmetry to nucleon masses and mass splittings [32, 98, 37, 25, 138, 38]. The CPV pion-nucleon couplings appearing at leading order (LO) can thus be extracted from existing lattice QCD calculations in the case of the QCD $\bar{\theta}$-term [40], or require relatively simple lattice QCD input in the case of BSM operators [38]. Over the last years significant efforts have been made to improve the description of EDMs in chiral EFT, with the derivation of the chiral Lagrangian at next-to-next-to-leading order (N$^2$LO) from the QCD $\bar{\theta}$-term and dimension-six sources of CPV [98, 39, 27], and of the N$^2$LO time-reversal ($T$) breaking potential [95, 26, 56, 35]. These developments made it possible to carry out chiral effective theory calculations of EDMs of light nuclei [25, 56, 139] which have complemented hybrid calculations using phenomenological nuclear potentials in conjunction with CPV potential derived in the effective theory [140, 37, 162, 163]. For recent reviews of EDMs of light nuclei see Refs. [47, 161, 35].

Such calculations, which employ a complete effective field theory approach to calculate the wave function of the nuclear bound state and for the construction of the nuclear current, promise to provide reliable uncertainty estimates and a path to the reduction of those quantified uncertainties. We however stress that, even in chiral EFT, a systematic connection between nuclear EDMs and their microscopic quark-level sources beyond LO requires the determination of CPV nucleon-nucleon couplings, and thus lattice QCD simulations in two- or three-nucleon systems. In addition, it was recently shown in Ref. [36] that long-standing issues with the renormalization of singular chiral EFT potentials [81, 102] demand the inclusion of LO CPV short-range nucleon-nucleon couplings whenever the CPV pion-nucleon interactions act in the ${}^1S_0$–${}^3P_0$ channel. While this has no consequence for the EDM of the deuteron, it significantly affects the chiral EFT uncertainties in the three-nucleon system [36].

The so-called pionless EFT, EFT($\not{\pi}$) [66], is an alternative EFT approach to light nuclei. It is an expansion in the ratio of the range of the nuclear interaction $R$ and the two-nucleon scattering length $a$ and has been shown to be a working, order-by-order renormalizable framework for two-, three- and four-nucleon system [82, 15, 14, 110]. The low-energy constants of this EFT can be related directly to scattering and bound state observables in few-nucleon systems and pionless EFT predictions are thereby inherently tied to a small number of these nuclear observables. The dependence of observables on the chosen regulators is also well-understood and indicates that the inherent uncertainties of the low-energy expansion are under control. This EFT can be applied to any system that displays a large scattering length $a$ and has therefore also found applications in atomic and particle physics.

Here we will use pionless EFT to calculate the EDM and the electric dipole form factor (EDFF) of the three-nucleon systems at leading order. This has several benefits: We can easily study the dependence of the EDFF on two- and three-nucleon observables. Furthermore, a non-zero EDM measurement can be directly related to a corresponding scattering amplitude using pionless EFT. We can thus retain predictive power by matching these amplitudes to chiral EFT, at least in those channels in which the CPV pion-exchange leads to regulator-independent results, or, even more promisingly, by taking advantage of the significant progress in lattice QCD calculations of few-nucleon matrix elements [101, 30, 74, 33], which can be directly related to the corresponding pionless EFT ones.

We will also calculate the EDFF in the so-called Wigner limit in which the two-nucleon spin-singlet and -triplet interactions are identical. This limit has been used for many decades to obtain a conceptual understanding of the three-nucleon system [49] and the unitary limit (a special case of the Wigner limit) has also recently been proposed as a starting point for a novel EFT description of light nuclei [91].

Finally, we will also study the regulator-dependence of the observables considered in our EFT framework. Strong regulator dependence in observables is the first signature of missing counterterms that have to be included in an EFT for it to become predictive. Our analysis will demonstrate that our framework is fully renormalized and has thereby has predictive power with the uncertainty deduced from the truncation error of the EFT.

This chapter is organized as follows. In Sec. 4.2, we summarize the theoretical building blocks and define the CPV interactions used in the calculation. The calculation of the EDFF is conveniently performed by introducing a trimer field, following Ref. [61, 149, 151]. We give the integral equation for the CP-even trimer-nucleon-dimer vertex function in Sec. 4.2.1, and derive the integral equations in the presence of CPV interactions in Sec. 4.3. In Sec. 4.4, we give the schematic diagrammatic expressions of the three-nucleon EDFF, leaving the detailed expressions to appendices E and F. In Sec. 4.5, we discuss the numerical results, and we conclude in Sec. 4.6.

## 4.2 Theoretical Building Blocks

The leading order CP-even effective Lagrangian in EFT($\not{\pi}$) for the three-nucleon system is [16]

$$\mathcal{L} = N^\dagger \left( i\partial_0 + eA_0 \frac{1+\tau_3}{2} + \frac{\vec{\nabla}^2}{2M_N} \right) N + \Delta_t t_i^\dagger t_i + \Delta_s s_a^\dagger s_a + y_t \left[ t_i^\dagger N^T \hat{P}_t^i N + \text{H.c.} \right]$$
$$+ y_s \left[ s_a^\dagger N^T \hat{P}_s^a N + \text{H.c.} \right] + \Omega \psi^\dagger \psi + \left[ \omega_t \psi^\dagger \sigma_i N t_i + \text{ H.c. } \right] - \left[ \omega_s \psi^\dagger \tau_a N s_a + \text{ H.c. } \right] , \quad (4.2.1)$$

where the auxiliary dimer fields $t_i$ and $s_a$ represent the ${}^3S_1$ and ${}^1S_0$ dibaryon field, respectively. The trimer field $\psi$ represents the three-nucleon field with total angular momentum 1/2. A three-nucleon force appears at LO because it was shown [16, 14, 15] to be necessary for the renormalization of three-body observables.

The operators $\hat{P}_t$ and $\hat{P}_s$,

$$\hat{P}_t^i = \frac{1}{\sqrt{8}} \sigma^2 \sigma^i \tau^2, \qquad \hat{P}_s^a = \frac{1}{\sqrt{8}} \sigma^2 \tau^2 \tau^a, \quad (4.2.2)$$

project on the spin-triplet, isospin-singlet and spin-singlet, isospin-triplet channels, respectively. For the coefficients in Eq. (4.2.1) we choose the conventions

$$y_t^2 = y_s^2 = \frac{4\pi}{M_N}, \quad \Delta_t = \gamma_t - \mu, \quad \Delta_s = \gamma_s - \mu, \quad (4.2.3)$$

where $\gamma_t \simeq 45.7$ MeV denotes the binding momentum of the deuteron, and $\gamma_s \simeq -7.9$ MeV is the $^1S_0$ virtual-state momentum. The renormalization scale $\mu$ is introduced through the use of the so-called power divergence subtraction scheme in the two-nucleon sector [82].

Using a matching calculation to a theory without trimer fields it can be shown that $\omega_s = \omega_t$ [149]. These parameters are functions of the ultraviolet cutoff in the three-nucleon Schrödinger equation. They are determined by adjusting them (at a given cutoff) to a three-nucleon observable such as a binding energy, e.g. $B(^3\mathrm{H}) = -8.48$ MeV.

The dressed spin-triplet and spin-singlet dibaryon propagators are calculated by summing over an infinite number of loop diagrams. At LO, they are given by

$$iD_{t,s}^{\mathrm{LO}}(p_0, p) = \frac{i}{\gamma_{t,s} - \sqrt{\frac{p^2}{4} - M_N p_0 - i\epsilon}} \ . \tag{4.2.4}$$

The renormalization of the deuteron wave function at LO is given by the residue about the deuteron pole,

$$Z_d^{\mathrm{LO}} = \frac{2\gamma_t}{M_N} \ . \tag{4.2.5}$$

CPV from BSM physics can be systematically classified in the framework of the Standard Model Effective Field Theory (SMEFT) [28, 59], where the SM is complemented by the most general set of higher-dimensional operators, expressed in terms of SM fields and invariant under the SM gauge group. The most important CPV operators arise at canonical dimension-six, and are suppressed by two powers of $v/\Lambda_X$, where $\Lambda_X$ is the BSM physics scale and $v = 246$ GeV is the Higgs vacuum expectation value. For EDM studies, heavy SM degrees of freedom can be integrated out, by matching the SMEFT onto an $SU(3)_c \times U(1)_{\mathrm{em}}$ invariant EFT [78, 77, 43]. Focusing on two light quark flavors and on operators that are induced by SMEFT operators at tree level, the dimension-six CPV Lagrangian relevant for light nuclear EDMs includes one dimension-four operator, the QCD $\bar{\theta}$ term, and nine dimension-six operators, the gluon chromo-electric dipole moment, the $u$ and $d$ quark electric and chromo-electric dipole moments, and four four-fermion operators. The operator set can be easily extended to include strange quarks [78, 77, 43, 96].

At low-energy, these operators manifest in CP-violating interactions between nucleons and photons. In the single nucleon sector, the most important CPV operators are the neutron and proton EDMs,

$$\begin{aligned}\mathcal{L}_{N\gamma} &= -eN^\dagger\left(d_p\frac{1+\tau_3}{2}+d_n\frac{1-\tau_3}{2}\right)\left(S^\mu v^\nu - S^\nu v^\mu\right)NF_{\mu\nu}\\ &= eN^\dagger\left(d_p\frac{1+\tau_3}{2}+d_n\frac{1-\tau_3}{2}\right)\boldsymbol{\sigma}\cdot\mathbf{E}\,N,\end{aligned} \tag{4.2.6}$$

where $v^\mu = (1,\mathbf{0})$ and $S^\mu = (0,\boldsymbol{\sigma}/2)$ in the nucleon rest frame, and $\mathbf{E}$ denotes the electric field. For all quark-level sources of CPV one expects $d_n \sim d_p$ [115, 41], but the calculation of the exact dependence of $d_{p,n}$ on CPV quark-level couplings requires non-perturbative techniques. The momentum dependence of the nucleon EDFF was computed in Refs. [73, 41]. Since the typical scale of the momentum variation is $q \sim m_\pi$, we ignore it in this chapter.

For the QCD $\bar\theta$-term, the neutron EDM can be estimated by the size of the long-range pion loop [32, 99, 73, 105, 41, 97, 137, 40]

$$d_n(\bar\theta) \simeq 2\cdot 10^{-3}\,\bar\theta\, e\,\mathrm{fm}, \tag{4.2.7}$$

in good agreement with the naive expectation $d_n = \mathcal{O}(m_\pi^2/\Lambda_\chi^3\,\bar\theta)$, where $\Lambda_\chi = 2\pi F_\pi$ is the chiral perturbation theory breakdown scale, with $F_\pi \simeq 92$ MeV the pion decay constant. Progress in lattice QCD calculations will soon allow a theoretical error to be attached to the estimate in Eq. (4.2.7) [76, 2, 21, 141, 86, 45]. The nucleon EDM induced by dimension-six operators has been estimated using QCD sum rules [113, 114, 115, 62] or chiral techniques [39, 137, 31]. With the exception of the contribution of the quark EDM, which is determined by the nucleon tensor charges [60, 8], these estimates have large uncertainties.

In EFT($\not\pi$), the leading two-nucleon operators resulting in a non-zero EDM are given by

$$\begin{aligned}\mathcal{L}_{\not P\not T} &= \frac{y_t}{\sqrt{8}}C_{^3S_1-^1P_1}\left(t_i^\dagger N^t\sigma_2\tau_2\overleftrightarrow{\nabla}^i N\right) + \frac{y_t}{\sqrt{8}}C_{^3S_1-^3P_1}i\varepsilon^{ilm}\left(t_i^\dagger N^t\sigma_2\tau_2\tau_3\overleftrightarrow{\nabla}^m\sigma^l N\right)\\ &+ \frac{y_s}{\sqrt{8}}\left(s_a^\dagger N^t\sigma_2\tau_2\tau_b\boldsymbol{\sigma}\cdot\overleftrightarrow{\nabla}N\right)\left(C^{(0)}_{^1S_0-^3P_0}\delta^{ab} + C^{(1)}_{^1S_0-^3P_0}i\varepsilon^{3ab} + C^{(2)}_{^1S_0-^3P_0}\left(\delta^{ab}-3\delta^{a3}\delta^{b3}\right)\right)\ .\end{aligned} \tag{4.2.8}$$

These operators were constructed in Refs. [95, 153, 35]. All operators mediate transitions between $S$ and $P$ waves, as denoted by the name of the coefficients. The operators $C_{^3S_1-^1P_1}$ and $C^{(0)}_{^1S_0-^3P_0}$ are isospin invariant, $C_{^3S_1-^3P_1}$ and $C^{(1)}_{^1S_0-^3P_0}$ break isospin by one unit, while $C^{(2)}_{^1S_0-^3P_0}$ is an isotensor operator. The couplings $C_{^3S_1-^1P_1}$, $C_{^3S_1-^3P_1}$ and $C^{(i)}_{^1S_0-^3P_0}$ have dimension of mass$^{-1}$, and are independent of the renormalization scale $\mu$. Ref. [95] provides a naive-dimensional-analysis estimate of the size of these coefficients in terms of quark-level couplings. Going beyond dimensional analysis requires first principle calculations of CPV matrix elements.

In this chapter we will thus express the EDMs of $^3$H and $^3$He in terms of $d_n$, $d_p$ and of the five couplings in Eq. (4.2.8), and discuss the minimal set of observables that is necessary to disentangle them.

### 4.2.1 The three-nucleon bound state vertex function

We will calculate the EDFF by integrating over three-particle irreducible diagrams that contain a single insertion of a CPV operator. Following the formalism defined in Refs. [149, 151], we define a diagram to be three-particle irreducible when it cannot be separated by cutting at a trimer field vertex. The resulting form factor diagrams contain necessarily infinite sums of nucleon-deuteron rescattering diagrams that are given by vertex functions that result from an integral equation, and pieces that include the photon coupling to a single nucleon line.

The LO vertex function $\boldsymbol{\mathcal{G}}(E,p)$ for a three-nucleon system in the center-of-mass frame with binding energy $E$ and relative momentum $\mathbf{p}$ between outgoing nucleon and dimer is given by the integral equation shown diagrammatically in Fig. 4.1 and given explicitly by

$$\boldsymbol{\mathcal{G}}(E,p) = \widetilde{\mathbf{1}} + \mathbf{K}^0(q,p,E) \otimes_q \widetilde{\boldsymbol{\mathcal{G}}}(E,q) \ . \tag{4.2.9}$$

We define the short-hand notation

$$\widetilde{\boldsymbol{\mathcal{G}}}(E,q) = \boldsymbol{D}\left(E - \frac{q^2}{2M_N}, q\right) \boldsymbol{\mathcal{G}}(E,q) \tag{4.2.10}$$

where

$$\boldsymbol{D}\left(E-\frac{q^2}{2M_N},q\right)=\begin{pmatrix} D_t\left(E-\frac{q^2}{2M_N},q\right) & 0 \\ 0 & D_s\left(E-\frac{q^2}{2M_N},q\right)\end{pmatrix}, \tag{4.2.11}$$

and the inhomogeneous term in this integral equation is

$$\widetilde{\mathbf{1}}=\begin{pmatrix} 1 \\ -1 \end{pmatrix} . \tag{4.2.12}$$

The convolution operator $\otimes_q$ is defined as

$$A(q)\otimes_q B(q)=\int_0^\Lambda dq\frac{q^2}{2\pi^2}A(q)B(q) , \tag{4.2.13}$$

where $\Lambda$ is a hard momentum-space cutoff. Observables will be $\Lambda$-independent for large cutoffs.

The homogeneous term is defined by

$$\mathbf{K}^\ell(q,p,E)=R_\ell(q,p,E)\begin{pmatrix} -1 & 3 \\ 3 & -1 \end{pmatrix} , \tag{4.2.14}$$

where the function $R_\ell$ is defined as

$$R_\ell(q,p,E)=\frac{2\pi}{qp}Q_\ell\left(\frac{q^2+p^2-M_NE-i\epsilon}{qp}\right) , \tag{4.2.15}$$

and $Q_l$ are functions proportionial to Legendre function of the second kind but differ from their conventional definition by a phase of $(-1)^\ell$,

$$Q_\ell(a)=\frac{1}{2}\int_{-1}^{1}\frac{P_\ell(x)}{a+x}\mathrm{d}x . \tag{4.2.16}$$

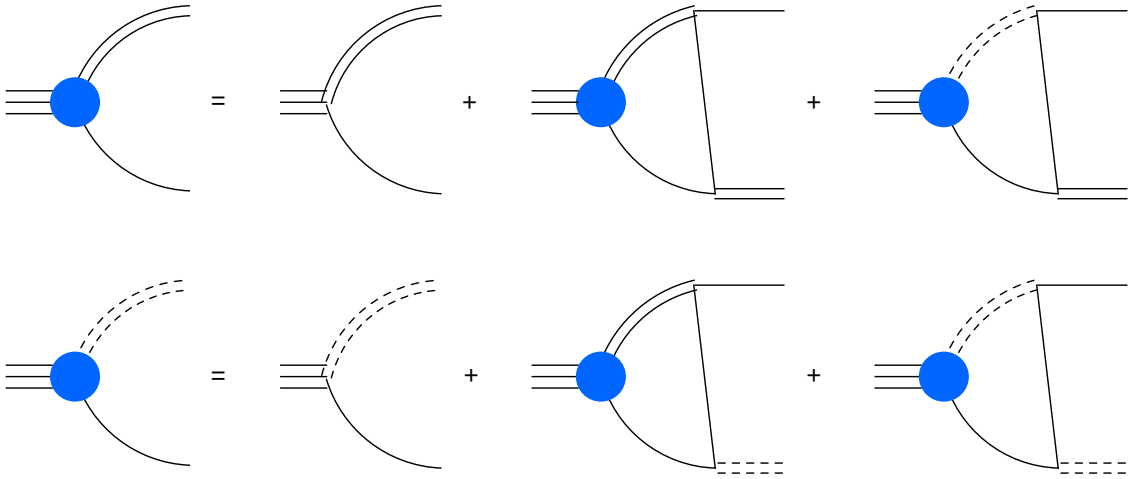

**Figure 4.1:** Diagrammatic representation of the LO three-body CP-even vertex function. The (dashed) double line denotes a dressed spin-singlet (spin-triplet) dibaryon propagator.

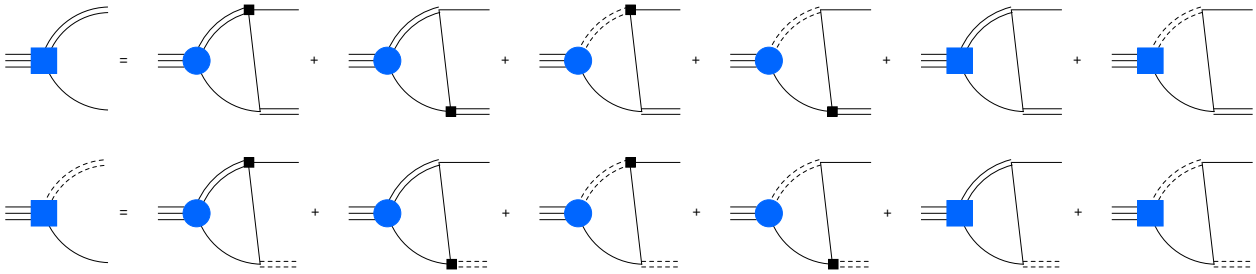

**Figure 4.2:** $\not{P}\not{T}$ vertex function. A blue square denotes the $\not{P}\not{T}$ vertex function, while a black square an insertion of the operators in Eq. (4.2.8). Remaining notation as in Fig. 4.1.

## 4.3 The T-odd vertex function

A three-particle irreducible diagram can contain repeated nucleon-dimer scattering between a nucleon-photon vertex and an insertion of a two-nucleon CP-odd vertex. We include these diagrams through two integral equations that generate a vertex function that contains a single insertion of the CP-odd two-nucleon interaction. The diagrammatic expression for these vertex functions is shown in Fig. 4.2.

The T-odd vertices convert the spin 1/2, isospin 1/2 trimer field $\psi$ into a nucleon-dimer with three possible spin/isospin quantum numbers: spin and isospin 1/2, spin 1/2 and isospin 3/2, as well as spin 3/2 and isospin 1/2. The latter does not contribute to the three-nucleon EDM at leading order, since the LO electromagnetic interaction does not change spin and the overlap of the spin 3/2 T-odd function with the triton or helion vanishes. The integral equations for the isospin 1/2 component, $\boldsymbol{\mathcal{T}}^{\frac{1}{2}}$, and the isospin 3/2 component, $\boldsymbol{\mathcal{T}}^{\frac{3}{2}}$, of the spin-1/2 T-odd vertex functions are given by

$$(\boldsymbol{\sigma}\cdot\mathbf{k})\boldsymbol{\mathcal{T}}^{\frac{1}{2}}(E,k) = (\boldsymbol{\sigma}\cdot\mathbf{k})\left\{\boldsymbol{R}^{\frac{1}{2}}_{\mathcal{T}}(E,k,q)\otimes_q \widetilde{\boldsymbol{\mathcal{T}}}^{\frac{1}{2}}(E,q) + \boldsymbol{R}^{\frac{1}{2}}(E,k,q)\otimes_q \widetilde{\boldsymbol{\mathcal{G}}}(E,q)\right\}\ , \tag{4.3.1}$$

$$\begin{aligned}(\boldsymbol{\sigma}\cdot\mathbf{k})(\delta^{3c}+\tau^3\tau^c)\boldsymbol{\mathcal{T}}^{\frac{3}{2}}(E,k) = (\boldsymbol{\sigma}\cdot\mathbf{k})(\delta^{3c}+\tau^3\tau^c)\Big\{&\boldsymbol{R}^{\frac{3}{2}}_{\mathcal{T}}(E,k,q)\otimes_q \widetilde{\boldsymbol{\mathcal{T}}}^{\frac{3}{2}}(E,q)\\ &+\boldsymbol{R}^{\frac{3}{2}}(E,k,q)\otimes_q \widetilde{\boldsymbol{\mathcal{G}}}(E,q)\Big\}\ ,\end{aligned} \tag{4.3.2}$$

where we show explicitly the spin/isospin structure of the vertex functions, and, similarly to the CP-even case, we introduced the shorthand notation for the product of a vertex function and a dressed dibaryon propagator

$$\widetilde{\boldsymbol{\mathcal{T}}}^{\frac{1}{2},\frac{3}{2}}(E,q) = \boldsymbol{D}\left(E-\frac{q^2}{2M_N},q\right)\boldsymbol{\mathcal{T}}^{\frac{1}{2},\frac{3}{2}}(E,q)\ . \tag{4.3.3}$$

The kernels of the homogeneous terms are

$$\boldsymbol{R}^{\frac{1}{2}}_{\mathcal{T}}(E,k,q) = \frac{q}{k}R_1(E,k,q)\begin{pmatrix}-1 & 3\\ 3 & -1\end{pmatrix}, \qquad \boldsymbol{R}^{\frac{3}{2}}_{\mathcal{T}}(E,k,q) = \frac{q}{k}R_1(E,k,q)\begin{pmatrix}0 & 0\\ 0 & 2\end{pmatrix}. \tag{4.3.4}$$

The inhomogeneous terms are driven by the T-odd operators in Eq. (4.2.8). The isospin 1/2 vertex functions receive contributions from both isoscalar and isovector operators in Eq. (4.2.8),

$$\boldsymbol{R}^{\frac{1}{2}}(E,k,q) = \left[R_0(E,k,q)\begin{pmatrix}-1 & 1\\ -2 & 0\end{pmatrix} + \frac{q}{k}R_1(E,k,q)\begin{pmatrix}1 & 2\\ -1 & 0\end{pmatrix}\right]\left(C_{^3S_1-^1P_1} + \frac{2}{3}\tau^3 C_{^3S_1-^3P_1}\right)$$
$$+\left[R_0(E,k,q)\begin{pmatrix}0 & 2\\ -1 & 1\end{pmatrix} - \frac{q}{k}R_1(E,k,q)\begin{pmatrix}0 & -1\\ 2 & 1\end{pmatrix}\right]\left(C^{(0)}_{^1S_0-^3P_0} - \frac{2}{3}\tau^3 C^{(1)}_{^1S_0-^3P_0}\right). \tag{4.3.5}$$

The isospin 3/2 component is induced by the isotensor operator $C^{(2)}_{^1S_0-^3P_0}$ and by the isovector operators yielding

$$\boldsymbol{R}^{\frac{3}{2}}(E,k,q) = \left[2R_0(E,k,q) + \frac{q}{k}R_1(E,k,q)\right]\begin{pmatrix}0 & 0\\ 1 & 0\end{pmatrix}\frac{4}{3}C_{^3S_1-^3P_1}$$
$$-\frac{1}{3}\left[R_0(E,k,q)\begin{pmatrix}0 & 0\\ 1 & 5\end{pmatrix} + \frac{q}{k}R_1(E,k,q)\begin{pmatrix}0 & 0\\ 2 & 4\end{pmatrix}\right]\left(C^{(1)}_{^1S_0-^3P_0} - 3\tau_3 C^{(2)}_{^1S_0-^3P_0}\right). \tag{4.3.6}$$

### 4.3.1 Integral equations in the SU(4) limit

Nuclear interactions exhibit an approximate $SU(4)$ spin-isospin (Wigner) symmetry, which would be exact in the limit [160, 155] of equal spin-triplet and singlet scattering lengths. $SU(4)$ breaking is parameterized by the difference $\gamma_t - \gamma_s$, and the expansion around the Wigner limit converges very well [155]. We will study the electric dipole form factor of the three-nucleon system in the $SU(4)$ limit, and provide the relevant formulae in this section.

In the $SU(4)$ limit, $D_t = D_s = D_{SU(4)}$ and from Eq. (4.2.9) one can see that $\widetilde{\mathcal{G}}_t = -\widetilde{\mathcal{G}}_s$. We can introduce the combinations

$$\mathcal{G}_\pm = \frac{1}{2}\left(\mathcal{G}_t \mp \mathcal{G}_s\right), \tag{4.3.7}$$

so that $\widetilde{\mathcal{G}}_-$ vanishes in the $SU(4)$ limit.

The structure of the T-odd vertex functions simplifies significantly in the $SU(4)$ limit. It can be shown that both the isospin 1/2 and isospin 3/2 components are proportional to a single function $\mathcal{T}_{SU(4)}$, which satisfies the integral equation

$$\mathcal{T}_{SU(4)}(E,k) = -\mathcal{R}_{SU(4)}(E,k,q) \otimes_q \widetilde{\mathcal{G}}_+(E,q) + 2\frac{q}{k} R_1(E,k,q) \otimes_q \widetilde{\mathcal{T}}_{SU(4)}(E,q)\ , \tag{4.3.8}$$

$$\mathcal{R}_{SU(4)}(E,k,q) = 2R_0(E,k,q) + \frac{q}{k} R_1(E,k,q). \tag{4.3.9}$$

In terms of $\mathcal{T}_{SU(4)}$, we can write

$$\boldsymbol{\mathcal{T}}^{\frac{1}{2}}_{SU(4)}(E,k) = \begin{pmatrix} 1 \\ 1 \end{pmatrix} \mathcal{T}^{\frac{1}{2}}_{SU(4)}(E,k)\ , \quad \boldsymbol{\mathcal{T}}^{\frac{3}{2}}_{SU(4)}(E,k) = \begin{pmatrix} 0 \\ 1 \end{pmatrix} \mathcal{T}^{\frac{3}{2}}_{SU(4)}(E,k)\ , \tag{4.3.10}$$

where

$$\mathcal{T}^{\frac{1}{2}}_{SU(4)}(E,k) = \left[C^{(0)}_{{}^1S_0-{}^3P_0} + C_{{}^3S_1-{}^1P_1} + \frac{2\tau^3}{3}(C_{{}^3S_1-{}^3P_1} - C^{(1)}_{{}^1S_0-{}^3P_0})\right]\mathcal{T}_{SU(4)}(E,k)\ , \tag{4.3.11}$$

$$\mathcal{T}^{\frac{3}{2}}_{SU(4)}(E,k) = \left[-\frac{2}{3}(2C_{{}^3S_1-{}^3P_1} + C^{(1)}_{{}^1S_0-{}^3P_0}) + 2\tau^3 C^{(2)}_{{}^1S_0-{}^3P_0}\right]\mathcal{T}_{SU(4)}(E,k)\ . \tag{4.3.12}$$

## 4.4 Three-nucleon form factors

The EDFF of a three-nucleon system can be obtained from the matrix element of the zero-component of the electromagnetic current $J^0$ in the presence of CP violation. Neglecting recoil corrections, we can write the matrix element of $J^0$ as

$$\langle \mathbf{p}', \alpha | J^0 | \mathbf{p}, \beta \rangle = F_C(q^2)\delta_{\alpha\beta} + [\boldsymbol{\sigma}\cdot\mathbf{q}]_{\alpha\beta} F_D(q^2), \tag{4.4.1}$$

where $\alpha$ and $\beta$ are spin indices of the in- and outgoing three-nucleon state, $\mathbf{q} = \mathbf{p} - \mathbf{p}'$ is the momentum injected by the current, and $q = |\mathbf{q}|$. $F_C$ denotes the charge form factor and $F_D$ the electric dipole form factor, which vanishes in the absence of CP-violation. We will write the EDFF in terms of two components,

$$F_D(q^2) = F_{\rm I}(q^2) + F_{\rm II}(q^2). \tag{4.4.2}$$

$F_{\rm I}$ denotes the EDFF generated by the T-odd component of the electromagnetic current, which is dominated by one-nucleon operators, namely the neutron and proton EDMs in Eqs. (4.2.6). CPV interactions can in addition generate a CP-odd component in the three-nucleon wavefunction, which is dominated by the two-body operators in Eq. (4.2.8). We denote the ensuing EDFF by $F_{\rm II}$.

The diagrams contributing to $F_I$ are shown in Fig. 4.3, where the black square denotes an insertion of the nucleon EDM, defined in Eq. (4.2.6). We therefore write the $F_{\rm I}$ as the sum of the three terms

$$F_{\rm I}(q^2) = F_{\rm I}^A(q^2) + F_{\rm I}^B(q^2) + F_{\rm I}^C(q^2)\ , \tag{4.4.3}$$

corresponding to the three diagrams shown in Fig. 4.3. We give explicit expressions for the diagrams in Appendix E. From the expression in Appendix E and the charge form factor in Refs. [149, 151], which we also report in Appendix E, it can be seen that in the $SU(4)$ limit, the one-body contribution to the triton and $^3$He EDFFs is identical to $F_C(q^2)$, weighted by the proton or neutron EDM,

$$F_{\rm I}(q^2, {}^3{\rm H}) \xrightarrow{SU(4)} d_p\, F_C(q^2), \qquad F_{\rm I}(q^2, {}^3{\rm He}) \xrightarrow{SU(4)} d_n F_C(q^2). \tag{4.4.4}$$

We will see that the results at the physical values of $\gamma_s$ and $\gamma_t$ deviate from this expectation by a few percent.

The second class of contributions arises from the two-nucleon operators given in Eq. (4.2.8). In Fig. 4.4 we show the EDFF topologies that include a CP-odd two-nucleon operator. Diagrams $(a)$, $(b)$ and $(c)$ include the T-odd vertex functions defined in Section 4.3.

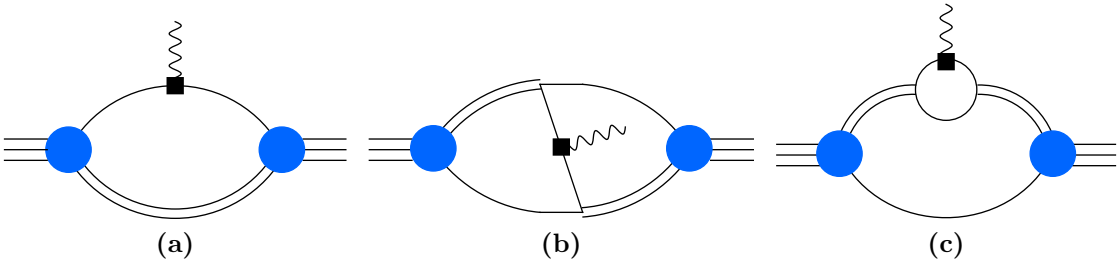


**Figure 4.3:** Diagrams contributing to the one-body component of the EDFF, defined in Eq. (4.4.3). Here, the double line can denote a spin-triplet or singlet dimer. The black square denotes an insertion of the nucleon EDM, defined in Eq. (4.2.6).

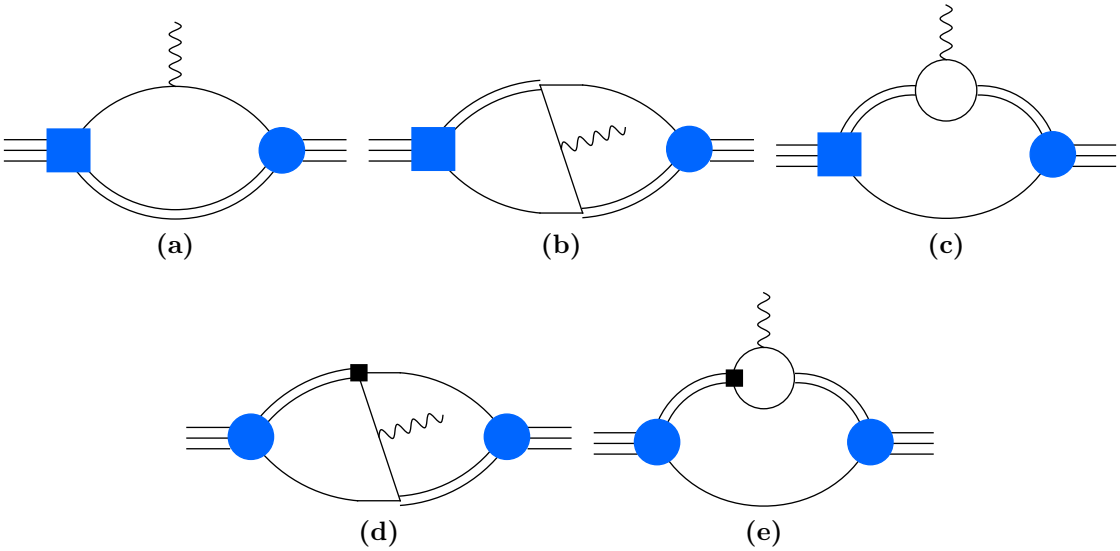


**Figure 4.4:** Diagrams for the three-nucleon EDM form factor at LO that involve a CP-odd two-nucleon interaction.

Diagram ($d$) and ($e$) include the CP-even $\mathcal{G}$ vertex functions, with an additional insertion of the T-odd nucleon-dimer operators. For simplicity, we only show one topology. The complete set of diagrams also includes the insertions of the T-odd operators to the right of the photon-nucleon vertex.

We write the sum of contributions to the EDFF that include two-body CP-odd interactions as

$$F_{\rm II}(q^2) = F_{\rm II}^A(q^2) + F_{\rm II}^B(q^2) + F_{\rm II}^C(q^2) + F_{\rm II}^D(q^2) + F_{\rm II}^E(q^2) \ , \tag{4.4.5}$$

where the superscript indicates the corresponding diagram in Fig. 4.4. We give explicit expressions for the individual diagrams in Appendix F.

In the $SU(4)$ limit, the two-body diagrams also undergo a noticeable simplification, and they become proportional to a single combination of T-odd coefficients,

$$F_{\rm II}(q^2,{}^3\,{\rm H}) \xrightarrow{SU(4)} \tilde{F}_{SU(4)}(q^2)\left(C_{^3S_1-^1P_1} + C^{(0)}_{^1S_0-3P_0} - 2C^{(2)}_{^1S_0-^3P_0} - 2C_{^3S_1-^3P_1}\right) , \tag{4.4.6}$$

$$F_{\rm II}(q^2,{}^3\,{\rm He}) \xrightarrow{SU(4)} -\tilde{F}_{SU(4)}(q^2)\left(C_{^3S_1-^1P_1} + C^{(0)}_{^1S_0-3P_0} - 2C^{(2)}_{^1S_0-^3P_0} + 2C_{^3S_1-^3P_1}\right) , \tag{4.4.7}$$

where $\tilde{F}_{SU(4)}(q^2)$ is a universal function that depends on $q$, on the scattering length in the Wigner limit and the three-body binding energy. In particular, the three-nucleon EDM becomes insensitive to the isospin-1 $C^{(1)}_{^1S_0-^3P_0}$ operator.

## 4.5 Results

We have calculated the numerical coefficients multiplying the low-energy constants that appear in a decomposition of the CP-odd form factor as a function of $q^2$. In the absence of the Coulomb interaction, we take the binding energy of $^3$H and $^3$He to be equal, *i.e.* $B(^3{\rm H}) = B(^3{\rm He})$. We estimate the numerical uncertainty of the results presented below to be 1 % or lower. The theoretical uncertainty of our results is determined by the expansion parameter of the pionless EFT which is $\gamma_t\rho_t \approx 0.4$, where $\rho_t$ is the effective range in the

triplet channel. The theoretical uncertainties of our results are therefore clearly larger than the numerical ones.

The EDFF results obtained for $^3$H are shown in Fig. 4.6. In Table. 4.1 we show the cutoff dependence of the dipole moment contributions arising from the different EFT operators. Furthermore, we observe that cutoffs larger than 1.5 GeV are needed to obtain numerically converged results. This convergence behavior is shown for the EDMs in Fig. 4.5.

At small $q^2$, we will expand the charge form factor as

$$F_C(q^2) \;=\; Z\left(1-\frac{q^2}{6}\langle r_c^2\rangle+\frac{1}{5!}\langle r_c^4\rangle q^4+\dots\right)\;, \tag{4.5.1}$$

where $r_c^2$ is the charge squared radius and $r_c^4$ the 4$^{\text{th}}$ Zeemach moment, $Z$ denotes the total charge of the nucleus considered and we omitted a label to denote the specific nucleus. We define a similar expansion for the one- and two-body EDFF,

$$F_i(q^2,C) \;=\; d_i(C)\left(1-\frac{q^2}{6}\langle r_{d,\,i}^2(C)\rangle+\frac{1}{5!}\langle r_{d,\,i}^4(C)\rangle q^4+\dots\right), \tag{4.5.2}$$

where $i=\mathrm{I},\mathrm{II}$. $C=d_{n,p}$ for the one-body term, while it denotes one of the nucleon-dimer T-odd operators in Eq. (4.2.8) for the two-body contribution. In the $SU(4)$ limit, all the dependence on couplings factorizes into the universal function $\tilde{F}_{SU(4)}(q^2)$ and a linear combination of low-energy constants, as shown in Eqs. (4.4.6) and (G.1). The square radius of the EDFF is particularly important since it determines the nuclear Schiff moment, and thus the EDMs of the atomic $^3$H and $^3$He species [132]. More precisely, the Schiff moment is proportional to the difference of the charge and dipole radii [34]

$$S_i(C)=-\frac{d_i(C)}{6}\left(\langle r_{d,\,i}^2(C)\rangle-\langle r_c^2\rangle\right)\;, \tag{4.5.3}$$

where again $i$ denotes either the one- (I) or two-body (II) contribution.

The three-nucleon charge form factor in EFT($\not\pi$) has already been computed in Refs. [111, 149, 151], including next-to-leading order (NLO) and next-to-next-to-leading order

($N^2LO$) corrections. At LO, and neglecting Coulomb interactions, one finds

$$\langle r_c^2(^3\mathrm{H})\rangle = 1.28\,\mathrm{fm}^2\ , \qquad \langle r_c^2(^3\mathrm{He})\rangle = 1.56\,\mathrm{fm}^2\ . \tag{4.5.4}$$

These results are in agreement with those in Refs. [149, 151]. We will use the charge form factor as a point of comparison for the momentum dependence of the EDFF. In the $SU(4)$ limit,

$$\langle r_c^2(^3\mathrm{H})\rangle = \langle r_c^2(^3\mathrm{He})\rangle = 1.32\,\mathrm{fm}^2. \tag{4.5.5}$$

The neutron and proton EDMs contributions to the $^3$H and $^3$He EDM are given by

$$d_{\mathrm{I}}(^3\mathrm{H}) \;=\; 0.99\,d_p + 9.7\cdot 10^{-3} d_n, \qquad d_{\mathrm{I}}(^3\mathrm{He}) = 0.99\,d_n + 9.7\cdot 10^{-3} d_p. \tag{4.5.6}$$

The EDM only deviates by 1% from the expectation in the Wigner limit. These results can be compared with chiral EFT calculations of Ref. [37, 25, 56]. These calculations include subleading effects in the strong potential, and thus in the three-nucleon wavefunctions, and typically find the $d_p$ ($d_n$) contribution to $^3$H ($^3$He) EDM to be roughly 10% smaller than Eq. (4.5.6). In Ref. [139], a hybrid approach was used to calculate the EDMs of the three-nucleon system. The current operators were taken from both pionless and pionfull effective field theory but the wave function was evaluated using a model potential. The results for the single-nucleon EDM contributions are roughly of the size found in the chiral EFT calculations and therefore smaller than our results. However, the size of the deviation depends on the specific model used in the calculations of Ref. [139].

The dominant momentum dependence of the EDFF is encoded by the dipole square radius, which we find to be

$$\langle r_{d,\mathrm{I}}^2(^3\mathrm{H}, d_n)\rangle \;=\; -18.3\,\mathrm{fm}^2, \qquad \langle r_{d,\mathrm{I}}^2(^3\mathrm{H}, d_p)\rangle = 1.28\,\mathrm{fm}^2, \tag{4.5.7}$$

$$\langle r_{d,\mathrm{I}}^2(^3\mathrm{He}, d_n)\rangle \;=\; 1.28\,\mathrm{fm}^2, \qquad \langle r_{d,\mathrm{I}}^2(^3\mathrm{He}, d_p)\rangle = -18.3\,\mathrm{fm}^2. \tag{4.5.8}$$

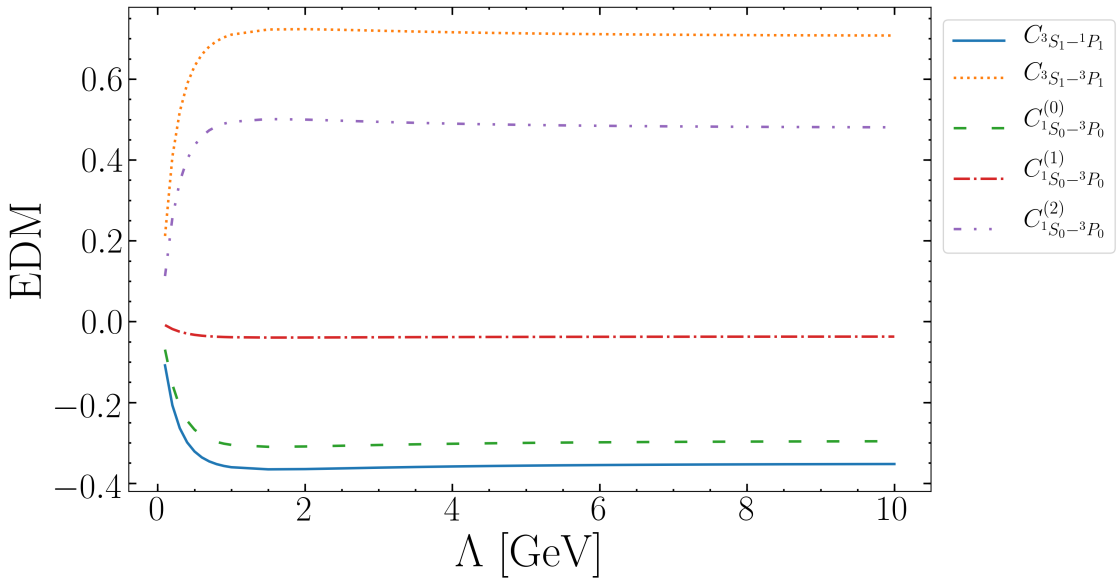


**Figure 4.5:** Cutoff dependence of the $^3$H EDM two-nucleon contributions.

**Table 4.1:** Coefficients of the $^3$H EDM low-energy constants for different values of the cutoff $\Lambda$.

| $\Lambda$ (GeV) | $d_p$ | $d_n$ | $C_{^3S_1-^1P_1}$ | $C_{^3S_1-^3P_1}$ | $C^{(0)}_{^1S_0-^3P_0}$ | $C^{(1)}_{^1S_0-^3P_0}$ | $C^{(2)}_{^1S_0-^3P_0}$ |
|---|---|---|---|---|---|---|---|
| 10 | 0.982 | 0.008 | -0.358 | 0.708 | -0.297 | -0.038 | 0.481 |
| 30 | 0.988 | 0.010 | -0.356 | 0.706 | -0.295 | -0.037 | 0.479 |
| 80 | 0.990 | 0.010 | -0.358 | 0.708 | -0.297 | -0.038 | 0.481 |
| 600 | 0.991 | 0.010 | -0.359 | 0.708 | -0.298 | -0.038 | 0.481 |

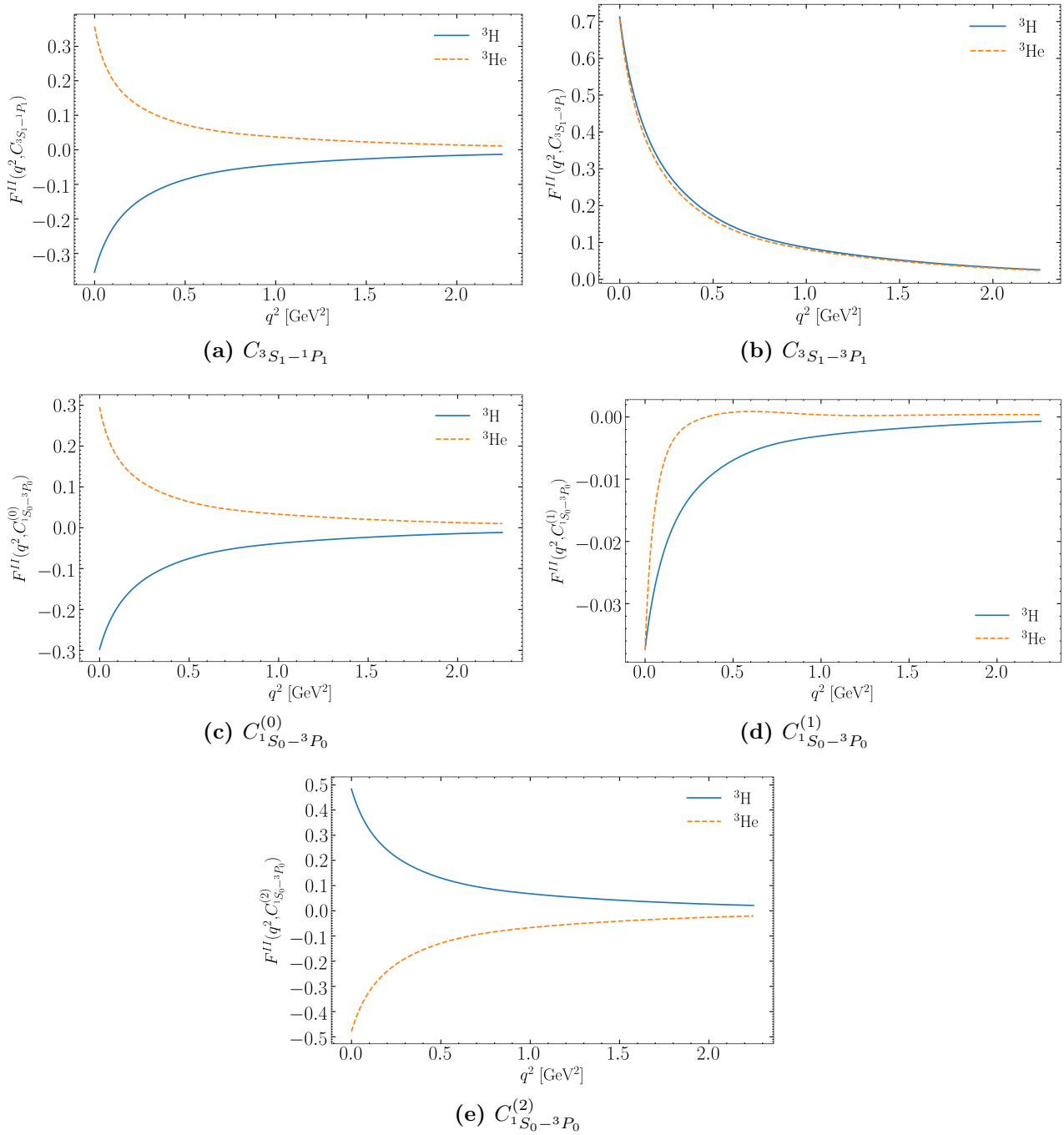


**(a)** $C_{^3S_1-^1P_1}$ **(b)** $C_{^3S_1-^3P_1}$

**(c)** $C^{(0)}_{^1S_0-^3P_0}$ **(d)** $C^{(1)}_{^1S_0-^3P_0}$

**(e)** $C^{(2)}_{^1S_0-^3P_0}$

**Figure 4.6:** The EDFF contributions arising from five different two-nucleon CP-odd operators as a function of $q^2$.

The square radii agree very well with the triton charge radius. This has consequences for the Schiff moment, and thus the EDMs of atomic $^3$He and $^3$H. We see that in the case of $^3$H, the one-body Schiff moment vanishes at LO in EFT($\not\pi$), $S_{\rm I}(^3{\rm H}, d_p) = 0$. The one-body Schiff moment of $^3$He is small, but non-vanishing,

$$S_{\rm I}(^3{\rm He}, d_n) = \frac{d_n}{6}\,(0.28)\ {\rm fm}^2. \tag{4.5.9}$$

We adopt the same expansion as Eq. (4.5.2) for the function $F_{SU(4)}(q^2)$ and obtain for the two-body form factor in the $SU(4)$ limit

$$d_{SU(4)} = -0.332, \qquad \langle r_d^2\rangle_{SU(4)} = 1.32\,{\rm fm}^2. \tag{4.5.10}$$

where we used the average of spin-singlet and triplet binding momentum and the triton binding energy in our calculation. In this limit, the momentum dependence of the form factor seems to be dictated by the charge form factor, and we find that, to very good approximation,

$$\frac{\tilde{F}_{SU(4)}(q^2)}{F_C(q^2)} = \text{constant}. \tag{4.5.11}$$

For $q$ between 0 and 500 MeV, this ratio deviates from a constant at the per mille level. At the physical value of the scattering lengths, the $^3$H and $^3$He EDMs from the two-body form factor $F_{\rm II}$ are given by

$$\begin{aligned} d_{\rm II}(^3{\rm H}) &= -0.358 C_{^3S_1-^1P_1} + 0.707 C_{^3S_1-^3P_1} - 0.297 C^{(0)}_{^1S_0-^3P_0} \\ &\quad -0.0368 C^{(1)}_{^1S_0-^3P_0} + 0.480 C^{(2)}_{^1S_0-^3P_0}, \qquad (4.5.12) \\ d_{\rm II}(^3{\rm He}) &= 0.358 C_{^3S_1-^1P_1} + 0.707 C_{^3S_1-^3P_1} + 0.297 C^{(0)}_{^1S_0-^3P_0} \\ &\quad -0.0375 C^{(1)}_{^1S_0-^3P_0} - 0.480 C^{(2)}_{^1S_0-^3P_0}. \qquad (4.5.13) \end{aligned}$$

where, as our central value, we took the EDFF at $\Lambda = 60$ GeV. As already remarked, the numerical accuracy is a the percent level, and smaller than the LO EFT($\not\pi$) theoretical uncertainty. The EDFF square radii induced by the CPV operators in Eq. (4.2.8) are given in Table .4.2.

We notice that, in the absence of the Coulomb interaction, the EDMs of $^3$H and $^3$He follow simple isospin relations. In particular, the isoscalar and isotensor operators give rise to an isovector EDM, while the isovector operators to an isoscalar three-nucleon EDM. These patterns can be understood by noticing that only the isovector piece of the CP-even one-body electromagnetic current $J^0$ contributes to $F_{\rm II}$ [93, 140, 37].

We observe that the EDM induced by the isoscalar operators $C_{^3S_1-^1P_1}$ and $C^{(0)}_{^1S_0-^3P_0}$ and by the isospin-1 operator $C_{^3S_1-^3P_1}$ deviate from the $SU(4)$ limit by about 10%. The EDM from the operators that connect the $^3S_1$ to $^1P_1$ and $^3P_1$ waves increases (in absolute value) by 10%, while the EDM from $C^{(0)}_{^1S_0-^3P_0}$ decreases by the same amount. We also note that the isotensor operator $C^{(2)}_{^1S_0-^3P_0}$ shows a larger, 30% variation, from the Wigner limit. Furthermore, we find that, with the exception of $C^{(1)}_{^1S_0-^3P_0}$, all operators induce matrix elements of $\mathcal{O}(1)$, as naively expected. The contribution of $C^{(1)}_{^1S_0-^3P_0}$ is suppressed by roughly a factor of ten. It is interesting to note that in the case of $^3$H, the momentum dependence of the form factor induced by $C_{^3S_1-^1P_1}$, $C_{^3S_1-^3P_1}$ and $C^{(0)}_{^1S_0-^3P_0}$ cannot be distinguished from the charged form factor within error. This leads to $S_{\rm II}$ being compatible with zero, implying that for these operators the Schiff moment vanishes at LO in pionless EFT. $C^{(2)}_{^1S_0-^3P_0}$ induces a non-zero, but small Schiff moment. Specifically, in the case of $^3$He, all operators induce a non-zero Schiff moment, but also in this case we expect subleading corrections in EFT($\not\pi$) to be important.

Finally, a comparison with the pionless two-nucleon operator coefficients of the hybrid calculations of Ref. [139] is problematic for a variety of reasons: the hybrid results vary based on the choice of potentials to calculate the wave functions. In addition, a different short-distance regulator is used for the CP-odd two-nucleon operators in these calculations. While we have shown that the results presented in this chapter are regulator independent, the pionless results of the hybrid calculation of Ref. [139] are only given for a single value (the pion mass) of the corresponding regulator. Changing this value from the pion mass to the $\eta$ mass changes some of the results by factors of close to 10. While the CP-odd two-nucleon operators are regulator-dependent in both approaches, the nuclear wave functions in the hybrid approach lack the necessary regulator dependence to compensate for these changes.

It is therefore unclear which values of each of the employed short-distance regulators should be chosen for a comparison.

## 4.6 Summary

In this chapter, we have shown that EFT($\not\pi$) is an efficient framework that facilitates a straightforward calculation of the EDMs and their corresponding form factors of three-nucleon systems. We focused on the $^3$H and $^3$He systems at leading order in the pionless EFT expansion and neglected Coulomb effects in the $^3$He system. At this order, the only (CP-even) parameters that enter our calculation are the deuteron binding energy, the two-nucleon spin-singlet scattering length, and the three-body binding energy of the state under consideration. Allowing for CP-odd interactions in the few-nucleon sectors leads to a total of 7 parameters, where two of them are the neutron and proton EDM and 5 arise from short-distance physics in the two-nucleon system.

The deuteron and the isoscalar combination of the $^3$H and $^3$He EDMs are mostly sensitive to the isovector coupling $C_{^3S_1-^3P_1}$ (see App. D for a derivation of the EDFF and resulting EDM in pionless EFT). These two observables are thus largely degenerate, and, neglecting the one-body piece, our calculation finds

$$\frac{d(^3\mathrm{H}) + d(^3\mathrm{He})}{2d(^2\mathrm{H})} = 0.71. \tag{4.6.1}$$

For comparison, the chiral EFT calculation of Ref. [56] finds the ratio to be between 0.77 and 0.80, for both the isovector pion-nucleon coupling $\bar{g}_1$ and for the linear combination $A_3 - A_4$, which corresponds to $C_{^3S_1-^3P_1}$. The isovector combination $d(^3\mathrm{H}) - d(^3\mathrm{He})$ probes the isoscalar couplings $C_{^3S_1-^1P_1}$, $C^{(0)}_{^1S_0-^3P_0}$ and the isotensor $C^{(2)}_{^1S_0-^3P_0}$, which are particularly important for the QCD $\bar{\theta}$ term. In chiral EFT, this linear combination cannot be expressed only in terms of pion-nucleon CPV couplings, but requires short-range nucleon-nucleon operators at LO [36].

Specializing to the QCD $\bar{\theta}$-term, we combine Eqs. (4.5.6) and (4.5.13) to obtain

$$d_{^3\mathrm{He}}(\bar{\theta}) \;=\; d_n + 0.358\; C_{^3S_1-^1P_1} + 0.297\; C_{^1S_0-^3P_0}\;. \tag{4.6.2}$$

We can then use Eq. (**??**) to write the above result in terms of the dimensionless couplings $c_{^3S_1-^1P_1}$ and $c^{(0)}_{^1S_0-^3P_0}$ with size of order one

$$\simeq \left(2.0 + 10\, c_{^3S_1-^1P_1} + 8.6\, c^{(0)}_{^1S_0-^3P_0}\right) \cdot 10^{-3}\, \bar{\theta}\, e\, \mathrm{fm}\ . \tag{4.6.3}$$

From Eq. (4.6.2) we see that the $^3$He EDM can receive a dominant two-body contribution, but of course more precise statements require a first principle determination of the LECs.

Our approach does not facilitate an as direct identification of the sources of possible non-zero EDMs in light nuclei as chiral EFT does. However, it offers order-by-order renormalizability, a clear understanding of the dependence of observables on the employed ultraviolet regulator and exhibits the dependence of observables on simple measurable two- and three-body observables such as the effective range parameters. At NLO, the effective ranges in the singlet and triplet channels contribute to this correction will be of the order $\gamma_t \rho_t \approx 0.4$ where $\rho_t$ is the triplet effective range. It will be very interesting to study the contributions to the EDFF at NLO. Such an NLO calculation of the CP-odd properties of the three-nucleon system will require the construction of NLO vertex functions to include the effects of NLO relevant two-body operators. We furthermore anticipate, based on results for similar parity-violating interactions in three-nucleon systems [152], that at NLO a CP-odd three-nucleon force will be required whose coefficient will have to be fixed with a CP-odd three-nucleon observable.

We note that Coulomb corrections can be included in EFT($\not{\pi}$) and are expected to give an approximately 10 % correction for $^3$He [90] and are thereby smaller than the expected size of NLO range corrections.

Finally, we are optimistic that our EFT($\not{\pi}$)calculation can be directly connected to QCD using lattice calculations, given recent results obtained with lattice QCD for electroweak matrix elements [131, 33] of two-nucleon system and the possibility to carry out this calculation in a finite volume [92].

**Table 4.2:** Square radii of the two-body EDFF induced by the CPV operators in Eq. (4.2.8), computed at $\Lambda = 60$ GeV. The $C^{(1)}_{^1S_0-^3P_0}$ squared radii have a numerical error of approximately 10 % since the corresponding dipole moments are relatively small. The other radii have few-percent numerical uncertainties, which we do not show.

| | | $C_{^3S_1-^1P_1}$ | $C_{^3S_1-^3P_1}$ | $C^{(0)}_{^1S_0-^3P_0}$ | $C^{(1)}_{^1S_0-^3P_0}$ | $C^{(2)}_{^1S_0-^3P_0}$ |
|---|---|---|---|---|---|---|
| $\langle r^2_{d,\,\mathrm{II}}(^3\mathrm{H})\rangle$ | (fm$^2$) | 1.31 | 1.30 | 1.24 | 1.48 | 1.19 |
| $\langle r^2_{d,\,\mathrm{II}}(^3\mathrm{He})\rangle$ | (fm$^2$) | 1.90 | 1.50 | 1.83 | 4.58 | 1.19 |

# Chapter 5

# $^3$He with Coulomb Interactions in the Pionless Effective Field Theory

## 5.1 Introduction

Three-body systems have been widely studied in the pionless EFT. One benefit of pionless EFT is that it is straightforward to study the impact of the Coulomb interactions [6, 89, 154]. Continuing previous chapter's work, here we provide both the analytical and numerical results of studying $^3$He in the pionless EFT framework with the Coulomb interaction included nonperturbatively at leading order (LO). The method we use is an extension of the previous chapter. We decouple the isospin triplet dimer into np and pp channels explicitly. The np-channel dimer is not modified by Coulomb interactions. Coulomb-photon exchanges inside the pp-channel are resumed to all orders to get the dressed pp-dimer. Since Coulomb interaction does not couple to isospin eigenstates, we do not project three-body bound states onto isospin doublet and quartet channel separately. Instead, three-body isospin doublet and quartet channels are included by picking up correct isospin indices. We calculate the charge form factors of $^3$He with coulomb contributions. Moments of $^3$He, like charge radius and the third Zemach moment, are evaluated. We also studied the cutoff dependence of our observables.

This chapter will provide rich details of the calculation, which are important due to the complexity of the diagrams. In Sec. 5.2, we will give the theoretical foundations of this

work. We will only cover the content that is not mentioned in the previous chapter. Then in Sec. 5.3, we will derive the $^3$He bound state vertex function with Coulomb contributions. In Sec. 5.3, the calculation of all form factor diagrams with Coulomb, contributions are discussed. The third Zemach moment is introduced later and we demonstrate our results in the end.

## 5.2 Effective Lagrangian

We use a very similar formalism to the one we have used in the EDM chapter, yet still different. To make this chapter self-contained, the effective Lagrangian for the $^3$He system in pionless EFT can be written as

$$\mathcal{L} = \mathcal{L}_2 + \mathcal{L}_3 + \mathcal{L}_{\text{photon}} \ , \tag{5.2.1}$$

where $\mathcal{L}_2$ denotes the two-body Lagrangian density, and $\mathcal{L}_3$ denotes the three-body Lagrangian density.

The two-body Lagrangian, $\mathcal{L}_2$, up to NLO is given by

$$\begin{aligned}\mathcal{L}_2 = N^\dagger &\left(i\partial_0 + eA_0\frac{1+\tau_3}{2} + \frac{\vec{\nabla}^2}{2M_N}\right) N \\ &+ t_i^\dagger\left[\Delta_t - c_{0t}\left(i\partial_0 + \frac{\vec{\nabla}^2}{4M_N} + \frac{\gamma_t^2}{M_N}\right)\right] t_i + s_a^\dagger\left[\Delta_s - c_{0s}\left(i\partial_0 + \frac{\vec{\nabla}^2}{4M_N} + \frac{\gamma_s^2}{M_N}\right)\right] s_a \\ &+ y_t\left[t_i^\dagger N^T \hat{P}_{2t}^i N + \text{H.c.}\right] + y_s[s_a^\dagger N^T \hat{P}_{2s}^a N + \text{H.c.}],\end{aligned} \tag{5.2.2}$$

where the auxiliary dimer fields $t_i$ and $s_a$ represent the $^3S_1$ and $^1S_0$ dibaryon field, respectively. For the coefficients, $y_t$, $y_s$, $\Delta_t$, and $\Delta_s$, we choose the same conventions as in Eq. (4.2.1). Again, $\gamma_t \simeq 45.7$ MeV denotes the binding momentum of the deuteron, and $\gamma_s \simeq -7.9$ MeV is the $^1S_0$ virtual-state momentum. $c_{0t}$ and $c_{0s}$ are given by

$$c_{0t} = (Z_t - 1)\frac{M_N}{2\gamma_t}, \ c_{0s} = (Z_s - 1)\frac{M_N}{2\gamma_s} \ , \tag{5.2.3}$$

where $Z_t = 1.6908$ and $Z_s = 0.9015$ are the residues about the deuteron and the virtual ${}^1S_0$ state poles, respectively [149].

The operators $\hat{P}_{2t}$ and $\hat{P}_{2s}$ are spin-triplet and spin singlet two-body projectors, defined by

$$\hat{P}^i_{2t} = \frac{1}{\sqrt{8}}\sigma^2\sigma^i\tau^2, \qquad \hat{P}^a_{2s} = \frac{1}{\sqrt{8}}\sigma^2\tau^2\tau^a, \tag{5.2.4}$$

Since in this chapter, we need to distinguish the $nn$, $np$, and $pp$ channels of the spin-singlet dimers, it is useful also to write down the two-body projectors and spin-singlet dimer in the spherical basis, given by,

$$\begin{aligned} P^{pp}_{2s} &= \tfrac{1}{\sqrt{2}}(iP^2_{2s} - P^1_{2s}) \ , & s_{pp} &= \tfrac{1}{\sqrt{2}}(is_2 - s_1) \ , \\ P^{np}_{2s} &= P^3_{2s} \ , & s_{np} &= s_3 \ , \\ P^{nn}_{2s} &= \tfrac{1}{\sqrt{2}}(iP^2_{2s} + P^1_{2s}) \ , & s_{nn} &= \tfrac{1}{\sqrt{2}}(is_2 + s_1) \ . \end{aligned} \tag{5.2.5}$$

One can prove the validity by noticing the fact,

$$\sum_a \tau^a s_a = -\frac{1}{\sqrt{2}}(\tau^1 + i\tau^2)s_{pp} + \tau^3 s_{np} + \frac{1}{\sqrt{2}}(\tau^1 - i\tau^2)s_{nn} \ . \tag{5.2.6}$$

More about the two-body projectors can be found in Appendix C.

The spin-triplet, spin-singlet-np, and spin-singlet-pp dibaryon propagators up to NLO are respectively given by,

$$iD_t(p_0,\boldsymbol{p}) = \frac{i}{\gamma_t - \sqrt{\frac{\boldsymbol{p}^2}{4} - M_N p_0 - i\epsilon}} \left[ \underbrace{1}_{\text{LO}} + \underbrace{\frac{Z_t - 1}{2\gamma_t}\left(\gamma_t + \sqrt{\frac{\overrightarrow{\mathbf{p}}^2}{4} - M_N p_0 - i\epsilon}\right)}_{\text{NLO}} \right] , \tag{5.2.7}$$

$$iD_s(p_0,\boldsymbol{p}) = \frac{i}{\gamma_s - \sqrt{\frac{\boldsymbol{p}^2}{4} - M_N p_0 - i\epsilon}} \left[ \underbrace{1}_{\text{LO}} + \underbrace{\frac{Z_s - 1}{2\gamma_s}\left(\gamma_s + \sqrt{\frac{\overrightarrow{\mathbf{p}}^2}{4} - M_N p_0 - i\epsilon}\right)}_{\text{NLO}} \right] , \tag{5.2.8}$$

$$iD_{pp}(p_0,\boldsymbol{p}) = \frac{i}{1/a_C + \alpha M_N \tilde{h}_0(i\eta)} \left[ \underbrace{1}_{\text{LO}} - \underbrace{\frac{r_C}{2}\frac{\frac{p^2}{4} - M_N p_0}{1/a_C + \alpha M_N \tilde{h}_0(i\eta)}}_{\text{NLO}} \right] ,$$

with

$$\tilde{h}_0(i\eta) = \psi(i\eta) + \frac{1}{2i\eta} - \log(i\eta) , \tag{5.2.9}$$

and

$$i\eta = \frac{\alpha M_N}{2\sqrt{p^2/4 - M_N p_0 - i\epsilon}} . \tag{5.2.10}$$

$r_C = 2.794$ fm is the Coulomb modified effective range [[cite]]. In LO calculation, only the LO part of the dimer propagators will be included.

For the three-body systems, in the doublet channel, Bedaque, Hammer, and van Kolck [12] found that a three-body force is required at the leading order. The Lagrangian for this three-body force up to LO is

$$\mathcal{L}_3 = \frac{M_N H(\Lambda)}{3\Lambda^2} \left[ y_t \hat{N}^\dagger (\vec{t}\cdot\overrightarrow{\boldsymbol{\sigma}})^\dagger - y_s \hat{N}^\dagger (\vec{s}\cdot\overrightarrow{\boldsymbol{\tau}})^\dagger \right] \left[ y_t (\vec{t}\cdot\overrightarrow{\boldsymbol{\sigma}})\hat{N} - y_s (\vec{s}\cdot\overrightarrow{\boldsymbol{\tau}})\hat{N} \right] . \tag{5.2.11}$$

Here, $\vec{t}$, $\vec{s}$ represent spin-triplet and spin-singlet dimer field, respectively. A three-nucleon force appears at LO because it was shown [16, 14, 15] to be necessary for the renormalization of three-body observables. The three-body force Lagrangian in Eq. (5.2.11), can be rewritten

with a trimer auxiliary field, $\psi$, with total angular momentum 1/2, as follows

$$\mathcal{L}_3 = \Omega\psi^\dagger\psi + \left(\omega_{t0}\psi^\dagger[P^i_{3t}]^\dagger N t_i - \omega_{s0}\psi^\dagger[P^{pp}_{3s}]^\dagger N s_{pp} - \omega_{s0}\psi^\dagger[P^{np}_{3s}]^\dagger N s_{np} + \text{h.c.}\right) \ , \tag{5.2.12}$$

where $s_{pp} = \frac{1}{\sqrt{2}}(is_2 - s_1)$, $P^{pp}_{3s} = \frac{1}{\sqrt{3}}\frac{1}{\sqrt{2}}(i\tau^2 - \tau^1)$, $P^{np}_{3s} = \frac{1}{\sqrt{3}}\tau^3$, and $P^i_{3t} = \frac{1}{\sqrt{3}}\sigma^i$, $P^a_{3s} = \frac{1}{\sqrt{3}}\tau^a$. The spin-singlet channel is split into $np$ and $pp$ channel explicitly. Here the $nn$ channel has zero contribution in the case of $^3$He. Using a matching calculation to a theory without trimer fields, one can show that $\omega_s = \omega_t$. The LO three-body force $H(\Lambda)$ is related to other parameters by ,

$$\frac{H(\Lambda)}{\Lambda^2} = -\frac{(\omega_{t0})^2}{4\pi\Omega} = -\frac{(\omega_{s0})^2}{4\pi\Omega} = -\frac{\omega_{t0}\omega_{s0}}{4\pi\Omega} \ . \tag{5.2.13}$$

More details can be found in [149].

The pure photon contributions is described in $\mathcal{L}_{\text{photon}}$, which is given in [65]. Here we only need to know the Coulomb photon propagator, given by

$$i\Delta_{\text{Coulomb}}(\boldsymbol{k}) = \frac{i}{\boldsymbol{k}^2 + \lambda^2} \ , \tag{5.2.14}$$

where $\boldsymbol{k}$ is the three-momentum of the photon. $\lambda$ is a photon mass to regulate infrared divergences.

## 5.3 $^3$He Vertex Function

We follow König's pd-scattering work [89]. We use this work's scattering equations for the bound state regime to construct the integral equations for the $^3$He vertex functions. The LO vertex function $\boldsymbol{\mathcal{C}}(E,p)$ for $^3$He with Coulomb interaction in the center-of-mass frame with binding energy $E$ and relative momentum $\mathbf{p}$ between outgoing nucleon and dimer is given by the integral equation shown diagrammatically in Fig. 5.1 and given explicitly by

$$\begin{aligned}\boldsymbol{\mathcal{C}}(B,p) = \widetilde{\boldsymbol{I}}_C + \Big(&K_s(B,p,k)\boldsymbol{M}_{ks} + K_c(B,p,k)\boldsymbol{M}_{kc} \\ &+ K_{t1}(B,p,k)\boldsymbol{M}_{kt1} + K_{t2}(B,p,k)\boldsymbol{M}_{kt2} + K_b(B,p,k)\boldsymbol{M}_{kb}\Big) \otimes_k \widetilde{\boldsymbol{\mathcal{C}}}(B,k),\end{aligned} \tag{5.3.1}$$

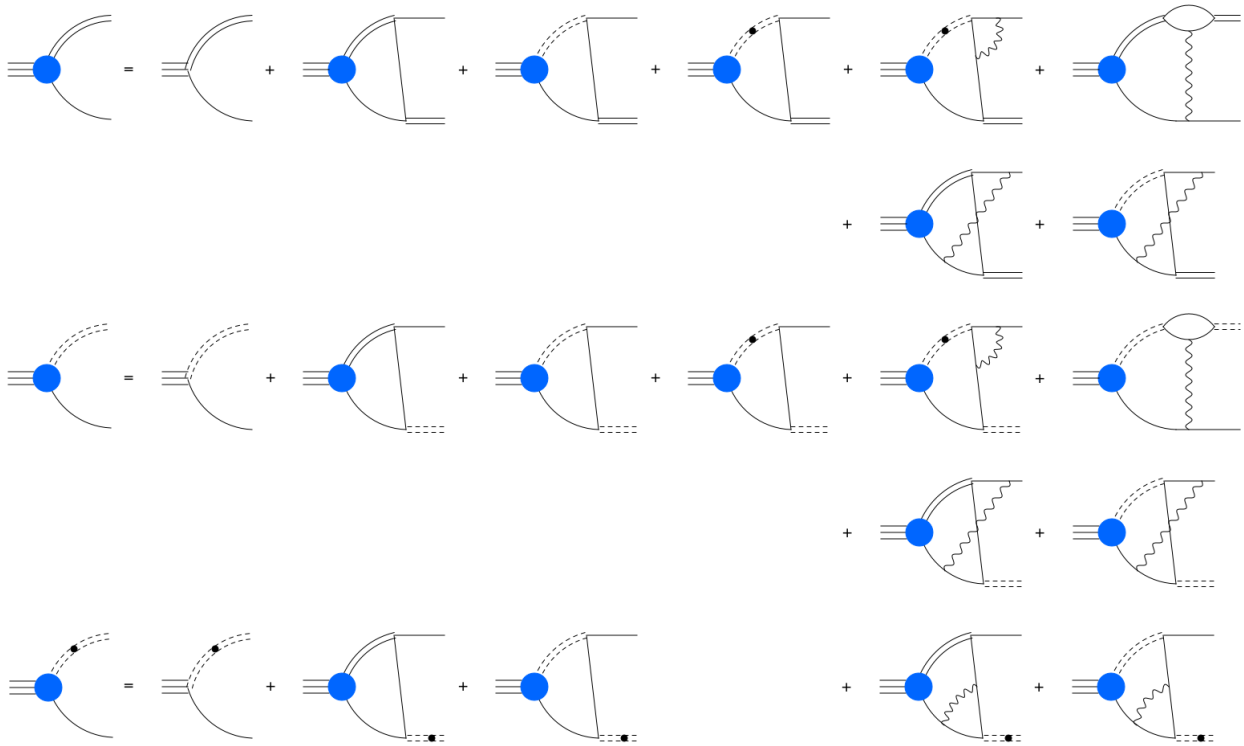

**Figure 5.1:** Diagrammatic representation of the LO three-body ($^3$He) coulomb vertex function. The double line denotes a dressed spin-triplet dibaryon propagator. The dashed double line (with dot) denotes a dressed spin-singlet np (pp) channel dibaryon propagator. The wavy lines represent Coulomb photon propagators.

where the three-component $^3$He vertex function is defined by

$$\boldsymbol{\mathcal{C}}(B,p) = \begin{pmatrix} C_t(B,p) \\ C_{np}(B,p) \\ C_{pp}(B,p) \end{pmatrix} . \tag{5.3.2}$$

$C_t(B,p)$ / $C_{np}(B,p)$ / $C_{pp}(B,p)$ is the vertex function for a $^3$He bound state goes into a nucleon and spin-triplet / spin-singlet-np / spin-singlet-pp dibaryon. The short-hand notation, $\widetilde{\boldsymbol{\mathcal{C}}}(B,k)$, is defined as

$$\widetilde{\boldsymbol{\mathcal{C}}}(B,k) = \boldsymbol{D}_C\left(E - \frac{k^2}{2M_N}, k\right)\boldsymbol{\mathcal{C}}(B,k) \ , \tag{5.3.3}$$

where

$$\boldsymbol{D}_C\left(E - \frac{k^2}{2M_N}, k\right) = \begin{pmatrix} D_t\left(E - \frac{k^2}{2M_N}, k\right) & 0 & 0 \\ 0 & D_s\left(E - \frac{k^2}{2M_N}, k\right) & 0 \\ 0 & 0 & D_{pp}\left(E - \frac{k^2}{2M_N}, k\right) \end{pmatrix} . \tag{5.3.4}$$

The inhomogeneous term of the integral equation is given by,

$$\widetilde{\boldsymbol{I}}_C = \begin{pmatrix} 1 \\ -\frac{1}{\sqrt{3}} \\ \sqrt{\frac{2}{3}} \end{pmatrix} . \tag{5.3.5}$$

The convolution operator $\otimes_k$ is defined the same as in the EDM calculation [[ref eq]]. The constant matrices in the homogeneous terms are obtained by two-body projections and

picking iso-spin indices appropriately, with

$$\boldsymbol{M}_{ks} = \begin{pmatrix} -1 & \sqrt{3} & -\sqrt{6} \\ \sqrt{3} & 1 & \sqrt{2} \\ -\sqrt{6} & \sqrt{2} & 0 \end{pmatrix} \ , \ \boldsymbol{M}_{kc} = \begin{pmatrix} 2 & 0 & 0 \\ 0 & 2 & 0 \\ 0 & 0 & 0 \end{pmatrix} \ ,$$
$$\boldsymbol{M}_{kt1} = -\begin{pmatrix} 0 & 0 & 0 \\ 0 & 0 & 0 \\ -\sqrt{6} & \sqrt{2} & 0 \end{pmatrix} \ , \ \boldsymbol{M}_{kt2} = -\begin{pmatrix} 0 & 0 & -\sqrt{6} \\ 0 & 0 & +\sqrt{2} \\ 0 & 0 & 0 \end{pmatrix} \ , \ \boldsymbol{M}_{kb} = -\begin{pmatrix} -1 & \sqrt{3} & 0 \\ \sqrt{3} & 1 & 0 \\ 0 & 0 & 0 \end{pmatrix} \ . \tag{5.3.6}$$

The additional $-1$ in front of each matrix in the second row is not from spin/isospin indices projection. It is taken from the kernel functions so that kernels can be easily compared with previous literature, for example, see [89]. More details are in Appendix C. One should notice that, we do not explicitly project isospin onto three-body doublet or quartet channels. However, we project spin onto three-body doublet channels since the Coulomb interaction only touches isospin. The kernel functions in the homogeneous terms represent contributions

from different diagrams in Fig. 5.1, given by,

$$K_s(B,p,k) = \frac{2\pi}{kp} Q_0\left(\frac{k^2+p^2-mB}{kp}\right) , \tag{5.3.7}$$

$$K_c(B,p,k) = \frac{\alpha M_N 2\pi}{kp}\left\{\frac{\arctan\frac{k-p}{2\Delta(B,p,k)}}{k-p} - \frac{\arctan\frac{k+p}{2\Delta(B,p,k)}}{k+p} + \frac{1}{4\Delta(B,p,k)}\left[\ln\left(\frac{k+p}{k-p}\right)^2 + \ln\frac{(k-p)^2+4\Delta^2(B,p,k)}{(k+p)^2+4\Delta^2(B,p,k)}\right]\right\} , \tag{5.3.8}$$

$$K_{t1}(B,p,k) = \frac{\alpha M_N 2\pi}{kp\sqrt{3p^2-4M_N B}}\left[\arctan^2\left(\frac{2k+p}{\sqrt{3p^2-4M_N B}}\right) - \arctan^2\left(\frac{2k-p}{\sqrt{3p^2-4M_N B}}\right)\right] , \tag{5.3.9}$$

$$K_{t2}(B,p,k) = \frac{\alpha M_N 2\pi}{kp\sqrt{3k^2-4M_N B}}\left[\arctan^2\left(\frac{2p+k}{\sqrt{3k^2-4M_N B}}\right) - \arctan^2\left(\frac{2p-k}{\sqrt{3k^2-4M_N B}}\right)\right] , \tag{5.3.10}$$

$$K_b(B,p,k) = \alpha M_N \pi \int_{-1}^{+1} dx \frac{1}{|\boldsymbol{k}-\boldsymbol{p}|}\frac{1}{k^2+p^2+kpx-M_N B} \times\left[\arctan\left(\frac{2p^2-k^2-kpx}{|\boldsymbol{k}-\boldsymbol{p}|\sqrt{3k^2-4M_N B}}\right) + \arctan\left(\frac{2k^2-p^2-kpx}{|\boldsymbol{k}-\boldsymbol{p}|\sqrt{3p^2-4M_N B}}\right)\right] , \tag{5.3.11}$$

where,

$$Q_0(a) = \frac{1}{2}\ln\frac{a+1}{a-1} , \tag{5.3.12}$$

$$\Delta(B,p,k) = \sqrt{3k^2-4M_N B} + \sqrt{3p^2-4M_N B} . \tag{5.3.13}$$

$K_s(B,p,k)$, $K_c(B,p,k)$, $K_{t1}(B,p,k)$ , $K_{t2}(B,p,k)$ , $K_b(B,p,k)$ denote the kernels of the homogeneous terms demonstrated in (a), (b), (c), (d) and (e) of Fig. 5.2, respectively. $k$ and $p$ are the relative momenta of between the dimer and nucleon in the inner loop and final state. $x$ is the cosine of the angle between $\boldsymbol{k}$ and $\boldsymbol{p}$. $\alpha$ is the fine structure constant. For all terms above, we have taken the photon mass to be zero. One can also leaves the photon mass small but non-zero, which is numerically unimportant but leads to more complicated

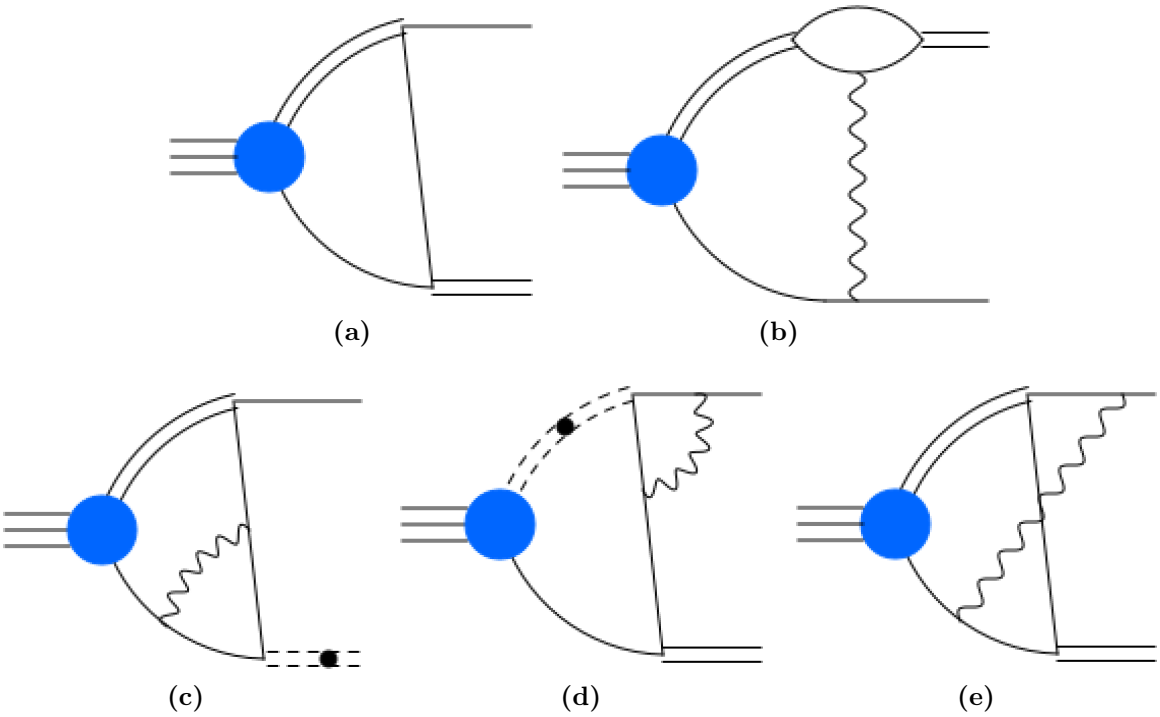


**Figure 5.2:** Partial diagrams contribute to the homogeneous terms of the $^3$He vertex function. The double solid line here represents either deuteron dimer propagator or a spin-singlet np dimer propagator to avoid verbosity. The dashed double line with dot denotes a spin-singlet pp dimer propagator. The wavy lines represent Coulomb photon propagators. The (c) and (d) are mostly called "triangular" diagrams in the literatures, while (e) is called the "box" diagram. The kernels of diagram (a) to (e) are denoted as $K_s$, $K_c$, $K_{t1}$, $K_{t2}$ and $K_b$, respectively.

expressions. For numerical convenience, we also project the vertex function onto S-wave. In addition, we have already used the on-shell nucleon energy, which is defined as,

$$p_0 = \frac{E}{3} - \frac{1}{2M_N}(\frac{\boldsymbol{K}}{3} - \boldsymbol{p})^2 \ , \tag{5.3.14}$$

where $E$ and $\boldsymbol{K}$ are the total energy and momentum of the three-body bound state. Before we show the derivation of the kernel functions later in this section, let us first take a look at the wavefunction renormalization.

### 5.3.1 Wavefunction Renormalization

As one can find, the inhomogeneous terms in the vertex function above is just a constant vector. We have normalized the vertex function to not include the three-body coupling constant, $\omega$, and thus the vertex function $\boldsymbol{\mathcal{C}}(B,p)$ is not the "physical" vertex function. The "physical" vertex function is given by

$$\boldsymbol{\Gamma}(B,p) = \sqrt{Z_{\psi C}}\boldsymbol{\mathcal{C}}(B,p) \ . \tag{5.3.15}$$

To get the Z factor used in this work, let us first look at the dressed trimer field, which is given by,

$$i\Delta_{3C}^{LO}(E) = \frac{i}{\Omega} + \frac{i}{\Omega} i\Sigma_C^P(E) i\Delta_{3C}^{LO}(E) \ , \tag{5.3.16}$$

where $\Sigma_C^P(E)$ is the trimmer-irreducible self-energy, represented by the sum of diagrams in Fig. 5.3. $\Sigma_C^P(E)$ is evaluated by

$$\begin{aligned} i\Sigma_C^P(E) &= \int \frac{d^4q}{(2\pi)^4} i\omega \frac{i}{E - q_0 - \frac{1}{2M_N}q^2 + i\epsilon} \widetilde{\boldsymbol{I}}_C^T i\boldsymbol{D}_C(E+q_0,q) i\omega \boldsymbol{\mathcal{C}}(B,q) \\ &= -i\omega^2 \widetilde{\boldsymbol{I}}_C^T \otimes_q \widetilde{\boldsymbol{\mathcal{C}}}(B,q) \ . \end{aligned} \tag{5.3.17}$$

The Z factor is the residue about the $^3$He pole,

$$Z_{\psi C} = \left( \frac{d}{dE} \frac{1}{\Delta_{3C}^{LO}(E)} \right)^{-1} \Bigg|_{E=B} \ . \tag{5.3.18}$$

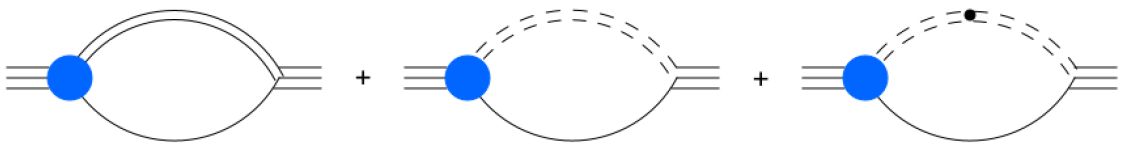


**Figure 5.3:** The self-energy is represented by the sum of three diagrams. The solid, dashed and dashed-dot double lines represents the spin-triplet, spin-singlet-np, and spin-singlet-pp dimer propagators, respectively.

In order to keep consistency with other literatures [149, 150], we use the numerically equivalent form given in the follows,

$$Z_{\psi C} = \frac{\pi}{\Sigma'_C(B)} \ , \tag{5.3.19}$$

where $\Sigma_C(E)$ is defined by

$$\Sigma_C(E) = -\pi \widetilde{\boldsymbol{I}}_C^T \otimes_q \widetilde{\boldsymbol{\mathcal{C}}}(E, q) \ . \tag{5.3.20}$$

In previous papers [6, 89, 154], they have more complicated expressions of vertex functions compare to what we present in this chapter. We found that those are numerically equivalent. In order to alleviate pains for future readers, we will provide more details of each piece in the following sections.

**Conventions for the vertex function calculation** In order to not be verbose, we explain the convent ions for calculating following kernel functions. $\boldsymbol{k}$ denotes the relative momentum of the dimer and the nucleon that connects to the $^3$He vertex inside the loop. $\boldsymbol{p}$ is the relative momentum of the outgoing final state. $\boldsymbol{l}$, if exists, denotes the loop momentum in between. $k_0$, $p_0$, and $l_0$ are the corresponding timelike components of 4-momenta. $\boldsymbol{K}$ is the momentum of the center of mass of the system and the total energy is denoted as $E = B + \frac{\boldsymbol{K}^2}{6M_N}$, in which $B$ is the $^3$He binding energy. A typical value of $\boldsymbol{K}$ is $-\boldsymbol{q}/2$, which is the momentum of the incoming side bound state in Breit frame. The final state is always projected onto S-wave by default. The on-shell energy is given above in Eq. (5.3.14). For a non-boosting vertex function, we always need this on-shell condition. A nucleon propagator with energy $p_0$ and momentum $\boldsymbol{p}$ is denoted as,

$$iS_N(p_0, \boldsymbol{p}) = \frac{i}{p_0 - \frac{1}{2M_N}\boldsymbol{p}^2 + i\epsilon} \ . \tag{5.3.21}$$

### 5.3.2 The "Ks" diagram

$K_s(B, p, k)$ denotes the kernel of Fig. 5.2 (a), which has no Coulomb photon but a single nucleon exchange. The four momenta of the dimer and the nucleon propagator associate with the $^3$He propagator are $(\frac{2}{3}E + k_0, \boldsymbol{k} + \frac{2}{3}\boldsymbol{K})$ and $(\frac{1}{3}E - k_0, -\boldsymbol{k} + \frac{1}{3}\boldsymbol{K})$, respectively. The

exchanged nucleon propagator has a four momentum given by $(\frac{1}{3}E + k_0 + p_0, \boldsymbol{k} + \boldsymbol{p} + \frac{1}{3}\boldsymbol{K})$. From dimer-NN vertices, we receive $(iy)^2$ with $y^2 = \frac{4\pi}{M_N}$. Notice that, in order to follow the conventions from the previous literatures, we also include the $(1/\sqrt{8})^2$ from the two-body projectors. From contractions, a $-4$ must be included as the symmetry factor. Thus, we give the expression below,

$$i\boldsymbol{\mathcal{H}}_s(B, \boldsymbol{K}, p_0, \boldsymbol{p}, \boldsymbol{k}) = \frac{y^2}{2} \int \frac{d^4k}{(2\pi)^4} iS_N(\frac{1}{3}E - k_0, -\boldsymbol{k} + \frac{1}{3}\boldsymbol{K}) iS_N(\frac{1}{3}E + k_0 + p_0, \boldsymbol{k} + \boldsymbol{p} + \frac{1}{3}\boldsymbol{K}) \\ \boldsymbol{M}_{ks}\ i\boldsymbol{D}_C(\frac{2}{3}E + k_0, \boldsymbol{k} + \frac{2}{3}\boldsymbol{K})\ i\boldsymbol{\mathcal{C}}(B, k)\ , \quad (5.3.22)$$

where $\boldsymbol{M}_{ks}$ is a constant matrix defined in Eq. (5.3.6). Picking the pole at $k_0 = \frac{E}{3} - \frac{1}{2M_N}(\frac{\boldsymbol{K}}{3} - \boldsymbol{k})^2$, we have a $(-2\pi i)$ from integrating over $k_0$, and get

$$\boldsymbol{\mathcal{H}}_s(B, \boldsymbol{K}, p_0, \boldsymbol{p}, \boldsymbol{k}) = \int \frac{dk}{2\pi^2} k^2 \frac{-y^2}{2} \boldsymbol{M}_{ks} \boldsymbol{D}_C(B - \frac{k^2}{2M_N}, \boldsymbol{k}) \boldsymbol{\mathcal{C}}(B, k) \\ \times \frac{1}{2} \int_{-1}^{+1} d\cos\theta \left[\frac{2}{3}E - \frac{1}{2M_N}(\frac{\boldsymbol{K}}{3} - \boldsymbol{k})^2 - \frac{1}{2M_N}(\boldsymbol{k} + \boldsymbol{p} + \frac{1}{3}\boldsymbol{K})^2 + p_0\right]^{-1}\ , \quad (5.3.23)$$

where $\theta$ is the angle between $\hat{\boldsymbol{k}}$ and $\hat{\boldsymbol{p}}$. We get,

$$\boldsymbol{\mathcal{H}}_s(B, \boldsymbol{K}, p_0, \boldsymbol{p}, \boldsymbol{k}) = \boldsymbol{M}_{ks} K_s(B, \boldsymbol{K}, p_0, \boldsymbol{p}, \boldsymbol{k}) \otimes_k \widetilde{\boldsymbol{\mathcal{C}}}(B, k)\ , \quad (5.3.24)$$

where $K_s(B, \boldsymbol{K}, p_0, \boldsymbol{p}, \boldsymbol{k})$ is

$$K_s(B, \boldsymbol{K}, p_0, \boldsymbol{p}, \boldsymbol{k}) = \frac{2\pi}{kp} Q_0(\frac{k^2 + p^2 - M_N(\frac{2}{3}B + p_0 + \frac{1}{2M_N}p^2 - \frac{1}{3}\boldsymbol{K}\cdot\boldsymbol{p})}{kp})\ . \quad (5.3.25)$$

The expression above is for general cases, which does not necessarily use an on-shell $p_0$. Taking on-shell $p_0$ in Eq. (5.3.14), we have,

$$K_s(B, p, k) = \frac{2\pi}{kp} Q_0(\frac{k^2 + p^2 - M_N B}{kp})\ . \quad (5.3.26)$$

### 5.3.3 The "Kc" diagram

$K_c(B,p,k)$ denotes the kernel of Fig. 5.2 (b), which has a Coulomb photon propagator that connects one nucleon of the inner loop and another nucleon associate with the trimer field. The four momenta of the dimer and the nucleon propagator associate with the $^3$He propagator are $(\frac{2}{3}E+k_0, \boldsymbol{k}+\frac{2}{3}\boldsymbol{K})$ and $(\frac{1}{3}E-k_0, -\boldsymbol{k}+\frac{1}{3}\boldsymbol{K})$, respectively. The Coulomb photon propagator carries momentum $(\boldsymbol{k}-\boldsymbol{p})$. The three nucleon propagators of the inner loop have four momenta $(-\ell_0, \boldsymbol{\ell})$, $(\frac{2}{3}E+k_0+\ell_0, \boldsymbol{k}+\boldsymbol{\ell}+\frac{2}{3}\boldsymbol{K})$, and $(\frac{2}{3}E+p_0+\ell_0, \boldsymbol{p}+\boldsymbol{\ell}+\frac{2}{3}\boldsymbol{K})$.

From dimer-NN vertices, we receive $(iy)^2$ with $y^2=\frac{4\pi}{M_N}$. Notice that, in order to follow the conventions from the previous literature, we also include the $(1/\sqrt{8})^2$ from the two-body projectors. From contractions, a $+4$ must be included as the symmetry factor. In addition, we have a factor $-e^2$ due to the photon exchange. To avoid complexity, we insert the on-shell $p_0$ in the very beginning. Later in this section, we will discuss how to boost the vertex functions. We give the expression for the homogeneous contribution below,

$$i\boldsymbol{\mathcal{H}}_c(B,p,k) = \frac{-y^2}{2}(ie)^2\int\frac{d^4k}{(2\pi)^4}\boldsymbol{M}_{kc}\; i\boldsymbol{D}_C(\frac{2}{3}E+k_0, \boldsymbol{k}+\frac{2}{3}\boldsymbol{K})\; i\boldsymbol{\mathcal{C}}(B,k)$$
$$iS_N(\frac{1}{3}E-k_0, -\boldsymbol{k}+\frac{1}{3}\boldsymbol{K})\frac{i}{(\boldsymbol{k}-\boldsymbol{p})^2+\lambda^2}\Omega_c(B,p,k)\ , \quad (5.3.27)$$

where $\Omega_c(B,p,k)$ represent the inner loop integration, given by

$$\Omega_c(B,p,k) = \int\frac{d^4\ell}{(2\pi)^4}iS_N(-\ell_0,\boldsymbol{\ell})$$
$$iS_N(\frac{2}{3}E+k_0+\ell_0, \boldsymbol{k}+\boldsymbol{\ell}+\frac{2}{3}\boldsymbol{K})iS_N(\frac{2}{3}E+p_0+\ell_0, \boldsymbol{p}+\boldsymbol{\ell}+\frac{2}{3}\boldsymbol{K})\ . \quad (5.3.28)$$

Picking the pole at $k_0=\frac{E}{3}-\frac{1}{2M_N}(\frac{\boldsymbol{K}}{3}-\boldsymbol{k})^2$, and $\ell_0=-\frac{1}{2M_N}\ell^2+i\epsilon$, we have a factor of $(-2\pi i)^2$ from integrating over $k_0$ and $\ell_0$, we get

$$\boldsymbol{\mathcal{H}}_c(B,p,k) = \frac{\alpha 4\pi^2}{M_N}\int\frac{dk}{2\pi^2}k^2\int_{-1}^{+1}d\cos\theta\boldsymbol{M}_{kc}\;\widetilde{\boldsymbol{\mathcal{C}}}(B,k)\frac{1}{(\boldsymbol{k}-\boldsymbol{p})^2+\lambda^2}\Omega_c(B,p,k)\ , \quad (5.3.29)$$

where $\cos\theta$ is the cosine value between the $\hat{\boldsymbol{k}}$ and $\hat{\boldsymbol{p}}$. The $\Omega_c(B,p,k)$ is reduced to

$$\Omega_c(B,p,k) = \int \frac{d^3\ell}{(2\pi)^3} S_N(\frac{2}{3}E + k_0 + \ell_0, \boldsymbol{k} + \boldsymbol{\ell} + \frac{2}{3}\boldsymbol{K}) S_N(\frac{2}{3}E + p_0 + \ell_0, \boldsymbol{p} + \boldsymbol{\ell} + \frac{2}{3}\boldsymbol{K}) \ . \tag{5.3.30}$$

Using the Feynman parameterization technique from Ref. [106], namely,

$$\frac{1}{AB} = \int_0^1 du \left[uA + (1-u)B\right]^{-2} = \int_0^1 du \left[\ell'^2 + \Delta_c\right]^{-2}, \tag{5.3.31}$$

where

$$\begin{aligned}
A &= -M_N/S_N(\frac{2}{3}E + k_0 + \ell_0, \boldsymbol{k} + \boldsymbol{\ell} + \frac{2}{3}\boldsymbol{K}) \ , \\
B &= -M_N/S_N(\frac{2}{3}E + p_0 + \ell_0, \boldsymbol{p} + \boldsymbol{\ell} + \frac{2}{3}\boldsymbol{K}) \ , \\
\boldsymbol{\ell}' &= \boldsymbol{\ell} + \frac{1}{2}\left(\boldsymbol{k}u + \frac{2\boldsymbol{K}}{3} + \boldsymbol{p}(1-u)\right) \ , \\
\Delta_c &= \frac{1}{4}\left(-4BM + k^2(-(u-4))u + 2kp\cos\theta(u-1)u - p^2(u-1)(u+3)\right) \ .
\end{aligned}$$

Notice that,

$$\int_0^1 du \int \frac{d^3\ell}{(2\pi)^3} \left[\ell'^2 + \Delta_c\right]^{-2} = \frac{M_N^2}{8\pi} \int_0^1 du \Delta_c^{-\frac{1}{2}} \ . \tag{5.3.32}$$

This integration can be done analytically, leave,

$$\boldsymbol{\mathcal{H}}_c(B,p,k) = \boldsymbol{M}_{kc} K_c(B,p,k) \otimes_k \widetilde{\boldsymbol{\mathcal{C}}}(B,k) \ , \tag{5.3.33}$$

where,

$$\begin{aligned}
K_c(B,p,k) = \alpha M_N 2\pi \int_{-1}^{+1} d\cos\theta \frac{1}{(\boldsymbol{k}-\boldsymbol{p})^2 + \lambda^2} \\
\times \frac{1}{|\boldsymbol{k}-\boldsymbol{p}|} \arctan \frac{|\boldsymbol{k}-\boldsymbol{p}|}{\sqrt{3k^2 - 4M_N B} + \sqrt{3p^2 - 4M_N B}} \ .
\end{aligned} \tag{5.3.34}$$

A finite but small $\lambda$ provides better numerical stability without affecting the accuracy. If one could handle the numerics very well taken $\lambda \to 0$, then it will be more efficient to use

the expression in Eq. (5.3.7), in which the angular integration is analytical done by setting a zero photon mass.

### 5.3.4 The triangle diagrams, "Kt1" and "Kt2"

$K_{t1}(B,p,k)$ and $K_{t2}(B,p,k)$ denote the kernels of Fig. 5.2 (c) and (d), which has a Coulomb photon propagator connects two nucleons associate with the pp-dimer propagator. Due to the fact that $K_{t1}(B,p,k)$ and $K_{t2}(B,p,k)$ are very similar to each other, we will only show the derivation of $K_{t1}(B,p,k)$ to avoid the repetition.

Consider now only the $K_{t1}(B,p,k)$, the four-momenta of the dimer and the nucleon propagator associate with the $^3$He propagator are $(\frac{2}{3}E+k_0, \boldsymbol{k}+\frac{2}{3}\boldsymbol{K})$ and $(\frac{1}{3}E-k_0, -\boldsymbol{k}+\frac{1}{3}\boldsymbol{K})$, respectively. The Coulomb photon propagator carries a momentum of $\boldsymbol{l}-\boldsymbol{k}$. The two nucleon propagators associate with the pp-dimer have four-momenta of $(\frac{1}{3}E-\ell_0, -\boldsymbol{\ell}+\frac{1}{3}\boldsymbol{K})$, and $(\frac{1}{3}E+p_0+\ell_0, \boldsymbol{p}+\boldsymbol{\ell}+\frac{1}{3}\boldsymbol{K})$. The other nucleon propagator has a four-momentum of $(\frac{1}{3}E+p_0+k_0, \boldsymbol{p}+\boldsymbol{k}+\frac{1}{3}\boldsymbol{K})$.

Similar to $K_c$, from dimer-NN vertices, we receive a factor $(iy)^2$ with $y^2=\frac{4\pi}{M_N}$. We also include the $(1/\sqrt{8})^2$ from the two-body projectors, as well as a $-4$ symmetry factor and a $-e^2$. $p_0$ is on-shell by default. We give the expression below,

$$
\begin{aligned}
i\boldsymbol{\mathcal{H}}_{t1}(B,p,k) = \frac{y^2}{2}(ie)^2 \int \frac{d^4k}{(2\pi)^4}(-\boldsymbol{M}_{kt1})\; i\boldsymbol{D}_C(\frac{2}{3}E+k_0, \boldsymbol{k}+\frac{2}{3}\boldsymbol{K})\; i\boldsymbol{\mathcal{C}}(B,k) \\
iS_N(\frac{1}{3}E-k_0, -\boldsymbol{k}+\frac{1}{3}\boldsymbol{K}) iS_N(\frac{1}{3}E+p_0+k_0, \boldsymbol{p}+\boldsymbol{k}+\frac{1}{3}\boldsymbol{K})\Omega_{t1}(B,p,k)\ , \quad (5.3.35)
\end{aligned}
$$

where $\boldsymbol{M}_{kt1}$ is a constant matrix, defined in Eq. (5.3.6). The additional $-1$ is not physical but a trick to have a positive form of kernel function. The function $\Omega_{t1}(B,p,k)$ represent the inner loop integration, given by

$$
\begin{aligned}
\Omega_{t1}(B,p,k) = \int \frac{d^4\ell}{(2\pi)^4}\frac{i}{(\boldsymbol{\ell}-\boldsymbol{k})^2+\lambda^2} \\
iS_N(\frac{1}{3}E-\ell_0, -\boldsymbol{\ell}+\frac{1}{3}\boldsymbol{K}) iS_N(\frac{1}{3}E+p_0+\ell_0, \boldsymbol{p}+\boldsymbol{\ell}+\frac{1}{3}\boldsymbol{K})\ . \quad (5.3.36)
\end{aligned}
$$

Picking the pole at $k_0 = \frac{E}{3} - \frac{1}{2M_N}(\frac{\boldsymbol{K}}{3} - \boldsymbol{k})^2 + i\epsilon$, and $\ell_0 = \frac{E}{3} - \frac{1}{2M_N}(\frac{\boldsymbol{K}}{3} - \boldsymbol{\ell})^2 + i\epsilon$, we get

$$\boldsymbol{\mathcal{H}}_{t1}(B,p,k) = -\alpha 4\pi^2 \int \frac{dk}{2\pi^2} k^2 \int_{-1}^{+1} d\cos\theta \boldsymbol{M}_{kt1}\, \widetilde{\boldsymbol{\mathcal{C}}}(B,k) \times \frac{1}{k^2+p^2+kp\cos\theta - M_N B} \Omega_{t1}(B,p,k) \ , \quad (5.3.37)$$

where $\cos\theta$ is the cosine value between the $\hat{\boldsymbol{k}}$ and $\hat{\boldsymbol{p}}$. The $\Omega_{t1}(B,p,k)$ is reduced to

$$\Omega_{t1}(B,p,k) = -\int \frac{d^3\ell}{(2\pi)^3} \frac{1}{(\boldsymbol{\ell}-\boldsymbol{k})^2+\lambda^2} S_N(\frac{1}{3}E + p_0 + \ell_0, \boldsymbol{p} + \boldsymbol{\ell} + \frac{1}{3}\boldsymbol{K}) \ . \quad (5.3.38)$$

We use the Feynman parametrization in $K_c$ calculation and set photon mass to be zero, and get

$$\boldsymbol{\mathcal{H}}_{t1}(B,p,k) = \boldsymbol{M}_{kt1} K_{t1}(B,p,k) \otimes_k \widetilde{\boldsymbol{\mathcal{C}}}(B,k) \ , \quad (5.3.39)$$

where,

$$K_{t1}(B,p,k) = \alpha M_N 2\pi \int_{-1}^{+1} d\cos\theta \frac{1}{k^2+p^2+kp\cos\theta - M_N B} \times \frac{1}{|2\boldsymbol{k}+\boldsymbol{p}|} \arctan \frac{|2\boldsymbol{k}+\boldsymbol{p}|}{\sqrt{3p^2 - 4M_N B}} \ . \quad (5.3.40)$$

Previous literature keep the form including non-zero photon mass. We tested both cases and found it is numerically legal to use such a form. Moreover, one could solve the angular integral analytically and get the expression in Eq. (5.3.7).

For future reference, consider now only the $K_{t2}(B,p,k)$. The four-momenta of the dimer and the nucleon propagator associate with the $^3$He propagator are $(\frac{2}{3}E + k_0, \boldsymbol{k} + \frac{2}{3}\boldsymbol{K})$ and $(\frac{1}{3}E - k_0, -\boldsymbol{k} + \frac{1}{3}\boldsymbol{K})$, respectively. The Coulomb photon propagator carries a momentum of $(\boldsymbol{l} - \boldsymbol{p})$. The two nucleon propagators associate with the pp-dimer have four-momenta of $(\frac{1}{3}E - \ell_0, -\boldsymbol{\ell} + \frac{1}{3}\boldsymbol{K})$, and $(\frac{1}{3}E + k_0 + \ell_0, \boldsymbol{k} + \boldsymbol{\ell} + \frac{1}{3}\boldsymbol{K})$. The other nucleon propagator has a four-momentum of $(\frac{1}{3}E + p_0 + k_0, \boldsymbol{p} + \boldsymbol{k} + \frac{1}{3}\boldsymbol{K})$. The rest of the calculation is identical to

$K_{t1}(B,p,k)$, given

$$K_{t2}(B,p,k) = \alpha M_N 2\pi \int_{-1}^{+1} d\cos\theta \frac{1}{k^2+p^2+kp\cos\theta - M_N B} \times \frac{1}{|2\boldsymbol{p}+\boldsymbol{k}|} \arctan \frac{|2\boldsymbol{p}+\boldsymbol{k}|}{\sqrt{3k^2-4M_N B}} \ . \quad (5.3.41)$$

### 5.3.5 The box diagram "Kb"

$K_b(B,p,k)$ denotes the kernel of Fig. 5.2 (e), which has a exchange nucleon propagator and a Coulomb photon propagator connects the other two nucleon propagators. However, due to its complicated structure, one may have difficulties using only Feynman parameterization. The four momenta of the dimer and the nucleon propagator associate with the $^3$He propagator are $(\frac{2}{3}E+k_0, \boldsymbol{k}+\frac{2}{3}\boldsymbol{K})$ and $(\frac{1}{3}E-k_0, -\boldsymbol{k}+\frac{1}{3}\boldsymbol{K})$, respectively. The Coulomb photon propagator carries a momentum of $\boldsymbol{\ell}$. The exchange nucleon propagator have a four momentum of $(\frac{1}{3}E+k_0-\ell_0+p_0, \boldsymbol{k}+\boldsymbol{\ell}+\boldsymbol{p}+\frac{1}{3}\boldsymbol{K})$. The other two nucleon propagator connects both a dimer and the Coulomb propagator have four momenta of $(\frac{1}{3}E-k_0+\ell_0, -\boldsymbol{k}-\boldsymbol{\ell}+\frac{1}{3}\boldsymbol{K})$, and $(\frac{1}{3}E-p_0+\ell_0, -\boldsymbol{p}-\boldsymbol{\ell}+\frac{1}{3}\boldsymbol{K})$, respectively.

Similar to $K_c$, from dimer-NN vertices, we receive a factor $(iy)^2$ with $y^2 = \frac{4\pi}{M_N}$. We also include the $(1/\sqrt{8})^2$ from the two-body projectors, as well as a $-4$ symmetry factor and a $(ie)^2$. $p_0$ is on-shell by default. We give the expression below,

$$i\boldsymbol{\mathcal{H}}_b(B,p,k) = \frac{y^2}{2}(ie)^2 \int \frac{d^4k}{(2\pi)^4}(-\boldsymbol{M}_{kb})\ i\boldsymbol{D}_C(\frac{2}{3}E+k_0, \boldsymbol{k}+\frac{2}{3}\boldsymbol{K})\ i\boldsymbol{\mathcal{C}}(B,k) \times iS_N(\frac{1}{3}E-k_0, -\boldsymbol{k}+\frac{1}{3}\boldsymbol{K}) \times (-i\Omega_b(B,p,k)) \ , \quad (5.3.42)$$

where $\boldsymbol{M}_{kb}$ is a constant matrix, defined in Eq. (5.3.6). The additional $-1$ is not physical but a trick to have a positive form of kernel function. The $-i\Omega_b(B,p,k)$ represent the inner

loop integration, given by

$$-i\Omega_b(B,p,k) = \int \frac{d^4\ell}{(2\pi)^4}\frac{i}{\boldsymbol{\ell}^2+\lambda^2} iS_N(\frac{1}{3}E + k_0 - \ell_0 + p_0, \boldsymbol{k}+\boldsymbol{\ell}+\boldsymbol{p}+\frac{1}{3}\boldsymbol{K})$$
$$iS_N(\frac{1}{3}E - k_0 + \ell_0, -\boldsymbol{k}-\boldsymbol{\ell}+\frac{1}{3}\boldsymbol{K}) iS_N(\frac{1}{3}E - p_0 + \ell_0, -\boldsymbol{p}-\boldsymbol{\ell}+\frac{1}{3}\boldsymbol{K}) \ . \quad (5.3.43)$$

Picking the pole at $k_0 = \frac{E}{3} - \frac{1}{2M_N}(\frac{\boldsymbol{K}}{3}-\boldsymbol{k})^2 + i\epsilon$, and $\ell_0 = \frac{E}{3} + p_0 + k_0 - \frac{1}{2M_N}(\frac{\boldsymbol{K}}{3}+\boldsymbol{k}+\boldsymbol{p}+\boldsymbol{\ell})^2 + i\epsilon$, we get

$$\boldsymbol{\mathcal{H}}_b(B,p,k) = \frac{\alpha 4\pi^2}{M_N}\int \frac{dk}{2\pi^2}k^2 \int_{-1}^{+1} d\cos\theta \boldsymbol{M}_{kb}\, \widetilde{\boldsymbol{\mathcal{C}}}(B,k)\Omega_b(B,p,k) \ , \quad (5.3.44)$$

where $\cos\theta$ is the cosine value between the $\hat{\boldsymbol{k}}$ and $\hat{\boldsymbol{p}}$. The $\Omega_b(B,p,k)$ is reduced to

$$\Omega_b(B,p,k) = \int \frac{d^3\ell}{(2\pi)^3}\frac{1}{\boldsymbol{\ell}^2+\lambda^2}$$
$$\times S_N(\frac{1}{3}E - k_0 + \ell_0, -\boldsymbol{k}-\boldsymbol{\ell}+\frac{1}{3}\boldsymbol{K}) S_N(\frac{1}{3}E - p_0 + \ell_0, -\boldsymbol{p}-\boldsymbol{\ell}+\frac{1}{3}\boldsymbol{K}) \ . \quad (5.3.45)$$

One can still try to use Feynman parametrization with

$$\frac{1}{ABC} = 2\int_0^1 du \int_0^{1-u} dv \left[uA + vB + (1-u-v)C\right]^{-3} \ . \quad (5.3.46)$$

However, here using such Feynman parameters will lead to extremely complicated expressions if one tries to get an simple and clean analytical results. Instead, we will only partially use Feynman parameters for two nucleon propagators and then take the advantage of Fourier transform. To simplify this expression further, consider

$$\frac{1}{AB} = \int_0^1 du \left[uA + (1-u)B\right]^{-2} = \int_0^1 du \left[\ell'^2 + \Delta_b\right]^{-2} \ , \quad (5.3.47)$$

with

$$
\begin{aligned}
A =& - M_N/S_N(\frac{1}{3}E - p_0 + \ell_0, -\boldsymbol{p} - \boldsymbol{\ell} + \frac{1}{3}\boldsymbol{K}) \ , \\
B =& - M_N/S_N(\frac{1}{3}E - k_0 + \ell_0, -\boldsymbol{k} - \boldsymbol{\ell} + \frac{1}{3}\boldsymbol{K}) \ , \\
\boldsymbol{\ell}' =& \boldsymbol{\ell} + \frac{1}{2}((2-u)\boldsymbol{k} + (1+u)\boldsymbol{p}) \\
\Delta_b =& \frac{1}{4}\left(-4BM_N + k^2(-(u-4))u + 2kp\cos\theta(u-1)u - p^2\left(u^2+2u-3\right)\right) \ .
\end{aligned}
$$

Notice we could make use the following Fourier transform formulae,

$$
\left(\ell^2 + a^2\right)^{-1} = \int d^3r \mathrm{e}^{i\boldsymbol{\ell}\cdot\boldsymbol{r}} \frac{1}{4\pi r}\mathrm{e}^{-ar} \ , \tag{5.3.48}
$$

$$
\left(\ell^2 + a^2\right)^{-2} = \int d^3r \mathrm{e}^{i\boldsymbol{\ell}\cdot\boldsymbol{r}} \frac{1}{8\pi a}\mathrm{e}^{-ar} \ . \tag{5.3.49}
$$

By setting photon mass to be zero, we have,

$$
\begin{aligned}
\Omega_b(B,p,k) = \int_0^1 du \int \frac{d^3\ell}{(2\pi)^3} \int d^3r_1 \mathrm{e}^{i\boldsymbol{\ell}'\cdot\boldsymbol{r}_1} \frac{1}{8\pi\sqrt{\Delta_b}}\mathrm{e}^{-\sqrt{\Delta_b}r_1} \ , \int d^3r_2 \mathrm{e}^{i\boldsymbol{\ell}\cdot\boldsymbol{r}_2}\frac{1}{4\pi r_2} \\
= \frac{M_N^2}{8\pi}\int_0^1 du \frac{1}{\sqrt{\Delta_b}}\frac{1}{(\boldsymbol{\ell}'-\boldsymbol{\ell})^2 + \Delta_b} \ .
\end{aligned} \tag{5.3.50}
$$

The integration over $u$ can be done analytically, and gives,

$$
\begin{aligned}
\Omega_b(B,p,k) =& \frac{M_N^2}{4\pi}\frac{1}{|\boldsymbol{k}-\boldsymbol{p}|}\frac{1}{k^2 + kp\cos\theta + p^2 - BM_N} \\
&\times \left(\tan^{-1}\left(\frac{2k^2 - kp\cos\theta - p^2}{\sqrt{3p^2 - 4BM_N}|\boldsymbol{k}-\boldsymbol{p}|}\right) + \tan^{-1}\left(\frac{2p^2 - kp\cos\theta - k^2}{\sqrt{3k^2 - 4BM_N}|\boldsymbol{k}-\boldsymbol{p}|}\right)\right) \ .
\end{aligned} \tag{5.3.51}
$$

Having a finite photon mass is not a problem, but numerically unnecessary for the box diagram. One thus has,

$$
\boldsymbol{\mathcal{H}}_b(B,p,k) = \boldsymbol{M}_{kb}K_b(B,p,k) \otimes_k \widetilde{\boldsymbol{\mathcal{C}}}(B,k) \ , \tag{5.3.52}
$$

where,

$$K_b(B,p,k) = \alpha M_N \pi \int_{-1}^{+1} d\cos\theta \frac{1}{|\boldsymbol{k}-\boldsymbol{p}|} \frac{1}{k^2 + kp\cos\theta + p^2 - BM_N}$$
$$\times \left( \tan^{-1}\left( \frac{2k^2 - kp\cos\theta - p^2}{\sqrt{3p^2 - 4BM_N}|\boldsymbol{k}-\boldsymbol{p}|} \right) + \tan^{-1}\left( \frac{2p^2 - kp\cos\theta - k^2}{\sqrt{3k^2 - 4BM_N}|\boldsymbol{k}-\boldsymbol{p}|} \right) \right) \quad . \quad (5.3.53)$$

### 5.3.6 Off-shell Vertex Functions Kernels

In the calculation above, we have only considered the case with only on-shell nucleon energy in Eq. (5.3.14), which is exactly what we need most of the time. However, later in this chapter, we would have to take off-shell nucleon energy. It is straightforward to define $\widetilde{B}$, which includes the binding energy and the energy shift from the three-body binding energy. With off-shell nucleon energy, the vertex kernel functions can be done in similar ways from previous sections, but may not be able to have as compact form as we have in Eq, [[cite eq]]. To sum up, the $^3$He vertex function with off-shell nucleon is given by,

$$\boldsymbol{\mathcal{C}}(B,\widetilde{B},p) = \boldsymbol{I}_C + \Big( \boldsymbol{M}_{ks} K_s(B,\widetilde{B},p,k) + \boldsymbol{M}_{kc} K_c(B,\widetilde{B},p,k)$$
$$+ \boldsymbol{M}_{kt1} K_{t1}(B,\widetilde{B},p,k) + \boldsymbol{M}_{kt2} K_{t2}(B,\widetilde{B},p,k) + \boldsymbol{M}_{kb} K_b(B,\widetilde{B},p,k) \Big) \otimes_k \boldsymbol{\mathcal{C}}(B,k), \quad (5.3.54)$$

where

$$K_s(B,\widetilde{B},p,k) = \frac{2\pi}{kp} Q_0\left(\frac{k^2+p^2-m\widetilde{B}}{kp}\right) \ , \tag{5.3.55}$$

$$\begin{aligned} K_c(B,\widetilde{B},p,k) =& \alpha M_N 2\pi \int_{-1}^{+1} d\cos\theta \frac{1}{(\boldsymbol{k}-\boldsymbol{p})^2+\lambda^2} \\ & \times \frac{1}{|\boldsymbol{k}-\boldsymbol{p}|} \arctan \frac{|\boldsymbol{k}-\boldsymbol{p}|}{\sqrt{3k^2-4M_N B}+\sqrt{3p^2-4M_N\widetilde{B}}} \ , \end{aligned} \tag{5.3.56}$$

$$\begin{aligned} K_{t1}(B,\widetilde{B},p,k) =& \alpha M_N 2\pi \int_{-1}^{+1} d\cos\theta \frac{1}{k^2+p^2+kp\cos\theta-M_N\widetilde{B}} \\ & \times \frac{1}{|2\boldsymbol{k}+\boldsymbol{p}|} \arctan \frac{|2\boldsymbol{k}+\boldsymbol{p}|}{\sqrt{3p^2-4M_N\widetilde{B}}} \end{aligned} \tag{5.3.57}$$

$$\begin{aligned} K_{t2}(B,\widetilde{B},p,k) =& \alpha M_N 2\pi \int_{-1}^{+1} d\cos\theta \frac{1}{k^2+p^2+kp\cos\theta-M_N\widetilde{B}} \\ & \times \frac{1}{|2\boldsymbol{p}+\boldsymbol{k}|} \arctan \frac{|2\boldsymbol{p}+\boldsymbol{k}|}{\sqrt{3k^2-4M_N B}} \ , \end{aligned} \tag{5.3.58}$$

$$\begin{aligned} K_b(B,\widetilde{B},p,k) =& \alpha M_N \pi \int_{-1}^{+1} d\cos\theta \int_0^1 du \frac{1}{M_N(1-u)(B-\widetilde{B})-BM_N+p^2+pq\cos\theta+q^2} \\ & \times \Big[4M_N(1-u)(B-\widetilde{B})-4BM_N-p^2\left(u^2+2u-3\right) \\ & -2pqu(1-u)\cos\theta+q^2(4-u)u\Big]^{-\frac{1}{2}} \ . \end{aligned} \tag{5.3.59}$$

One should notice that, choosing $\widetilde{B}=B$, we are able to restore the on-shell expressions in the previous sections. In $K_b(B,\widetilde{B},p,k)$, we keep the integral over $u$, the Feynman parameter. Due to the fact that Feynman parameters can be applied in varies ways, the expression of $K_b(B,\widetilde{B},p,k)$ above is not the only correct one. However, all legit expressions are expected to have the same numerical values.

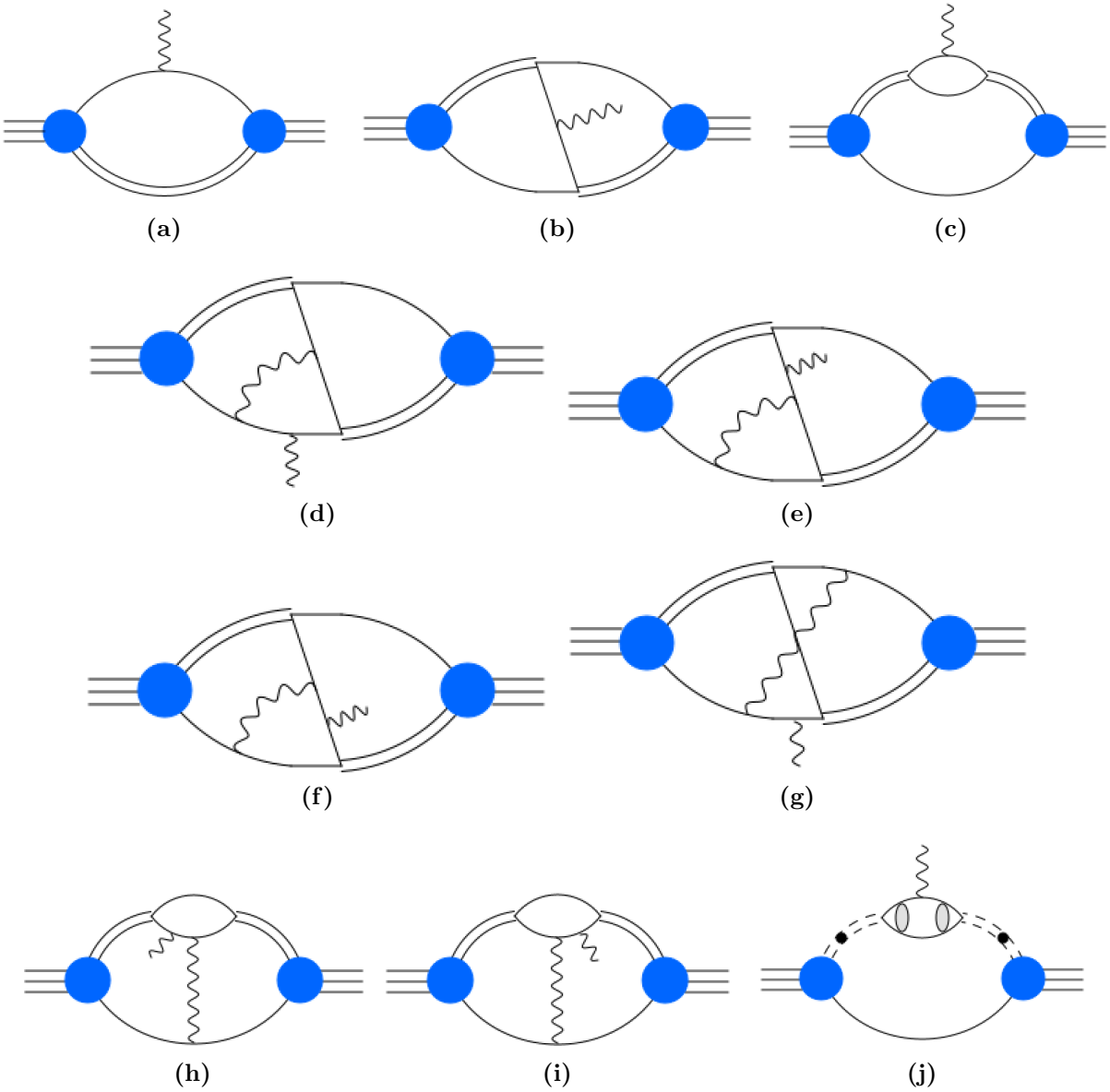


**Figure 5.4:** Diagrams contributing to the $^3$He charge form factor. Blue circles represent the $^3$He vertex function with full Coulomb interactions. Wavy lines are Coulomb photons. The double line denotes either spin-triplet or spin-singlet dimers. Solid ellipse in (j) represent Coulomb bubbles. The complex conjugate diagrams of (d), (e), (f) and (g), which are not displayed here for simplicity, also contributing to the charge form factors. (a), (b) and (c) are also the full diagrams contribute to charge form factors without Coulomb, but with no Coulomb vertex functions.

## 5.4 Calculations of Charge Form Factor Diagrams

We will write the charge form factors of $^3$He in terms of the sum of a few diagrams,

$$F_{\rm 3He}(q^2) = F^A_{\rm 3He}(q^2) + F^B_{\rm 3He}(q^2) + F^C_{\rm 3He}(q^2) \\ + F^{Bt1}_{\rm 3He}(q^2) + F^{Bt2}_{\rm 3He}(q^2) + F^{Bt3}_{\rm 3He}(q^2) + F^{Bbox}_{\rm 3He}(q^2) + F^{Cs}_{\rm 3He}(q^2) + F^{Cpp}_{\rm 3He}(q^2) \ , \quad (5.4.1)$$

where $F^A_{\rm 3He}(q^2)$, $F^B_{\rm 3He}(q^2)$ and $F^C_{\rm 3He}(q^2)$ corresponding to diagram (a), (b) and (c) of Fig. 5.4, respectively. $F^{Bt1}_{\rm 3He}(q^2)$, $F^{Bt2}_{\rm 3He}(q^2)$ , $F^{Bt3}_{\rm 3He}(q^2)$ and $F^{Bbox}_{\rm 3He}(q^2)$ represent contributions respectively from Fig. 5.4 (d), (e), (f) and (g) together with their own complex conjugate. We only display one topology here for simplicity. $F^{Cs}_{\rm 3He}(q^2)$ is the sum of diagrams (h) and (i) of Fig. 5.4, while $F^{Cpp}_{\rm 3He}(q^2)$ corresponds to diagram (j).

Here I provide details for calculating charge form factor diagrams. Conventions of calculations are provided here. It is used for all form factor diagram calculations.

**Conventions for the form factor calculation** Form factor diagrams calculations are performed in the Breit frame. Initial and final momenta of the $^3$He are $\boldsymbol{K}$ and $\boldsymbol{P}$. The external Coulomb photon inject no energy to the system but a momentum of $\boldsymbol{q} = \boldsymbol{P} - \boldsymbol{K}$. The total energy of $^3$He in the Breit frame is given by $E = B - \frac{1}{24M_N}\boldsymbol{q}^2$, where B is the $^3$He binding energy.

### 5.4.1 Diagram A

Diagram A is shown in panel (a) of Fig. 5.4. It has the simplest structure among all diagrams but is the most difficult one to calculate. The two pole structure inside the loop forces us to boost the vertex functions. The four-momentum of the dimer, the nucleon on the left, and the nucleon on the right are $(\frac{2}{3}E + k_0, \boldsymbol{k} + \frac{2}{3}\boldsymbol{K})$, $(\frac{1}{3}E - k_0, -\boldsymbol{l} + \frac{1}{3}\boldsymbol{K})$, $(\frac{1}{3}E - k_0, -\boldsymbol{l} + \frac{1}{3}\boldsymbol{K} + \boldsymbol{q})$, respectively. Thus, diagram A is given by,

$$F^A_{\rm 3He}(q^2) = Z_{\psi C} \int \frac{d^4k}{(2\pi)^4} i\boldsymbol{\mathcal{C}}(B, \widetilde{B}, k) i\boldsymbol{D}_C(\frac{2}{3}E + k_0, \boldsymbol{k} + \frac{2}{3}\boldsymbol{K}) \boldsymbol{M}^A_{\rm 3He} i\boldsymbol{\mathcal{C}}(B, \widetilde{B}, p) \\ iS_N(\frac{1}{3}E - k_0, -\boldsymbol{l} + \frac{1}{3}\boldsymbol{K}) iS_N(\frac{1}{3}E - k_0, -\boldsymbol{l} + \frac{1}{3}\boldsymbol{K} + \boldsymbol{q}) \ , \quad (5.4.2)$$

where $p = \sqrt{k^2 - \frac{4}{3}kqx + \frac{4}{9}q^2}$ is the relative momentum of the final $^3$He propagator. $x = \hat{\boldsymbol{k}} \cdot \hat{\boldsymbol{q}}$ represents the cosine value of the angle between $\boldsymbol{k}$ and $\boldsymbol{q}$. The constant matrix, $\boldsymbol{M}^A_{^3\mathrm{He}}$, is given by

$$\boldsymbol{M}^A_{^3\mathrm{He}} = \begin{pmatrix} 1 & 0 & 0 \\ 0 & 1 & 0 \\ 0 & 0 & 0 \end{pmatrix} . \tag{5.4.3}$$

There are two poles at,

$$k_0^1 = \frac{1}{3}E - \frac{1}{M_N}(-\boldsymbol{k} + \frac{1}{3}\boldsymbol{K})^2 + i\epsilon \ , \tag{5.4.4}$$

$$k_0^0 = \frac{1}{3}E - \frac{1}{M_N}(-\boldsymbol{k} + \frac{1}{3}\boldsymbol{K} + \boldsymbol{q})^2 + i\epsilon \ . \tag{5.4.5}$$

Notice that $k_0^1$ is on-shell for the initial vertex function but off-shell for the final. $k_0^0$ is the other way around. Remind reader that on-shell nucleon energy is Eq. (5.3.14). Define the quantity, $\Delta E$, represents the difference between two poles, by,

$$\Delta E = k_0^1 - k_0^0 = \frac{1}{M_N}(-\boldsymbol{k} \cdot \boldsymbol{q} + \frac{1}{3}\boldsymbol{q}^2) \ . \tag{5.4.6}$$

The expression of boosted vertex function is discussed at Eq. (5.3.54). At $k_0^1$ and $k_0^0$, $F^{A1}_{^3\mathrm{He}}(q^2)$ and $F^{A0}_{^3\mathrm{He}}(q^2)$ are given separately by,

$$F^{A1}_{^3\mathrm{He}}(q^2) = Z_{\psi C} \int \frac{dk}{2\pi^2} k^2 \int_{-1}^{+1} dx \frac{1}{2} \frac{M_N}{kqx - \frac{1}{3}q^2} \boldsymbol{\mathcal{C}}(B, B + \Delta E, p) \boldsymbol{M}^A_{^3\mathrm{He}} \boldsymbol{D}(B - \frac{k^2}{2M_N}, k) \boldsymbol{\mathcal{C}}(B, k) \ , \tag{5.4.7}$$

$$\begin{aligned} F^{A0}_{^3\mathrm{He}}(q^2) = & Z_{\psi C} \int \frac{dk}{2\pi^2} k^2 \int_{-1}^{+1} dx \frac{1}{2} \frac{-M_N}{kqx - \frac{1}{3}q^2} \\ & \times \boldsymbol{\mathcal{C}}(B, p) \boldsymbol{M}^A_{^3\mathrm{He}} \boldsymbol{D}(B - \Delta E - \frac{k^2}{2M_N}, k) \boldsymbol{\mathcal{C}}(B, B - \Delta E, k) \ , \end{aligned} \tag{5.4.8}$$

with $p$ and $x$ defined previously in this subsection. In numerical implementation, it is always better to combine the two parts together to avoid numerical singularities, we get

$$F^A_{^3\mathrm{He}}(q^2) = Z_{\psi C}\int \frac{dk}{2\pi^2}k^2\int_{-1}^{+1}dx\frac{1}{2}\frac{M_N}{kqx-\frac{1}{3}q^2} \times\Bigg(\boldsymbol{\mathcal{C}}(B,B+\Delta E,p)\boldsymbol{M}^A_{^3\mathrm{He}}\boldsymbol{D}(B-\frac{k^2}{2M_N},k)\boldsymbol{\mathcal{C}}(B,k) -\boldsymbol{\mathcal{C}}(B,p)\boldsymbol{M}^A_{^3\mathrm{He}}\boldsymbol{D}(B-\Delta E-\frac{k^2}{2M_N},k)\boldsymbol{\mathcal{C}}(B,B-\Delta E,k)\Bigg) \ . \quad (5.4.9)$$

One should notice that, we do not take $\boldsymbol{k}\to\boldsymbol{k}+\frac{1}{3}\boldsymbol{q}$, like in Sec. 4.4, to make the time reversal symmetry of the expressions.

### 5.4.2 Diagram B

Diagram B is shown in panel (b) of Fig. 5.4. The four-momenta of the dimer and the nucleon propagator associate with the $^3$He initial propagator are $(\frac{2}{3}E+k_0,\boldsymbol{k}+\frac{2}{3}\boldsymbol{K})$ and $(\frac{1}{3}E-k_0,-\boldsymbol{k}+\frac{1}{3}\boldsymbol{K})$, respectively. While for the dimer and the nucleon associate with the final $^3$He state, the four-momenta are $(\frac{2}{3}E+p_0,\boldsymbol{p}+\frac{2}{3}\boldsymbol{P})$ and $(\frac{1}{3}E-p_0,-\boldsymbol{p}+\frac{1}{3}\boldsymbol{P})$, respectively. The other two nucleon propagators have four-momenta of $(\frac{1}{3}E+k_0+p_0,\boldsymbol{k}+\boldsymbol{p}+\frac{2}{3}\boldsymbol{K}-\frac{1}{3}\boldsymbol{P})$ and $(\frac{1}{3}E+k_0+p_0,\boldsymbol{k}+\boldsymbol{p}+\frac{2}{3}\boldsymbol{K}-\frac{1}{3}\boldsymbol{P}+\frac{1}{3}\boldsymbol{q})$. From dimer-NN vertices, we received $(iy)^2$ with $y^2=\frac{4\pi}{M_N}$. We also include the $(1/\sqrt{8})^2$ from the two-body projectors, as well as a $-4$ symmetry factor. $F^B_{^3\mathrm{He}}(q^2)$ is thus, given by,

$$F^B_{^3\mathrm{He}}(q^2) = (\frac{y^2}{2})Z_{\psi C}\int\frac{d^4k}{(2\pi)^4}\int\frac{d^4p}{(2\pi)^4}i\boldsymbol{\mathcal{C}}(B,p)i\boldsymbol{D}_C(\frac{2}{3}E+p_0,\boldsymbol{p}+\frac{2}{3}\boldsymbol{P})\boldsymbol{M}^B_{^3\mathrm{He}} \times i\boldsymbol{D}_C(\frac{2}{3}E+k_0,\boldsymbol{k}+\frac{2}{3}\boldsymbol{K})i\boldsymbol{\mathcal{C}}(B,k)iS_N(\frac{1}{3}E-k_0,-\boldsymbol{k}+\frac{1}{3}\boldsymbol{K})iS_N(\frac{1}{3}E-p_0,-\boldsymbol{p}+\frac{1}{3}\boldsymbol{P}) \times iS_N(\frac{1}{3}E+k_0+p_0,\boldsymbol{k}+\boldsymbol{p}+\frac{2}{3}\boldsymbol{K}-\frac{1}{3}\boldsymbol{P})iS_N(\frac{1}{3}E+k_0+p_0,\boldsymbol{k}+\boldsymbol{p}+\frac{2}{3}\boldsymbol{K}-\frac{1}{3}\boldsymbol{P}+\frac{1}{3}\boldsymbol{q}) \ , \quad (5.4.10)$$

where the constant matrix $\boldsymbol{M}^B_{^3\mathrm{He}}$ is

$$\boldsymbol{M}^B_{\rm 3He} = \begin{pmatrix} 0 & 0 & -\sqrt{6} \\ 0 & 0 & \sqrt{2} \\ -\sqrt{6} & \sqrt{2} & 0 \end{pmatrix} . \tag{5.4.11}$$

Picking the pole at $k_0 = \frac{E}{3} - \frac{1}{2M_N}(\frac{\boldsymbol{K}}{3} - \boldsymbol{k})^2 + i\epsilon$, and $p_0 = \frac{E}{3} - \frac{1}{2M_N}(\frac{\boldsymbol{P}}{3} - \boldsymbol{p})^2 + i\epsilon$, we get

$$\begin{aligned} F^B_{\rm 3He}(q^2) = Z_{\psi C} \int \frac{dk}{2\pi^2} k^2 \int \frac{dk}{2\pi^2} p^2 \widetilde{\boldsymbol{\mathcal{C}}}(B,p) \boldsymbol{M}^B_{\rm 3He} \widetilde{\boldsymbol{\mathcal{C}}}(B,k) \int_{-1}^{+1} dx \int_{-1}^{+1} dy \int_0^{2\pi} d\phi \left(-\frac{M}{4}\right) \\ \times \left[k^2 + p^2 + kpz - \frac{1}{3}kqx - \frac{2}{3}pqy + \frac{1}{9}q^2 - M_N B\right]^{-1} \\ \times \left[k^2 + p^2 + kpz + \frac{2}{3}kqx + \frac{1}{3}pqy + \frac{1}{9}q^2 - M_N B\right]^{-1} , \end{aligned} \tag{5.4.12}$$

where $x = \hat{\boldsymbol{k}} \cdot \hat{\boldsymbol{q}}$, $y = \hat{\boldsymbol{p}} \cdot \hat{\boldsymbol{q}}$, and $z = \hat{\boldsymbol{k}} \cdot \hat{\boldsymbol{p}}$ are the cosines of the angle between $\boldsymbol{k}$ and $\boldsymbol{q}$, $\boldsymbol{p}$ and $\boldsymbol{q}$ and $\boldsymbol{k}$ and $\boldsymbol{p}$, respectively. $z$ is expressed by $x$, $y$ and $\phi$ as

$$z = xy + \sqrt{1-x^2}\sqrt{1-y^2}\cos\phi . \tag{5.4.13}$$

### 5.4.3 Diagram C

Diagram C is shown in panel (c) of Fig. 5.4. The four-momenta of the dimer propagators associate with the $^3$He initial and final state are $(\frac{2}{3}E + k_0, \boldsymbol{k} + \frac{2}{3}\boldsymbol{K})$ and $(\frac{2}{3}E + k_0, \boldsymbol{k} + \frac{2}{3}\boldsymbol{K} + \boldsymbol{q})$, respectively. The nucleon propagator connects both vertex function carries a four-momentum of $(\frac{1}{3}E - k_0, -\boldsymbol{k} + \frac{1}{3}\boldsymbol{K})$. Three nucleon propagator in the inner loop have four-momenta of $(\frac{2}{3}E + k_0 + \ell_0, \boldsymbol{k} + \frac{2}{3}\boldsymbol{K} + \boldsymbol{\ell})$, $(\frac{2}{3}E + k_0 + \ell_0, \boldsymbol{k} + \frac{2}{3}\boldsymbol{K} + \boldsymbol{\ell} + \boldsymbol{q})$, and $(-\ell_0, -\boldsymbol{\ell})$. With a symmetry factor +4, and $(iy/\sqrt{8})^2$ from dimer-NN vertices, we give the expression for $F^C_{\rm 3He}(q^2)$, by,

$$\begin{aligned} F^C_{\rm 3He}(q^2) = (-\frac{y^2}{2}) Z_{\psi C} \int \frac{d^4k}{(2\pi)^4} i\boldsymbol{\mathcal{C}}(B,p) i\boldsymbol{D}_C(\frac{2}{3}E + k_0, \boldsymbol{k} + \frac{2}{3}\boldsymbol{K} + \boldsymbol{q}) \boldsymbol{M}^C_{\rm 3He} \\ \times i\boldsymbol{D}_C(\frac{2}{3}E + k_0, \boldsymbol{k} + \frac{2}{3}\boldsymbol{K}) i\boldsymbol{\mathcal{C}}(B,k) i S_N(\frac{1}{3}E - k_0, -\boldsymbol{k} + \frac{1}{3}\boldsymbol{K}) \Gamma^C_{\rm 3He}(B,q,k,p), \end{aligned} \tag{5.4.14}$$

where $p = \sqrt{k^2 + \frac{2}{3}\boldsymbol{k}\cdot\boldsymbol{q} + \frac{1}{9}q^2}$. $\Gamma^C_{^3\mathrm{He}}(B,q,k,p)$ represent the inner loop,

$$\Gamma^C_{^3\mathrm{He}}(B,q,k,p) = \int \frac{d^4\ell}{(2\pi)^4} iS_N(-\ell_0,-\boldsymbol{\ell}) \\ \times iS_N(\frac{2}{3}E + k_0 + \ell_0, \boldsymbol{k} + \frac{2}{3}\boldsymbol{K} + \boldsymbol{\ell}) iS_N(\frac{2}{3}E + k_0 + \ell_0, \boldsymbol{k} + \frac{2}{3}\boldsymbol{K} + \boldsymbol{\ell} + \boldsymbol{q}) \ . \quad (5.4.15)$$

The constant matrix $\boldsymbol{M}^C_{^3\mathrm{He}}$ is

$$\boldsymbol{M}^C_{^3\mathrm{He}} = \begin{pmatrix} 2 & 0 & 0 \\ 0 & 2 & 0 \\ 0 & 0 & 0 \end{pmatrix} \ . \quad (5.4.16)$$

We stress that $(\frac{1}{\sqrt{8}})^2$ from the two-body projectors are not included in the constant matrix. Picking up the pole at $k_0 = \frac{E}{3} - \frac{1}{2M_N}(\frac{\boldsymbol{K}}{3} - \boldsymbol{k})^2 + i\epsilon$, and $\ell_0 = -\frac{1}{2M_N}\ell^2 + i\epsilon$, we get

$$F^C_{^3\mathrm{He}}(q^2) = Z_{\psi C} \int \frac{dk}{2\pi^2} k^2 \int_{-1}^{+1} dx\, \widetilde{\boldsymbol{\mathcal{C}}}(B,p) \boldsymbol{M}^C_{^3\mathrm{He}} \widetilde{\boldsymbol{\mathcal{C}}}(B,k) \frac{M_N}{2q} \\ \times \arctan\left[ q \left( \sqrt{3k^2 - 4M_N B} + \sqrt{3p^2 - 4M_N B} \right)^{-1} \right] \ , \quad (5.4.17)$$

where $p = \sqrt{k^2 + \frac{2}{3}\boldsymbol{k}\cdot\boldsymbol{q} + \frac{1}{9}q^2}$ is the relative momentum of the final state. $x$ is the cosine of the angle between $\boldsymbol{k}$ and $\boldsymbol{q}$. The inner loop is evaluated with the Feynman parameterization very similar to $K_c$. I attach the inner loop result here for future readers checking their partial results,

$$\Gamma^C_{^3\mathrm{He}}(B,q,k,p) = \frac{M_N^2}{2\pi q} \arctan\left[ q \left( \sqrt{3k^2 - 4M_N B} + \sqrt{3p^2 - 4M_N B} \right)^{-1} \right] \ . \quad (5.4.18)$$

### 5.4.4 Diagram B-tri 1

The first set of "triangular" B diagrams are partially shown in panel (d) of Fig. 5.4. Full set of $F^{Bt1}_{^3\mathrm{He}}(q^2)$ includes both Fig. 5.4 (d) and its complex conjugation.

The four-momenta of the dimer and the nucleon propagator associate with the $^3$He initial propagator are $(\frac{2}{3}E + k_0, \boldsymbol{k} + \frac{2}{3}\boldsymbol{K})$ and $(\frac{1}{3}E - k_0, -\boldsymbol{k} + \frac{1}{3}\boldsymbol{K})$, respectively. While for the dimer

and the nucleon associate with the final $^3$He state, the four-momenta are $(\frac{2}{3}E+p_0, \boldsymbol{p}+\frac{2}{3}\boldsymbol{P})$ and $(\frac{1}{3}E-p_0, -\boldsymbol{p}+\frac{1}{3}\boldsymbol{P})$, respectively. The nucleon propagator which is outside of the triangular loop has a four-momentum of $(\frac{1}{3}E+k_0+p_0, \boldsymbol{k}+\boldsymbol{p}+\frac{2}{3}\boldsymbol{K}-\frac{1}{3}\boldsymbol{P})$. The other three nucleon propagators inside the triangular loop have four-momenta of $(\frac{1}{3}E+p_0-\ell_0, -\boldsymbol{\ell}+\boldsymbol{p}+\frac{2}{3}\boldsymbol{K}-\frac{1}{3}\boldsymbol{P})$, $(\frac{1}{3}E+\ell_0, \boldsymbol{\ell}+\frac{1}{3}\boldsymbol{K})$ and $(\frac{1}{3}E+\ell_0, \boldsymbol{\ell}+\frac{1}{3}\boldsymbol{K}+\boldsymbol{q})$. The Coulomb photon propagator carries a momentum of $\boldsymbol{k}+\boldsymbol{\ell}$.

From dimer-NN vertices, we received $(iy)^2$ with $y^2=\frac{4\pi}{M_N}$. We also include the $(1/\sqrt{8})^2$ from the two-body projectors, as well as a $-4$ symmetry factor. Notice that, due to the symmetry of the diagram's structure, Fig. 5.4 (d) numerically has the same value with its own complex conjugation. Here we only demonstrate one diagram's derivation for concision. $\frac{1}{2}F^{Bt1}_{\rm 3He}(q^2)$ is thus, given by,

$$\begin{aligned}\frac{1}{2}F^{Bt1}_{\rm 3He}(q^2) &= (\frac{y^2}{2})Z_{\psi C}\int\frac{d^4k}{(2\pi)^4}\int\frac{d^4p}{(2\pi)^4}i\boldsymbol{\mathcal{C}}(B,p)i\boldsymbol{D}_C(\frac{2}{3}E+p_0,\boldsymbol{p}+\frac{2}{3}\boldsymbol{P})(-1)\boldsymbol{M}^{Bt1}_{\rm 3He}\\ &\times i\boldsymbol{D}_C(\frac{2}{3}E+k_0,\boldsymbol{k}+\frac{2}{3}\boldsymbol{K})i\boldsymbol{\mathcal{C}}(B,k)iS_N(\frac{1}{3}E-k_0,-\boldsymbol{k}+\frac{1}{3}\boldsymbol{K})iS_N(\frac{1}{3}E-p_0,-\boldsymbol{p}+\frac{1}{3}\boldsymbol{P})\\ &\times iS_N(\frac{1}{3}E+k_0+p_0,\boldsymbol{k}+\boldsymbol{p}+\frac{2}{3}\boldsymbol{K}-\frac{1}{3}\boldsymbol{P})i\Gamma^{Bt1}_{\rm 3He}(B,q,k,p)\ ,\end{aligned}\tag{5.4.19}$$

where the constant matrix $\boldsymbol{M}^{Bt1}_{\rm 3He}$ is

$$\boldsymbol{M}^{Bt1}_{\rm 3He}=\begin{pmatrix}0&0&0\\0&0&0\\\sqrt{6}&-\sqrt{2}&0\end{pmatrix}\ .\tag{5.4.20}$$

$\boldsymbol{M}^{Bt1}_{\rm 3He}$ includes an additional minus sign from the rest part. Notice that, one should carefully use the $\boldsymbol{M}^{Bt1}_{\rm 3He}$ in numerical calculation. Use the $\boldsymbol{M}^{Bt1\dagger}_{\rm 3He}$ without being carefully checked the order of initial and final state vertex function will lead to numerical mistakes. $i\Gamma^{Bt1}_{\rm 3He}(B,q,k,p)$ represent the results from the triangular loop, given by

$$\begin{aligned}i\Gamma^{Bt1}_{\rm 3He}(B,q,k,p) &= \int\frac{d^4\ell}{(2\pi)^4}\frac{-ie^2}{(\boldsymbol{k}+\boldsymbol{\ell})^2+\lambda^2}iS_N(\frac{1}{3}E+p_0-\ell_0,-\boldsymbol{\ell}+\boldsymbol{p}+\frac{2}{3}\boldsymbol{K}-\frac{1}{3}\boldsymbol{P})\\ &\times iS_N(\frac{1}{3}E+\ell_0,\boldsymbol{\ell}+\frac{1}{3}\boldsymbol{K})iS_N(\frac{1}{3}E+\ell_0,\boldsymbol{\ell}+\frac{1}{3}\boldsymbol{K}+\boldsymbol{q})\ .\end{aligned}\tag{5.4.21}$$

Picking the pole at $k_0 = \frac{E}{3} - \frac{1}{2M_N}(\frac{\boldsymbol{K}}{3} - \boldsymbol{k})^2 + i\epsilon$, $p_0 = \frac{E}{3} - \frac{1}{2M_N}(\frac{\boldsymbol{P}}{3} - \boldsymbol{p})^2 + i\epsilon$, and $\ell_0 = \frac{E}{3} + p_0 - \frac{1}{2M_N}(\boldsymbol{p} - \boldsymbol{\ell} - \frac{1}{2}\boldsymbol{q})^2 + i\epsilon$ for all three loops, we get

$$\Gamma^{Bt1}_{^3\mathrm{He}}(B,q,k,p) = \int \frac{d^3\ell}{(2\pi)^3} \frac{\alpha 4\pi}{(\boldsymbol{k}+\boldsymbol{\ell})^2 + \lambda^2} S_N(\frac{1}{3}E + \ell_0, \boldsymbol{\ell} + \frac{1}{3}\boldsymbol{K}) S_N(\frac{1}{3}E + \ell_0, \boldsymbol{\ell} + \frac{1}{3}\boldsymbol{K} + \boldsymbol{q}) \ . \tag{5.4.22}$$

Recall in Sec. 5.3.5 we use Feynman parametrization for the two nucleon propagators and then fourier transform for the remaining integration. Put everything together we have,

$$\begin{aligned}
\frac{1}{2}F^{Bt1}_{^3\mathrm{He}}(q^2) = Z_{\psi C} \int \frac{dk}{2\pi^2} k^2 \int \frac{dp}{2\pi^2} p^2 \widetilde{\boldsymbol{\mathcal{C}}}(B,p) \boldsymbol{M}^{Bt1}_{^3\mathrm{He}} \widetilde{\boldsymbol{\mathcal{C}}}(B,k) \\
\times \int_{-1}^{+1} dx \int_{-1}^{+1} dy \int_0^{2\pi} d\phi \left[ k^2 + p^2 + kpz - \frac{1}{3}kqx - \frac{2}{3}pqy + \frac{1}{9}q^2 - M_N B \right]^{-1} \\
\times \int_0^1 du \frac{-\alpha M_N}{4} \left( 3p^2 - 2pquy + \frac{1}{3}q^2 u(4-3u) - 4BM_N \right)^{-\frac{1}{2}} \\
\times \left( k^2 + kpz + kqux - \frac{4kqx}{3} + p^2 - \frac{2pqy}{3} - \frac{q^2 u}{3} + \frac{4q^2}{9} - BM_N \right)^{-1} \ ,
\end{aligned} \tag{5.4.23}$$

where $u$ is a Feynman parameter. Due to different ways applying Feynman parameters, the expression can have different equivalent forms. $x$, $y$, and $z$ are defined the same as in diagram B. In numerical implementation, do not forget to multiply a 2 to include also contribution from the complex conjugate diagram. For reference, from the inner loop we get,

$$\begin{aligned}
\Gamma^{Bt1}_{^3\mathrm{He}}(B,q,k,p) = \alpha M_N^2 \int_0^1 du \left( 3p^2 - 2pquy + \frac{1}{3}q^2 u(4-3u) - 4BM_N \right)^{-\frac{1}{2}} \\
\times \left( k^2 + kpz + kqux - \frac{4kqx}{3} + p^2 - \frac{2pqy}{3} - \frac{q^2 u}{3} + \frac{4q^2}{9} - BM_N \right)^{-1} \ .
\end{aligned} \tag{5.4.24}$$

### 5.4.5 Diagram B-tri 2

The second set of "triangular" B diagrams are partially shown in panel (e) of Fig. 5.4. Full set of $F^{Bt2}_{^3\mathrm{He}}(q^2)$ includes both Fig. 5.4 (e) and its complex conjugation. $F^{Bt2}_{^3\mathrm{He}}(q^2)$ is relatively

easy due to the fact that using Feynman parameters can already leave a good analytical result. The four-momenta of the dimer and the nucleon propagator associate with the $^3$He initial propagator are $(\frac{2}{3}E + k_0, \boldsymbol{k} + \frac{2}{3}\boldsymbol{K})$ and $(\frac{1}{3}E - k_0, -\boldsymbol{k} + \frac{1}{3}\boldsymbol{K})$, respectively. While for the dimer and the nucleon associate with the final $^3$He state, the four-momenta are $(\frac{2}{3}E+p_0, \boldsymbol{p}+\frac{2}{3}\boldsymbol{P})$ and $(\frac{1}{3}E-p_0, -\boldsymbol{p}+\frac{1}{3}\boldsymbol{P})$, respectively. The two nucleon propagators which are outside of the triangular loop has four-momenta of $(\frac{1}{3}E+k_0+p_0, \boldsymbol{k}+\boldsymbol{p}+\frac{2}{3}\boldsymbol{K}-\frac{1}{3}\boldsymbol{P})$, and $(\frac{1}{3}E+k_0+p_0, \boldsymbol{k}+\boldsymbol{p}+\frac{2}{3}\boldsymbol{K}-\frac{1}{3}\boldsymbol{P}+\boldsymbol{q})$. The other two nucleon propagators inside the triangular loop have four-momenta of $(\frac{1}{3}E + p_0 + \ell_0, \boldsymbol{\ell} + \boldsymbol{p} + \frac{2}{3}\boldsymbol{K} - \frac{1}{3}\boldsymbol{P} + \boldsymbol{q})$ and $(\frac{1}{3}E - \ell_0, -\boldsymbol{\ell} + \frac{1}{3}\boldsymbol{K})$. The Coulomb photon propagator carries a momentum of $-\boldsymbol{k} + \boldsymbol{\ell}$.

Again, from dimer-NN vertices, we received $(iy)^2$ with $y^2 = \frac{4\pi}{M_N}$. We also include the $(1/\sqrt{8})^2$ from the two-body projectors, as well as a $-4$ symmetry factor. Notice that, due to the symmetry of the diagram's structure, Fig. 5.4 (f) numerically has the same value with its own complex conjugation. Here we only demonstrate one diagram's derivation for concision. $\frac{1}{2}F^{Bt2}_{^3\mathrm{He}}(q^2)$ is thus, given by,

$$\begin{aligned}
\frac{1}{2}F^{Bt2}_{^3\mathrm{He}}(q^2) = (\frac{y^2}{2})Z_{\psi C}\int\frac{d^4k}{(2\pi)^4}\int\frac{d^4p}{(2\pi)^4}i\boldsymbol{\mathcal{C}}(B,p)i\boldsymbol{D}_C(\frac{2}{3}E+p_0,\boldsymbol{p}+\frac{2}{3}\boldsymbol{P})(-1)\boldsymbol{M}^{Bt2}_{^3\mathrm{He}} \\
\times i\boldsymbol{D}_C(\frac{2}{3}E+k_0,\boldsymbol{k}+\frac{2}{3}\boldsymbol{K})i\boldsymbol{\mathcal{C}}(B,k)iS_N(\frac{1}{3}E-k_0,-\boldsymbol{k}+\frac{1}{3}\boldsymbol{K})iS_N(\frac{1}{3}E-p_0,-\boldsymbol{p}+\frac{1}{3}\boldsymbol{P}) \\
\times iS_N(\frac{1}{3}E+k_0+p_0,\boldsymbol{k}+\boldsymbol{p}+\frac{2}{3}\boldsymbol{K}-\frac{1}{3}\boldsymbol{P}) \\
\times iS_N(\frac{1}{3}E+k_0+p_0,\boldsymbol{k}+\boldsymbol{p}+\frac{2}{3}\boldsymbol{K}-\frac{1}{3}\boldsymbol{P}+\boldsymbol{q})\int\frac{d^4\ell}{(2\pi)^4}\frac{-ie^2}{(-\boldsymbol{k}+\boldsymbol{\ell})^2+\lambda^2} \\
\times iS_N(\frac{1}{3}E+p_0+\ell_0,\boldsymbol{\ell}+\boldsymbol{p}+\frac{2}{3}\boldsymbol{K}-\frac{1}{3}\boldsymbol{P}+\boldsymbol{q})iS_N(\frac{1}{3}E-\ell_0,-\boldsymbol{\ell}+\frac{1}{3}\boldsymbol{K})\ . \qquad (5.4.25)
\end{aligned}$$

where the constant matrix $\boldsymbol{M}^{Bt2}_{^3\mathrm{He}}$ is

$$\boldsymbol{M}^{Bt2}_{^3\mathrm{He}} = \begin{pmatrix} 0 & 0 & 0 \\ 0 & 0 & 0 \\ \sqrt{6} & -\sqrt{2} & 0 \end{pmatrix}\ . \qquad (5.4.26)$$

The inner loop can be done very similar to what we have in Sec[[cite kc]], use Feynman parametrization, one easily get,

$$
\begin{aligned}
&\frac{1}{2}F^{Bt2}_{^3\mathrm{He}}(q^2) = Z_{\psi C}\int\frac{dk}{2\pi^2}k^2\int\frac{dp}{2\pi^2}p^2\widetilde{\boldsymbol{\mathcal{C}}}(B,p)\boldsymbol{M}^{Bt2}_{^3\mathrm{He}}\widetilde{\boldsymbol{\mathcal{C}}}(B,k)\\
&\times\int_{-1}^{+1}dx\int_{-1}^{+1}dy\int_0^{2\pi}d\phi\int_0^1 du\frac{-\alpha M_N}{4}\left[k^2+p^2+kpz-\frac{1}{3}kqx-\frac{2}{3}pqy+\frac{1}{9}q^2-M_NB\right]^{-1}\\
&\qquad\times\left[k^2+p^2+kpz+\frac{2}{3}kqx+\frac{1}{3}pqy+\frac{1}{9}q^2-M_NB\right]^{-1}\\
&\qquad\quad\times\left(k^2+\frac{1}{4}p^2+kpz+\frac{2}{3}kqx+\frac{1}{3}pqy+\frac{1}{9}q^2\right)^{-\frac{1}{2}}\\
&\qquad\qquad\times\arctan\sqrt{\frac{k^2+\frac{1}{4}p^2+kpz+\frac{2}{3}kqx+\frac{1}{3}pqy+\frac{1}{9}q^2}{\frac{3}{4}p^2-BM_N}}\ .
\end{aligned}
\tag{5.4.27}
$$

$x$, $y$, and $z$ are defined the same as in diagram B. In numerical implementation, do not forget to multiply a 2 to include also contribution from the complex conjugate diagram.

### 5.4.6 Diagram B-tri 3

The third set of "triangular" B diagrams are partially shown in (f) of Fig. 5.4. Full set of $F^{Bt3}_{^3\mathrm{He}}(q^2)$ includes both Fig. 5.4 (f) and its complex conjugation. $F^{Bt3}_{^3\mathrm{He}}(q^2)$ is alike to $F^{Bt1}_{^3\mathrm{He}}(q^2)$, we will not provide too much details here. The four-momenta of the dimer and the nucleon propagator associate with the $^3$He initial propagator are $(\frac{2}{3}E+k_0,\boldsymbol{k}+\frac{2}{3}\boldsymbol{K})$ and $(\frac{1}{3}E-k_0,-\boldsymbol{k}+\frac{1}{3}\boldsymbol{K})$, respectively. While for the dimer and the nucleon associate with the final $^3$He state, the four-momenta are $(\frac{2}{3}E+p_0,\boldsymbol{p}+\frac{2}{3}\boldsymbol{P})$ and $(\frac{1}{3}E-p_0,-\boldsymbol{p}+\frac{1}{3}\boldsymbol{P})$, respectively. The nucleon propagator which is outside of the triangular loop has a four-momentum of $(\frac{1}{3}E+k_0+p_0,\boldsymbol{k}+\boldsymbol{p}+\frac{2}{3}\boldsymbol{K}-\frac{1}{3}\boldsymbol{P})$. The other three nucleon propagators inside the triangular loop have four-momenta of $(\frac{1}{3}E+p_0+\ell_0,\boldsymbol{\ell}+\boldsymbol{p}+\frac{2}{3}\boldsymbol{K}-\frac{1}{3}\boldsymbol{P})$, $(\frac{1}{3}E+p_0+\ell_0,\boldsymbol{\ell}+\boldsymbol{p}+\frac{2}{3}\boldsymbol{K}-\frac{1}{3}\boldsymbol{P}+\boldsymbol{q})$ and $(\frac{1}{3}E-\ell_0,-\boldsymbol{\ell}+\frac{1}{3}\boldsymbol{K})$. The Coulomb photon propagator carries a momentum of $-\boldsymbol{k}+\boldsymbol{\ell}$.

Again, from dimer-NN vertices, we received $(iy)^2$ with $y^2=\frac{4\pi}{M_N}$. We also include the $(1/\sqrt{8})^2$ from the two-body projectors, as well as a $-4$ symmetry factor. Notice that, due to the symmetry of the diagram's structure, Fig. 5.4 (f) numerically has the same value with its own complex conjugation. Here we only demonstrate one diagram's derivation for concision.

$\frac{1}{2}F^{Bt3}_{\rm 3He}(q^2)$ is thus, given by,

$$\begin{aligned}\frac{1}{2}F^{Bt3}_{\rm 3He}(q^2) = (\frac{y^2}{2})Z_{\psi C}\int\frac{d^4k}{(2\pi)^4}\int\frac{d^4p}{(2\pi)^4}i\boldsymbol{\mathcal{C}}(B,p)i\boldsymbol{D}_C(\frac{2}{3}E+p_0,\boldsymbol{p}+\frac{2}{3}\boldsymbol{P})(-1)\boldsymbol{M}^{Bt1}_{\rm 3He}\\ \times i\boldsymbol{D}_C(\frac{2}{3}E+k_0,\boldsymbol{k}+\frac{2}{3}\boldsymbol{K})i\boldsymbol{\mathcal{C}}(B,k)iS_N(\frac{1}{3}E+k_0+p_0,\boldsymbol{k}+\boldsymbol{p}+\frac{2}{3}\boldsymbol{K}-\frac{1}{3}\boldsymbol{P})\\ \times iS_N(\frac{1}{3}E-k_0,-\boldsymbol{k}+\frac{1}{3}\boldsymbol{K})iS_N(\frac{1}{3}E-p_0,-\boldsymbol{p}+\frac{1}{3}\boldsymbol{P})\\ \times\int\frac{d^4\ell}{(2\pi)^4}\frac{-ie^2}{(-\boldsymbol{k}+\boldsymbol{\ell})^2+\lambda^2}iS_N(\frac{1}{3}E+p_0+\ell_0,\boldsymbol{\ell}+\boldsymbol{p}+\frac{2}{3}\boldsymbol{K}-\frac{1}{3}\boldsymbol{P})\\ \times iS_N(\frac{1}{3}E+p_0+\ell_0,\boldsymbol{\ell}+\boldsymbol{p}+\frac{2}{3}\boldsymbol{K}-\frac{1}{3}\boldsymbol{P}+\boldsymbol{q})iS_N(\frac{1}{3}E-\ell_0,-\boldsymbol{\ell}+\frac{1}{3}\boldsymbol{K})\ . \quad (5.4.28)\end{aligned}$$

where the constant matrix $\boldsymbol{M}^{Bt3}_{\rm 3He}$ is

$$\boldsymbol{M}^{Bt3}_{\rm 3He} = \begin{pmatrix} 0 & 0 & 0 \\ 0 & 0 & 0 \\ \sqrt{6} & -\sqrt{2} & 0 \end{pmatrix}\ . \quad (5.4.29)$$

We do the same analysis like in diagram $Bt1$, where Feynman parameterization and Fourier transform are performed, leaving,

$$\begin{aligned}\frac{1}{2}F^{Bt3}_{\rm 3He}(q^2) = Z_{\psi C}\int\frac{dk}{2\pi^2}k^2\int\frac{dp}{2\pi^2}p^2\widetilde{\boldsymbol{\mathcal{C}}}(B,p)\boldsymbol{M}^{Bt1}_{\rm 3He}\widetilde{\boldsymbol{\mathcal{C}}}(B,k)\\ \times\int_{-1}^{+1}dx\int_{-1}^{+1}dy\int_0^{2\pi}d\phi\int_0^1du\frac{-\alpha M_N}{4}\left[k^2+p^2+kpz-\frac{1}{3}kqx-\frac{2}{3}pqy+\frac{1}{9}q^2-M_NB\right]^{-1}\\ \times\left(-4BM_N+3p^2-2pquy+\frac{1}{3}q^2u(4-3u)\right)^{-\frac{1}{2}}\\ \times\left(-BM_N+k^2+kpz+\frac{1}{3}kq(2-3u)x+p^2+\frac{1}{3}pq(1-3u)y+\frac{q^2}{9}\right)^{-1}\ . \quad (5.4.30)\end{aligned}$$

where $u$ is a Feynman parameter. Due to different ways applying Feynman parameters, the expression can have different equivalent forms. $x$, $y$, and $z$ are defined the same as in diagram B. In numerical implementation, do not forget to multiply a 2 to include also contribution

from the complex conjugate diagram. For reference, from the inner loop we get,

$$\Gamma^{Bt3}_{^3\mathrm{He}}(B,q,k,p) = \alpha M_N^2 \int_0^1 du \left(-4BM_N + 3p^2 - 2pquy + \frac{1}{3}q^2u(4-3u)\right)^{-\frac{1}{2}} \times \left(-BM_N + k^2 + kpz + \frac{1}{3}kq(2-3u)x + p^2 + \frac{1}{3}pq(1-3u)y + \frac{q^2}{9}\right)^{-1} . \quad (5.4.31)$$

### 5.4.7 Diagram B-box

Diagram B-box is partially shown in panel (g) of Fig. 5.4. Full set of $F^{Bb}_{^3\mathrm{He}}(q^2)$ includes both Fig. 5.4 (f) and the one with external photon connects to the nucleon field at the top. The four-momenta of the dimer and the nucleon propagator associate with the $^3$He initial propagator are $(\frac{2}{3}E + k_0, \boldsymbol{k} + \frac{2}{3}\boldsymbol{K})$ and $(\frac{1}{3}E - k_0, -\boldsymbol{k} + \frac{1}{3}\boldsymbol{K})$, respectively. While for the dimer and the nucleon associate with the final $^3$He state, the four-momenta are $(\frac{2}{3}E + p_0, \boldsymbol{p} + \frac{2}{3}\boldsymbol{P})$ and $(\frac{1}{3}E - p_0, -\boldsymbol{p} + \frac{1}{3}\boldsymbol{P})$, respectively. There are four nucleon propagators in the loop with four-momenta of $(\frac{1}{3}E + \ell_0 - p_0, -\boldsymbol{p} - \boldsymbol{\ell} + \frac{1}{6}\boldsymbol{q})$, $(\frac{1}{3}E + \ell_0 - k_0, -\boldsymbol{k} - \boldsymbol{\ell} - \frac{1}{6}\boldsymbol{q})$, $(\frac{1}{3}E + \ell_0 - k_0, -\boldsymbol{k} - \boldsymbol{\ell} + \frac{5}{6}\boldsymbol{q})$, and $(\frac{1}{3}E + k_0 + p_0 - \ell_0, \boldsymbol{k} + \boldsymbol{p} + \boldsymbol{\ell} - \frac{1}{2}\boldsymbol{q})$. The Coulomb photon propagator carries a momentum of $+\boldsymbol{\ell}$. From dimer-NN vertices, we received $(iy)^2$ with $y^2 = \frac{4\pi}{M_N}$. We also include the $(1/\sqrt{8})^2$ from the two-body projectors, as well as a $-4$ symmetry factor. Like previous calculation, we only loop at one specific diagram in this set. $\frac{1}{2}F^{B}_{^3\mathrm{He}}(q^2)$ is thus, given by,

$$F^{Bb}_{^3\mathrm{He}}(q^2) = (\frac{y^2}{2})Z_{\psi C} \int \frac{d^4k}{(2\pi)^4} \int \frac{d^4p}{(2\pi)^4} i\boldsymbol{\mathcal{C}}(B,p) i\boldsymbol{D}_C(\frac{2}{3}E + p_0, \boldsymbol{p} + \frac{2}{3}\boldsymbol{P})(-1)\boldsymbol{M}^{Bb}_{^3\mathrm{He}} \times i\boldsymbol{D}_C(\frac{2}{3}E + k_0, \boldsymbol{k} + \frac{2}{3}\boldsymbol{K}) i\boldsymbol{\mathcal{C}}(B,k) \times iS_N(\frac{1}{3}E - k_0, -\boldsymbol{k} + \frac{1}{3}\boldsymbol{K}) iS_N(\frac{1}{3}E - p_0, -\boldsymbol{p} + \frac{1}{3}\boldsymbol{P}) \times \Gamma^{Bb}_{^3\mathrm{He}}(B,q,k,p) \quad (5.4.32)$$

where the constant matrix $\boldsymbol{M}^{Bb}_{\rm 3He}$ is

$$\boldsymbol{M}^{Bb}_{\rm 3He} = \begin{pmatrix} 1 & -\sqrt{3} & 0 \\ -\sqrt{3} & -1 & 0 \\ 0 & 0 & 0 \end{pmatrix} . \tag{5.4.33}$$

$\Gamma^{Bb}_{\rm 3He}(B,q,k,p)$ represent the results from the inner loop, given by

$$\begin{aligned}\Gamma^{Bb}_{\rm 3He}(B,q,k,p) = \int \frac{d^4\ell}{(2\pi)^4} iS_N(\frac{1}{3}E+\ell_0-p_0, -\boldsymbol{p}-\boldsymbol{\ell}+\frac{1}{6}\boldsymbol{q}) iS_N(\frac{1}{3}E+\ell_0-k_0, -\boldsymbol{k}-\boldsymbol{\ell}-\frac{1}{6}\boldsymbol{q}) \\ \times iS_N(\frac{1}{3}E+\ell_0-k_0, -\boldsymbol{k}-\boldsymbol{\ell}+\frac{5}{6}\boldsymbol{q}) iS_N(\frac{1}{3}E+k_0+p_0-\ell_0, \boldsymbol{k}+\boldsymbol{p}+\boldsymbol{\ell}-\frac{1}{2}\boldsymbol{q}) \frac{-ie^2}{\ell^2+\lambda^2} .\end{aligned} \tag{5.4.34}$$

We pick the poles at $k_0 = \frac{E}{3} - \frac{1}{2M_N}(\frac{\boldsymbol{K}}{3} - \boldsymbol{k})^2 + i\epsilon$, $p_0 = \frac{E}{3} - \frac{1}{2M_N}(\frac{\boldsymbol{P}}{3} - \boldsymbol{p})^2 + i\epsilon$, and $\ell_0 = \frac{E}{3} + k_0 + p_0 - \frac{1}{2M_N}(\boldsymbol{k}+\boldsymbol{p}+\boldsymbol{\ell}-\frac{1}{2}\boldsymbol{q})^2 + i\epsilon$ for all three loops. We get,

$$\begin{aligned}\frac{1}{2}F^{Bb}_{\rm 3He}(q^2) = Z_{\psi C} \int \frac{dk}{2\pi^2}k^2 \int \frac{dp}{2\pi^2}p^2 \widetilde{\boldsymbol{\mathcal{C}}}(B,p)\boldsymbol{M}^{Bt1}_{\rm 3He}\widetilde{\boldsymbol{\mathcal{C}}}(B,k) \\ \times \frac{-\alpha M_N}{16}\int_{-1}^{+1}dx\int_{-1}^{+1}dy\int_0^{2\pi}d\phi\int_0^1 du\int_0^{1-u}dv\frac{3a^2+Q^2}{a^3(Q^2+a^2)^2} ,\end{aligned} \tag{5.4.35}$$

where,

$$\begin{aligned}a^2 = -BM_N + \frac{1}{4}k^2\left(-u^2-2u(v+1)-v^2-2v+3\right) + \frac{1}{2}kpz(u+v-1)(u+v) \\ - \frac{1}{6}kqx(u-2v)(u+v-1) + \frac{1}{36}p^2\left(-9u^2-18uv+36u-9v^2+36v\right) \\ + \frac{1}{36}pqy\left(6u^2-6uv-24u-12v^2+12v\right) + \frac{1}{36}q^2\left(-u^2+4uv+4u-4v^2+4v\right) ,\end{aligned} \tag{5.4.36}$$

and

$$
\begin{aligned}
Q^2 = & \frac{1}{36}k^2\left(9u^2+18uv+18u+9v^2+18v+9\right)-\frac{1}{2}kpz(u+v-2)(u+v+1) \\
& +\frac{1}{6}kqx(u+v+1)(u-2v-2)+\frac{1}{36}p^2\left(9u^2+18uv-36u+9v^2-36v+36\right) \\
& -\frac{1}{6}pqy(u-2v-2)(u+v-2)+\frac{1}{36}q^2\left(u^2-4uv-4u+4v^2+8v+4\right) \ . \quad (5.4.37)
\end{aligned}
$$

$u$ and $v$ are Feynman parameters defined in Eq. (5.3.46). Due to the different ways of applying Feynman parameters, one could expect several equivalent expressions. Here we use the Feynman parametrization on the three remaining nucleon fields of the inner loop. Then we perform a Fourier transform with the equation below,

$$
\left(\ell^2+a^2\right)^{-3}=\frac{1}{4}\int d^3r\mathrm{e}^{i\boldsymbol{\ell}\cdot\boldsymbol{r}}\frac{1}{8\pi a^2}\mathrm{e}^{-ar}\left(\frac{1}{a}+r\right) \ . \quad (5.4.38)
$$

All other notations, $x$, $y$, $z$ and $\phi$ retain the same definition as in diagram B.

### 5.4.8 Diagram C-spectators

$F^{Cs}_{^3\mathrm{He}}(q^2)$ is represented by the sum of panel (h) and (i) of Fig. 5.4. The four-momenta of the dimer and the nucleon propagator associate with the $^3$He initial propagator are $(\frac{2}{3}E+k_0, \boldsymbol{k}+\frac{2}{3}\boldsymbol{K})$ and $(\frac{1}{3}E-k_0, -\boldsymbol{k}+\frac{1}{3}\boldsymbol{K})$, respectively. While for the dimer and the nucleon associate with the final $^3$He state, the four-momenta are $(\frac{2}{3}E+p_0, \boldsymbol{p}+\frac{2}{3}\boldsymbol{K}+\boldsymbol{q})$ and $(\frac{1}{3}E-p_0, -\boldsymbol{p}+\frac{1}{3}\boldsymbol{K})$, respectively. The Coulomb photon propagator carries a momentum of $(\boldsymbol{k}-\boldsymbol{p})$. The inner loop of Fig. 5.4 (h) and (i) are labeled by $\Gamma^{cs1}_{^3\mathrm{He}}(B,q,k,p)$ and $\Gamma^{cs2}_{^3\mathrm{He}}(B,q,k,p)$, respectively. Like the diagram C, a +4 symmetry factor and $(iy/\sqrt{8})^2$ are included. The full expression is simply,

$$
\begin{aligned}
F^{Cs}_{^3\mathrm{He}}(q^2) = & (-\frac{y^2}{2})Z_{\psi C}\int\frac{d^4k}{(2\pi)^4}\int\frac{d^4p}{(2\pi)^4}i\boldsymbol{\mathcal{C}}(B,p')i\boldsymbol{D}_C(\frac{2}{3}E+p_0,\boldsymbol{p}+\frac{2}{3}\boldsymbol{K}+\boldsymbol{q})\boldsymbol{M}^{Cs}_{^3\mathrm{He}} \\
& \times i\boldsymbol{D}_C(\frac{2}{3}E+k_0,\boldsymbol{k}+\frac{2}{3}\boldsymbol{K})i\boldsymbol{\mathcal{C}}(B,k)\frac{-ie^2}{(\boldsymbol{k}-\boldsymbol{p})^2+\lambda^2}iS_N(\frac{1}{3}E-k_0,-\boldsymbol{k}+\frac{1}{3}\boldsymbol{K}) \\
& \times iS_N(\frac{1}{3}E-p_0,-\boldsymbol{p}+\frac{1}{3}\boldsymbol{K})\Big(i\Gamma^{Cs1}_{^3\mathrm{He}}(B,q,k,p)+i\Gamma^{Cs2}_{^3\mathrm{He}}(B,q,k,p)\Big) \ , \quad (5.4.39)
\end{aligned}
$$

where $p' = |\boldsymbol{p} + \frac{1}{3}\boldsymbol{q}|$ is the relative momentum of the final vertex function, and the constant matrix is given by

$$\boldsymbol{M}^{Cs}_{\rm 3He} = \begin{pmatrix} 2 & 0 & 0 \\ 0 & 2 & 0 \\ 0 & 0 & 0 \end{pmatrix} . \tag{5.4.40}$$

$\Gamma^{Cs1}_{\rm 3He}(B,q,k,p)$ and $\Gamma^{Cs2}_{\rm 3He}(B,q,k,p)$ denotes the inner loop of Fig. 5.4 (h) and (i), given separately by

$$\begin{aligned} i\Gamma^{Cs1}_{\rm 3He}(B,q,k,p) = \int \frac{d^4\ell}{(4\pi)^2} iS_N(-\ell_0,-\boldsymbol{\ell}) iS_N(\frac{2}{3}E + k_0 + \ell_0, \boldsymbol{k} + \boldsymbol{\ell} + \frac{2}{3}\boldsymbol{K}) \\ \times iS_N(\frac{2}{3}E + k_0 + \ell_0, \boldsymbol{k} + \boldsymbol{\ell} + \frac{2}{3}\boldsymbol{K} + \boldsymbol{q}) iS_N(\frac{2}{3}E + p_0 + \ell_0, \boldsymbol{p} + \boldsymbol{\ell} + \frac{2}{3}\boldsymbol{K} + \boldsymbol{q}) \ , \end{aligned} \tag{5.4.41}$$

and

$$\begin{aligned} i\Gamma^{Cs2}_{\rm 3He}(B,q,k,p) = \int \frac{d^4\ell}{(4\pi)^2} iS_N(-\ell_0,-\boldsymbol{\ell}) iS_N(\frac{2}{3}E + k_0 + \ell_0, \boldsymbol{k} + \boldsymbol{\ell} + \frac{2}{3}\boldsymbol{K}) \\ \times iS_N(\frac{2}{3}E + p_0 + \ell_0, \boldsymbol{p} + \boldsymbol{\ell} + \frac{2}{3}\boldsymbol{K}) iS_N(\frac{2}{3}E + p_0 + \ell_0, \boldsymbol{p} + \boldsymbol{\ell} + \frac{2}{3}\boldsymbol{K} + \boldsymbol{q}) \ . \end{aligned} \tag{5.4.42}$$

Picking up poles at $\ell_0 = -\frac{\ell^2}{2M_N} + i\epsilon$, $k_0 = \frac{1}{3}E - \frac{1}{2M_N}(-\boldsymbol{k} + \frac{1}{3}\boldsymbol{K})^2 + i\epsilon$, and $p_0 = \frac{1}{3}E - \frac{1}{2M_N}(-\boldsymbol{p} + \frac{1}{3}\boldsymbol{K})^2 + i\epsilon$, we get,

$$\begin{aligned} F^{Cs}_{\rm 3He}(q^2) = Z_{\psi C} \int \frac{dk}{2\pi^2} k^2 \int \frac{dp}{2\pi^2} p^2 \int_{-1}^{+1} dx \int_{-1}^{-1} dy \int_0^{2\pi} d\phi \, \widetilde{\boldsymbol{\mathcal{C}}}(B,p') \boldsymbol{M}^{Cs}_{\rm 3He} \widetilde{\boldsymbol{\mathcal{C}}}(B,k) \\ \times \frac{-\alpha M_N^2}{16} \frac{1}{(\boldsymbol{k}-\boldsymbol{p})^2 + \lambda^2} \int_0^1 du \int_0^{1-u} dv \left( [\Delta^{Cs1}]^{-\frac{3}{2}} + [\Delta^{Cs2}]^{-\frac{3}{2}} \right) \ , \end{aligned} \tag{5.4.43}$$

where $\Delta^{Cs1}$ and $\Delta^{Cs2}$ are defined by

$$\begin{aligned} \Delta^{Cs1} = \frac{1}{12} \Big( -12BM_N - 3k^2(u+v-4)(u+v) - 6p(u+v-1)(q(u+1)y \\ - kz(u+v)) + 6kqx(u(u+v-1)+v) - 3p^2(u+v-1)(u+v+3) + q^2(u(2-3u)+1) \Big) \ , \end{aligned} \tag{5.4.44}$$

and

$$\Delta^{Cs2} = \frac{1}{12}\Bigg( -12BM_N - 3k^2(u+v-1)(u+v+3) + 6k(u+v-1)(pz(u+v)+qux) \\ - 3p^2(u+v-4)(u+v) - 6pquy(u+v-2) + q^2u(4-3u)\Bigg) \ . \quad (5.4.45)$$

To get this result, we use Feynman parametrization for the inner loop with $u$ and $v$ denoted as Feynman parameters. Since there are three propagators,

### 5.4.9 Diagram C-pp

Diagram Cpp is shown in panel (j) of Fig. 5.4. The four-momenta of the dimer propagators associate with the $^3$He initial and final state are $(\frac{2}{3}E+k_0, \boldsymbol{k}+\frac{2}{3}\boldsymbol{K})$ and $(\frac{2}{3}E+k_0, \boldsymbol{k}+\frac{2}{3}\boldsymbol{K}+\boldsymbol{q})$, respectively. The nucleon propagator connects both vertex function carries a four-momentum of $(\frac{1}{3}E-k_0, -\boldsymbol{k}+\frac{1}{3}\boldsymbol{K})$. With a symmetry factor +4, and $(iy/\sqrt{8})^2$ from dimer-NN vertices, we give the expression for $F^{Cpp}_{\rm 3He}(q^2)$, by,

$$F^{Cpp}_{\rm 3He}(q^2) = (-\frac{y^2}{2})Z_{\psi C}\int \frac{d^4k}{(2\pi)^4} i\boldsymbol{\mathcal{C}}(B,p) i\boldsymbol{D}_C(\frac{2}{3}E+k_0, \boldsymbol{k}+\frac{2}{3}\boldsymbol{K}+\boldsymbol{q})\boldsymbol{M}^{Cpp}_{\rm 3He} \\ \times i\boldsymbol{D}_C(\frac{2}{3}E+k_0, \boldsymbol{k}+\frac{2}{3}\boldsymbol{K}) i\boldsymbol{\mathcal{C}}(B,k) iS_N(\frac{1}{3}E-k_0, -\boldsymbol{k}+\frac{1}{3}\boldsymbol{K})(-\Gamma^{cpp}_{\rm 3He}(B,q,k)), \quad (5.4.46)$$

where $p = \sqrt{k^2 + \frac{2}{3}\boldsymbol{k}\cdot\boldsymbol{q} + \frac{1}{9}q^2}$. The constant matrix $\boldsymbol{M}^{C}_{\rm 3He}$ is

$$\boldsymbol{M}^{Cpp}_{\rm 3He} = \begin{pmatrix} 0 & 0 & 0 \\ 0 & 0 & 0 \\ 0 & 0 & 4 \end{pmatrix} \ . \quad (5.4.47)$$

$-\Gamma^{Cpp}_{\rm 3He}(B,q,k)$ represent the inner loop integral. The inner loop is actually alike to a LO two-body charge form factor diagram. Define following quantities,

$$E' = \frac{2}{3} + k_0, \ \boldsymbol{k}' = \boldsymbol{k} + \frac{2}{3}\boldsymbol{K} + \frac{1}{2}\boldsymbol{q} \ . \quad (5.4.48)$$

The benefit of defining those quantities is to keep symmetric forms of the equations. While the two nucleon propagators connects to the initial dimer have four-momenta of $(-k_{10}, -\boldsymbol{k}_1)$ and $(E' + k_{10}, \boldsymbol{k}' - \frac{1}{2}\boldsymbol{q} + \boldsymbol{k}_1)$. The two nucleon propagators connects to the final dimer have four-momenta of $(-k_{30}, -\boldsymbol{k}_3)$ and $(E' + k_{30}, \boldsymbol{k}' + \frac{1}{2}\boldsymbol{q} + \boldsymbol{k}_3)$. The three nucleon propagators in the middle loop have four-momenta of $(-k_{20}, -\boldsymbol{k}_2)$, $(E' + k_{20}, \boldsymbol{k}' - \frac{1}{2}\boldsymbol{q} + \boldsymbol{k}_2)$, and $(E' + k_{20}, \boldsymbol{k}' + \frac{1}{2}\boldsymbol{q} + \boldsymbol{k}_2)$. Define the two nucleon propagator,

$$iS_{2N}(E,p) = \left(E - \frac{1}{M_N}p^2 + i\epsilon\right)^{-1} . \tag{5.4.49}$$

We can write down the expression for the inner loop,

$$\begin{aligned}
-\Gamma^{Cpp}_{^3\mathrm{He}}(B,q,k) = &\int \frac{d^4k_1}{(2\pi)^4}\int \frac{d^4k_2}{(2\pi)^4}\int \frac{d^4k_3}{(2\pi)^4} \\
&\times iS_N(-k_{10}, -\boldsymbol{k}_1) iS_N(-k_{20}, -\boldsymbol{k}_2) iS_N(-k_{30}, -\boldsymbol{k}_3) \\
\times iS_N(E'+k_{30}, \boldsymbol{k}'+\frac{1}{2}\boldsymbol{q}+\boldsymbol{k}_3) &i\chi_b(\boldsymbol{k}_3+\frac{1}{2}\boldsymbol{k}'+\frac{1}{4}\boldsymbol{q}, \boldsymbol{k}_2+\frac{1}{2}\boldsymbol{k}'+\frac{1}{4}\boldsymbol{q}, E_{\chi_b}) iS_N(E'+k_{20}, \boldsymbol{k}'+\frac{1}{2}\boldsymbol{q}+\boldsymbol{k}_2) \\
\times iS_N(E'+k_{20}, \boldsymbol{k}'-\frac{1}{2}\boldsymbol{q}+\boldsymbol{k}_2) &i\chi_a(\boldsymbol{k}_2+\frac{1}{2}\boldsymbol{k}'-\frac{1}{4}\boldsymbol{q}, \boldsymbol{k}_1+\frac{1}{2}\boldsymbol{k}'-\frac{1}{4}\boldsymbol{q}, E_{\chi_a}) iS_N(E'+k_{10}, \boldsymbol{k}'-\frac{1}{2}\boldsymbol{q}+\boldsymbol{k}_1) ,
\end{aligned} \tag{5.4.50}$$

where $\chi$ is the momentum-space Coulomb four-point function in the center of mass frame, related by the full Coulomb Green's function $G_C(E)$ by,

$$S_{2N}(E,\boldsymbol{k})\chi(\boldsymbol{k},\boldsymbol{p},E)S_{2N}(E,\boldsymbol{p}) = -\langle \boldsymbol{k}|G_C(E)|\boldsymbol{p}\rangle . \tag{5.4.51}$$

More about the full Coulomb Green's function can be found in Appendix A.4. $E_{\chi_a}$ and $E_{\chi_b}$ are defined by

$$E_{\chi_a} = E' - \frac{1}{4M_N}(\boldsymbol{k}' - \frac{\boldsymbol{q}}{2})^2 , \tag{5.4.52}$$

$$E_{\chi_b} = E' - \frac{1}{4M_N}(\boldsymbol{k}' + \frac{\boldsymbol{q}}{2})^2 . \tag{5.4.53}$$

Picking up the pole at $k_{10} = -\frac{k_1^2}{2M_N} + i\epsilon$, $k_{20} = -\frac{k_2^2}{2M_N} + i\epsilon$, and $k_{30} = -\frac{k_3^2}{2M_N} + i\epsilon$, one can find

$$\begin{aligned}
S_N(E' + k_{10}, \boldsymbol{k}' - \frac{1}{2}\boldsymbol{q} + \boldsymbol{k}_1) \to & S_{2N}(E_{\chi_a}, \boldsymbol{k}_1 + \frac{1}{2}(\boldsymbol{k}' - \frac{1}{2}\boldsymbol{q}))\ , \\
S_N(E' + k_{20}, \boldsymbol{k}' - \frac{1}{2}\boldsymbol{q} + \boldsymbol{k}_2) \to & S_{2N}(E_{\chi_a}, \boldsymbol{k}_2 + \frac{1}{2}(\boldsymbol{k}' - \frac{1}{2}\boldsymbol{q}))\ , \\
S_N(E' + k_{30}, \boldsymbol{k}' + \frac{1}{2}\boldsymbol{q} + \boldsymbol{k}_3) \to & S_{2N}(E_{\chi_b}, \boldsymbol{k}_3 + \frac{1}{2}(\boldsymbol{k}' + \frac{1}{2}\boldsymbol{q}))\ , \\
S_N(E' + k_{20}, \boldsymbol{k}' + \frac{1}{2}\boldsymbol{q} + \boldsymbol{k}_2) \to & S_{2N}(E_{\chi_b}, \boldsymbol{k}_2 + \frac{1}{2}(\boldsymbol{k}' + \frac{1}{2}\boldsymbol{q}))\ .
\end{aligned}$$

$\Gamma^{Cpp}_{\rm 3He}(B, q, k)$ can be reduced to

$$\begin{aligned}
\Gamma^{Cpp}_{\rm 3He}(B, q, k) = & \int \frac{d^3k_1}{(2\pi)^3} \int \frac{d^3k_2}{(2\pi)^3} \int \frac{d^4k_3}{(2\pi)^3} \\
\times S_{2N}(E_{\chi_b}, \boldsymbol{k}_3 + \frac{1}{2}(\boldsymbol{k}' + \frac{1}{2}\boldsymbol{q}))\chi_b(\boldsymbol{k}_3 + \frac{1}{2}\boldsymbol{k}' + \frac{1}{4}\boldsymbol{q}, \boldsymbol{k}_2 + \frac{1}{2}\boldsymbol{k}' + \frac{1}{4}\boldsymbol{q}, E_{\chi_b}) S_{2N}(E_{\chi_b}, \boldsymbol{k}_2 + \frac{1}{2}(\boldsymbol{k}' + \frac{1}{2}\boldsymbol{q})) \\
\times S_{2N}(E_{\chi_a}, \boldsymbol{k}_2 + \frac{1}{2}(\boldsymbol{k}' - \frac{1}{2}\boldsymbol{q}))\chi_a(\boldsymbol{k}_2 + \frac{1}{2}\boldsymbol{k}' - \frac{1}{4}\boldsymbol{q}, \boldsymbol{k}_1 + \frac{1}{2}\boldsymbol{k}' - \frac{1}{4}\boldsymbol{q}, E_{\chi_a}) S_{2N}(E_{\chi_a}, \boldsymbol{k}_1 + \frac{1}{2}(\boldsymbol{k}' - \frac{1}{2}\boldsymbol{q}))\ ,
\end{aligned} \tag{5.4.54}$$

Notice that here we have removed the $-1$ in front of $\Gamma^{Cpp}_{\rm 3He}(B, q, k)$. Define,

$$\boldsymbol{k}'_1 = \boldsymbol{k}_1 + \frac{1}{2}(\boldsymbol{k}' - \frac{1}{2}\boldsymbol{q}),\ \ \boldsymbol{k}'_3 = \boldsymbol{k}_3 + \frac{1}{2}(\boldsymbol{k}' + \frac{1}{2}\boldsymbol{q})\ . \tag{5.4.55}$$

We get

$$\begin{aligned}
\Gamma^{Cpp}_{\rm 3He}(B, q, k) = & \int \frac{d^3k'_1}{(2\pi)^3} \int \frac{d^3k_2}{(2\pi)^3} \int \frac{d^4k'_3}{(2\pi)^3} \\
& \times \langle \boldsymbol{k}'_3 | G_C(E_{\chi_b}) | \boldsymbol{k}_2 + \frac{1}{2}(\boldsymbol{k}' + \frac{1}{2}\boldsymbol{q}) \rangle \langle \boldsymbol{k}_2 + \frac{1}{2}(\boldsymbol{k}' - \frac{1}{2}\boldsymbol{q} | G_C(E_{\chi_a}) | \boldsymbol{k}'_1 \rangle\ ,
\end{aligned} \tag{5.4.56}$$

where Eq. (5.4.51) is used to reduce the expression. Using the equation,

$$\int d^3r \int \frac{d^3k}{(2\pi)^3} \langle \boldsymbol{k} | r)(r| = (0|, \tag{5.4.57}$$

where $\langle\ |$ and $(\ |$ are used to represent the momentum space and coordinate space, respectively. We find,

$$\Gamma^{Cpp}_{\rm 3He}(B,q,k) \ = \ \int \frac{d^3k_2}{(2\pi)^3}(0|G_C(E_{\chi_b})|\boldsymbol{k}_2 + \frac{1}{2}(\boldsymbol{k}' + \frac{1}{2}\boldsymbol{q})\rangle\langle\boldsymbol{k}_2 + \frac{1}{2}(\boldsymbol{k}' - \frac{1}{2}\boldsymbol{q}|G_C(E_{\chi_a})|0) \ . \tag{5.4.58}$$

Similarly, we have

$$\begin{aligned}\Gamma^{Cpp}_{\rm 3He}(B,q,k) = \int d^3r e^{i\mathbf{r}\cdot\mathbf{q}/2}(0|G_C(E_{\chi_b})|r)(r|G_C(E_{\chi_a})|0) \\ = 4\pi\int drr^2 j_0\left(\frac{qr}{2}\right)G_C(E_{\chi_b};0,r)G_C(E_{\chi_a};r,0) \ .\end{aligned} \tag{5.4.59}$$

Notice that the Coulomb Green's functions have one end at zero separation, only the S-wave part of these will contribute. Here we will take only S-wave from the partial wave expansion of the Coulomb Green's function, given by

$$G^{(0)}_C(E;0,r) = -\frac{M_R}{2\pi}\Gamma(1+\frac{k_C}{\gamma})\frac{W_{-\frac{k_C}{\gamma},1/2}(2\gamma r)}{r} \ , \tag{5.4.60}$$

where

$$\gamma = \sqrt{-2M_R E} = \sqrt{-M_N E} \tag{5.4.61}$$

$$k_C = Z_1 Z_2 M_R \alpha = \frac{M_N\alpha}{2} \ . \tag{5.4.62}$$

$M_R$ is reduced mass. In this case, $M_R = \frac{M_N}{2}$. $Z_1$ and $Z_2$ are charge number of particles. $\alpha$ is the fine structure constant. $W_{-\frac{k_C}{\gamma},1/2}(2\gamma r)$ is the Whittaker-W function defined in Appendix. A.5.

Back to the $F^{Cpp}_{\rm 3He}(q^2)$, we get,

$$\begin{aligned}F^{Cpp}_{\rm 3He}(q^2) = Z_{\psi C}\int\frac{dk}{2\pi^2}k^2\int_{-1}^{+1}dx\frac{4\pi^2}{M_N}\widetilde{\boldsymbol{\mathcal{C}}}(B,p)\boldsymbol{M}^{Cpp}_{\rm 3He}\widetilde{\boldsymbol{\mathcal{C}}}(B,k) \\ \times\int drr^2 j_0(\frac{qr}{2})G_C(E_{\chi_b};0,r)G_C(E_{\chi_a};r,0) \ .\end{aligned} \tag{5.4.63}$$

The coordinate space integral receive its major contribution from the low $r$ range. The integrand decreases and gets close to zero rapidly due to the Whittaker-W function, which is proportional to $\mathrm{e}^{-\gamma r}$. If one integrates from 0 to $+\infty$ or to a large hard cutoff, there will be huge errors. On the contrary, if one puts too many mesh points at a super small r range, python may not be able to give correct results. Only with carefully selected parameters or with Mathematica can one get stable and reliable numerical results.

## 5.5 The Third Zemach Moment and Numerical Implementation

The third Zemach moment is a quantity that is relevant for the calculation of the lamb shift. It is defined by [44]

$$\left\langle R_E^3 \right\rangle_{(2)} = \frac{48}{\pi} \int_0^\infty \frac{dq}{q^4} \left[ F_E^2\left(q^2\right) - 1 + \frac{q^2 \left\langle R_E^2 \right\rangle}{3} \right] , \tag{5.5.1}$$

where $F_E(q^2)$ is the electric form factor. $\langle R_E^2 \rangle$ is a numerical value from fitting form factor data. At $q^2 \to 0$, $F_E(q^2)$ can be expanded by

$$F_E\left(q^2\right) = 1 - \frac{1}{3!} \left\langle R_E^2 \right\rangle q^2 + \frac{1}{5!} \left\langle R_E^4 \right\rangle q^4 + \ldots . \tag{5.5.2}$$

We calculate the third Zemach moments numerically by separating the integration region into 3 parts,

$$\begin{aligned} \left\langle R_E^3 \right\rangle_{(2)} = \frac{48}{\pi} \Bigg[ & \int_0^{q_1} \frac{dq}{q^4} \left( F^2_{\text{expansion}}(q^2) - 1 + \frac{q^2 \left\langle R_E^2 \right\rangle}{3} \right) \\ & + \int_{q_1}^{q_2} \frac{dq}{q^4} \left( F^2_{\text{interpolation}}(q^2) - 1 + \frac{q^2 \left\langle R_E^2 \right\rangle}{3} \right) + \int_{q_2}^{+\infty} \frac{dq}{q^4} \left( -1 + \frac{q^2 \left\langle R_E^2 \right\rangle}{3} \right) \Bigg] , \end{aligned} \tag{5.5.3}$$

where $q_1$ is a small value up to a few hundred MeV. $q_2$ is a value smaller than the cutoff but large enough to ensure $F_E(q_2^2) \to 0$.

At very small $q$, the $\frac{1}{q^4}$ can cause numerical problems. Taking the expansion of $F_E(q^2)$ gives,

$$F^2_{\text{expansion}}(q^2) = 1 - \frac{1}{3}\left\langle R_E^2 \right\rangle q^2 + \left( \frac{\left\langle R_E^2 \right\rangle^2}{36} + \frac{\left\langle R_E^4 \right\rangle}{60} \right) q^4 + \mathcal{O}(q^6). \tag{5.5.4}$$

The first two terms in the expansion are canceled with the other terms in the integrand, leave

$$\frac{1}{q^4}\left( F^2_{\text{expansion}}(q^2) - 1 + \frac{q^2 \left\langle R_E^2 \right\rangle}{3} \right) = \left( \frac{\left\langle R_E^2 \right\rangle^2}{36} + \frac{\left\langle R_E^4 \right\rangle}{60} \right) + \mathcal{O}(q^2)\ . \tag{5.5.5}$$

However, the expansion fails at larger $q > q_1$. In this case, instead, we use interpolated function, $F^2_{\text{interpolation}}(q^2)$. Since we have used hard cutoff for our numerical implementation of form factors, we are not able to get meaningful data as $q \to \infty$. Notice that, at $q > q_2$, $F_E(q^2) \ll 1$, we could ignore $F_E(q^2)$ terms and are able to integrate $q$ from $q_2$ to $+\infty$.

## 5.6 Results

The charge form factor results of $^3$H and $^3$He as functions of $q$, in the absence of Coulomb interactions at leading order, are shown in Fig. 5.5. The hard cutoff we use is at 20 GeV.

Leading order charge form factor results of $^3$He with and without Coulomb interactions as functions of $q$ are shown in Fig. 5.6. The hard cutoff is also 20 GeV. The result without Coulomb is evaluated at triton binding energy, while with Coulomb we take the $^3$He binding energy. We observe the Coulomb interaction has obvious effects to $^3$He charge form factors.

At small $q^2$, we are able to expand the charge form factor like in Eq. (4.5.1). By fitting the data, at LO, for $^3$H without Coulomb interactions, one finds

$$\langle r_c^2(^3\text{H}, \not{C}, \text{LO})\rangle = 1.28\ \text{fm}^2, \langle r^4(^3\text{H}, \not{C}, \text{LO})\rangle = 5.80\ \text{fm}^4\ , \tag{5.6.1}$$

where $\not{C}$ denotes without Coulomb interactions. For $^3$He without Coulomb interactions, one finds,

$$\langle r_c^2(^3\text{He}, \not{C}, \text{LO})\rangle = 1.57\ \text{fm}^2, \langle r^4(^3\text{He}, \not{C}, \text{LO})\rangle = 9.05\ \text{fm}^4\ . \tag{5.6.2}$$

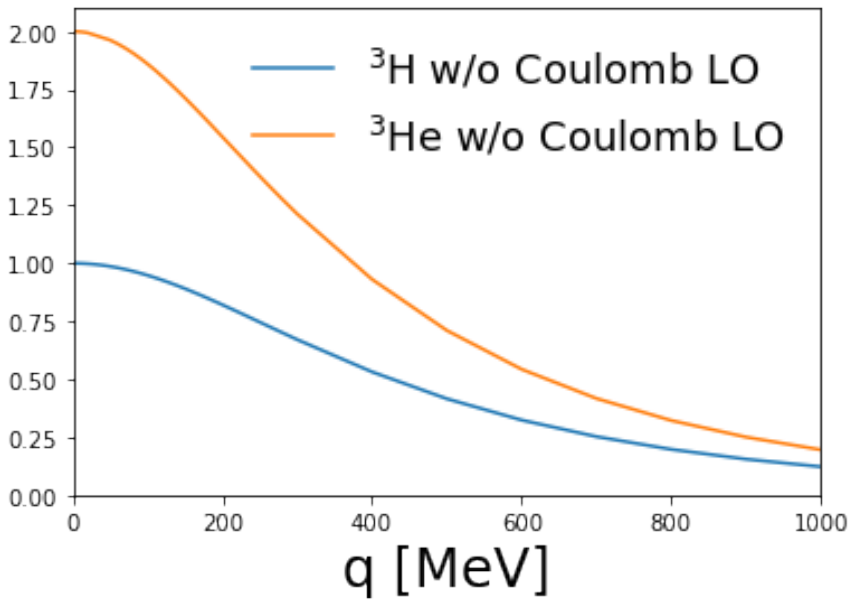


**Figure 5.5:** Leading order results, in the absence of Coulomb interactions, of the charge form factors of $^3$H and $^3$He as functions of $q$.

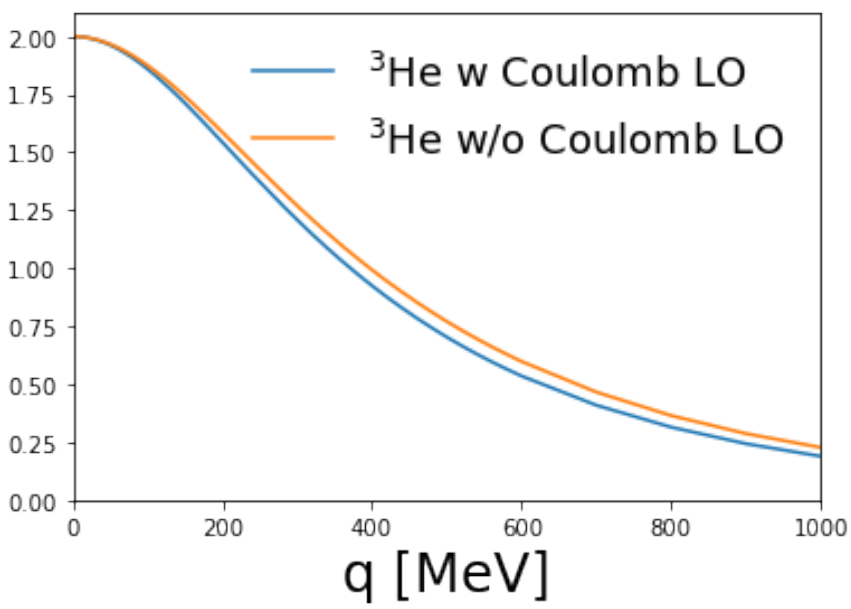


**Figure 5.6:** Leading order results of the charge form factors of $^3$He with and without Coulomb interactions as functions of $q$. The charge form factor without Coulomb is evaluated at triton binding energy.

By adding Coulomb interactions at leading order, we have

$$\langle r_c^2(^3\text{He, C, LO})\rangle = 1.66 \text{ fm}^2, \langle r^4(^3\text{He, C, LO})\rangle = 10.87 \text{ fm}^4 \ . \tag{5.6.3}$$

The third Zemach moment is defined in Eq. (5.5.1). We find third Zemach moments with and without Coulomb interactions at LO are

$$\langle R_E^3(^3\text{He, } \not{C}\text{, LO})\rangle_{(2)} = 8.34 \text{ fm}^3, \ \langle R_E^3(^3\text{He, C, LO})\rangle_{(2)} = 9.91 \text{ fm}^3 \ . \tag{5.6.4}$$

We will work NLO in the future work.

# Bibliography

[1] Abel, C. et al. (2020). Measurement of the permanent electric dipole moment of the neutron. *Phys. Rev. Lett.*, 124(8):081803. 43

[2] Abramczyk, M., Aoki, S., Blum, T., Izubuchi, T., Ohki, H., and Syritsyn, S. (2017). Lattice calculation of electric dipole moments and form factors of the nucleon. *Phys. Rev.*, D96(1):014501. 48

[3] Abusaif, F. et al. (2019). Storage Ring to Search for Electric Dipole Moments of Charged Particles - Feasibility Study. 43

[4] Ajzenberg-Selove, F. (1988). Energy levels of light nuclei a= 5- 10. *Nuclear Physics A*, 490(1):1–225. 18

[5] Ajzenberg-Selove, F. (1990). Energy levels of light nuclei A = 11-12. *Nucl. Phys. A*, 506:1–158. 18

[6] Ando, S.-i. and Birse, M. C. (2010). Effective field theory of 3he. *Journal of Physics G: Nuclear and Particle Physics*, 37(10):105108. 67, 79

[7] Andreev, V. et al. (2018). Improved limit on the electric dipole moment of the electron. *Nature*, 562(7727):355–360. 43

[8] Aoki, S. et al. (2020). FLAG Review 2019: Flavour Lattice Averaging Group (FLAG). *Eur. Phys. J. C*, 80(2):113. 48

[9] Ayyad, Y. et al. (2019). Direct observation of proton emission in $^{11}$Be. *Phys. Rev. Lett.*, 123(8):082501. xiv, 2, 26, 36, 37, 38, 39

[10] Ban, S., Dobaczewski, J., Engel, J., and Shukla, A. (2010). Fully self-consistent calculations of nuclear Schiff moments. *Phys. Rev. C*, 82:015501. 43

[11] Baye, D. and Tursunov, E. M. (2011). Beta delayed emission of a proton by a one-neutron halo nucleus. *Phys. Lett.*, B696:464–467. xiv, 26, 27, 34, 35, 36

[12] Bedaque, P., Hammer, H.-W., and van Kolck, U. (2000a). Effective theory of the triton. *Nuclear Physics A*, 676(1-4):357–370. 70

[13] Bedaque, P., Hammer, H.-W., and van Kolck, U. (2003a). Narrow resonances in effective field theory. *Physics Letters B*, 569(3-4):159–167. 18

[14] Bedaque, P. F., Hammer, H., and van Kolck, U. (1999a). Renormalization of the three-body system with short range interactions. *Phys. Rev. Lett.*, 82:463–467. 45, 46, 70

[15] Bedaque, P. F., Hammer, H., and van Kolck, U. (1999b). The Three boson system with short range interactions. *Nucl. Phys. A*, 646:444–466. 45, 46, 70

[16] Bedaque, P. F., Hammer, H., and van Kolck, U. (2000b). Effective theory of the triton. *Nucl. Phys. A*, 676:357–370. 46, 70

[17] Bedaque, P. F., Hammer, H.-W., and Van Kolck, U. (1999c). Renormalization of the three-body system with short-range interactions. *Physical Review Letters*, 82(3):463. 14

[18] Bedaque, P. F., Hammer, H. W., and van Kolck, U. (2003b). Narrow resonances in effective field theory. *Phys. Lett.*, B569:159–167. 26

[19] Bertulani, C., Hammer, H.-W., and van Kolck, U. (2002a). Effective field theory for halo nuclei: shallow -wave states. *Nuclear Physics A*, 712(1-2):37–58. 18

[20] Bertulani, C. A., Hammer, H. W., and Van Kolck, U. (2002b). Effective field theory for halo nuclei. *Nucl. Phys.*, A712:37–58. 26

[21] Bhattacharya, T., Yoon, B., Gupta, R., and Cirigliano, V. (2018). Neutron Electric Dipole Moment from Beyond the Standard Model. 48

[22] Bishof, M. et al. (2016). Improved limit on the $^{225}$Ra electric dipole moment. *Phys. Rev. C*, 94(2):025501. 43

[23] Borge, M. J. G., Fraile, L. M., Fynbo, H. O. U., Jonson, B., Kirsebom, O. S., Nilsson, T., Nyman, G., Possnert, G., Riisager, K., and Tengblad, O. (2013). Rare $\beta$p decays in light nuclei. *J. Phys.*, G40:035109. 26, 36

[24] Braaten, E. and Hammer, H.-W. (2006). Universality in few-body systems with large scattering length. *Physics Reports*, 428(5-6):259–390. 9

[25] Bsaisou, J., de Vries, J., Hanhart, C., Liebig, S., Meissner, U.-G., Minossi, D., Nogga, A., and Wirzba, A. (2015a). Nuclear Electric Dipole Moments in Chiral Effective Field Theory. *JHEP*, 03:104. [Erratum: JHEP 05, 083 (2015)]. 43, 44, 59

[26] Bsaisou, J., Hanhart, C., Liebig, S., Meissner, U.-G., Nogga, A., and Wirzba, A. (2013). The electric dipole moment of the deuteron from the QCD $\theta$-term. *Eur. Phys. J. A*, 49:31. 44

[27] Bsaisou, J., Meißner, U.-G., Nogga, A., and Wirzba, A. (2015b). P- and T-Violating Lagrangians in Chiral Effective Field Theory and Nuclear Electric Dipole Moments. *Annals Phys.*, 359:317–370. 44

[28] Buchmuller, W. and Wyler, D. (1986). Effective Lagrangian Analysis of New Interactions and Flavor Conservation. *Nucl. Phys. B*, 268:621–653. 47

[29] Cairncross, W. B., Gresh, D. N., Grau, M., Cossel, K. C., Roussy, T. S., Ni, Y., Zhou, Y., Ye, J., and Cornell, E. A. (2017). Precision Measurement of the Electron's Electric Dipole Moment Using Trapped Molecular Ions. *Phys. Rev. Lett.*, 119(15):153001. 43

[30] Chang, E., Davoudi, Z., Detmold, W., Gambhir, A. S., Orginos, K., Savage, M. J., Shanahan, P. E., Wagman, M. L., and Winter, F. (2018). Scalar, Axial, and Tensor Interactions of Light Nuclei from Lattice QCD. *Phys. Rev. Lett.*, 120(15):152002. 45

[31] Cirigliano, V., Dekens, W., de Vries, J., and Mereghetti, E. (2017). An $\epsilon'$ improvement from right-handed currents. *Phys. Lett. B*, 767:1–9. 48

[32] Crewther, R., Di Vecchia, P., Veneziano, G., and Witten, E. (1979). Chiral Estimate of the Electric Dipole Moment of the Neutron in Quantum Chromodynamics. *Phys. Lett. B*, 88:123. [Erratum: Phys.Lett.B 91, 487 (1980)]. 44, 48

[33] Davoudi, Z., Detmold, W., Orginos, K., Parreño, A., Savage, M. J., Shanahan, P., and Wagman, M. L. (2020). Nuclear matrix elements from lattice QCD for electroweak and beyond-Standard-Model processes. 45, 65

[34] de Jesus, J. and Engel, J. (2005). Time-reversal-violating Schiff moment of Hg-199. *Phys. Rev. C*, 72:045503. 58

[35] de Vries, J., Epelbaum, E., Girlanda, L., Gnech, A., Mereghetti, E., and Viviani, M. (2020a). Parity- and time-reversal-violating nuclear forces. 44, 49

[36] de Vries, J., Gnech, A., and Shain, S. (2020b). Strong CP violation in nuclear physics. 44, 64

[37] de Vries, J., Higa, R., Liu, C.-P., Mereghetti, E., Stetcu, I., Timmermans, R., and van Kolck, U. (2011a). Electric Dipole Moments of Light Nuclei From Chiral Effective Field Theory. *Phys. Rev. C*, 84:065501. 43, 44, 59, 63

[38] de Vries, J., Mereghetti, E., Seng, C.-Y., and Walker-Loud, A. (2017). Lattice QCD spectroscopy for hadronic CP violation. *Phys. Lett. B*, 766:254–262. 44

[39] de Vries, J., Mereghetti, E., Timmermans, R., and van Kolck, U. (2013). The Effective Chiral Lagrangian From Dimension-Six Parity and Time-Reversal Violation. *Annals Phys.*, 338:50–96. 44, 48

[40] de Vries, J., Mereghetti, E., and Walker-Loud, A. (2015). Baryon mass splittings and strong CP violation in SU(3) Chiral Perturbation Theory. *Phys. Rev. C*, 92(4):045201. 44, 48

[41] de Vries, J., Timmermans, R., Mereghetti, E., and van Kolck, U. (2011b). The Nucleon Electric Dipole Form Factor From Dimension-Six Time-Reversal Violation. *Phys. Lett. B*, 695:268–274. 48

[42] Dekens, W., de Vries, J., Bsaisou, J., Bernreuther, W., Hanhart, C., Meißner, U.-G., Nogga, A., and Wirzba, A. (2014). Unraveling models of CP violation through electric dipole moments of light nuclei. *JHEP*, 07:069. 43

[43] Dekens, W. and Stoffer, P. (2019). Low-energy effective field theory below the electroweak scale: matching at one loop. *JHEP*, 10:197. 47

[44] Dinur, N. N., Hernandez, O., Bacca, S., Barnea, N., Ji, C., Pastore, S., Piarulli, M., and Wiringa, R. (2019). Zemach moments and radii of h 2, 3 and he 3, 4. *Physical Review C*, 99(3):034004. 109

[45] Dragos, J., Luu, T., Shindler, A., de Vries, J., and Yousif, A. (2019). Confirming the Existence of the strong CP Problem in Lattice QCD with the Gradient Flow. 48

[46] Elkamhawy, W., Yang, Z., Hammer, H.-W., and Platter, L. (2019). $\beta$-delayed proton emission from $^{11}$Be in effective field theory. 25

[47] Engel, J., Ramsey-Musolf, M. J., and van Kolck, U. (2013). Electric Dipole Moments of Nucleons, Nuclei, and Atoms: The Standard Model and Beyond. *Prog. Part. Nucl. Phys.*, 71:21–74. 43, 44

[48] Fornal, B. and Grinstein, B. (2018). Dark Matter Interpretation of the Neutron Decay Anomaly. *Phys. Rev. Lett.*, 120(19):191801. 1, 26

[49] Friar, J. L., Gibson, B. F., and Payne, G. L. (1984). Recent progress in understanding trinucleon properties. *Ann. Rev. Nucl. Part. Sci.*, 34:403–433. 45

[50] Fynbo, H. O. U., Janas, Z., Mazzocchi, C., Pfuetzner, M., Refsgaard, J., Riisager, K., and Sokolowska, N. (2019). Comment on "Direct Observation of Proton Emission in $^{11}$Be". 26, 38

[51] Gaspard, D. (2018). Connection formulas between coulomb wave functions. *Journal of Mathematical Physics*, 59(11):112104. 130

[52] Gavela, M., Hernandez, P., Orloff, J., and Pene, O. (1994a). Standard model CP violation and baryon asymmetry. *Mod. Phys. Lett. A*, 9:795–810. 2, 43

[53] Gavela, M., Hernandez, P., Orloff, J., Pene, O., and Quimbay, C. (1994b). Standard model CP violation and baryon asymmetry. Part 2: Finite temperature. *Nucl. Phys. B*, 430:382–426. 2, 43

[54] Gavela, M., Lozano, M., Orloff, J., and Pene, O. (1994c). Standard model CP violation and baryon asymmetry. Part 1: Zero temperature. *Nucl. Phys. B*, 430:345–381. 2, 43

[55] Georgi, H. (1993). Effective field theory. *Annual review of nuclear and particle science*, 43(1):209–252. 4

[56] Gnech, A. and Viviani, M. (2020). Time Reversal Violation in Light Nuclei. *Phys. Rev. C*, 101(2):024004. 44, 59, 64

[57] Graner, B., Chen, Y., Lindahl, E., and Heckel, B. (2016). Reduced Limit on the Permanent Electric Dipole Moment of Hg199. *Phys. Rev. Lett.*, 116(16):161601. [Erratum: Phys.Rev.Lett. 119, 119901 (2017)]. 43

[58] Griesshammer, H. W. (2004). Improved convergence in the three-nucleon system at very low energies. *Nuclear Physics A*, 744:192–226. 146

[59] Grzadkowski, B., Iskrzynski, M., Misiak, M., and Rosiek, J. (2010). Dimension-Six Terms in the Standard Model Lagrangian. *JHEP*, 10:085. 47

[60] Gupta, R., Yoon, B., Bhattacharya, T., Cirigliano, V., Jang, Y.-C., and Lin, H.-W. (2018). Flavor diagonal tensor charges of the nucleon from (2+1+1)-flavor lattice QCD. *Phys. Rev. D*, 98(9):091501. 48

[61] Hagen, P., Hammer, H.-W., and Platter, L. (2013). Charge form factors of two-neutron halo nuclei in halo EFT. *Eur. Phys. J. A*, 49:118. 46

[62] Haisch, U. and Hala, A. (2019). Sum rules for CP-violating operators of Weinberg type. *JHEP*, 11:154. 48

[63] Hammer, H., Ji, C., and Phillips, D. (2017a). Effective field theory description of halo nuclei. *Journal of Physics G: Nuclear and Particle Physics*, 44(10):103002. 4

[64] Hammer, H. W., Ji, C., and Phillips, D. R. (2017b). Effective field theory description of halo nuclei. *J. Phys.*, G44(10):103002. 26

[65] Hammer, H.-W. and König, S. (2017). General aspects of effective field theories and few-body applications. In *An Advanced Course in Computational Nuclear Physics*, pages 93–153. Springer. 10, 71

[66] Hammer, H.-W., König, S., and van Kolck, U. (2020). Nuclear effective field theory: status and perspectives. *Rev. Mod. Phys.*, 92(2):025004. 45

[67] Hammer, H. W. and Phillips, D. R. (2011). Electric properties of the Beryllium-11 system in Halo EFT. *Nucl. Phys.*, A865:17–42. 19, 26, 29, 36

[68] Hansen, P. and Jonson, B. (1987). The neutron halo of extremely neutron-rich nuclei. *EPL (Europhysics Letters)*, 4(4):409. 16

[69] Hansen, P. G., Jensen, A. S., and Jonson, B. (1995). Nuclear halos. *Ann. Rev. Nucl. Part. Sci.*, 45:591–634. 16

[70] Hardy, J. C. and Towner, I. S. (2005). Superallowed 0+ —¿ 0+ nuclear beta decays: A Critical survey with tests of CVC and the standard model. *Phys. Rev.*, C71:055501. 31

[71] Higa, R., Hammer, H. W., and van Kolck, U. (2008). alpha alpha Scattering in Halo Effective Field Theory. *Nucl. Phys.*, A809:171–188. 33, 140, 143

[72] Higa, R., Rupak, G., and Vaghani, A. (2018). Radiative $^3$He$(\alpha,\gamma)^7$Be reaction in halo effective field theory. *Eur. Phys. J.*, A54(5):89. 26

[73] Hockings, W. and van Kolck, U. (2005). The Electric dipole form factor of the nucleon. *Phys. Lett. B*, 605:273–278. 48

[74] Hörz, B. et al. (2020). Two-nucleon S-wave interactions at the $SU(3)$ flavor-symmetric point with $m_{ud} \simeq m_s^{\rm phys}$: a first lattice QCD calculation with the stochastic Laplacian Heaviside method. 45

[75] Huet, P. and Sather, E. (1995). Electroweak baryogenesis and standard model CP violation. *Phys. Rev. D*, 51:379–394. 2, 43

[76] Izubuchi, T., Abramczyk, M., Blum, T., Ohki, H., and Syritsyn, S. (2017). Calculation of Nucleon Electric Dipole Moments Induced by Quark Chromo-Electric Dipole Moments. *PoS*, LATTICE2016:398. 48

[77] Jenkins, E. E., Manohar, A. V., and Stoffer, P. (2018a). Low-Energy Effective Field Theory below the Electroweak Scale: Anomalous Dimensions. *JHEP*, 01:084. 47

[78] Jenkins, E. E., Manohar, A. V., and Stoffer, P. (2018b). Low-Energy Effective Field Theory below the Electroweak Scale: Operators and Matching. *JHEP*, 03:016. 47

[79] Jonson, B. (2004). Light dripline nuclei. *Physics Reports*, 389(1):1 – 59. 16

[80] Kaplan, D. B. (2005). Five lectures on effective field theory. *arXiv preprint nucl-th/0510023*. 4, 9, 14

[81] Kaplan, D. B., Savage, M. J., and Wise, M. B. (1996). Nucleon - nucleon scattering from effective field theory. *Nucl. Phys. B*, 478:629–659. 44

[82] Kaplan, D. B., Savage, M. J., and Wise, M. B. (1998a). A New expansion for nucleon-nucleon interactions. *Phys. Lett.*, B424:390–396. 21, 45, 47

[83] Kaplan, D. B., Savage, M. J., and Wise, M. B. (1998b). A new expansion for nucleon-nucleon interactions. *Physics Letters B*, 424(3-4):390–396. 10, 13, 14

[84] Kaplan, D. B., Savage, M. J., and Wise, M. B. (1998c). Two-nucleon systems from effective field theory. *Nuclear Physics B*, 534(1-2):329–355. 10, 13, 14

[85] Kelley, J. H., Kwan, E., Purcell, J. E., Sheu, C. G., and Weller, H. R. (2012). Energy levels of light nuclei. *Nucl. Phys.*, A880:88–195. 27, 34, 38

[86] Kim, J., Dragos, J., Shindler, A., Luu, T., and de Vries, J. (2018). Towards a determination of the nucleon EDM from the quark chromo-EDM operator with the gradient flow. In *36th International Symposium on Lattice Field Theory (Lattice 2018) East Lansing, MI, United States, July 22-28, 2018*. 48

[87] Kobayashi, M. and Maskawa, T. (1973). CP Violation in the Renormalizable Theory of Weak Interaction. *Prog. Theor. Phys.*, 49:652–657. 43

[88] Kong, X. and Ravndal, F. (1999). Proton proton fusion in leading order of effective field theory. *Nucl. Phys.*, A656:421–429. 27, 32, 33, 140

[89] König, S., Grießhammer, H. W., and Hammer, H. (2015). The proton–deuteron system in pionless eft revisited. *Journal of Physics G: Nuclear and Particle Physics*, 42(4):045101. 67, 71, 74, 79

[90] König, S., Grießhammer, H. W., Hammer, H., and van Kolck, U. (2016). Effective theory of $^3$H and $^3$He. *J. Phys. G*, 43(5):055106. 65

[91] König, S., Grießhammer, H. W., Hammer, H. W., and van Kolck, U. (2017). Nuclear Physics Around the Unitarity Limit. *Phys. Rev. Lett.*, 118(20):202501. 45

[92] Kreuzer, S. and Hammer, H.-W. (2011). The Triton in a finite volume. *Phys. Lett. B*, 694:424–429. 65

[93] Liu, C.-P. and Timmermans, R. (2004). P- and T-odd two-nucleon interaction and the deuteron electric dipole moment. *Phys. Rev. C*, 70:055501. 63

[94] Luna, B. K. and Papenbrock, T. (2019). Low-energy bound states, resonances, and scattering of light ions. *Phys. Rev. C*, 100(5):054307. 38

[95] Maekawa, C., Mereghetti, E., de Vries, J., and van Kolck, U. (2011). The Time-Reversal- and Parity-Violating Nuclear Potential in Chiral Effective Theory. *Nucl. Phys. A*, 872:117–160. 44, 49

[96] Mereghetti, E. (2018). Electric dipole moments: a theory overview. In *13th Conference on the Intersections of Particle and Nuclear Physics*. 47

[97] Mereghetti, E., de Vries, J., Hockings, W., Maekawa, C., and van Kolck, U. (2011). The Electric Dipole Form Factor of the Nucleon in Chiral Perturbation Theory to Sub-leading Order. *Phys. Lett. B*, 696:97–102. 48

[98] Mereghetti, E., Hockings, W., and van Kolck, U. (2010). The Effective Chiral Lagrangian From the Theta Term. *Annals Phys.*, 325:2363–2409. 44

[99] Narison, S. (2008). A Fresh Look into the Neutron EDM and Magnetic Susceptibility. *Phys. Lett. B*, 666:455–461. 48

[100] National Nuclear Data Center, B. N. L. (2008). Nudat (nuclear structure and decay data). 16

[101] Nicholson, A., Berkowitz, E., Rinaldi, E., Vranas, P., Kurth, T., Joo, B., Strother, M., and Walker-Loud, A. (2016). Two-nucleon scattering in multiple partial waves. *PoS*, LATTICE2015:083. 45

[102] Nogga, A., Timmermans, R., and van Kolck, U. (2005). Renormalization of one-pion exchange and power counting. *Phys. Rev. C*, 72:054006. 44

[103] Okołowicz, J., Płoszajczak, M., and Nazarewicz, W. (2020). Convenient location of a near-threshold proton-emitting resonance in $^{11}$B. *Phys. Rev. Lett.*, 124(4):042502. 39

[104] Orlov, Y. F., Morse, W. M., and Semertzidis, Y. K. (2006). Resonance method of electric-dipole-moment measurements in storage rings. *Phys. Rev. Lett.*, 96:214802. 43

[105] Ottnad, K., Kubis, B., Meissner, U.-G., and Guo, F.-K. (2010). New insights into the neutron electric dipole moment. *Phys. Lett. B*, 687:42–47. 48

[106] Peskin, M. (2018). *An introduction to quantum field theory*. CRC press. 82

[107] Pfützner, M., Karny, M., Grigorenko, L., and Riisager, K. (2012). Radioactive decays at limits of nuclear stability. *Reviews of modern physics*, 84(2):567. 31

[108] Pfützner, M. and Riisager, K. (2018). Examining the possibility to observe neutron dark decay in nuclei. *Phys. Rev.*, C97(4):042501. 26

[109] Platter, L. (2009). Low-energy universality in atomic and nuclear physics. *Few-Body Systems*, 46(3):139–171. 4

[110] Platter, L., Hammer, H., and Meissner, U.-G. (2004). The Four boson system with short range interactions. *Phys. Rev. A*, 70:052101. 45

[111] Platter, L. and Hammer, H.-W. (2006). Universality in the triton charge form-factor. *Nucl. Phys. A*, 766:132–141. 58

[112] Polchinski, J. (1992). Effective field theory and the fermi surface. *arXiv preprint hep-th/9210046*. 4

[113] Pospelov, M. and Ritz, A. (1999). Theta induced electric dipole moment of the neutron via QCD sum rules. *Phys. Rev. Lett.*, 83:2526–2529. 48

[114] Pospelov, M. and Ritz, A. (2000). Theta vacua, QCD sum rules, and the neutron electric dipole moment. *Nucl. Phys. B*, 573:177–200. 48

[115] Pospelov, M. and Ritz, A. (2005). Electric dipole moments as probes of new physics. *Annals Phys.*, 318:119–169. 43, 48

[116] Premarathna, P. and Rupak, G. (2019). Bayesian analysis of capture reactions $^3$He$(\alpha,\gamma)^7$Be and $^3$H$(\alpha,\gamma)^7$Li. 26

[117] Pretz, J. (2013). Measurement of Permanent Electric Dipole Moments of Charged Hadrons in Storage Rings. *Hyperfine Interact.*, 214(1-3):111–117. 43

[118] Refsgaard, J., Büscher, J., Arokiaraj, A., Fynbo, H. O. U., Raabe, R., and Riisager, K. (2019). Clarification of large-strength transitions in the beta decay of 11Be. *Phys. Rev.*, C99(4):044316. 27

[119] Riisager, K. (2013). Halos and related structures. *Phys. Scripta*, T152:014001. 16

[120] Riisager, K. (2014). Beta decay to continuum states: the case of $^{11}$Be. *EPJ Web Conf.*, 66:02090. 26, 36

[121] Riisager, K. et al. (2014). $^{11}Be(\beta p)$, a quasi-free neutron decay? *Phys. Lett.*, B732:305–308. 26, 27, 36

[122] Riisager, K. et al. (2020). Search for beta-delayed proton emission from $^{11}$Be. 26, 38

[123] Rupak, G. and Higa, R. (2011). Model-Independent Calculation of Radiative Neutron Capture on Lithium-7. *Phys. Rev. Lett.*, 106:222501. 26

[124] Ryberg, E. (2016). *Cluster Effective Field Theory*. Chalmers University of Technology. 130

[125] Ryberg, E., Forssén, C., Hammer, H. W., and Platter, L. (2016). Range corrections in Proton Halo Nuclei. *Annals Phys.*, 367:13–32. 38

[126] Ryberg, E., Forssén, C., Hammer, H. W., and Platter, L. (2014a). Constraining Low-Energy Proton Capture on Beryllium-7 through Charge Radius Measurements. *Eur. Phys. J.*, A50:170. 26

[127] Ryberg, E., Forssén, C., Hammer, H. W., and Platter, L. (2014b). Effective field theory for proton halo nuclei. *Phys. Rev.*, C89(1):014325. 32

[128] Sachdeva, N. et al. (2019). New Limit on the Permanent Electric Dipole Moment of $^{129}$Xe using $^{3}$He Comagnetometry and SQUID Detection. *Phys. Rev. Lett.*, 123(14):143003. 43

[129] Sakharov, A. (1991). Violation of CP Invariance, C asymmetry, and baryon asymmetry of the universe. *Sov. Phys. Usp.*, 34(5):392–393. 2, 43

[130] Sakurai, J. J. and Commins, E. D. (1995). Modern quantum mechanics, revised edition. 9

[131] Savage, M. J., Shanahan, P. E., Tiburzi, B. C., Wagman, M. L., Winter, F., Beane, S. R., Chang, E., Davoudi, Z., Detmold, W., and Orginos, K. (2017). Proton-Proton Fusion and Tritium $\beta$ Decay from Lattice Quantum Chromodynamics. *Phys. Rev. Lett.*, 119(6):062002. 65

[132] Schiff, L. (1963). Measurability of Nuclear Electric Dipole Moments. *Phys. Rev.*, 132:2194–2200. 58

[133] Schmickler, C. H., Hammer, H. W., and Volosniev, A. G. (2019). Universal physics of bound states of a few charged particles. *Phys. Lett. B*, 798:135016. 38

[134] Schmidt, M., Platter, L., and Hammer, H. W. (2019). Neutron transfer reactions in halo effective field theory. *Phys. Rev.*, C99(5):054611. 41

[135] Schwartz, M. D. (2014). *Quantum field theory and the standard model*. Cambridge University Press. 4

[136] Seng, C.-Y. (2015). Reexamination of The Standard Model Nucleon Electric Dipole Moment. *Phys. Rev. C*, 91(2):025502. 43

[137] Seng, C.-Y., de Vries, J., Mereghetti, E., Patel, H. H., and Ramsey-Musolf, M. (2014). Nucleon electric dipole moments and the isovector parity- and time-reversal-odd pion–nucleon coupling. *Phys. Lett. B*, 736:147–153. 48

[138] Seng, C.-Y. and Ramsey-Musolf, M. (2017). Parity-violating and time-reversal-violating pion-nucleon couplings: Higher order chiral matching relations. *Phys. Rev. C*, 96(6):065204. 44

[139] Song, Y.-H., Lazauskas, R., and Gudkov, V. (2013). Nuclear electric dipole moment of three-body systems. *Physical Review C*, 87(1):015501. 44, 59, 63

[140] Stetcu, I., Liu, C.-P., Friar, J. L., Hayes, A., and Navratil, P. (2008). Nuclear Electric Dipole Moment of He-3. *Phys. Lett. B*, 665:168–172. 44, 63

[141] Syritsyn, S., Izubuchi, T., and Ohki, H. (2019). Calculation of Nucleon Electric Dipole Moments Induced by Quark Chromo-Electric Dipole Moments and the QCD $\theta$-term. In *13th Conference on Quark Confinement and the Hadron Spectrum (Confinement XIII) Maynooth, Ireland, July 31-August 6, 2018*. 48

[142] 't Hooft, G. (1976a). Computation of the Quantum Effects Due to a Four-Dimensional Pseudoparticle. *Phys. Rev. D*, 14:3432–3450. [Erratum: Phys.Rev.D 18, 2199 (1978)]. 43

[143] 't Hooft, G. (1976b). Symmetry Breaking Through Bell-Jackiw Anomalies. *Phys. Rev. Lett.*, 37:8–11. 43

[144] Talman, R. (2018). A doubly-magic storage ring EDM measurement method. 43

[145] Tanabashi, M. et al. (2018). Review of particle physics. *Phys. Rev. D*, 98:030001. 29

[146] Tanihata, I. (2016). Nuclear Physics with RIB's: How it all started. *Eur. Phys. J. Plus*, 131(4):90. 16

[147] Tanihata, I., Hamagaki, H., Hashimoto, O., Shida, Y., Yoshikawa, N., Sugimoto, K., Yamakawa, O., Kobayashi, T., and Takahashi, N. (1985). Measurements of interaction cross sections and nuclear radii in the light p-shell region. *Physical Review Letters*, 55(24):2676. 16

[148] Tanihata, I., Savajols, H., and Kanungo, R. (2013). Recent experimental progress in nuclear halo structure studies. *Progress in Particle and Nuclear Physics*, 68:215–313. xiii, 17

[149] Vanasse, J. (2017a). Triton charge radius to next-to-next-to-leading order in pionless effective field theory. *Phys. Rev. C*, 95(2):024002. 46, 47, 49, 55, 58, 59, 69, 71, 79, 151, 155

[150] Vanasse, J. (2017b). Triton charge radius to next-to-next-to-leading order in pionless effective field theory. *Physical Review C*, 95(2). 79

[151] Vanasse, J. (2018). Charge and Magnetic Properties of Three-Nucleon Systems in Pionless Effective Field Theory. *Phys. Rev. C*, 98(3):034003. 46, 49, 55, 58, 59

[152] Vanasse, J. (2019). Parity-violating three-nucleon interactions at low energies and large $N_C$. *Phys. Rev. C*, 99(5):054001. 65

[153] Vanasse, J. and David, A. (2019). Time-Reversal-Invariance Violation in the *Nd* System and Large-$N_C$. 49

[154] Vanasse, J., Egolf, D. A., Kerin, J., König, S., and Springer, R. P. (2014). $^3$He and *pd* Scattering to Next-to-Leading Order in Pionless Effective Field Theory. *Phys. Rev. C*, 89(6):064003. 67, 79

[155] Vanasse, J. and Phillips, D. R. (2017). Three-nucleon bound states and the Wigner-SU(4) limit. *Few Body Syst.*, 58(2):26. 53

[156] Weinberg, S. (1990). Nuclear forces from chiral lagrangians. *Physics Letters,(Section) B;(Netherlands)*, 251(2). 5

[157] Weinberg, S. (1991). Effective chiral lagrangians for nucleon-pion interactions and nuclear forces. *Nuclear Physics B*, 363(1):3–18. 5

[158] Weinberg, S. (1995). *The quantum theory of fields*, volume 2. Cambridge university press. 4, 12

[159] Wietfeldt, F. E. and Greene, G. L. (2011). Colloquium: The neutron lifetime. *Reviews of Modern Physics*, 83(4):1173. 1

[160] Wigner, E. (1937). On the consequences of the symmetry of the nuclear hamiltonian on the spectroscopy of nuclei. *Phys. Rev.*, 51:106–119. 53

[161] Yamanaka, N. (2017). Review of the electric dipole moment of light nuclei. *Int. J. Mod. Phys. E*, 26(4):1730002. 44

[162] Yamanaka, N. and Hiyama, E. (2015). Enhancement of the CP-odd effect in the nuclear electric dipole moment of $^6$Li. *Phys. Rev. C*, 91(5):054005. 44

[163] Yamanaka, N. and Hiyama, E. (2016). Standard model contribution to the electric dipole moment of the deuteron,$^3$H, and$^3$He nuclei. *JHEP*, 02:067. 43, 44

[164] Yamanaka, N. and Hiyama, E. (2017). Electric dipole moment of the deuteron in the standard model with NN $-$ $\Lambda$ N $-$ $\Sigma$ N coupling. *Nucl. Phys. A*, 963:33–51. 43

[165] Yang, Z., Mereghetti, E., Platter, L., Schindler, M. R., and Vanasse, J. (2020). Electric dipole moments of three-nucleon systems in the pionless effective field theory. *arXiv preprint arXiv:2011.01885*. 42

[166] Zhang, X., Nollett, K. M., and Phillips, D. R. (2015). Halo effective field theory constrains the solar $^7\mathrm{Be} + \mathrm{p} \to {}^8\mathrm{B} + \gamma$ rate. *Phys. Lett.*, B751:535–540. 26

[167] Zhang, X., Nollett, K. M., and Phillips, D. R. (2019). $S$-factor and scattering-parameter extractions from $^3\mathrm{He} + {}^4\mathrm{He} \to {}^7\mathrm{Be} + \gamma$. 26

# Appendices

# A Special Functions

Most of the special functions involved in this dissertation are related to the Coulomb related problems. For more information, David Gaspard's paper is a good reference about the regular and irregular Coulomb functions [51]. Emil Ryberg also has valuable discussions about the Coulomb wave functions [124].

## A.1 Coulomb wave function

The Coulomb wave function is a solution of the Coulomb wave equation. They are used to describe the behavior of charged particles in a Coulomb potential. It is a special case of the confluent hypergeometric function of the first kind.

The partial wave expansion of the Coulomb wavefunction in the coordinate space is given by

$$\psi^C_{\mathbf{p}}(\mathbf{r}) = \frac{1}{\rho}\sum_{\ell=0}^{\infty}(2\ell+1)i^\ell \mathrm{e}^{i\sigma_\ell} F_\ell(\eta,\rho)P_\ell(\hat{\mathbf{p}}\cdot\hat{\mathbf{r}}) \ . \tag{A.1}$$

Here, we define that $\rho = pr$, and $\eta = k_C/p$, where the Coulomb momentum is defined by $k_C = Z_1 Z_2 \alpha M_R$. The $\alpha$ is the fine structure constant. The $\sigma_l = \arg\Gamma(\ell+1+i\eta)$. The $Z_1$ and $Z_2$ are the charge numbers of the relative point-like particles. For example, the hydrogen atom would expect an overall $Z_1 Z_2 = -1$. The nucleus of $^{11}$B, with a tightly bound $^{10}$Be core and a halo proton, would expect a $Z_1 Z_2 = 4$. $F_\ell(\eta,\rho)$ is the Coulomb function of the first kind discussed in Sec. A.2.

Note that,

$$\sigma_\ell = \arg\Gamma(\ell+1+i\eta) = \sqrt{\frac{\Gamma(\ell+1+i\eta)}{\Gamma(\ell+1-i\eta)}} \ . \tag{A.2}$$

For convenience, here we provide s- and p-wave Coulomb wave functions,

$$\psi^C_{\mathbf{p},0}(\mathbf{r}) = C_\eta e^{i\sigma_0} e^{-i\rho} M(1-i\eta, 2, 2i\rho) \ , \tag{A.3}$$

$$\psi^C_{\mathbf{p},1}(\mathbf{r}) = i\rho C_\eta(1) e^{i\sigma_1} e^{-i\rho} M(2-i\eta, 4, 2i\rho) P_1(\hat{\mathbf{p}}\cdot\hat{\mathbf{r}}) \ . \tag{A.4}$$

The Gamow-Sommerfeld factors are defined in Sec. A.8.

## A.2 The Coulomb function of the first kind

The Coulomb function of the first kind, also known as the regular Coulomb function, $F_\ell(\eta,\rho)$, is given by,

$$F_\ell(\eta,\rho) = A_\ell(\eta) M_{i\eta,l+1/2}(2i\rho) \ , \tag{A.5}$$

where $M_{i\eta,l+1/2}(2i\rho)$ is the Whittaker-M function defined in Eq. (A.18). The $A_\ell(\eta)$ is defined by,

$$A_\ell(\eta) = \frac{|\Gamma(\ell+1+i\eta)|}{2\Gamma(2\ell+2)} \mathrm{e}^{-\pi\eta/2-i(\ell+1)\pi/2}. \tag{A.6}$$

Note that,

$$|\Gamma(\ell+1+i\eta)| = \sqrt{\Gamma(\ell+1+i\eta)\Gamma(\ell+1-i\eta)} \tag{A.7}$$

Define the Gamow-Sommerfeld factor $C_\eta = \mathrm{e}^{-\pi\eta/2}|\Gamma(1+i\eta)|$, we have,

$$C_\eta^2 = \frac{2\pi\eta}{\mathrm{e}^{2\pi\eta}-1} \ , \tag{A.8}$$

which is proved in Sec. A.8

$F_\ell(\eta,\rho)$ is sometimes also defined in the following form,

$$F_\ell(\eta,\rho) = C_\ell(\eta)\rho^{\ell+1}\mathrm{e}^{\pm i\rho} M(\ell+1\pm i\eta, 2\ell+2, \mp 2\mathrm{i}\rho) \ . \tag{A.9}$$

The choice of signs is immaterial. In the paper, we will go with

$$F_\ell(\eta,\rho) = C_\ell(\eta)\rho^{\ell+1}\mathrm{e}^{-i\rho} M(\ell+1-i\eta, 2\ell+2, 2\mathrm{i}\rho) \ ,$$

for consistency.

$C_\ell(\eta)$ is the normalization coefficient, defined as,

$$C_\ell(\eta) = \frac{|\Gamma(\ell+1+i\eta)|}{\Gamma(2\ell+2)} 2^\ell \mathrm{e}^{-\pi\eta/2} \ . \tag{A.10}$$

One can easily show that these two expressions of $F_\ell(\eta,\rho)$ are equivalent.

## A.3 The Coulomb function of the second kind

The Coulomb function of the second kind, also known as the irregular Coulomb wave function, $G_l(\eta,\rho)$, is given by

$$G_l(\eta,\rho) = iF_l(\eta,\rho) + B_l(\eta) W_{i\eta,\ell+1/2}(2i\rho) \ , \tag{A.11}$$

where $W_{i\eta,\ell+1/2}(2i\rho)$ is the Whittaker-W function defined in Eq. A.18 and the coefficient $B_l$ is defined as,

$$B_\ell(\eta) = \frac{\mathrm{e}^{\pi\eta/2+i\ell\pi/2}}{\arg\Gamma(\ell+1+i\eta)} \ . \tag{A.12}$$

## A.4 Partial-wave projected Coulomb Green's function

The full Coulomb propagator, $G_C(E)$, is defined recursively. The Coulomb Green's function, in the coordinate space (using round brackets), can be expressed by the Coulomb wave function, as

$$G_C(E;\mathbf{r},\mathbf{r}') = (\mathbf{r}|G_C(E)|\mathbf{r}') = \int \frac{d^3p}{(2\pi)^3} \frac{\psi^C_{\mathbf{p}}(\mathbf{r})\psi^{C*}_{\mathbf{p}}(\mathbf{r}')}{E - \mathbf{p}^2/2M_R + i\epsilon} \ . \tag{A.13}$$

In the momentum space (using angle brackets), the Coulomb Green's function is defined as

$$G_C(E;\mathbf{k},\mathbf{k}') = \langle\mathbf{k}|G_C(E)|\mathbf{k}'\rangle \ . \tag{A.14}$$

The partial wave expanded Coulomb Green's function is

$$(\mathbf{r}_1|G_C(E)|\mathbf{r}_2) = \sum_{\ell=0}^{\infty}(2\ell+1)G_C^{(\ell)}(E;r_1,r_2)P_\ell(\hat{\mathbf{r}}_1\cdot\hat{\mathbf{r}}_2) \ . \tag{A.15}$$

The Green's function for a specific partial wave is given by

$$G_C^{(\ell)}(E; r_1, r_2) = \int \frac{d^3p}{(2\pi^3)} \frac{F_\ell(\eta, \rho_1) F_\ell^*(\eta, \rho_2)}{\rho_1 \rho_2} \frac{1}{E - \frac{\mathbf{p}^2}{2M_R}} \ . \tag{A.16}$$

For the bound-state partial wave Coulomb Green's function, it is possible to have a non-integral from. The calculation take advantages of the independence of Coulomb function of the first and the second kind. The boundary conditions at $r = 0$ and $r \to \infty$ are considered. Since we don't actually use too many details in our paper, here we will just provide expression of a special case at $\ell = 0$, $\rho' \to 0$,

$$G_C^{(0)}(-B; 0, \rho) = -\frac{M_R p}{2\pi} \Gamma(1 + i\eta) \frac{W_{-i\eta, 1/2}(-2i\rho)}{\rho} \ . \tag{A.17}$$

## A.5 Whittaker function

A Whittaker function is a special solution of the Whittaker's equation. Two solutions are given by the Whittaker-M function and the Whittaker-W function by

$$\begin{aligned} M_{\kappa,\mu}(z) &= \mathrm{e}^{-z/2} z^{\mu+\frac{1}{2}} M\left(\mu - \kappa + \tfrac{1}{2}, 1 + 2\mu, z\right) \ , \\ W_{\kappa,\mu}(z) &= \mathrm{e}^{-z/2} z^{\mu+\frac{1}{2}} U\left(\mu - \kappa + \tfrac{1}{2}, 1 + 2\mu, z\right) \ . \end{aligned} \tag{A.18}$$

The Kummer function, $M(a, b, z)$, is defined in Eq. (A.21). The Tricomi function, $U(a, b, z)$, is defined in Eq. (A.23).

For future convenience, a particular Whittaker-M function is given,

$$M_{i\eta, \ell+1/2}(2i\rho) = \mathrm{e}^{-i\rho} (2i\rho)^{\ell+1} M(\ell + 1 - i\eta, 2\ell + 2, 2i\rho) \ , \tag{A.19}$$

and a particular Whittaker-W function is given,

$$W_{-i\eta, \ell+1/2}(-2i\rho) = \mathrm{e}^{i\rho} (-2i\rho)^{\ell+1} U(\ell + 1 + i\eta, 2\ell + 2, -2i\rho) \ . \tag{A.20}$$

## A.6 Kummer functions

Kummer's function $M(a, b, z)$ is also known as the confluent hypergeometric function of the first kind.

It is defined as follows,

$$M(a, b, z) =_1 F_1(a; b; z) = \sum_{n=0}^{\infty} \frac{a^{(n)} z^n}{b^{(n)} n!} \ . \tag{A.21}$$

where

$$\begin{aligned} a^{(0)} &= 1 \ , \\ a^{(n)} &= a(a+1)(a+2)\cdots(a+n-1) \ , \end{aligned} \tag{A.22}$$

is the rising factorial. $a^{(n)}$ is sometimes written as $(a)_n = \Gamma(a+n)/\Gamma(a)$, which is called the Pochhammer symbol.

## A.7 Tricomi function

The Tricomi function, $U(\alpha, \beta, z)$, which is also known as the confluent hypergeometric function of the second kind, is given by

$$U(\alpha, \beta, z) = \frac{\Gamma(1-\beta)}{\Gamma(\alpha-\beta+1)} M(\alpha, \beta, z) + \frac{\Gamma(\beta-1)}{\Gamma(\alpha)} z^{1-\beta} M(\alpha-\beta+1, 2-\beta, z) \ . \tag{A.23}$$

The $M(a, b, z)$ is known as the Kummer function.

## A.8 Gamow-Sommerfeld factor

The Gamow-Sommerfeld factor is used in both halo-EFT and EDM projects, defined by,

$$C_\eta = \mathrm{e}^{-\pi\eta/2} |\Gamma(1 - i\eta)| \ .$$

The squared value is then,

$$C_\eta^2 = \mathrm{e}^{-\pi\eta} |\Gamma(1 - i\eta)|^2 = \mathrm{e}^{-\pi\eta} \Gamma(1 + i\eta)\Gamma(1 - i\eta) \ .$$

The $\Gamma(1+i\eta)\Gamma(1-i\eta)$ is evaluated as follows,

$$\begin{aligned}\Gamma(1+i\eta)\Gamma(1-i\eta) &= \int_0^\infty s^{i\eta}\mathrm{e}^{-s}ds\int_0^\infty t^{-i\eta}\mathrm{e}^{-t}dt \\ &= \int_0^\infty \frac{v^{i\eta}}{(v+1)^2}dv\underbrace{\int_0^\infty u\mathrm{e}^{-u}du}_{=1} \\ &= \frac{\pi\eta}{\sinh\pi\eta}\ ,\end{aligned}$$

where $u = s+t, v = s/t$.

Thus we get that,

$$C_\eta^2 = \frac{2\pi\eta}{\mathrm{e}^{2\pi\eta}-1}\ . \tag{A.24}$$

Note that, this is in particular for the s-wave. To generalize it to higher partial wave, we define,

$$C_\eta(\ell) = \mathrm{e}^{-\pi\eta/2}|\Gamma(\ell+1+i\eta)|\ . \tag{A.25}$$

For convenience, we also write down the expression for $|\Gamma(2+i\eta)|$,

$$\begin{aligned}|\Gamma(2+i\eta)| &= \sqrt{\Gamma(2+i\eta)\Gamma(2-i\eta)} = \sqrt{(1+i\eta)(1-i\eta)}\sqrt{\Gamma(1+i\eta)\Gamma(1-i\eta)} \\ &= \sqrt{1+\eta^2}|\Gamma(1+i\eta)| = \left((1+\eta^2)\frac{\pi\eta}{\sinh\pi\eta}\right)^{\frac{1}{2}}\ .\end{aligned} \tag{A.26}$$

# B Hadronic Amplitudes for Gamow-Teller and Fermi Transitions

Below we will discuss the calculations for the hadronic matrix elements for $S$- and $P$-wave halo nuclei. The weak vertex factors are moved into the leptonic part. In all calculations, we have ignored the recoil effects. This is treated the same as textbooks. Let us firstly look at the energy conservation with recoil effects and we are able to see it is truly negligible. Then we take the simple energy conservation relation without recoil effects in our calculations. Next, we give details of hadronic currents of S-wave with and without final state interactions. P-wave amplitude without a final state interaction is given as well.

## B.1 Energy conservation (with recoil)

The energy conservation relation in our system is simply

$$E_0 = \Delta m - S_n = T_{kc} + T_{kp} + E_e + E_{\nu e} \ , \tag{B.1}$$

where $S_n$ is the one neutron separation energy. $\Delta m = m_n - m_p \simeq 1.29$ MeV is the mass difference between neutron and proton. $T_{kc}$ and $T_{kp}$ are the non-relativistic kinetic energies of the core and proton. $E_e$ and $E_{\nu e}$ are the energies of the electron and neutrino. The mass of neutrino is negligible is our case.

Considering the recoil effect, we arrive at an equation of $E_{\nu e}$,

$$E_0 = \frac{p^2}{2m_R} + \frac{1}{2m_A}(p_e^2 + E_{\nu_e}^2 - 2p_e E_{\nu e}\cos\theta_{\nu_e}) + \sqrt{p_e^2 + m_e^2} + E_{\nu_e} \ , \tag{B.2}$$

where $m_R$ is reduced mass. $m_A$ is the total mass of proton and core. The $\cos\theta$ is the cosine between outgoing electron and neutrino. The equation above is a quadratic equation about $E_{\nu e}$,

$$(\frac{1}{2m_A})E_{\nu_e}^2 + (1 - \frac{p_e}{m_A}cos\theta_{\nu_e})E_{\nu_e} + (-E_0 + \frac{p^2}{2m_R} + \sqrt{p_e^2 + m_e^2} + \frac{p_e^2}{2m_A}) = 0 \ .$$

We could solve the $E_{\nu_e}$ easily, given that

$$E_{\nu_e} = \frac{-b + \sqrt{b^2 - 4ac}}{2a} \ , \tag{B.3}$$

$$a = \frac{1}{2m_A} \ , \tag{B.4}$$

$$b = (1 - \frac{p_e}{m_A} cos\theta_{\nu_e}) \ , \tag{B.5}$$

$$c = (-E_0 + \frac{p^2}{2m_R} + \sqrt{p_e^2 + m_e^2} + \frac{p_e^2}{2m_A}) \ . \tag{B.6}$$

By using the notation above, we could express the S-wave decay rate without final state interactions with the recoil effects,

$$\Gamma_l = \frac{G_F^2 m_A^2 (1 + 3g_A^2)}{8\pi^5} \int dp \int dp_e p^2 p_e^2 F_e(\eta, E) \Big\{ (4 + \frac{4p_e^2}{3m_A^2}) \\ - \frac{4}{m_A} c + \frac{2m_A}{3p_e} \Big[ [(1 - \frac{p_e}{m_A})^2 - \frac{2c}{m_A}]^{\frac{3}{2}} - [(1 + \frac{p_e}{m_A})^2 - \frac{2c}{m_A}]^{\frac{3}{2}} \Big] \Big\} |\mathcal{A}_l|^2 \ . \tag{B.7}$$

One can numerically implement this expression and find that it basically has no difference from the case with no recoil effects. So we are correct to make the assumption of ignoring recoil effect. Thus, we are allowed to use the energy conservation below.

## B.2 Energy Conservation (without recoil)

Start from $E_0 = \Delta m - S_n = T_{kc} + T_{kp} + E_e + E_{\nu e}$ , if we ignore recoil terms we have,

$$E_0 = \frac{p^2}{2m_R} + \sqrt{p_e^2 + m_e^2} + E_{\nu e} \ . \tag{B.8}$$

This is what we used in the main body.

## B.3 Hadronic current without resonant final state interactions in S-wave

Here we give the amplitude in diagram $(a)$ of Fig. 3.1, which describes the most simple process in halo beta decay. The two body dressed propagator, which stands for the two

body halo system bound state, firstly breaks up into two parts due to the weak decay. Then the proton and core are scattered by Coulomb interaction. The initial state and the final state are,

$$\text{initial state: } |\psi_d\rangle \text{ dressed dimer field ,}$$
$$\text{final state: } |\psi_c\rangle \text{ two-body Coulomb state .}$$

The total amplitude shown in the diagram above is simply given by,

$$\mathcal{A}_C^{(a)}(\mathbf{p}) = \langle\psi_c|\psi_d\rangle = \int \frac{d^3\mathbf{p}}{(2\pi)^3}\langle\psi_c|\mathbf{p}\rangle\langle\mathbf{p}|\psi_d\rangle \tag{B.9}$$

where

$$\langle\mathbf{p}|\psi_d\rangle = \psi_d(\mathbf{p}) = \frac{2m_R\sqrt{Z}g}{\mathbf{p^2}+\gamma_0^2} \ , \tag{B.10}$$

is the wave function of the dimeron. Note that we have ignored $-i$ here in the appendix. $Z$ is the renormalization factor. $\gamma_0$ is related to the one neutron separation energy by $\gamma_0 = \sqrt{2\pi S_n}$. Another piece is the well-known Coulomb wave function in the momentum space, given by

$$\langle\psi_c|\mathbf{p}\rangle = \psi_c^*(\mathbf{p}) = \int \frac{d^3\mathbf{r}}{(2\pi)^3}\langle\psi_c|\mathbf{r}\rangle\langle\mathbf{r}|\mathbf{p}\rangle = \int \frac{d^3\mathbf{r}}{(2\pi)^3}e^{-i\mathbf{p}\cdot\mathbf{r}}\psi_c^*(\mathbf{r}) \ . \tag{B.11}$$

The subscript $c$ indicates that this is a Coulomb wave function. Put everything together, we have

$$\mathcal{A}_C^{(a)}(\mathbf{p}) = \sqrt{Z}g\int \frac{d^3\mathbf{k}}{(2\pi)^3}\frac{2m_R}{\mathbf{k}^2+\gamma_0^2}\psi_c^*(\mathbf{k}) \ . \tag{B.12}$$

Here we consider only the S-wave Coulomb wave function, which is well known. One can easily get higher order results with similar calculations. Thus, in S-wave, we have the

following expressions,

$$\mathcal{A}_C^{(a)}(\mathbf{p}) = \sqrt{Z} g C(\eta_p) \frac{2m_R}{\mathbf{p}^2 + \gamma_0^2} e^{2\eta_p \arctan(|\mathbf{p}|/\gamma_0)} \ , \tag{B.13}$$

$$|\mathcal{A}_C^{(a)}(\mathbf{p})|^2 = Z g^2 C(\eta_p)^2(p) \left( \frac{2m_R}{\mathbf{p}^2 + \gamma_0^2} \right)^2 e^{4\eta_p \arctan(|\mathbf{p}|/\gamma_0)} \ . \tag{B.14}$$

The Sommerfeld factor is defined previously. $\eta_p$ is the Sommerfeld parameter, which is defined as $\eta_p = \alpha Z_p Z_c m_R/|\mathbf{p}| = k_C/|\mathbf{p}|$, with $Z_p = 1$ and $Z_c = 4$.

## B.4 Hadronic current without resonant final state interactions in P-wave

Here we provide P-wave calculation as well. $^{31}$Ne is an ideal system for a P-wave calculation. The following results would be useful in the future with more experimental progresses. Note that all P-wave related notations only apply to this P-wave subsection. Notations elsewhere are in S-wave by default.

The $P$-wave contribution is given as

$$\mathcal{A}_{C1m}^{(a)}(\mathbf{p}) = \sqrt{Z_\pi} g_1 \int \frac{d^3k}{(2\pi)^3} \frac{k_m}{(\boldsymbol{k}^2 + \gamma_0^2)/(2m_R)} \psi_{c1}(\boldsymbol{k}, \theta_{kr}) \ , \tag{B.15}$$

where $g1$ and $Z_\pi$ are defined in Sec. 2.4. $\psi_{c1}(\boldsymbol{k}, \theta_{kr})$ is the Fourier transformed P-wave Coulomb wave function, which is given as follows,

$$\psi_{c1}(\boldsymbol{k}, \theta_{kr}) = \int \frac{d^3r}{(2\pi)^3} \mathrm{e}^{-i\vec{k}\cdot\vec{r}} \tilde{\psi}_{c1}(E; \boldsymbol{r}, \theta_{kr}) \ , \tag{B.16}$$

where $\rho = kr$. Thus, the P-wave Coulomb amplitude can be expressed by

$$\mathcal{A}_{C1m}^{(a)}(\mathbf{p}) = 2m_R g_1 \sqrt{Z_\pi} \int \frac{d^3k}{(2\pi)^3} \frac{k_m}{(\boldsymbol{k}^2 + \gamma_0^2)} \int \frac{d^3r}{(2\pi)^3} \mathrm{e}^{-i\vec{k}\cdot\vec{r}} \tilde{\psi}_{c1}(E; \boldsymbol{r}, \theta_{kr}) \ . \tag{B.17}$$

Using the expression of the $P$-wave Coulomb function in coordinate space given in the Appendix A.1 and integrate over $k$, we get

$$\mathcal{A}^{(a)}_{C1m}(\mathbf{p}) = -\frac{im_R}{4\pi^2}\int dr\phi_1(\rho)\mathrm{e}^{-\gamma_0 r}(1+\gamma_0 r)\frac{1}{3\pi}\sqrt{\frac{4\pi}{3}}\mathcal{Y}_{1m}(\hat{p}) \ , \tag{B.18}$$

where $\phi_1(\rho) = \rho\, C_{\eta_p}(1)e^{i\sigma_1}e^{-i\rho}M(2-i\eta_p, 4, 2i\rho)$ as in Appendix A.1. Solving the coordinate space integrals leads to

$$\begin{aligned}\mathcal{A}^{(a)}_{C1m}(\mathbf{p}) = \sqrt{Z_\pi}\frac{im_R g_1}{4\pi^2}\sqrt{1+\eta_p^2}C_{\eta_p}\mathrm{e}^{i\sigma_1} \\ \times\frac{1}{3\pi}\sqrt{\frac{4\pi}{3}}\mathcal{Y}_{1m}(\hat{p})\frac{p}{\boldsymbol{p}^2+\gamma_0^2}\Bigg( {}_2F_1(2-i\eta_p,4;2;\frac{2ip}{ip+\gamma_0})+ \\ \frac{2\gamma_0}{ip+\gamma_0}\ {}_2F_1(2-i\eta_p,4;3;\frac{2ip}{ip+\gamma_0})\Bigg) \ ,\end{aligned} \tag{B.19}$$

where, ${}_2F_1(a,b;c;z)$ is the famous Gauss hypergeometric function, given by,

$${}_2F_1(a,b;c;z) = \sum_{n=0}^{\infty}\frac{(a)_n(b)_n}{(c)_n}\frac{z^n}{n!} = 1+\frac{ab}{c}\frac{z}{1!}+\frac{a(a+1)b(b+1)}{c(c+1)}\frac{z^2}{2!}+\cdots \ . \tag{B.20}$$

## B.5 $S$-wave halo nuclei with final state interaction

We also consider resonance and large negative scattering length as final state interaction. In each case, we need to sum over infinite possible re-scattering diagrams to get the total amplitude. The calculation of such T-matrices was previously considered in Refs. [71, 88].

To include the final state interaction, we introduce a final state interaction Lagrangian here,

$$\begin{aligned}\mathcal{L}_{fsi} = p^\dagger\left(i\partial_t+\frac{\nabla^2}{2m_p}\right)p \ +\chi_s^\dagger\left[\eta_0'\left(i\partial_t+\frac{\nabla^2}{2M_{pc}}\right)+\Delta_0'\right]\chi_s \\ -g_0'\left[c^\dagger p^\dagger\chi_s+\mathrm{H.c.}\right] \ .\end{aligned} \tag{B.21}$$

where $c$, $p$ and $\chi$ are core, proton and $^{11}$B dimeron field, respectively. The free core Lagrangian is as in Eq. (3.2.1). The notations are the same as in Appendix B.3. Fig. 7 expresses the first Coulomb re-scattering process. Again, like in the case without final state interaction, we define the initial and final state as,

$$\text{initial state: } |\psi_d\rangle \text{ dressed dimer field ,}$$
$$\text{final state: } |\psi_c\rangle \text{ two-body Coulomb state .}$$

The Coulomb bubble in the middle is evaluated by the Coulomb propagator,

$$\text{Coulomb Propagator: } \hat{G_C}(E) = 2m_R \int \frac{d^3\mathbf{q}}{(2\pi)^3} \frac{|\psi_c\rangle \langle\psi_c|}{\mathbf{p}^2 - \mathbf{q}^2 + i\varepsilon} \ , \tag{B.22}$$

$$G_C\left(E;\mathbf{k},\mathbf{k}'\right) = \langle\mathbf{k}'|\hat{G_C}(E)|\mathbf{k}\rangle = 2m_R \int \frac{d^3\mathbf{q}}{(2\pi)^3} \frac{\psi_c^*(\mathbf{k}')\psi_c(\mathbf{k})}{\mathbf{p}^2 - \mathbf{q}^2 + i\varepsilon} \ . \tag{B.23}$$

The amplitude of this diagram is given by

$$B_0(\mathbf{p}) = \langle\psi_c|\hat{V}_s\hat{G}_C(E)|\psi_d\rangle \ , \tag{B.24}$$

$$= \int \frac{d^3\mathbf{k}_1}{(2\pi)^3} \int \frac{d^3\mathbf{k}_2}{(2\pi)^3} \int \frac{d^3\mathbf{k}}{(2\pi)^3} \langle\psi_c|\mathbf{k}\rangle\langle\mathbf{k}|\hat{V}_s|\mathbf{k}_2\rangle\langle\mathbf{k}_2|\hat{G_C}|\mathbf{k}_1\rangle\langle\mathbf{k}_1|\psi_d\rangle \ , \tag{B.25}$$

$\langle\mathbf{k}_2\left|\hat{G_c}\right|\mathbf{k}_1\rangle = G_C\left(E;\mathbf{k}_2,\mathbf{k}_1\right)$, which is defined above. $\langle\mathbf{p}'\left|V_S\right|\mathbf{p}\rangle$ is the local potential, denoted as $\langle V_s\rangle$, defined as follows,

$$\langle\boldsymbol{k}|\hat{V}_S|\boldsymbol{k}_2\rangle = g_0'^2 D_d(E;\mathbf{0}) = \frac{g_0'^2}{\eta_0' E + \Delta_0' + i\epsilon}. \tag{B.26}$$

Notice we could perform a Fourier transform on $\psi_c(\mathbf{k})$ like follows,

$$\tilde{\psi}_c(E;\mathbf{r}=0) = \int \frac{d^3\mathbf{k}}{(2\pi)^3}\psi_c(\mathbf{k}) = C(\eta_k)\mathrm{e}^{i\sigma_0} \ . \tag{B.27}$$

$\tilde{\psi}_c(E;\mathbf{r}=0)$ is S-wave Coulomb wave function with zero separation in coordinate space. Notice that this $E$ is dependent on $\mathbf{p}$ and is able to take out of the integrand. Put those

above back to the amplitude and get,

$$B_0(\mathbf{p}) = \langle V_s \rangle \tilde{\psi}_c(E; \mathbf{r}=0) \int \frac{d^3\mathbf{k}_1}{(2\pi)^3} \int \frac{d^3\mathbf{k}_2}{(2\pi)^3} \left( 2m_R \int \frac{d^3\mathbf{q}}{(2\pi)^3} \frac{\psi_c^*(\mathbf{k}_2)\psi_c(\mathbf{k}_1)}{\mathbf{p}^2 - \mathbf{q}^2 + i\epsilon} \right) \psi_d(\mathbf{k}_1) \quad \text{(B.28)}$$

Do another Fourier transform on the $\mathbf{k}_2$ piece,

$$\int \frac{d^3\mathbf{k}_2}{(2\pi)^3} \psi_c^*(\mathbf{k}_2) = \tilde{\psi}_c^*(E_q; \mathbf{r}=0) \ , \quad \text{(B.29)}$$

where $E_q$ denotes that the energy is $\mathbf{q}$-dependent. The amplitude is simplified to,

$$\begin{aligned} B_0(\mathbf{p}) &= \langle V_s \rangle \tilde{\psi}_c(E; \mathbf{r}=0) 2m_R \int \frac{d^3\mathbf{k}_1}{(2\pi)^3} \int \frac{d^3\mathbf{q}}{(2\pi)^3} \tilde{\psi}_c^*(E_q; \mathbf{r}=0) \frac{\psi_c(\mathbf{k}_1)}{\mathbf{p}^2 - \mathbf{q}^2 + i\epsilon} \psi_d(\mathbf{k}_1) \ , \\ &= \langle V_s \rangle \tilde{\psi}_c(E; \mathbf{r}=0) 2m_R \int \frac{d^3\mathbf{q}}{(2\pi)^3} \frac{\tilde{\psi}_c^*(E_q; \mathbf{r}=0)}{\mathbf{p}^2 - \mathbf{q}^2 + i\epsilon} \left\{ \int \frac{d^3\mathbf{k}_1}{(2\pi)^3} \psi_c(\mathbf{k}_1)\psi_d(\mathbf{k}_1) \right\} \ . \end{aligned} \quad \text{(B.30)}$$

Content inside the braces is simply $\mathcal{A}_C^{(a)}(\mathbf{p})$, which is the S-wave without final state interaction we had previously.

Thus, we could express our expression as follows,

$$B_0(\mathbf{p}) = \langle V_s \rangle C(\eta_p) \mathrm{e}^{i\sigma_0} (2m_R)^2 \sqrt{Z} g \ \mathcal{I} \ , \quad \text{(B.31)}$$

where, $\langle V_s \rangle$ is defined as in Eq. (B.26) and

$$\mathcal{I} = \int \frac{d^3\mathbf{q}}{(2\pi)^3} \frac{C^2(\eta_q) \mathrm{e}^{2\eta_q \arctan(|\mathbf{q}|/\gamma_0)}}{\mathbf{q}^2 + \gamma_0^2} \frac{1}{\mathbf{p}^2 - \mathbf{q}^2 + i\epsilon} \ , \quad \text{(B.32)}$$

is a convergent integral, which gives a complex result. The convergence of the integral can by easily proved by evaluating the integrand at $q \to \infty$. The real part of $\mathcal{I}$ is the principal value, and the complex part is evaluated near the pole on the positive real axis by

$$\mathrm{Im}[\mathcal{I}] = \frac{p}{4\pi(p^2 + \gamma_0^2)} C_\eta^2(p) \mathrm{e}^{2\eta \arctan(p/\gamma_0)} \ . \quad \text{(B.33)}$$

All the following possible re-scattering diagrams together with $B_0(\mathbf{p})$ form a geometry series. $n$th order is denoted as $B_n(\mathbf{p})$, means $n+1$ times re-scattering process. Those

processes could be simply calculated by adding Coulomb bubbles and dimer propagators based on $B_0(\mathbf{p})$. The dimer propagator is defined before, and the Coulomb bubble is evaluated by PDS scheme,

$$\begin{aligned} J_0(E) = J_0(E;0,0) &= \int \frac{d^3\mathbf{k}'}{(2\pi)^3} \int \frac{d^3\mathbf{k}}{(2\pi)^3} G_C(E,\mathbf{k}',\mathbf{k}) \ , \\ &= \int \frac{d^3\mathbf{q}}{(2\pi)^3} \frac{1}{\mathbf{p}^2 - \mathbf{q}^2 + i\epsilon} C^2(\eta_q) \ , \\ &= -\frac{\mu}{2\pi} \left\{ \frac{\kappa}{D-3} + 2k_C \left[ H(\eta) + \frac{1}{D-4} - \ln\left(\frac{\kappa\sqrt{\pi}}{2k_C}\right) - 1 + \frac{3}{2}C_E \right\} \ , \end{aligned} \tag{B.34}$$

in which $\kappa$ , $D$ and $C_E \simeq 0.577$ are the renormalization scale, dimensionality of spacetime and the Euler-Mascheroni constant, respectively. $k_C = \eta k$ is a constant. For a real $\eta$, $H(\eta)$ can be expressed as

$$H(\eta) = \mathrm{Re}[\psi(1+i\eta)] - \ln\eta + \frac{i}{2\eta} C^2(\eta) \ , \tag{B.35}$$

in terms of digamma function $\psi(z)$.

Thus, the $n$th diagram is simply given by,

$$B_n(\mathbf{p}) = B_0(\mathbf{p})(\langle V_s \rangle J_0(E))^n \ . \tag{B.36}$$

Thus the sum of all the re-scattering diagrams is,

$$\mathcal{A}_{CS}^{(b)} = \sum_{n=0}^{\infty} B_n(\mathbf{p}) = B_0(\mathbf{p}) \sum_{n=0}^{\infty} (\langle V_s \rangle J_0(E))^n \ , \tag{B.37}$$

$$= \sqrt{Z} g 4 m_R^2 C(\eta_p) \mathrm{e}^{i\sigma_0} \mathcal{I} T_{CS} \ . \tag{B.38}$$

Again, like in Appendix. B.3, we have ignored the $-i$. $T_{CS}$ is given in Sec. 3.6, and in [71].

# C Projectors and Indices Projections

In this section we show how projectors are derived and how to use them to do projections.

## C.1 Two and Three Body Projectors

The two and three body projectors are convenient ways to handle the Clebsch-Gordon coefficients.

### Two-body projectors

Consider spin and isospin couplings of two nucleon fields,

$$N^T P N \ ,$$

where $P$ is a two-body projectors. A single nucleon is spin-1/2-isospin-1/2. A projector will handle couplings in both spin and isospin spaces. We will firstly consider only spin-space. The iso-spin space would be handled in exactly the same way. Denote,

$$\begin{aligned} \uparrow \ &:= |\tfrac{1}{2}, \tfrac{1}{2}\rangle \\ \downarrow \ &:= |\tfrac{1}{2}, -\tfrac{1}{2}\rangle \end{aligned} \ . \tag{C.1}$$

A spin-singlet, denoted by $|0,0\rangle$, can be written as

$$|0,0\rangle = \frac{1}{\sqrt{2}}(\uparrow\downarrow - \downarrow\uparrow) = \begin{pmatrix} \uparrow & \downarrow \end{pmatrix} \frac{1}{\sqrt{2}} \begin{pmatrix} 0 & 1 \\ -1 & 0 \end{pmatrix} \begin{pmatrix} \uparrow \\ \downarrow \end{pmatrix} = \begin{pmatrix} \uparrow & \downarrow \end{pmatrix} \frac{i}{\sqrt{2}} \sigma^2 \begin{pmatrix} \uparrow \\ \downarrow \end{pmatrix} \ . \tag{C.2}$$

Thus, if want to project a NN onto spin-singlet channel, we could use the projector $\frac{i}{\sqrt{2}}\sigma^2$ instead. Spin-triplet could be expressed similarly,

$$\begin{aligned} |1,+\rangle &= \uparrow\uparrow \\ |1,0\rangle &= \tfrac{1}{\sqrt{2}}(\uparrow\downarrow + \downarrow\uparrow) \\ |1,-\rangle &= \downarrow\downarrow \end{aligned} \ . \tag{C.3}$$

The corresponding projectors are,

$$
\begin{aligned}
P^{+}_{\text{spin-triplet}} &= -\tfrac{i}{\sqrt{2}}\sigma^2\tfrac{1}{\sqrt{2}}(i\sigma^2-\sigma^1)\ ,\\
P^{0}_{\text{spin-triplet}} &= -\tfrac{i}{\sqrt{2}}\sigma^2\sigma^3\ ,\\
P^{-}_{\text{spin-triplet}} &= -\tfrac{i}{\sqrt{2}}\sigma^2\tfrac{1}{\sqrt{2}}(i\sigma^2+\sigma^1)\ .
\end{aligned}
$$

One can easily prove these are equal to Clebsch-Gordon coefficients. Combined the projectors of spin and isospin spaces, we get the two body projectors,

$$\text{Spin-triplet-isospin-singlet: } P^{i}_{2t} = \frac{1}{\sqrt{8}}\sigma^2\sigma^i\tau^2\ , \tag{C.4}$$

$$\text{Spin-singlet-isospin-triplet: } P^{A}_{2s} = \frac{1}{\sqrt{8}}\sigma^2\tau^2\tau^A\ , \tag{C.5}$$

$$\text{Spin-singlet-isospin-pp: } P^{pp}_{2s} = \frac{1}{\sqrt{8}}\sigma^2\tau^2\frac{1}{\sqrt{2}}(i\tau^2-\tau^1)\ , \tag{C.6}$$

$$\text{Spin-singlet-isospin-np: } P^{np}_{2s} = \frac{1}{\sqrt{8}}\sigma^2\tau^2\tau^3\ , \tag{C.7}$$

$$\text{Spin-singlet-isospin-nn: } P^{nn}_{2s} = \frac{1}{\sqrt{8}}\sigma^2\tau^2\frac{1}{\sqrt{2}}(i\tau^2+\tau^1)\ . \tag{C.8}$$

The $P^{i}_{2t}$ and $P^{A}_{2s}$ are in coordinate space. $P^{pp}_{2s}$, $P^{np}_{2s}$, and $P^{nn}_{2s}$ are in spherical space. Notice that when combining the spin and isospin projectors, we add an addition constant factor of $1/\sqrt{2}$. This implies we consider the nucleon fields distinguishable when doing contractions.

### Three-body projectors

Three-body projectors handle the coupling between the trimer field and the combination of a dimer and a nucleon field. Notice that the three-body projectors we introduced in this dissertation are equal to Clebsch-Gordon coefficients only in our particular cases of $^3$H and $^3$He. But we will not have a three-neutron or three-proton state anyway. By doing a very similar but even easier analysis, we directly give the doublet channel projectors,

$$P^{i}_{3t} = \frac{1}{\sqrt{3}}\sigma^i\ ,\ P^{A}_{3s} = \frac{1}{\sqrt{3}}\tau^A, \tag{C.9}$$

where $P^i_{3t}$ project onto spin-doublet channel and $P^A_{3s}$ project onto isospin-doublet channel. It is intuitive to also provide the isospin doublet projectors in spherical basis,

$$P^{pp}_{3s} = \frac{1}{\sqrt{6}}(i\tau^2 - \tau^1)\ , P^{np}_{3s} = \frac{1}{\sqrt{3}}\tau^3\ , P^{nn}_{3s} = \frac{1}{\sqrt{6}}(i\tau^2 + \tau^1)\ . \tag{C.10}$$

The quartet channel projectors are complicated. We provide the definition here,

$$P^{i,j}_{3t,q} = \delta^{i,j} - \frac{1}{3}\sigma^i\sigma^j, P^{A,B}_{3s,q} = \delta^{A,B} - \frac{1}{3}\sigma^A\sigma^B. \tag{C.11}$$

For more details, see [58].

## C.2 Indices of the $^3$He Vertex Functions

The $^3$He vertex function is shown in Fig. 5.1. Note that $T = 1/2$, $S = 1/2$ for the three-nucleon systems. The time goes from left to right in the diagram, while the initial state is to the right of the final state in our calculation. We first look at the inhomogeneous terms. The spin, isospin indices of the initial trimer field and final nucleon field are denoted as $(\alpha, a)$ and $(\beta, b)$. Here the Greek letters represents the spin-indices while the latin letters denote the isospin indices. The spin-triplet/singlet dimer field in the final state carries a spin/isospin polarization of $j/B$.

We project the final state of $C_t$ onto spin doublet channel, while for $C_{np}$ and $C_{pp}$ we leave them unprojected. Read directly from the 3-body Lagrangian in Eq. (5.2.12), the inhomogeneous term is given by,

$$\boldsymbol{I}_C = i\omega \begin{pmatrix} (P^{j\dagger}_{3t})^{bb'}_{\beta\beta'}(P^{j}_{3t})^{b'a}_{\beta'\alpha} \\ -(P^{np}_{3s})^{ba}_{\beta\alpha} \\ -(P^{pp}_{3s})^{ba}_{\beta\alpha} \end{pmatrix}\ . \tag{C.12}$$

The superscripts are isospin indices and the subscripts are spin indices. The first and the second indices will always denote the row and column indices, respectively. Notice the fact that the $C_{pp}$ is the only one with an outgoing pp-dimer and a neutron field. We get the

inhomogeneous term by,

$$\boldsymbol{I}_C = i\omega \begin{pmatrix} \delta_{\beta\alpha}\mathbb{1}^{ba}\big|_{a=1,b=1} \\ -\delta_{\beta\alpha}\frac{1}{\sqrt{3}}(\tau_3)^{ba}\big|_{a=1,b=1} \\ -\delta_{\beta\alpha}\frac{1}{\sqrt{6}}(i\tau_2-\tau_1)^{ba}\big|_{a=1,b=2} \end{pmatrix} = i\omega \begin{pmatrix} 1 \\ -\frac{1}{\sqrt{3}} \\ \sqrt{\frac{2}{3}} \end{pmatrix} , \tag{C.13}$$

where $\delta_{\beta\alpha}$ is Kronecker delta function.

The homogeneous terms can be analysed similarly. We first work on the $K_s$ kernel. $K_{t1}$, $K_{t2}$ and $K_b$ have similar process as $K_s$, and we will not repeat them. The spin, isospin indices of the initial trimer field and final nucleon field are denoted as $(\alpha, a)$ abd $(\beta, b)$. The nucleon field connect to the trimer carries spin and isospin indices of $(\gamma, c)$. The spin and isospin indices of the exchanged nucleon field is denoted as $(\delta, d)$. The spin-triplet/singlet dimer field in the initial and final state carry spin/isospin polarization of $i/A$ and $j/B$, respectively. There are nine elements in total. It is concise to express them all in matrix form, given by

$$\begin{aligned} \boldsymbol{M}_{ks} &= \begin{pmatrix} (P^{j\dagger}_{3t})^{bb'}_{\beta\beta'}(P^{i\dagger}_{2t})^{b'd}_{\beta'\delta}(P^{j}_{2t})^{dc'}_{\delta\gamma'}(P^{i}_{3t})^{c'a}_{\gamma'\alpha} & (P^{j\dagger}_{3t})^{bb'}_{\beta\beta'}(P^{np\dagger}_{2s})^{b'd}_{\beta'\delta}(P^{j}_{2t})^{dc}_{\delta\gamma} & (P^{j\dagger}_{3t})^{bb'}_{\beta\beta'}(P^{pp\dagger}_{2s})^{b'd}_{\beta'\delta}(P^{j}_{2t})^{dc}_{\delta\gamma} \\ (P^{i\dagger}_{2t})^{bd}_{\beta\delta}(P^{np}_{2s})^{dc'}_{\delta\gamma'}(P^{i}_{3t})^{c'a}_{\gamma'\alpha} & (P^{np\dagger}_{2s})^{bd}_{\beta\delta}(P^{np}_{2s})^{dc}_{\delta\gamma} & (P^{pp\dagger}_{2s})^{bd}_{\beta\delta}(P^{np}_{2s})^{dc}_{\delta\gamma} \\ (P^{i\dagger}_{2t})^{bd}_{\beta\delta}(P^{pp}_{2s})^{dc'}_{\delta\gamma'}(P^{i}_{3t})^{c'a}_{\gamma'\alpha} & (P^{np\dagger}_{2s})^{bd}_{\beta\delta}(P^{pp}_{2s})^{dc}_{\delta\gamma} & (P^{pp\dagger}_{2s})^{bd}_{\beta\delta}(P^{pp}_{2s})^{dc}_{\delta\gamma} \end{pmatrix} \\ &= \begin{pmatrix} \left(P^{j\dagger}_{3t}P^{i\dagger}_{2t}P^{j}_{2t}P^{i}_{3t}\right)^{ba}_{\beta\alpha} & \left(P^{j\dagger}_{3t}P^{np\dagger}_{2s}P^{j}_{2t}\right)^{bc}_{\beta\gamma} & \left(P^{j\dagger}_{3t}P^{pp\dagger}_{2s}P^{j}_{2t}\right)^{bc}_{\beta\gamma} \\ \left(P^{i\dagger}_{2t}P^{np}_{2s}P^{i}_{3t}\right)^{ba}_{\beta\alpha} & \left(P^{np\dagger}_{2s}P^{np}_{2s}\right)^{bc}_{\beta\gamma} & \left(P^{pp\dagger}_{2s}P^{np}_{2s}\right)^{bc}_{\beta\gamma} \\ \left(P^{i\dagger}_{2t}P^{pp}_{2s}P^{i}_{3t}\right)^{ba}_{\beta\alpha} & \left(P^{np\dagger}_{2s}P^{pp}_{2s}\right)^{bc}_{\beta\gamma} & \left(P^{pp\dagger}_{2s}P^{pp}_{2s}\right)^{bc}_{\beta\gamma} \end{pmatrix} , \end{aligned} \tag{C.14}$$

where the first, second and third row/column of the matrix correspond to the channel with an outgoing/incoming spin-triplet, spin-singlet-np, and spin-singlet-pp dimer propagator, respectively. For a pp channel, one need to pick up the isospin index to be 2. For the other two channel, isospin index is selected as 1. By inserting projectors and picking up correct

indices, one get

$$\boldsymbol{M}_{ks} = \begin{pmatrix} -1 & \sqrt{3} & -\sqrt{6} \\ \sqrt{3} & 1 & \sqrt{2} \\ -\sqrt{6} & \sqrt{2} & 0 \end{pmatrix} . \tag{C.15}$$

Similarly, one can get $M_{kt1}$, $M_{kt2}$ and $M_{kb}$ by adding $\frac{1+\tau^3}{2}$ between corresponding projectors. We will not cover details here.

# D The deuteron electric dipole form factor and EDM

The diagrams that give the deuteron EDM are given in Fig. 8. The EDFF of the deuteron $F(q^2, {}^2\mathrm{H})$ is only sensitive to the isospin-one $C_{{}^3S_1-{}^3P_1}$ coupling, and we obtain

$$F(q^2, {}^2\mathrm{H}) = \left(d_n + d_p - C_{{}^3S_1-{}^3P_1}\right)\frac{4\gamma_t}{q}\arctan\frac{q}{4\gamma_t} \tag{D.1}$$

$$= \left(d_n + d_p - C_{{}^3S_1-{}^3P_1}\right) F_c(q^2, {}^2\mathrm{H}) \ , \tag{D.2}$$

where $F_c(q^2, {}^2\mathrm{H})$ denotes the charge form factor of the deuteron. The resulting EDM is obtained by taking the $q \to 0$ limit,

$$d = \left(d_n + d_p - C_{{}^3S_1-{}^3P_1}\right) \ . \tag{D.3}$$

The direct proportionality of the EDFF to the charge form factor causes the Schiff moment of the deuteron to be zero.

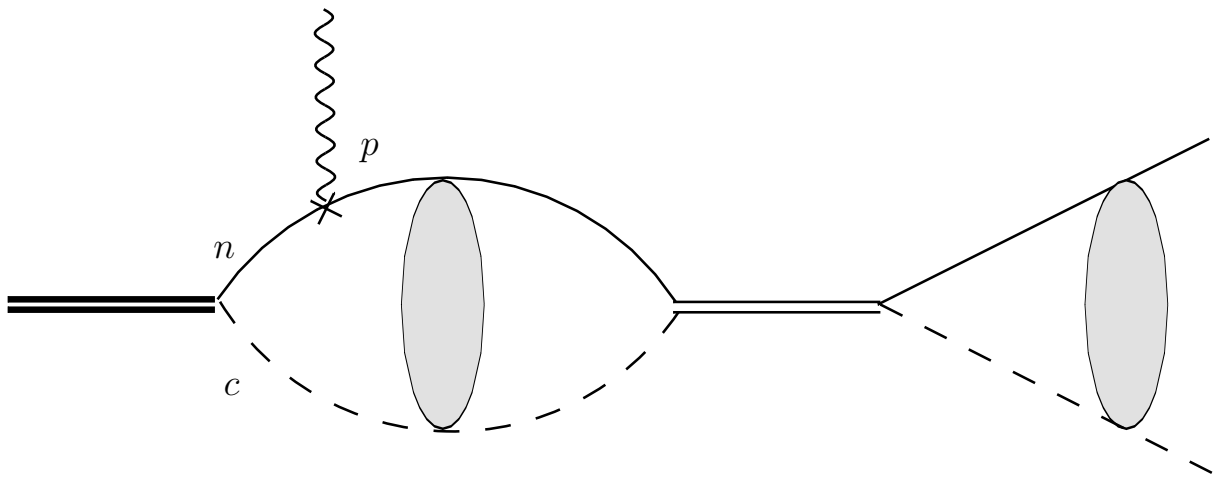


**Figure 7:** The first re-scattering process considered in the final state interaction. The thin double line in the middle is the bare boron-11 dimer propagator. Solid eclipses are coulomb bubbles. Single solid and dashed line are nucleon field and core field, respectively.

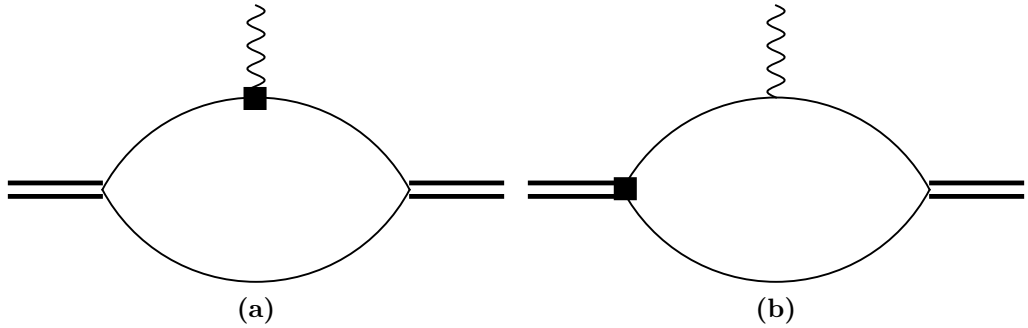


**Figure 8:** Diagrams contribute to the deuteron EDM. The black squares denote insertions of CP-odd operators. We omitted the diagrams that have the CP-odd operators to the right of the photon-nucleon vertex.

# E Expressions for electric form factors $F_C$ and $F_{\mathrm{I}}$

In this section, we give complete expressions for the diagrams contributing to the form factor $F_{\mathrm{I}}$. To avoid confusion, we note that we write $q = |\boldsymbol{q}|$. The three-nucleon wave function renormalization $Z_\psi$ is defined as

$$Z_\psi = \pi \left( \frac{d\Sigma(E)}{dE}\bigg|_{E=B} \right)^{-1} , \tag{E.1}$$

where the self-energy $\Sigma$ can be calculated via

$$\Sigma(E) = -\pi \widetilde{\mathbf{1}}^T \otimes_q \widetilde{\boldsymbol{\mathcal{G}}}(E,q) , \tag{E.2}$$

and $B$ is the three-nucleon binding energy.

We simultaneously give expressions for the LO contributions to the CP-even three-nucleon form factor; also see Ref. [149], and the LO contributions to the CP-odd form factor $F_I$. The CP-even form factor is denoted with a subscript "$C$", while the CP-odd form factor is denoted with a subscript "$I$". The corresponding diagrams (a), (b), and (c) are the same as Fig. 4.3, but with a CP-even photon vertex.

**Diagram A:** The calculation of the form factor diagrams is carried out in the Breit frame. The vertex functions in diagram (a) that were originally defined in the center-of-mass frame need to be boosted; for details see Ref. [149]. The sum of the three terms simplifies to

$$F^A_{C\backslash\mathrm{I}}\left(q^2\right) = Z_\psi \Big[ \mathcal{A}^{(a)}_{C\backslash\mathrm{I}}(q) + 2\widetilde{\boldsymbol{\mathcal{G}}}^T(B,p) \otimes_p \boldsymbol{\mathcal{A}}^{(b)}_{C\backslash\mathrm{I}}(q,p) + \widetilde{\boldsymbol{\mathcal{G}}}^T(B,p) \otimes_p \boldsymbol{\mathcal{A}}^{(c)}_{C\backslash\mathrm{I}}(q,p,k) \otimes_k \widetilde{\boldsymbol{\mathcal{G}}}(B,k) \Big] . \tag{E.3}$$

In this equation and below, $B$ denotes the binding energy of the three-nucleon state under consideration. For the CP-even and one-body CP-odd photon vertex, we define the following

matrices,

$$\boldsymbol{M}_C^A = \begin{pmatrix} \frac{1+\tau_3}{2} & 0 \\ 0 & \frac{3-\tau_3}{6} \end{pmatrix}, \ \boldsymbol{M}_{\mathrm{I}}^A = \frac{1}{6}\begin{pmatrix} d_n(\tau^3-1) - d_p(\tau^3+1) & 0 \\ 0 & d_n(\tau^3+3) - d_p(\tau^3-3) \end{pmatrix}. \tag{E.4}$$

The first term in Eq. (E.3) is given by

$$\mathcal{A}^{(a)}_{C\backslash\mathrm{I}}(q) = \frac{M_N}{4\pi^2}\Big|_0^1 \int_0^\Lambda dl \int_{-1}^1 dx \frac{l}{qx} \widetilde{\mathbf{1}}^T \boldsymbol{M}^A_{C\backslash\mathrm{I}} \boldsymbol{\mathcal{D}}(B,q,l,x,y)\widetilde{\mathbf{1}} \ , \tag{E.5}$$

where

$$\boldsymbol{\mathcal{D}}(B,q,l,x,y) = \boldsymbol{D}\left(B - \frac{l^2}{2M_N} - \frac{q^2}{12M_N} + \big(\frac{1}{2}-y\big)\frac{lqx}{M_N}, l\right) \ , \tag{E.6}$$

and

$$\Big|_0^1 f(y) = f(1) - f(0) \ . \tag{E.7}$$

The second term of Eq. (E.3) includes the CP-even vertex function and the function $\mathcal{A}^{(b)}_{C\backslash\mathrm{I}}(q,p)$ that is defined as

$$\boldsymbol{\mathcal{A}}^{(b)}_{C\backslash\mathrm{I}}(q,p) = \frac{M_N}{2\pi}\Big|_0^1 \int_0^\Lambda dl \int_{-1}^1 dx \frac{l}{qx} \frac{1}{p\sqrt{l^2 - \frac{2}{3}lqx + \frac{1}{9}q^2}} Q_0^{\mathrm{boost}}(q,l,p,x,y,2) \times \begin{pmatrix} -1 & 3 \\ 3 & -1 \end{pmatrix} \boldsymbol{M}^A_{C\backslash\mathrm{I}} \boldsymbol{\mathcal{D}}(B,q,l,x,y)\widetilde{\mathbf{1}} \ , \tag{E.8}$$

where $x$ is defined through $\boldsymbol{l}\cdot\boldsymbol{q} = lqx$. We also defined a boosted version of the function $Q_0$,

$$Q_0^{\mathrm{boost}}(q,l,k,x,y,z) = Q_0\left(\frac{k^2 + l^2 + \frac{q^2}{9} + (y - \frac{z}{3})lqx - M_N B}{k\sqrt{l^2 + \frac{q^2}{9} - (-1)^z \frac{2}{3}lqx}}\right) \ . \tag{E.9}$$

The third term in Eq. (E.3) includes the function

$$\boldsymbol{\mathcal{A}}^{(c)}_{C\backslash\mathrm{I}}(q,p,k) = M_N\Big|_0^1 \int_0^\Lambda dl \int_{-1}^1 dx \frac{l}{qx} \frac{Q_0^{\mathrm{boost}}(q,l,k,x,y,1) Q_0^{\mathrm{boost}}(q,l,p,x,y,2)}{kp\sqrt{l^2+\frac{2}{3}lqx+\frac{1}{9}q^2}\sqrt{l^2-\frac{2}{3}lqx+\frac{1}{9}q^2}}$$
$$\times \begin{pmatrix} -1 & 3 \\ 3 & -1 \end{pmatrix} \boldsymbol{M}^A_{C\backslash\mathrm{I}} \boldsymbol{\mathcal{D}}(B,q,l,x,y) \begin{pmatrix} -1 & 3 \\ 3 & -1 \end{pmatrix} . \tag{E.10}$$

**Diagram B:** For the CP-even and one-body CP-odd photon vertex, we define the following matrices,

$$\boldsymbol{M}^B_C = \begin{pmatrix} \frac{\tau^3-1}{2} & \frac{3+\tau^3}{2} \\ \frac{3+\tau^3}{2} & -\frac{3+5\tau^3}{6} \end{pmatrix},$$
$$\boldsymbol{M}^B_{\mathrm{I}} = \frac{1}{12} \begin{pmatrix} 5d_p(\tau^3-1) - 5d_n(\tau^3+1) & d_p(\tau^3+3) - d_n(\tau^3-3) \\ d_p(\tau^3+3) - d_n(\tau^3-3) & d_p(5\tau^3+3) - d_n(5\tau^3-3) \end{pmatrix}. \tag{E.11}$$

The contribution from diagram (b) in Fig. 4.3 is given by

$$F^B_{C\backslash\mathrm{I}}\left(q^2\right) = Z_\psi \int_{-1}^1 dx \int_{-1}^1 dy\, \widetilde{\boldsymbol{\mathcal{G}}}^T(B,p) \otimes_p \Gamma^B(q,p,k,x,y) \boldsymbol{M}^B_{C\backslash\mathrm{I}} \otimes_k \widetilde{\boldsymbol{\mathcal{G}}}(B,k) , \tag{E.12}$$

where we defined

$$\Gamma^B(q,p,k,x,y) = -\frac{M_N}{4} \int_0^{2\pi} d\phi$$
$$\times \left[k^2+p^2+kp(xy+\sqrt{1-x^2}\sqrt{1-y^2}\cos\phi) + \frac{1}{3}q(kx+2py) + \frac{1}{9}q^2 - M_N B\right]^{-1}$$
$$\times \left[k^2+p^2+kp(xy+\sqrt{1-x^2}\sqrt{1-y^2}\cos\phi) - \frac{1}{3}q(2kx+py) + \frac{1}{9}q^2 - M_N B\right]^{-1} , \tag{E.13}$$

and the x-, y- and $\phi$-integrals are angular integrals,

$$\mathbf{k}\cdot\mathbf{q} = kqx \ , \tag{E.14}$$

$$\mathbf{p}\cdot\mathbf{q} = pqy \ , \tag{E.15}$$

$$\mathbf{k}\cdot\mathbf{p} = kp\cos\phi. \tag{E.16}$$

Note that $y$ in $F^B_{C\backslash \mathrm{I}}(q^2)$ represents $\cos\theta_{pq}$, which is different from the $y$ defined in Eq. (E.7).

**Diagram C:** Finally, for the CP-even and one-body CP-odd photon vertex, we define the matrices

$$\boldsymbol{M}^C_C = \begin{pmatrix} 1 & 0 \\ 0 & 1+\frac{2\tau^3}{3} \end{pmatrix}, \ \boldsymbol{M}^C_{\mathrm{I}} = \begin{pmatrix} 2\tau^3(d_n+d_p) & d_p-d_n \\ d_p-d_n & 0 \end{pmatrix}. \tag{E.17}$$

The contribution from diagram (c) in Fig. 4.3 is given by

$$F^C_{C\backslash \mathrm{I}}\left(q^2\right) = Z_\psi \int_{-1}^{1} dx\, \Gamma^C(q,k,x) \otimes_k \left[\widetilde{\boldsymbol{\mathcal{G}}}^T(B,p)\boldsymbol{M}^C_{C\backslash \mathrm{I}}\widetilde{\boldsymbol{\mathcal{G}}}(B,k)\right] \ , \tag{E.18}$$

where $x$ is defined through $\mathbf{k}\cdot\mathbf{q} = kqx$ and the function $\Gamma^C(q,k)$ is defined as

$$\Gamma^C(q,k,x) = \frac{M_N}{q}\arctan\left(\frac{q}{2\sqrt{\frac{3}{4}p^2 - M_N B} + 2\sqrt{\frac{3}{4}k^2 - M_N B}}\right) \ , \tag{E.19}$$

and

$$\mathbf{p} = \mathbf{k} + \frac{1}{3}\mathbf{q} \ . \tag{E.20}$$

# F Expressions for form factor $F_{\rm II}$

Below we give the expressions for the contributions to the CP-odd form factor arising from CP-odd two-nucleon operators.

## F.1 Boosted vertex functions (of Diagram A)

The transition to the Breit frame again requires us to relate vertex functions that were defined in the center of mass frame to boosted ones. The boosted CP-even vertex function $\mathcal{G}$ is given by the integral (see also Ref. [149])

$$\boldsymbol{\mathcal{G}}^{\rm boost}(q,l,x,y,z) = \widetilde{\mathbf{1}} + R_0^{\rm boost}(q,l,k,x,y,z) \begin{pmatrix} -1 & 3 \\ 3 & -1 \end{pmatrix} \otimes_k \tilde{\boldsymbol{\mathcal{G}}}(B,k) \ . \tag{F.1}$$

Here $x$ denotes the cosine of the angle between the boost momentum $q$ and the relative momentum $l$ between the dimer and the nucleon field. We have also already carried out the $l_0$ loop integration that enters when the vertex functions is folded with the remaining parts of the diagrams for the matrix elements. The factor $z$ is introduced for convenience to have a short-hand notation for the kinematically different vertex functions on the left or right hand side of the photon vertex. The boosted function $R_0^{\rm boost}$ is given by

$$R_0^{\rm boost}(q,l,k,x,y,z) = \frac{2\pi}{k\sqrt{l^2+\frac{q^2}{9}-(-1)^z\frac{2}{3}lqx}} Q_0^{\rm boost}(q,l,k,x,y,z), \tag{F.2}$$

with $Q_0^{\rm boost}$ defined in Eq. (E.9).

We also need the boosted CP-odd vertex function $\mathcal{T}$:

$$\boldsymbol{\mathcal{T}}_A^{\rm boost}(q,l,x,y,z) = \left(\frac{lx}{q} - \frac{(-1)^z}{3}\right) \left[ \begin{pmatrix} \frac{1+\tau^3}{2} & 0 \\ 0 & \frac{3-\tau^3}{6} \end{pmatrix} \boldsymbol{\mathcal{T}}^{\frac{1}{2},\rm boost}(q,l,x,y,z) \right. \\ \left. + \begin{pmatrix} 0 & 0 \\ 0 & \frac{2}{3} \end{pmatrix} \boldsymbol{\mathcal{T}}^{\frac{3}{2},\rm boost}(q,l,x,y,z) \right] \ . \tag{F.3}$$

The boosted isospin-projected CP-odd vertex functions required in Eq. (F.3) are given by

$$\begin{aligned}
\boldsymbol{\mathcal{T}}^{\frac{1}{2},\text{boost}}(q,l,x,y,z) =& \boldsymbol{R}_{\mathcal{T}}^{\frac{1}{2},\text{boost}}(q,l,k,x,y,z) \otimes_k \widetilde{\boldsymbol{\mathcal{T}}}^{\frac{1}{2}}(B,k) + \boldsymbol{R}^{\frac{1}{2},\text{boost}}(q,l,k,x,y,z) \otimes_k \widetilde{\boldsymbol{\mathcal{G}}}(B,k) \ , \\
\boldsymbol{\mathcal{T}}^{\frac{3}{2},\text{boost}}(q,l,x,y,z) =& \boldsymbol{R}_{\mathcal{T}}^{\frac{3}{2},\text{boost}}(q,l,k,x,y,z) \otimes_k \widetilde{\boldsymbol{\mathcal{T}}}^{\frac{3}{2}}(B,k) + \boldsymbol{R}^{\frac{3}{2},\text{boost}}(q,l,k,x,y,z) \otimes_k \widetilde{\boldsymbol{\mathcal{G}}}(B,k) \ ,
\end{aligned} \tag{F.4}$$

where

$$\begin{aligned}
\boldsymbol{R}_{\mathcal{T}}^{\frac{1}{2},\text{boost}}(q,l,k,x,y,z) =& R_1^{\text{boost}}(q,l,k,x,y,z) \begin{pmatrix} -1 & 3 \\ 3 & -1 \end{pmatrix} , \\
\boldsymbol{R}_{\mathcal{T}}^{\frac{3}{2},\text{boost}}(q,l,k,x,y,z) =& R_1^{\text{boost}}(q,l,k,x,y,z) \begin{pmatrix} 0 & 0 \\ 0 & 2 \end{pmatrix} , \\
\boldsymbol{R}^{\frac{1}{2},\text{boost}}(q,l,k,x,y,z) =& \left[ R_0^{\text{boost}}(q,l,k,x,y,z) \begin{pmatrix} -1 & 1 \\ -2 & 0 \end{pmatrix} + R_1^{\text{boost}}(q,l,k,x,y,z) \begin{pmatrix} 1 & 2 \\ -1 & 0 \end{pmatrix} \right] \\
& \times \left( C_{^3S_1-^1P_1} + \frac{2}{3}\tau^3 C_{^3S_1-^3P_1} \right) \\
& + \left[ R_0^{\text{boost}}(q,l,k,x,y,z) \begin{pmatrix} 0 & 2 \\ -1 & 1 \end{pmatrix} - R_1^{\text{boost}}(q,l,k,x,y,z) \begin{pmatrix} 0 & -1 \\ 2 & 1 \end{pmatrix} \right] \\
& \times \left( C^{(0)}_{^1S_0-^3P_0} - \frac{2}{3}\tau^3 C^{(1)}_{^1S_0-^3P_0} \right) , \\
\left(\boldsymbol{R}^{\frac{3}{2},\text{boost}}\right)^T(q,l,k,x,y,z) =& R_0^{\text{boost}}(q,l,k,x,y,z) \frac{1}{3} \begin{pmatrix} 0 & 8C_{^3S_1-^3P_1} - C^{(1)}_{^1S_0-^3P_0} + 3\tau_3 C^{(2)}_{^1S_0-^3P_0} \\ 0 & -5(C^{(1)}_{^1S_0-^3P_0} - 3\tau_3 C^{(2)}_{^1S_0-^3P_0}) \end{pmatrix} \\
& + R_1^{\text{boost}}(q,l,k,x,y,z) \frac{1}{3} \begin{pmatrix} 0 & 4C_{^3S_1-^3P_1} - 2\left(C^{(1)}_{^1S_0-^3P_0} - 3\tau_3 C^{(2)}_{^1S_0-^3P_0}\right) \\ 0 & -4\left(C^{(1)}_{^1S_0-^3P_0} - 3\tau_3 C^{(2)}_{^1S_0-^3P_0}\right) \end{pmatrix} \ .
\end{aligned} \tag{F.5}$$

The function $R_0^{\text{boost}}$ is given in Eq. (F.2) while

$$R_1^{\text{boost}}(q,l,k,x,y,z) = \frac{2\pi}{l^2+\frac{q^2}{9}-(-1)^z\frac{2}{3}lqx} \times \left(1-\frac{k^2+l^2+\frac{q^2}{9}+(y-\frac{z}{3})lqx-M_N B}{k\sqrt{l^2+\frac{q2}{9}-(-1)^z\frac{2}{3}lqx}}Q_0^{\text{boost}}(q,l,k,x,y,z)\right). \tag{F.6}$$

## F.2 Diagram A

Diagram (a) in Fig. 4.4 is given by

$$F_{\text{II}}^A(q^2) = Z_\psi\Big|_0^1\int_0^\Lambda dl\int_{-1}^1 dx\frac{M_N}{4\pi^2}\frac{2}{3}\frac{l}{qx}\Big[\left(\boldsymbol{\mathcal{G}}^{\text{boost}}\right)^T(q,l,x,y,2)\boldsymbol{\mathcal{D}}(B,q,l,x,y)\boldsymbol{\mathcal{T}}_A^{\text{boost}}(q,l,x,y,1) - \left(\boldsymbol{\mathcal{T}}_A^{\text{boost}}\right)^T(q,l,x,y,2)\boldsymbol{\mathcal{D}}(B,q,l,x,y)\boldsymbol{\mathcal{G}}^{\text{boost}}(q,l,x,y,1)\Big], \tag{F.7}$$

where the boosted CP-even and CP-odd vertex functions were defined above.

## F.3 Diagrams B and D

**Diagram B:** Diagram (b) in Fig. 4.4 is given by

$$F_{\text{II}}^B(q^2) = Z_\psi\frac{1}{q^2}\int_{-1}^1 dx\int_{-1}^1 dy\left\{\widetilde{\boldsymbol{\mathcal{G}}}^T(B,p)\otimes_p\left(\Gamma^B(q,p,k,x,y)\,\mathbf{k}\cdot\mathbf{q}\right)\otimes_k\widetilde{\boldsymbol{\mathcal{T}}}_B(B,k) - \widetilde{\boldsymbol{\mathcal{T}}}_B^T(B,p)\otimes_p\left(\mathbf{p}\cdot\mathbf{q}\,\Gamma^B(q,p,k,x,y)\right)\otimes_k\widetilde{\boldsymbol{\mathcal{G}}}(B,k)\right\}, \tag{F.8}$$

where

$$\widetilde{\boldsymbol{\mathcal{T}}}_B(B,k) = \begin{pmatrix}\frac{\tau^3-1}{2} & \frac{\tau^3+3}{2}\\ \frac{\tau^3+3}{2} & \frac{-5\tau^3-3}{6}\end{pmatrix}\widetilde{\boldsymbol{\mathcal{T}}}^{\frac{1}{2}}(B,k) + \begin{pmatrix}0 & -2\\ 0 & -\frac{2}{3}\end{pmatrix}\widetilde{\boldsymbol{\mathcal{T}}}^{\frac{3}{2}}(B,k). \tag{F.9}$$

**Diagram D:** Diagram (d) in Fig. 4.4 can be written as

$$F_{\rm II}^{D}(q^2) = Z_\psi \int_{-1}^{1} dx \int_{-1}^{1} dy\, \widetilde{\boldsymbol{\mathcal{G}}}^T(B,p) \otimes_p \Bigg\{ \Gamma^B(q,p,k,x,y) \times \left[ \frac{kx+2py-\frac{2}{3}q}{q} \boldsymbol{M}_D^T - \frac{2kx+py+\frac{2}{3}q}{q} \boldsymbol{M}_D \right] \Bigg\} \otimes_k \widetilde{\boldsymbol{\mathcal{G}}}(B,k) \ , \quad \text{(F.10)}$$

where

$$\boldsymbol{M}_D = \begin{pmatrix} \frac{\tau^3-1}{6}(3C_{^3S_1-^1P_1} - 2C_{^3S_1-^3P_1}) & \frac{3+\tau^3}{6} C^{(0)}_{^1S_0-^3P_0} - \frac{1+\tau^3}{3} C^{(1)}_{^1S_0-^3P_0} + \frac{2\tau^3}{3} C^{(2)}_{^1S_0-^3P_0} \\ -\frac{3+\tau^3}{6}\left(C_{^3S_1-^1P_1} + 2C_{^3S_1-^3P_1}\right) & \frac{3+5\tau^3}{6} C^{(0)}_{^1S_0-^3P_0} - \frac{1+\tau^3}{3} C^{(1)}_{^1S_0-^3P_0} - \frac{2\tau^3}{3} C^{(2)}_{^1S_0-^3P_0} \end{pmatrix} . \quad \text{(F.11)}$$

The variables $x$, $y$ and the function $\Gamma^B(q,p,k,x,y)$ are defined in Eq. (E.14), Eq. (E.15) and Eq. (E.13).

## F.4 Diagrams C and E

**Diagram C:** Diagram (c) in Fig. 4.4 leads to

$$F_{\rm II}^{C}(q^2) = Z_\psi \int_{-1}^{1} dx\, \Gamma^C(q,k,x) \otimes_k \frac{1}{q^2} \left[ (\mathbf{k}\cdot\mathbf{q}) \widetilde{\boldsymbol{\mathcal{G}}}^T(B,p) \widetilde{\boldsymbol{\mathcal{T}}}_C(B,k) - (\mathbf{p}\cdot\mathbf{q}) \widetilde{\boldsymbol{\mathcal{T}}}_C^T(B,p) \widetilde{\boldsymbol{\mathcal{G}}}(B,k) \right] , \quad \text{(F.12)}$$

where

$$\widetilde{\boldsymbol{\mathcal{T}}}_C(B,k) = \begin{pmatrix} 1 & 0 \\ 0 & 1+\frac{2}{3}\tau^3 \end{pmatrix} \widetilde{\boldsymbol{\mathcal{T}}}^{\frac{1}{2}}(B,k) + \begin{pmatrix} 0 & 0 \\ 0 & -\frac{2}{3} \end{pmatrix} \widetilde{\boldsymbol{\mathcal{T}}}^{\frac{3}{2}}(B,k) \ . \quad \text{(F.13)}$$

**Diagram E:** Diagram (e) in Fig. 4.4 is given by

$$F_{\rm II}^{E}(q^2) = 2Z_\psi \int_{-1}^{1} dx\, \Gamma^C(q,k,x) \otimes_k \widetilde{\boldsymbol{\mathcal{G}}}^T(B,p) \left[ \frac{\mathbf{p}\cdot\mathbf{q} + \frac{q^2}{3}}{q^2} + \frac{1}{2q} \left( \sqrt{-M_N B + \frac{3}{4}k^2} - \sqrt{-M_N B + \frac{3}{4}p^2} \right) \right] \boldsymbol{M}_E \widetilde{\boldsymbol{\mathcal{G}}}(B,k) \ , \quad \text{(F.14)}$$

and we define the matrix $\boldsymbol{M}_E$,

$$\boldsymbol{M}_E = \frac{\tau^3}{3} \begin{pmatrix} 2\tau^3 C_{^3S_1-^3P_1} & C_{^3S_1-^1P_1} \\ -(C^{(0)}_{^1S_0-^3P_0} - 2C^{(2)}_{^1S_0-^3P_0}) & 0 \end{pmatrix} . \tag{F.15}$$

The function $\Gamma^C(q,k,x)$ and $p$ are defined in Eq. (E.19) and in Eq. (E.20), respectively.

# G Expressions for form factor $F_{SU(4)}$

In the SU(4) limit, the two-body diagrams can be simplified to a universal function depending on $q$ times a combination of T-odd coefficients,

$$F_{\rm II}(q^2, SU(4)) = \widetilde{F}_{SU(4)}(q^2)\left(\tau^3 C_{^3S_1-^1P_1} + 2C_{^3S_1-^3P_1} + \tau^3 C^{(0)}_{^1S_0-^3P_0} - 2\tau^3 C^{(2)}_{^1S_0-^3P_0}\right), \quad \text{(G.1)}$$

Thus, the universal electric dipole form factor also has five terms,

$$\widetilde{F}_{SU(4)}(q^2) = \widetilde{F}_{SU(4),A}(q^2) + \widetilde{F}_{SU(4),B}(q^2) + \widetilde{F}_{SU(4),C}(q^2) + \widetilde{F}_{SU(4),D}(q^2) + \widetilde{F}_{SU(4),E}(q^2). \quad \text{(G.2)}$$

The first term is given by

$$\begin{aligned}\widetilde{F}_{SU(4),A}(q^2) =& Z_\psi \Bigg|_0^1 \int_0^\Lambda dl \int_{-1}^1 dx \frac{M_N}{4\pi^2}\frac{4l\mathcal{D}_+(B,q,l,x,y)}{9qx}\Bigg[\mathcal{G}_+^{\rm boost}(q,l,x,y,2)\mathcal{T}_{SU(4)}(q,l,x,y,1)\left(\frac{lx}{q}-\frac{1}{3}\right)\\ &-\left(\frac{lx}{q}+\frac{1}{3}\right)\mathcal{T}_{SU(4)}(q,l,x,y,2)\mathcal{G}_+^{\rm boost}(q,l,x,y,1)\Bigg], \quad \text{(G.3)}\end{aligned}$$

where the boosting is carried out analogously to Appendix F. The function $\mathcal{D}_+(B,q,l,x,y)$ is defined as

$$\mathcal{D}_+(B,q,l,x,y) = \frac{1}{2}\left(\mathcal{D}_t(B,q,l,x,y) - \mathcal{D}_s(B,q,l,x,y)\right), \quad \text{(G.4)}$$

where $\mathcal{D}_t$ and $\mathcal{D}_s$ are the diagonal elements of the matrix defined in Eq. (E.6). The second term is given by

$$\begin{aligned}\widetilde{F}_{SU(4),B}(q^2) =& Z_\psi \frac{1}{q^2}\int_{-1}^1 dx \int_{-1}^1 dy\, \frac{4}{3}\Bigg\{\widetilde{\mathcal{G}}_+(B,p)\otimes_p\left(\Gamma^B(q,p,k,x,y)\mathbf{k}\cdot\mathbf{q}\right)\otimes_k \widetilde{\mathcal{T}}_{SU(4)}(B,k)\\ &-\widetilde{\mathcal{T}}_{SU(4)}(B,p)\otimes_p\left(\mathbf{p}\cdot\mathbf{q}\Gamma^B(q,p,k,x,y)\right)\otimes_k\widetilde{\mathcal{G}}_+(B,k)\Bigg\}, \quad \text{(G.5)}\end{aligned}$$

where $\mathcal{G}_+(B,k)$ and $\mathcal{T}_{SU(4)}$ are defined in Eq. (4.3.7) and Eq. (4.3.8). Similarly, the remaining terms are

$$\widetilde{F}_{SU(4),C}(q^2) = Z_\psi \int_{-1}^{1} dx\, \Gamma^C(q,k,x) \otimes_k \frac{1}{q^2}\frac{-2}{3}\Big[(\mathbf{k}\cdot\mathbf{q})\widetilde{\mathcal{G}}_+(B,p)\widetilde{\mathcal{T}}_{SU(4)}(B,k) - (\mathbf{p}\cdot\mathbf{q})\widetilde{\mathcal{G}}_+(B,p)\widetilde{\mathcal{T}}_{SU(4)}(B,k)\Big] \ , \quad \text{(G.6)}$$

$$\widetilde{F}_{SU(4),D}(q^2) = -\int_{-1}^{1} dx \int_{-1}^{1} dy\, \widetilde{\mathcal{G}}_+(B,p) \otimes_p \Gamma^B(q,p,k,x,y) \otimes_k \widetilde{\mathcal{G}}_+(B,k) \times \frac{2}{3}\frac{kx - py + \frac{4}{3}q}{q} \ , \quad \text{(G.7)}$$

and

$$\widetilde{F}_{SU(4),E}(q^2) = Z_\psi \int_{-1}^{1} dx \frac{1}{3}\Gamma^C(q,k,x) \otimes_k \widetilde{\mathcal{G}}_+(B,p)\widetilde{\mathcal{G}}_+(B,k) \ . \quad \text{(G.8)}$$

Recall that $\Gamma^B(q,p,k,x,y)$, $\Gamma^C(q,k,x)$ and other variables are defined previously in the corresponding subsections in Appendix E.

# Vita

Zichao Yang grew up in Henan Province, China. In 2012, as one of the first class students of the university, he attended the Southern University of Science and Technology(SUSTech), Shenzhen, China, which was founded in 2011. At SUSTech, he did all kinds of spectroscopies and obtained a Bachelor of Science in Physics. He played soccer, scored, and won trophies. In Aug, 2016, he became a PhD student of the Department of Physics at the University of Tennessee, Knoxville (UTK). At UTK, he made progress in theoretical nuclear physics and earned himself a PhD degree. He traveled and saw good nature. He went to concerts before old school rockers died. He made new good friends as he always did. He shaped and educated himself, and became a better and happier guy. Leaving academia was not his first choice, but he was married and should be more responsible. After his graduation, he is going to be a software developer. He likes coding as well. But he will always be a physicist. He is ready for new adventures.